

Structure–Property–Relationships of Supramolecular Systems from First Principles Calculations

Daniel Sebastiani

Habilitation Thesis

June 2006

Johannes-Gutenberg Universität Mainz

Max-Planck-Institut für Polymerforschung Mainz

Contents

1	Introduction	
	Electronic structure computer simulations: Between experiment and analytical theory	3
2	Complexity in supramolecular systems	5
2.1	Length and time scales in nature and in simulations: Different degrees of complexity	5
2.2	System complexity and simulation detail – a reciprocal correlation	8
2.3	Ab-initio calculations of structure–property relationships in supramolecular systems	10
2.4	Scope of this work	14
3	Structure-Property relationships: from single molecules to complex supramolecular systems	15
3.1	Molecules and oligomers	15
3.1.1	Molecular conformations, electronic structure calculations, and spectroscopy	15
3.1.2	Benzoxazines: From dimers to oligomers	15
3.1.3	Aromaticity and homoaromaticity: Nucleus independent chemical shift maps of barbaralane and derivatives	19
3.2	Crystalline systems	22
3.2.1	Characterization and structure determination of crystals .	22
3.2.2	Bulk chemical shifts in strongly hydrogen bonded amino acid systems	24
3.2.3	NH···N hydrogen bonds in proton conducting materials .	26
3.2.4	Temperature-dependent deuteron nuclear quadrupole coupling constants	28
3.3	Surfaces and adsorbates	30
3.3.1	Electronic structure of surfaces: between bulk and molecule	30

3.3.2	Hydrogen bonding on metallic surfaces: water oligomers on nickel	32
3.4	Nanotubes as host/guest systems	34
3.4.1	Hydrogen-bonded molecular nanotubes from calixhydroquinone building blocks	34
3.4.2	Carbon nanotubes	37
3.5	Liquids and solutions	39
3.5.1	Hydrochloric acid: signatures of H_3O^+ and Cl^- solvation from ^1H NMR chemical shift spectra	39
4	Conclusion	43
A	Nucleus independent chemical shift maps	45
B	Published Habilitation work	49
C	Acknowledgements	52

1 Introduction

Electronic structure computer simulations: Between experiment and analytical theory

The theoretical description and prediction of experimental processes and system properties is an important aspect of scientific work. Theoretical scientists consider the initial conditions and the results of experiments and try to deduce general laws and principles. Based on these laws, predictions for novel systems can be made and subsequently tested against the corresponding experimental results. This procedure can lead to agreement, but equally well to disagreement of the postulated law with reality. Historically, the discovery of new fundamental laws has often been induced by the refutation of principles which had previously been “accepted knowledge” for considerable times.

It is a crucial criterion in science to be able to *invalidate* a statement; also today, such tests are an important part in the process of finding new principles. Since no physical or chemical theory can be *verified* in the sense of a mathematical proof, the inverse way has to be followed: it has to be shown that other principles – that are contradictory to the new proposed theory – lead to wrong predictions.

The prototype of this process is what happened in the late 19th and early 20th century, when the theory of quantum mechanics was developed. Experimentalists started to measure the energy flux $u(T, \lambda)$ of a black body as a function of temperature and wavelength with high accuracy and asked for a theoretical explanation. The Rayleigh-Jeans-law for the emitted radiation power of a black body, stating that $u(T, \lambda) \propto T^2/\lambda$, was found to be valid for high temperatures and large wavelengths, while Wien’s law, $u(T, \lambda) \propto \lambda^{-3}e^{-A/\lambda T}$, explained the black-body-radiation for low temperatures and small wavelengths. Obviously, both laws could not easily be brought to a mutual agreement. When Planck initially proposed an “interpolated” formula, it was mainly because both (only asymptotically correct) laws had been invalidated.

Planck had not yet constructed the full picture of quantum mechanics, but his hypothesis of some kind of oscillators which should change their energies in integer multiples of a fundamental energy unit, was groundbreaking. Planck said about his new idea of energy quanta: “Experience will prove whether this

hypothesis is realised in nature". It turned out to be the case.

The kind of law that describes an isolated phenomenon like the emitted radiation of a perfect black body can be used for direct comparison between a fundamental theoretical law and the experimental reality. Nowadays, however, many scientific problems and questions have become much less fundamental and cannot be answered by a single new formula proposing a novel basic idea. Instead, a significant part of modern research focuses on the *realistic* description of systems that actually exist in nature (or at least in the laboratory). The small fragments from which such a real system is composed are governed by fundamental physical laws that are generally assumed to be known, e.g. from quantum mechanics. However, the fact that the fragments are mutually strongly coupled makes the behavior of these fragments and therefore of the total system very complex. As a consequence, the general solution for the evolution of these coupled fragments becomes very difficult or even impossible.

Hence, a further step is necessary for the prediction of the properties of more complex systems: the construction of simplified models and realistic approximations, which provide simplifications, but nevertheless describe the system in a realistic way.

This is the aim of the work presented here. A variety of real-world molecular and supramolecular systems, taken directly from the physical chemistry laboratory, shall be described by a particular computational approach, which is capable of modeling the atomistic structure and dynamics at a high level of accuracy and reliability. For this purpose, the method of choice is electronic structure density functional theory (DFT), combined with density functional perturbation theory for the calculation of spectroscopic parameters, as well as Car-Parrinello molecular dynamics simulations for the efficient incorporation of atomistic motion at a given temperature. Since many chemically relevant systems are actually measured in condensed phases (liquid or solid), the modeling is done under periodic boundary conditions, enabling the simulation of extended systems.

2 Complexity in supramolecular systems

2.1 Length and time scales in nature and in simulations: Different degrees of complexity

Our universe exhibits a vast variety of physical and chemical phenomena at very different scales in time and length. Many of these are beyond the normal range of human perception, both at the “small” and “large” ends of the scale. The spatial dimension of a nucleon is about 10^{-15}m , more than 11 orders of magnitude smaller than any structure visible to the eye, and nuclear processes typically happen in less than 10^{-24}s . On the other end, structure formation in interstellar space occurs on timescales that exceeds human lifetimes by about seven orders of magnitude, and involves distances that are more than 15 orders of magnitude longer than the length of man-made objects [28].

However, also for problems that are within the direct range of human experience, we observe order phenomena that span many orders of magnitude. A typical example is the earth’s atmosphere, in which small water and ice particles accumulate and form clouds, which may then move over large distances before they finally release their water as rain. The processes in such atmospheric phenomena start at length scales of about 10^{-5}m , the size of an ice crystallite in a cloud, pass over to 10^2m , the spatial extension of a cloud, arrive at 10^5m , the distance that the cloud may travel, and return to 10^{-3}m , the size of a rain drop [29, 30].

In this example of a cloud, it appears obvious that although the different processes and phenomena are closely related to each other, they must be described with completely different models and techniques. A model developed for the assembly of ice crystallites will not predict the shape and motion of the cloud as a whole, nor will it be suitable for the formation of rain droplets. Even though the underlying physical principles – such as the laws of thermodynamics and the mutual interaction of water molecules – are very general, different approaches are required for processes on different time- and length scales.

The same statement holds for a very specific subset of systems, which are at the main focus of this work: molecular and supramolecular aggregates and the theoretical calculation of their electronic, structural, dynamical, and spectro-

scopic properties: The simulation of solvent effects around a molecule immersed in a liquid environment cannot be done with the same computational tools which are used to calculate electronic correlation effects.

In principle, there is only a single theory, and even only a single equation – the Schrödinger equation – which governs these phenomena, but in practice, the bare Schrödinger equation is only useful for textbook problems which are exactly solvable, like the isolated hydrogen atom. For all cases that require the use of quantum mechanics but involve many particles, models with suitable approximations and simplifications are needed. They should still cover the essential part of the physics of the system, while at the same time, the complexity of the problem should be reduced in order to allow for a direct numerical solution.

To cover the required length and time scales of molecular problems, a variety of wavefunction theories and simulation methods has been developed in the theoretical chemistry community [31, 32]. A necessarily incomplete overview is presented in table 1, including a comparison of the approximate length scales and system sizes. Coupled-cluster theory (CC) as a reference method represents the most accurate electronic structure method which is available today for a quasi-exact determination of electronic correlation [33, 34, 35, 36]. Due to the high computational cost, only small molecular systems can be described with such cutting-edge precision. An approximate treatment of correlation effects is pos-

Method	Time scale	Length scale	Number of atoms
Coupled-cluster theory	static	0.5nm	20
Møller-Plesset theory (MP2)	static	1nm	100
Hartree-Fock methods, Density functional theory	static	5nm	1000
Car-Parrinello molecular dynamics	50ps	3nm	500
Hybrid quantum/classical (QM/MM)	100ps	10nm	100.000
Classical molecular dynamics	100ns	10nm	100.000
Coarse-graining methods	1 μ s	10 μ m	1.000.000

Table 1: Approximate limits for length- and timescales for different methods in computational chemistry. The figures indicate orders of magnitude and may vary for specific cases.

sible using Møller-Plesset perturbation theory (MP2) [37, 38, 39, 40, 41]. This approach has a reduced computational cost, thus enabling calculation of medium-sized molecules and small clusters. Larger supramolecular systems are accessible with Hartree-Fock (HF) or density functional theory (DFT) methods [42], which provide a good description of electrostatic effects, but lack a consistent description of electron correlation. Within HF and DFT schemes, it is also possible to treat systems in the condensed phase, by adopting periodic boundary conditions for atoms and periodic Bloch states for electronic orbitals [32, 43]. Another technique, which is not mentioned in table 1, is the Quantum Monte Carlo (QMC) approach, allows a direct representation of many-body effects in the wavefunction [44, 45]. QMC is able to describe correlation effects even in real solids (and without having to resort to approximate exchange-correlation energy functionals as in DFT), in principle at an accuracy comparable to CI and CC methods. However, QMC is also very demanding in view of the necessary computational resources.

Using the methods mentioned above, it is possible to calculate molecular conformations, their energies and atomic forces *ab-initio*, without any empirical system-specific parameters. While HF, MP2, CC and related methods do not contain any kind of empirical element and represent well-defined approximations of an *exact* Ansatz, DFT is based on a functional (the so-called exchange-correlation functional) whose exact form is unknown and which probably cannot be formulated as a closed expression. Instead, several approximate expressions exist for this functional, with varying degrees of empirical contributions. However, no systematic improvement is known which would eventually lead to an exact form. For this reason, DFT is sometimes not regarded as an *ab-initio* method, but rather as a semi-empirical approach. However, this distinction shall not be made in this work, in order to simplify the nomenclature.

On top of these electronic structure methods, atomic motion can be incorporated by assigning velocities to the atoms and propagating them via Newton's equations of motion. An efficient scheme to perform such a molecular dynamics in the framework of DFT is the Car-Parrinello technique [46, 47]. It allows a realistic description of molecular processes and hence the explicit consideration of finite (non-zero) temperatures.

For even larger systems, the calculation of electronic structure based energies

and forces is no longer affordable, and it is necessary to resort to parametrized force fields [48, 49, 50, 51]. These classical calculations provide less accurate data for local phenomena such as hydrogen bonds, but dramatically increase the accessible system size for a given amount of computational resources. Finally, the atomistic description can be abandoned, replacing larger fragments of molecules by metaparticles, and hence enabling the modeling of mesoscopic systems [52, 51].

2.2 System complexity and simulation detail – a reciprocal correlation

The use of stronger simplifications, when dealing with larger molecular systems, requires a certain price to be paid, which is a lower detail level in the structural and dynamical data that can be extracted from the numerical simulations. The more intrinsic complexity a system has, the more approximate the computational model has to be, and hence the lower will be the accuracy in the description of individual effects on the molecular and atomic level. For a subset of molecular and

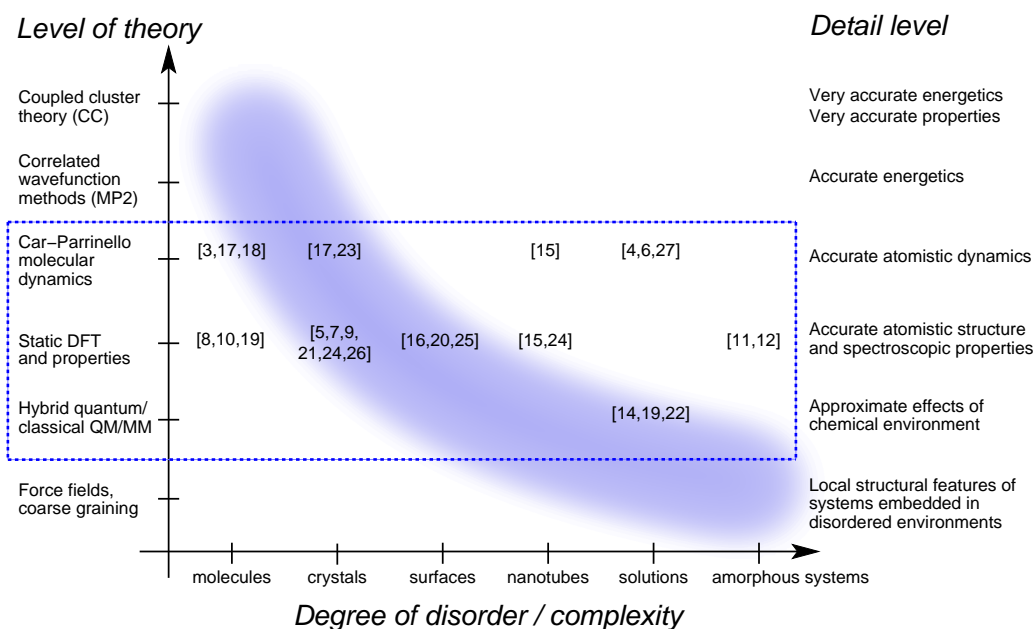


Figure 1: The reciprocal dependence of the possible detail level that can be obtained from computational chemistry with the complexity of a system. Numbers in brackets are references of own publications (see the list on page 53); the methodological focus of this work is indicated by the dotted frame.

supramolecular systems, the correlation between the complexity and disorder of a system, the suitable computational methods, and the detail level of the resulting calculated data is sketched in figure 1. The complexity of the scientific problem (bottom axis) defines which methods could be used; the theoretical approach is chosen accordingly (left axis), which in turn determines structural features that can be determined accurately (right axis). Intuitively, there is a reciprocal correlation between size or complexity of a system and the detail level that can be achieved in a simulation. The notions of size and complexity are complementary. A (small) molecule may possess a variety of accessible conformations, rendering its structural description very complex (see for example the barbaralane molecule in section 3.1.3). On the other hand, a (very large) crystal may be less complex due to the higher ordering in the periodic crystal structure. Finally, the disorder of a liquid can be handled by simulating a large number of independent molecules, making it more complex (and thus computationally more expensive) to model.

In some cases, it is advantageous to combine computational techniques from more than one level of theory. In particular for amorphous or liquid systems, it is important to perform a thorough phase-space sampling of the simulated particles, while at the same time, local hydrogen bonding networks and spectroscopic signatures of individual atoms are of high interest. In such cases, the thermodynamic sampling is done with classical molecular dynamics techniques, while the refinement of local configurations and the calculation of the corresponding spectroscopic parameters is performed in the framework of quantum chemical methods. To a certain extent, this is similar to the hybrid *quantum mechanical/mechanical modeling* approach (QM/MM), which describes a small part of the total system with the more accurate quantum techniques, in order to treat a more delicate situation (like an active site of an enzyme) appropriately [53, 54, 55, 56]. The bigger remaining part of the system, often including a large aqueous solvation environment, is modeled with classical force fields. In this way, the advantages of both types of simulation can be combined.

This work considers systems exhibiting all degrees of disorder and complexity mentioned in figure 1. One common technique – density functional theory under periodic boundary conditions – shall be applied, in order to represent the versatility of this theory for the description of a broad variety of problems in physical chemistry. Since experiments are naturally indispensable in chemical sciences, this work goes beyond the mere calculation of forces, geometries and dynamical

conformations. The real goal shall be to obtain quantities which are directly accessible from experiment, allowing a direct comparison – and thus enabling a possible invalidation – of the computed results. Since molecular conformations alone, in the form of atomic cartesian coordinates, are difficult to verify experimentally except for very well-ordered systems, the path will very often lead to spectroscopy. Being included in the same computational framework, the calculation of spectroscopic parameters is a tool to enable the dialogue with experimental physical chemistry. The particularly powerful combination of experimental spectroscopy with the corresponding ab-initio calculations will be discussed in more detail in the following section.

2.3 Ab-initio calculations of structure–property relationships in supramolecular systems

The determination of local structural properties, intra- and intermolecular conformations of molecular systems and supramolecular assemblies has always been and still is a challenge for modern physics and chemistry. Many advanced techniques are capable of contributing to this quest, some of the most prominent being X-ray [57] and neutron scattering [58], electron crystallography [59, 60], infrared (IR) spectroscopy [61] and nuclear magnetic resonance (NMR) spectroscopy [62, 63].

In crystalline systems, scattering experiments can provide very accurate atomic coordinates. Many systems, however, lack long-range order, which is required for these scattering techniques and limits their applicability. Complementary to this, NMR experiments are able to probe local structure without the need of long-range order. While magnetic resonance techniques cannot provide the full structure in terms of three-dimensional atomic coordinates, the sensitivity to the local chemical environment of an atom is one of the key advantages of this method. Therefore, NMR is well suited to investigate molecular and supramolecular systems and their mechanisms of structure formation [64, 65, 66, 67, 68, 69, 70, 71].

While liquid-state NMR is a widespread routine characterisation method for many areas of science and medicine, its application to solid-state systems is not as frequent. This is partially due to the higher requirements concerning the experimental setup, as well as the complexity of the underlying theory. In addition,

there are stronger anisotropic interactions in solids, which give rise to very broad lines in the NMR spectra. However, in the last decades, important progress has been made in this field, notably regarding magic-angle-spinning (MAS) techniques, which are capable of average parts of the anisotropic interactions, hence reducing the experimental line widths. Using those novel techniques, both an increase in resolution and in sensitivity could be achieved, leading to the reliable experimental measurements of individual NMR resonances in the solid state, even for ^1H chemical shifts [72, 66, 67, 68, 73, 74, 75].

It has become increasingly common to supplement the experimental data with adequate numerical simulations. The interaction of experimental and computational techniques for the determination of structural properties is outlined in figure 2. Classical molecular dynamics (MD) techniques are performed for structures obtained via X-ray, electron diffraction or solution NMR methods in order to test their conformational stability [76, 77, 78, 79]; quantum chemical calculations of vibrational frequencies can often help interpreting IR spectra [61, 80, 81, 27, 82]. In NMR, dihedral angles are probed by spin-spin coupling constants; cross-relaxation rates due to dipole-dipole interactions provide

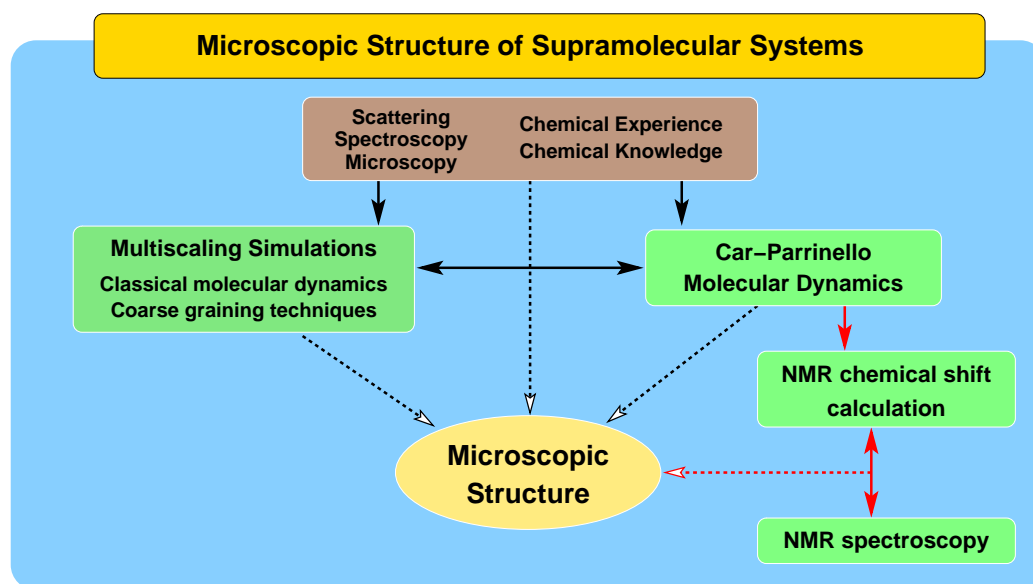


Figure 2: Interconnection between experimental and computational techniques for the determination of structural details on the atomic and molecular scale. The focus of this work is the symbiosis of *ab-initio* molecular dynamics simulations, property calculations and the corresponding experiments, indicated by red arrows.

distance constraints [83, 62, 67, 68, 66, 84, 73, 74]. For magnetic resonance experiments, accompanying ab-initio calculations have become standard for isolated molecules [85, 86, 87], and are becoming increasingly popular also for the solid state [10, 88, 89, 23, 90], as well as for liquids and solutions.

The ab-initio simulation of the structure and properties of liquid water, where the dynamically fluctuating hydrogen bond network is the central structural driving force, is a difficult problem in computational chemistry. Important progress has been achieved in the direct simulation of the molecular structure in the liquid phase [91, 92], the understanding of its IR spectrum [81, 93], the Raman spectrum of ice [94], the NMR parameters in the liquid and supercritical phases [6, 95], and last but not least the hydrogen bond network of water on surfaces [20, 96, 97].

Supramolecular and biomimetic systems are extremely complex, both in structure and dynamics – not to mention their functionality. In order to investigate such systems with magnetic resonance methods, a great deal of knowledge regarding the relationships between structure, atomistic dynamics and spectroscopic properties is crucial [98]. This is particularly true if magnetic parameters such as chemical shifts or spin-spin couplings [62, 63] are to be used as sources of information. Therefore, a clear validation of the signatures of condensed phase packing effects both in NMR experiment and in quantum-chemical calculations is essential for a real understanding of such complex systems.

In this work, microscopic systems of very different types are investigated. Molecules, crystalline and amorphous solids as well as surfaces and nanotubes are covered. Many of these systems can be studied with the symbiotic combination of solid-state NMR experiments and ab-initio calculations. The direct comparison to experimentally accessible data can provide significantly more insight into physical and chemical questions than either of these methods alone.

It is well-known that for the reliable calculation of NMR parameters, in particular for chemical shifts, the chemical environment of the considered atoms is of crucial importance. Besides the classical geometrical variables of molecules – bond distances and bond angles – there are also non-covalent parameters to which the NMR chemical shifts can provide access. The most prominent example among these are hydrogen bonds, for which an example is shown in the left part of figure 3: The ^1H NMR chemical shift of the hydrogen bonding proton of the

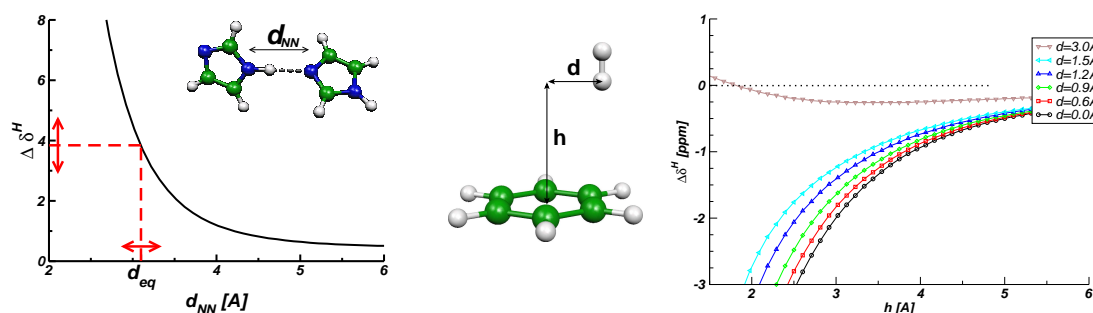


Figure 3: Illustration of the dependence of NMR chemical shifts on the chemical environment: An imidazole-dimer (left) and a benzene- H_2 complex (right). For both, the calculated dependence of the ^1H NMR chemical shift spectra on the geometrical parameters are shown. Note that no covalent bonds are involved; the entire chemical shift variation is due to non-covalent interactions.

left imidazole molecule varies strongly on the intermolecular N-N distance.

Further, there is a through-space effect that deserves special attention, shown in the right of figure 3: When a given nucleus (here: the lower H atom in the H_2 molecule) approaches a neighboring benzene, its NMR chemical shift changes significantly before the electronic densities of the two molecules overlap with each other. This effect, shown in the graph on the right of figure 3, is known as the “ring-current”-effect, and is presented in more detail later in sections 3.1.3 and 3.4.2 in this work. Both effects can be calculated with good accuracy from electronic structure methods. They are very useful to obtain information about structural parameters of complex molecules which can be compared against NMR experiments.

Highly accurate electronic structure methods on the explicitly correlated level of theory are available for the calculation of structure [99, 100] and magnetic resonance properties [101, 102] of small molecular systems, but not for the condensed phase. Density functional theory (DFT) represents a compromise between accuracy and computational efficiency, and has been proven many times to yield good agreement with experimental data. Although DFT based methods are sometimes erratic for particularly difficult cases of electronic structure [103, 104, 105, 106], they allow for a parameter-free prediction of structural and spectroscopic properties in complex systems, be it molecules, crystals, surfaces or liquids and solutions [86, 85, 90, 13].

2.4 Scope of this work

The central purpose of the present work is to show that with a particular set of methods, namely pseudopotential plane-wave based ab-initio calculations of atomistic structure, molecular dynamics, and spectroscopic properties, it is possible to provide quantitative answers to a variety of chemical problems on different intrinsic time and length scales. These methods can normally not deliver the full structural solution directly, but their combination allows to model specific aspects and parameters of the problem. The latter can help understanding the basic driving forces which govern the behaviour of the system on time and length scales which up to today are not directly accessible for atomistic simulation methods.

This versatility is illustrated in figure 1, where the methodological basis is outlined via the dotted frame. The articles included in this work start with calculations of chemical properties of isolated molecules; a second important topic are packing effects in regular crystals; at the next levels of complexity, surfaces and nanotubes are covered; and finally, structural questions of liquids and solutions are addressed.

The figure also illustrates the limits of calculations based on density functional theory. While electronic correlation effects are in principle taken into account in the DFT approach, a quantitative description can only be achieved in the high-level configuration interaction and coupled-cluster approaches, or also in the perturbative Møller-Plesset treatment. Similarly, the statistical simulation of very large ensembles of particules is the domain of classical force-field (molecular mechanics) simulations and coarse-graining approaches [52, 51].

3 Structure-Property relationships: from single molecules to complex supramolecular systems

3.1 Molecules and oligomers

3.1.1 Molecular conformations, electronic structure calculations, and spectroscopy

The calculation of the equilibrium geometry (not considering thermal motion, i.e. at $T=0\text{K}$) of isolated molecules represents the lowest level of structural complexity that will be considered in this work.

However, the complexity of the electronic structure does not depend primarily on the size of the system, but rather on the specific properties of the involved atoms. A realistic theoretical description of the electronic structure of an isolated molecule can be very difficult. For example, the calculation of the electronic structure of systems with sum formulas as simple as $\text{CCH}\cdot$ and $\text{OOH}\cdot$ requires methods at the coupled cluster level of theory – an extraordinary high level of accuracy [99, 100], which exceeds by far the common electronic structure methods that are sufficient for most closed-shell molecules.

The knowledge of the electronic orbitals is only one of the goals of computational chemistry. In itself, the electronic wavefunction has relatively little value, but many important physical and chemical quantities can be derived from it. The most prominent ones are the atomic forces and molecular energies as well as second-order properties like spectroscopic parameters (e.g. IR-, UV-, Raman- and NMR frequencies). The usefulness of the computational approach is demonstrated in the following sections, where experimentally obtained results will be interpreted and explained by means of computed nuclear magnetic resonance (NMR) spectra.

3.1.2 Benzoxazines: From dimers to oligomers

Polybenzoxazines exhibit a number of unusual properties, including a lack of water absorption and excellent resistance to chemicals and UV light [107, 108], as well as surprisingly high glass transition temperatures given the low cross-

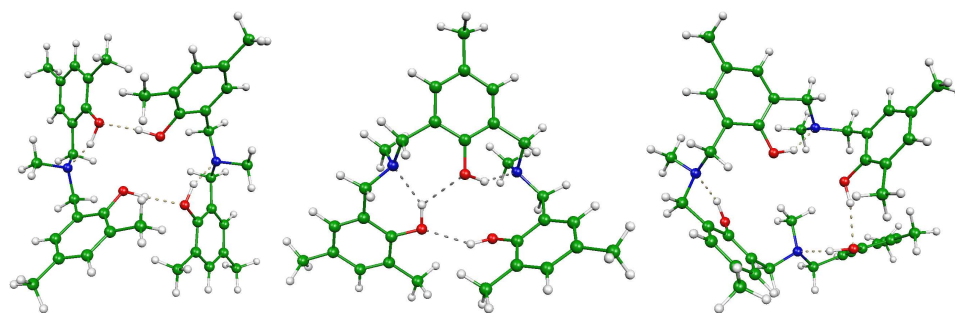


Figure 4: Molecular structure of the benzoxazine oligomers, the dimer (left), trimer (middle), and tetramer (right). Note that the notions of di-, tri- and tetramers refer to the number of phenyl rings within the same molecule, not the number of agglomerated molecules.

linking density [109]. These properties, which make them attractive candidates for many commercial applications, have been attributed to the unique hydrogen bonding structure found in benzoxazines. Therefore, this property has been the focus of recent investigations; in particular, extensive crystallographic, NMR, and IR studies of the dimer precursors [110, 111] have provided much insight.

Their basic molecular structures are shown in figures 4, 5, 6, and 7, illustrating the intramolecular $\text{OH} \cdots \text{N}$, which have a tendency to impose a helical structure on the molecules. In addition, benzoxazines also have the potential to form intermolecular hydrogen bonds, which could act as a driving force for the generation of molecular chains, or also beta-sheet structures as known from biomolecules. While the present computations have been performed for isolated molecules, the influence of self-assembly and hydrogen bonding are also frequently observed in

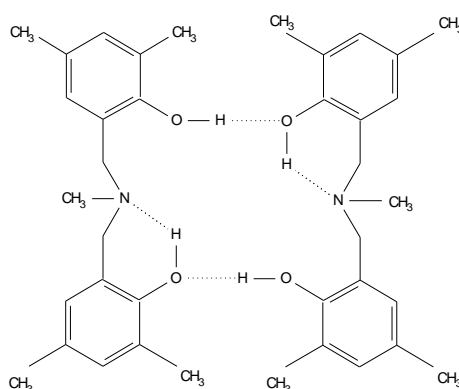


Figure 5: Two benzoxazine dimers, illustrating the intra- and intermolecular hydrogen bonding.

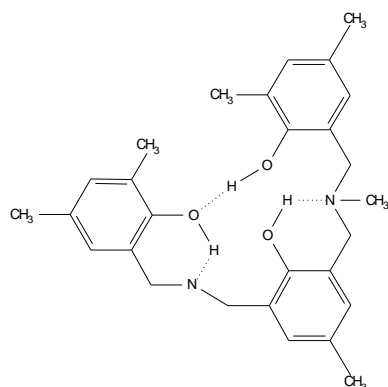


Figure 6: The benzoxazine trimer with only intramolecular hydrogen bonding.

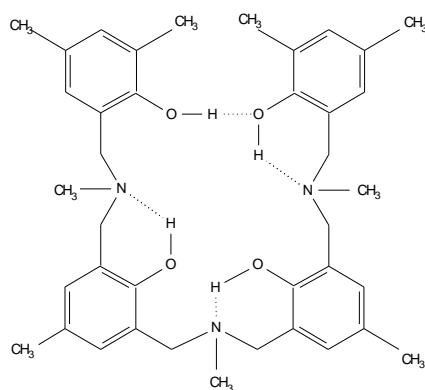


Figure 7: The benzoxazine tetramer with only intramolecular hydrogen bonding.

supramolecular structures and polymeric architectures. The objective in this work was to improve the understanding of the polymer architecture of benzoxazines in the solid state through studies of the hydrogen bonding in the oligomers, and thereby understand the remarkable physical characteristics of the polymers.

Only very few of the available benzoxazine oligomers form well diffracting crystals, while most of them are amorphous. Hence, a direct experimental verification of computed structures via X-ray scattering is difficult. Instead, a different route has been chosen to compare theory to experiment: the calculation of the spectroscopic signatures of the hydrogen bonds. ¹H NMR chemical shift spectra of the benzoxazine oligomers were computed from DFT methods in the optimized molecular geometries. These theoretical spectra for the dimer, trimer and tetramer are compared to the experimental ones in figure 8.

The most intense NMR signatures in all oligomers at about 1-2ppm and

6ppm stem from aliphatic and aromatic protons; these resonances are similar in the dimer, trimer and tetramer structures. However, the strongly hydrogen bonded protons, located at about 10-13ppm, are distinct for the three oligomers. They represent specific variations in the hydrogen bond strength of the $\text{OH}\cdots\text{N}$ and $\text{OH}\cdots\text{O}$ bonds, which are all in very good agreement with experiment. This H-bonding strength can also be seen in the computed $\text{H}\cdots\text{N}$ and $\text{H}\cdots\text{O}$ distances, which vary between 1.9Å and 1.7Å: a shorter distance generally induces a stronger deshielding. Further, some of the protons are H-bond donators for an N and an O acceptor atom at the same time, which further increases the ^1H chemical shift.

It is interesting to note that there is no distinct line for H-bonded protons in the polymer. This indicates that there is not a uniform type of hydrogen bonding (which would correspond to a helical or similarly organized structure), but rather a distribution of hydrogen bonds of different strength.

Besides this, a structural motif for the methyl benzoxazine trimer and tetramer can be established. In contrast to the dimer pairs, the oligomers are characterized exclusively by intramolecular hydrogen bonds. Extrapolating from the trends found among these oligomers, there is evidence that the polybenzoxazines form

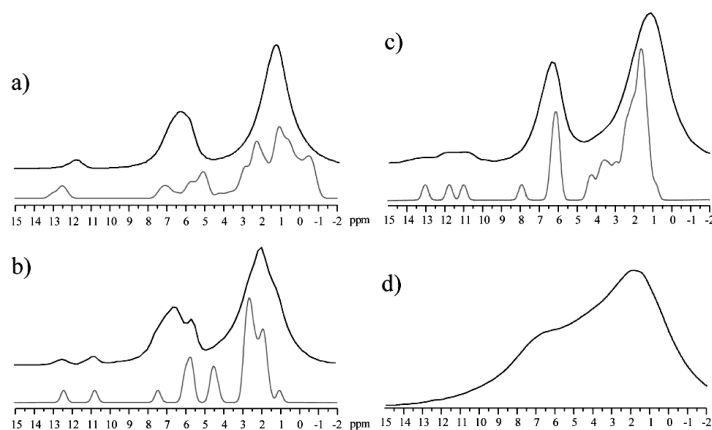


Figure 8: ^1H NMR chemical shift spectra of the benzoxazine dimer (a), trimer (b), tetramer (c) and polymer (d). Black lines show the experimental spectra, grey lines represent the calculated ones; for the polymer (bottom right), a calculation is not available since the structure is not known. The computed shifts were convoluted with Gaussians for a better comparison with experiment. Intensities are in arbitrary units.

helices in the solid state. Such a structural conformation, as seen very frequently in biological molecules, also provides a rationale for their favorable chemical properties [10].

In all oligomers, the agreement between theory and experiment enables a direct assignment of the experimental peaks, which in turn provides a characterization of the polymeric material, whose structure is unknown.

3.1.3 Aromaticity and homoaromaticity: Nucleus independent chemical shift maps of barbaralane and derivatives

Another interesting way of accessing the characteristics of electrons in molecules is by looking at their aromaticity. Aromaticity as a molecular property is not a measurable "hard fact", but rather a chemical concept, which nevertheless is so fundamentally important that it is commonly taught in first year chemistry [112, 113, 114]. Historically, aromaticity has its roots in the discovery of the ring topology of the benzene molecule by Loschmidt in 1862 and Kekulé in 1865. It is often used in an intuitive way to describe delocalized electronic states, conjugated bonds and particular structural conformations (mostly planarity) of molecules. This rather cloudy use of the term aromaticity has been seeking supplementary clarification and further investigation since its first appearance.

One semi-quantitative way of describing degrees of aromaticity is the analysis of the electronic reaction on external magnetic fields. In an intuitive way, the field induces electronic ring-type currents which are normally restricted to regions of high electronic density of each single (localized) electron, i.e. around atoms and chemical bonds. However, in systems with delocalized electronic orbitals, such as in benzene, extended current densities may develop. These are often a sign of aromaticity.

The visualization of these ring currents can be done via the current densities themselves, or by means of the magnetic fields induced by them. The latter is known as Nucleus Independent Chemical Shift (NICS) maps, a term which was introduced as early as 1958 by Johnson and Bovey [115], and made popular 38 years later by Schleyer [116]. Many derived works have been published since then, most of them investigating NICS-based aromaticity of static molecules. An extended approach which also covers NICS fields of periodic systems is presented

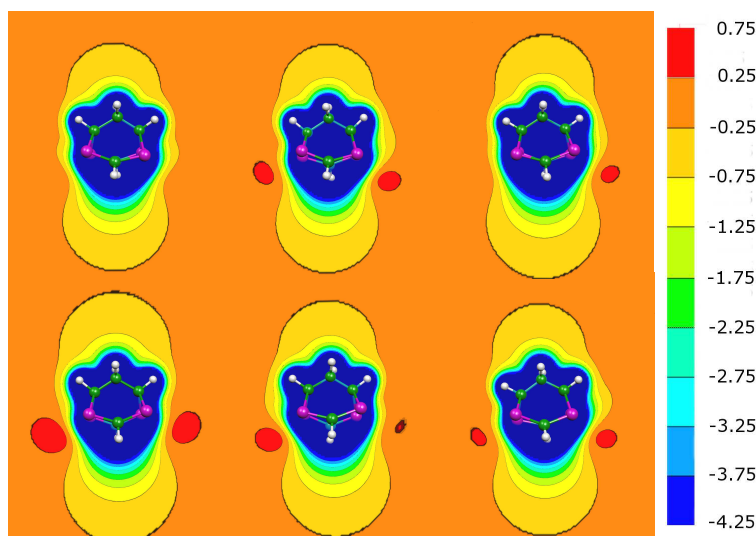


Figure 9: The NICS maps for a phospho-barbaralane molecule during a Car-Parrinello molecular dynamics simulation. The elapsed time between the snapshots shown is about 100fs, and the color coding of the NICS map is again in ppm.

in ref. [24] and outlined in section A (appendix). Hence, the NICS idea as such will not be discussed in detail in this section.

The notion of aromaticity is also closely linked with other electronic and geometric properties, such as planarity and the conjugation of chemical bonds. In systems where one or more aromaticity criteria are not satisfied, the notion of “homoaromaticity” has emerged in the late sixties [117]. A particular difficulty arises when a molecule is considered at ambient temperature, where its atoms are in thermal motion. The geometric and even the electronic structure of the molecule may change during this dynamical evolution, which in turn may affect its aromaticity.

This question has been addressed in ref. [18], where homoaromatic barbaralane molecules (whose structures are sketched in figure 10) have been studied at

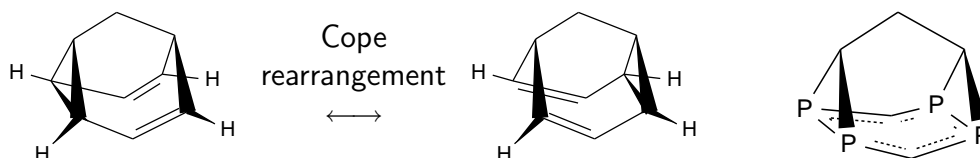


Figure 10: The C- and P-Barbaralane molecules, including the Cope rearrangement reaction for the C-Barbaralane.

T=300K using Car-Parrinello molecular dynamics simulations, combined with the calculation of NICS maps along the molecular dynamics trajectory. The question was whether the considered molecules conserve their aromatic properties during the simulation, despite significant structural changes such as Cope rearrangement reaction. The basic principle of a Cope reaction is also depicted in figure 10; it involves a displacement of four carbon atoms, followed by the rearrangement of several electronic bonds. The P-barbaralane molecule is symmetric in its ground state and thus does not exhibit such a reaction.

The main result, the time evolution of the NICS field of a homoaromatic phospho-barbaralane molecule, is shown in figure 9. Several snapshots of the molecular dynamics simulation have been used to calculate the NICS map at different stages of the Cope rearrangement mode of the molecule. Representative conformations are plotted in the figure; they show that the spatial extension of the induced NICS field is widely independent of the actual atomic coordinates which occur at ambient temperature. Hence, the aromatic character of the molecule is not only a feature in the static optimized geometry, but persists at common ambient conditions.

3.2 Crystalline systems

3.2.1 Characterization and structure determination of crystals

A different level of complexity is found in crystalline systems, where all atoms are located on regular lattice positions. The periodic lattice is characterized by the three basis vectors \mathbf{a}_1 , \mathbf{a}_2 and \mathbf{a}_3 , and with the help of these, the coordinates \mathbf{R}_i of all atoms (indexed by i) can be written as

$$\mathbf{R}_i = \mathbf{R}_i^{(0)} + n\mathbf{a}_1 + k\mathbf{a}_2 + l\mathbf{a}_3 \quad (1)$$

where (n, k, l) are three integer numbers, and $\mathbf{R}_i^{(0)}$ denotes the position in a given reference atom [43, 118, 119]. This periodicity in the atomic positions enables the complete description of such a crystal by means of just a single reference unit, which is then thought to be periodically replicated in all directions of space. The repeat unit is called unit cell and may contain any atomic or molecular system. Several classes of crystals can be distinguished: In the first case, the unit cell is composed of one or a few atoms which are covalently bonded to atoms of neighboring cells throughout the crystal. Hence, the entire macroscopic crystal is – chemically speaking – one big molecule. Examples for this kind of crystals are diamond, silicon, or quartz. Such systems have a high mechanical stability and may exhibit many interesting long-ranged electronic properties, such as conductivity, magnetism or optical properties. To some extent, also crystallized polymers may be associated with this type of crystals, although crystallized

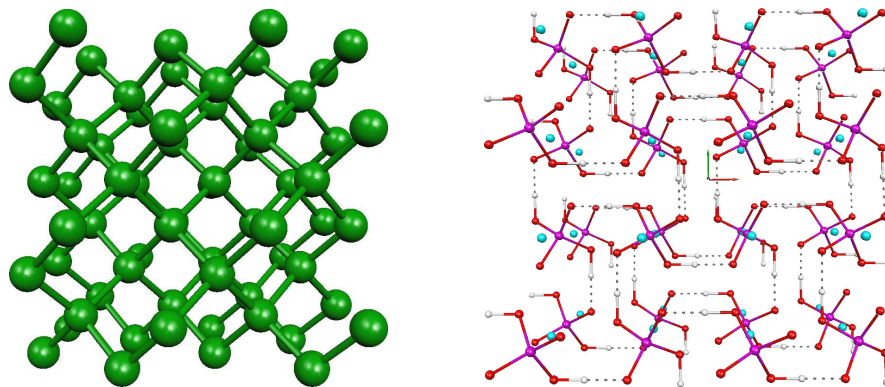


Figure 11: Illustration of different crystal types. Left: a covalent crystal, diamond; right: an ionic crystal, potassium dihydrogen phosphate crystal, $K^+ H_2PO_4^-$.

polymers are normally only piecewise crystalline and therefore rather a class on their own.

Another closely related kind of crystals are ionic crystals. Here, the atoms are not linked through covalent, but by ionic bonds, which have a more electrostatic nature. All salts are within this category, like NaCl, KCl, or KH_2PO_4 . As an example of a more complex salt, the crystal structure of the potassium dihydrogen phosphate crystal (KDP) is shown in figure 11. KDP and partially deuterated KDP are widely used for high-power laser frequency conversion, since they are ideal crystals for second-harmonic generation of femtosecond laser pulses in non-linear optics [120, 121]. Further, it exhibits a ferroelectric phase transition at a low temperature ($T_c=124\text{K}$). Below T_c , it has a non-zero electric dipole moment (in the absence of an external electric field) due to a symmetry breaking in the $\text{P}\cdots\text{K}\cdots\text{P}$ distances. At higher temperatures, the $\text{P}\cdots\text{K}$ and $\text{K}\cdots\text{P}$ distances converge, and the crystal becomes paraelectric.

The KDP crystal provides the bridge to a somewhat different crystal type: molecular crystals. For this class of systems, the elementary building blocks are independent neutral molecules, which are kept together by means of hydrogen bonds or van-der-Waals interactions. These systems have physical properties that differ significantly from those of covalent or ionic crystals. Molecular crystals do not typically form a monolithic and mechanically hard material, but are more flexible, since their cohesive forces stem from weaker interactions. Hydrogen bonds, for example, possess only an energy of about 15-30kJ/mol, while a covalent bond is normally around ten times stronger. In turn, molecular crystals have many abilities that hard compounds are lacking, which are determined by the functionalities of the underlying molecules. This flexibility enables their use for many specialized purposes of growing importance, such as proton conducting membranes in fuel cell applications, nanosized tubes as transmembrane channels, and host-guest systems for drug delivery.

In principle, the three-dimensional atomistic structure of all perfectly ordered crystals can be obtained via diffraction methods. X-ray structure determination is fast and reliable, but has difficulties in locating hydrogen atoms. This problem is due to the relatively low electron density close to the protons, which do not have any core electrons attached to them. Neutron scattering is capable of delivering very accurate atomic positions, including those of very light atoms, but it is

comparably expensive in view of the experimental setup.

In many systems, however, scattering techniques face a principal difficulty: If the required long-range order is lacking, the applicability of both X-ray-scattering and neutron diffraction is limited. Complementary to these methods, NMR techniques rather probe the average chemical environment of specific atoms – without the need of long-range order in the sample. Although the full three-dimensional structure in terms of atomic positions cannot be delivered by NMR, these experiments are very sensitive to small changes in the local structure, such as bond distances, bond angles, but also to the occurrence of hydrogen bonding and π - π -stacking [122, 123]. This feature enables the application of NMR to the study of supramolecular systems and their mechanisms of structure formation [66, 67, 68, 74]. The following computational investigations were done in combination with this powerful experimental technique.

3.2.2 Bulk chemical shifts in strongly hydrogen bonded amino acid systems

The dependence of NMR chemical shifts of a molecule on its chemical environment is well-established for solutions, where the change in the NMR resonance is called solvent shift. It is due to the interaction of the solvent molecules with the solute, which may be hydrogen bond networks, van-der-Waals forces, or other non-bonded interactions. In solid phases, these packing effects are frozen out, due to the lack of fast diffusive atomic motion. In analogy to solvent shifts, the term *crystal chemical shift* denotes the change in the NMR resonance due to the packing of molecules [26]. Since the packing is more stable in the solid state, the spectroscopic signatures are usually stronger than in solution [122, 123]. In crystalline systems, the packing is also very well-defined, as opposed to amorphous systems. Hence, the study of structure-property relationships in crystals enables us to understand also effects which are seen in much more complex non-crystalline systems. Bulk chemical shifts are particularly large in the proton NMR spectra, where they can reach up to about 6ppm, which is very large when comparing to the normal hydrogen NMR chemical shift range.

Because of the importance of hydrogen bonds in proteins, crystalline amino acids were considered as model systems for biological macromolecules. Nevertheless, the molecular crystals exhibit the same structural features – H-bonding

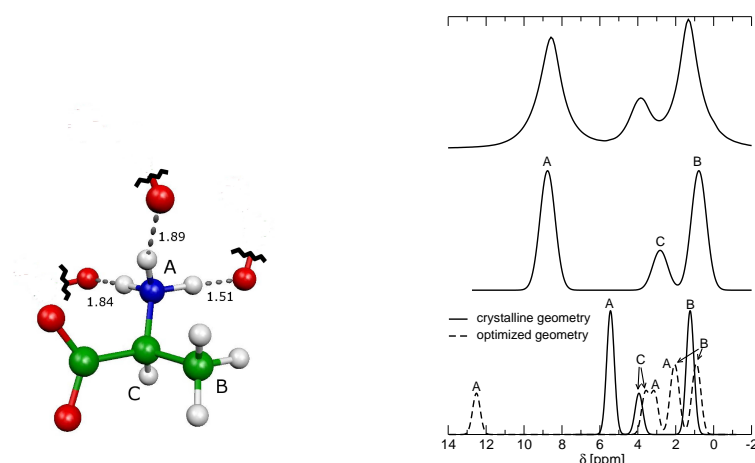


Figure 12: Left: Crystal structure of L-alanine, with some $\text{NH} \cdots \text{O}$ hydrogen bond distances (in Ångstroms) to the hydrogen-bond acceptor oxygen atoms from neighboring molecules. Right: Experimental solid-state MAS (top) and computed first principles proton NMR chemical shift spectra for Alanine in the condensed phase (center) and for the isolated molecule (bottom) in its crystalline and equilibrium geometries. In the computed solid-state spectra, the CH_3 and NH_3 shifts have been averaged.

and π -electron interactions – as the much more complex proteins. It could be shown that the computed NMR bulk shifts of L-Alanine, L-Tyrosine, L-Histidine-hydrochloride-monohydrate, and Adenine-hydrochloride-monohydrate are in very good agreement with experiment. Some representative data is shown in figure 12. With the help of the ab-initio calculations of the NMR spectra, the contributions to the bulk shift from hydrogen bonding, π -stacking and changes in the intramolecular structure could be analyzed in a series of biologically relevant crystalline compounds. As seen from figure 12, the packing results in ^1H NMR chemical shift changes of up to $\Delta\delta \approx 4\text{ppm}$, which illustrates again the sensitivity of solid-state ^1H NMR spectroscopy to the local chemical environment of the hydrogens.

This combined computational and experimental study shows that already very simple model systems exhibit packing effects which are characteristic for much larger biological systems [15, 12]. Their molecular building blocks feature hydrogen bonding and aromatic π -stacking, which are clearly visible in the ^1H NMR pattern, and much easier to study than the real target systems which are present in nature.

Last but not least, the direct benchmarking of computed magnetic resonance

spectra against experimental data shows to which degree property calculations from first principles are capable of realizing the sometimes subtle details in real spectra. This is highly important in situations where the theoretical support regarding the interpretation of spectroscopic data is needed, in particular when only little experience is available from previous studies on similar and related systems [10, 12]. The growing importance of direct simulations of chemical processes and the increasing complexity of today's atomic structures in realistic systems will give rise to more of such combined experimental/theoretical investigations. This holds also for other spectroscopic properties like EPR g-tensors, scalar spin-spin-couplings (J-couplings) or nuclear quadrupolar coupling constants [87]. In addition, further developments on the experimental side – e.g. for resolution enhancement in NMR [67] – will pave the way for substantially better descriptions of the more and more complex disordered systems of modern chemistry.

3.2.3 NH...N hydrogen bonds in proton conducting materials

Proton conducting compounds are materials where the interplay of hydrogen bonding networks and local molecular mobility has direct implications for industrial applications [124, 125]. Their major use lies in the field of fuel cell technologies, on which the quest for clean portable energy sources – especially for automotive applications – has focused in the past decade. In particular, the development of fuel cells made with polymer electrolyte membranes (PEM) has been crucial to this area [126]. The potential of PEMs has attracted a strong industrial interest in the further development of more flexible fuel cells, which could ideally operate with hydrogen gas, or alternatively other hydrogen-rich fuels such as methanol. Other challenges in the search for the optimal fuel cell membrane material are the high operating temperature of the cell, as well as the effect of carbon monoxide, which degrades the efficiency of the fuel cell catalyst. These questions are intrinsically linked with the microscopic structure and dynamics of the material. This involves in particular the interplay of hydrogen bonding networks, defects therein, and the resulting mobility of protons [126, 75].

A basic key to new materials for fuel cell applications is thus the understanding of the atomistic structure of the packing effects which lead to proton conduction. To this purpose, a new class of materials has been designed in

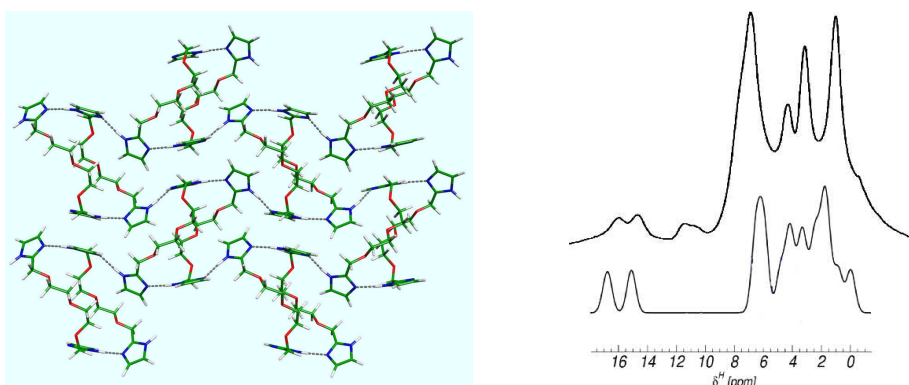


Figure 13: Crystal structure of Imidazole-ethyleneoxide₂ with its one-dimensional NH \cdots N hydrogen bonding chains (left), and the corresponding ^1H NMR chemical shift spectra (right). Both the experimental (upper right) and the computed spectra (lower right) are shown.

which proton-conducting units – here: imidazole molecules – are tethered to a ethyleneoxide polymer backbone. An illustration of the molecular structure is shown in figure 14. Such compounds are designed to operate at intermediate temperatures, where the polymer backbone acts as a immobilizing agent on the proton-donating moieties. In membranes based on such a material, the mechanism of proton transport must involve structural diffusion, which is also known as the Grotthuss transport mechanism. In this process, protons must hop from one molecule to another. The molecules are free to rearrange their orientation, while their spatial diffusion is hindered by the anchoring to the backbone.

To characterize the hydrogen bonding network which is responsible for the directional proton conduction of these materials, the ^1H chemical shifts for crystalline Imi-2EO in the crystalline phase were computed and found to be in excellent agreement with the experimental results. In particular, these calculations provided a structurally specific assignment of the strongly hydrogen-bonded

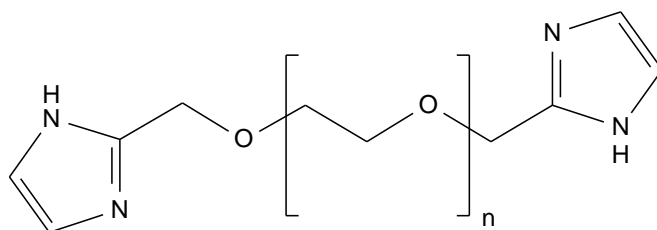


Figure 14: The structure of the imidazole-(ethyleneoxide)_n-imidazole (Imi-*n*-EO) molecule.

NH \cdots N resonances, as well as the protons in the ethylene oxide backbone that are shifted to lower frequency due to their orientation with respect to the aromatic rings. Moreover, comparison of the calculated chemical shifts for the periodic structures versus isolated molecules supports the assignment of the lower frequency NH resonances (10-12ppm in the experimental NMR spectrum, see fig. 13) to weakly hydrogen-bonded and non-crystalline molecules [75].

3.2.4 Temperature-dependent deuteron nuclear quadrupole coupling constants

Spectroscopic parameters, accessible both from experiment and theory, are a crucial ingredient in the determination of microscopic structure. Most calculations are done on optimized geometries, which means that the atoms are moved until the atomic forces fall below a small threshold value, i.e. until the atoms are close to their equilibrium positions. This state corresponds to a temperature of $T=0\text{K}$. For experimentalists, however, it is significantly more convenient to record their spectra at ambient conditions – temperature and pressure – instead of very low temperatures, where atomic motion is frozen.

A common assumption in quantum chemistry is that at first order, atomic motion at ambient temperatures is harmonic. In this case, the time evolution of the position variables of the involved particles (or, in a quantum description, the presence probabilities of the particles) is symmetric around the equilibrium positions. Assuming further (at first order) a linear dependence of spectroscopic parameters on the particles' coordinates, the observed average spectroscopic value is equal to that in the equilibrium state. Hence, it is often justified to compare finite-temperature experimental spectra with zero-temperature calculations.

However, the two assumptions made above do not always hold. Both the harmonic approximation as well as the linear relation between structural variables and spectroscopic parameters are only valid for small fluctuations around equilibrium. At elevated temperatures, these approximations may lead to incorrect predictions, caused by the complex concerted atomic motion.

Such a situation can even be found in relatively simple systems, such as crystalline benzoic acid, shown in the left of figure 15 in its crystal structure; the isolated dimer is depicted in figure 16. Deuteron nuclear quadrupole coupling

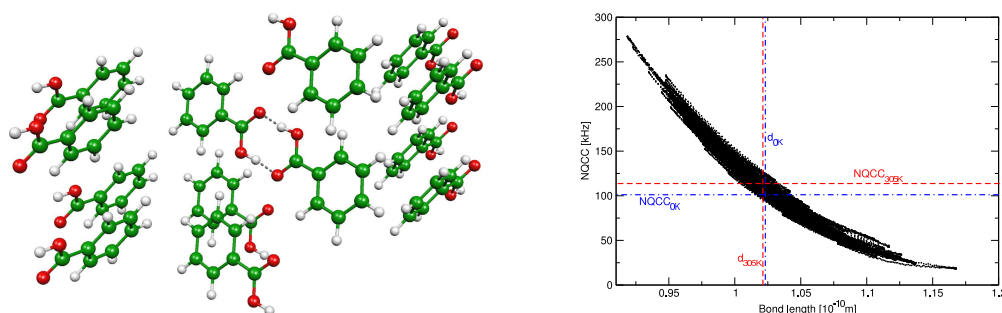


Figure 15: Crystal structure of benzoic acid (left) and the correlation of the electric field gradient (V_{zz}) of the hydrogen bonded deuteron (right, black points) during the Car-Parrinello molecular dynamics trajectory at $T=305\text{K}$. The average value of both the OD-distance and electric field gradients at this temperature are indicated by red lines. For comparison, the computed values at zero temperature are also shown (blue lines).

constants have been computed as a function of temperature in such a benzoic acid crystal by means of first principles Car-Parrinello molecular dynamics simulations. For $T=300\text{K}$, the correlation of the instantaneous electric field gradient of the hydrogen bonded deuteron with the O–D bond distance is shown in the right of fig. 15. Clearly, the dependence is *not* linear. Further, the simplest possible model based on the anharmonicity of the O–D \cdots O bond would lead to a larger O–D bond length, and thus to a lowering of the field gradient, when increasing the temperature. This behavior is actually experimentally observed in many systems [127, 128, 129]. However, the ab-initio calculation shows that from $T=0\text{K}$ to $T=300\text{K}$, the coupling actually increases instead. This effect could be assigned to the nonlinear dependency of the electric field gradient on the O–D bond length.

The final results agree very well with experiments and provide a microscopic explanation of the anomalous increase of the quadrupole coupling in this class of systems. The simple model based on the anharmonicity of the hydrogen bond potential fails to describe the temperature dependence of the couplings

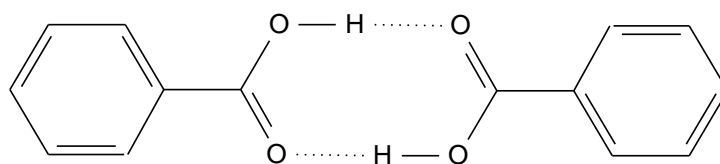


Figure 16: The structure of a benzoic acid dimer.

even qualitatively. Instead, the inclusion of fluctuations and disorder in terms of atomic motion of the surrounding molecules turns out to be important to obtain the correct magnitude of the temperature effect [23, 130].

3.3 Surfaces and adsorbates

3.3.1 Electronic structure of surfaces: between bulk and molecule

Surfaces are the interface that separates a bulk material from a different phase, be it vacuum, a gas or a liquid. The peculiarity of surfaces is that they mix properties from both cases: Towards one side, the atoms and electrons feel the environment of the infinite crystalline phase. Towards the other side, there is only vacuum beyond the last atomic layer at the surface, as in the case of an isolated molecule.

Due to this twofold character of the chemical environment of atoms near the surface, the computational description of its electronic structure is more difficult than in crystalline phases and for isolated molecules. A proper theoretical model has to consider the Bloch character of the electrons in two dimensions, as well as the unsaturated bonding situation of the surface atoms. In order to achieve this, the most common representation of a real surface is a periodically repeated slab, with a thickness of a few atoms [131, 132, 97].

This model can take advantage of the well-established plane-wave basis set for Bloch electrons, which requires a three-dimensional periodicity of the system. At the same time, a sufficient distance between the slabs ensures that the surface atoms have adequately unsaturated bonds towards the vacuum.

For insulating crystals, it is often sufficient to assume flat bands, which can be described correctly by a single reciprocal space vector (also called \mathbf{k} -vector or \mathbf{k} -point), normally the Γ -point ($\mathbf{k}=0$). For metallic systems, however, this approximation is not adequate, since a metal is characterized by a Fermi surface crossed by partially occupied bands. This metallic behavior requires that several points of the Brillouin zone be considered explicitly in the calculation.

The theoretical formalism for the treatment of metals is very often based on the Mermin functional [133, 134], which can be seen as an extension to standard density functional theory. To a certain extent, it can be understood as

an approach to achieve fractional occupation numbers $f_{\mathbf{k},n}$ of the bands according to the Fermi distribution function:

$$f_{\mathbf{k},n} = \left(1 + e^{\beta(\varepsilon_{\mathbf{k},n} - \mu)}\right)^{-1}. \quad (2)$$

For insulators, the chemical potential μ lies between two energy levels, and the occupation numbers $f_{\mathbf{k},n}$ in eq. (2) are either 0 or 1. For systems with more metallic character, where the Brillouin zone dispersion cannot be neglected, the chemical potential is located inside a band. Then, the electronic potential is defined implicitly by the condition of charge conservation, i.e. by a fixed total number of electrons:

$$N = \sum_{\mathbf{k},n} f_{\mathbf{k},n}. \quad (3)$$

The Mermin functional eventually leads to an electronic density of the form:

$$n(\mathbf{r}) = \sum_{\mathbf{k},n} f_{\mathbf{k},n} |\Psi_{\mathbf{k},n}(\mathbf{r})|^2. \quad (4)$$

The standard Kohn-Sham equations of DFT also have to be modified appropriately [134, 135, 136], in order to take into account the fractional occupation numbers of the electronic orbitals and the effect of \mathbf{k} -points other than $\mathbf{k} = 0$. Due to this additional complexity, the numerical solution of the final equations is computationally significantly more expensive than comparable calculations for insulators. However, they have become feasible for realistic systems consisting of unit cells of up to four layers of 5×5 atoms, using a Monkhorst-Pack mesh [137] of $4 \times 4 \times 1$ \mathbf{k} -points.

From the chemical and physical point of view, surfaces are interesting because of their unsaturated bonds of the outermost atoms. These orbitals provide the key to many of the interesting properties of surfaces, of which catalytic abilities are probably the most prominent ones. Before surfaces can act as catalysts, the reactants first have to adsorb onto them. The adsorption process and its dynamics is not yet well understood, even for very small systems. Therefore, the theoretical and experimental study of the adsorption of molecules and clusters on surfaces is a very active area of research [138, 139, 140, 141, 131, 132, 97].

3.3.2 Hydrogen bonding on metallic surfaces: water oligomers on nickel

In this section, the adsorption of water oligomers (molecule, dimer and trimer) on metallic nickel surfaces are presented, both on a perfect (flat) surface and on a surface with a periodic step defect [20, 25]. In particular, the energetics, molecular geometries, electronic density rearrangements and the redshift in IR frequencies are studied. Of particular interest is the interplay of hydrogen bonding between the water molecules, and their interaction with the surface. The first goal is to investigate the preferred adsorption geometries and adsorption energies, and to analyze the binding mechanisms by means of electronic density difference maps. Special attention is devoted to the incremental adsorption process, i.e. the way additional molecules attach to an already adsorbed water.

The first water molecule is bound to the surface with an energy of about 0.2-0.4 eV, which is up to twice the strength of a water-water hydrogen bond. Surprisingly, subsequent water molecules increase the total adsorption energy by typically 0.5 eV, which represents the strength of about 2.5 standard hydrogen bonds. A table with all relevant energetic and geometrical data for different adsorption sites is given in ref. [20].

However, the redistribution of electronic density upon adsorption indicates that this additional attraction is not due to the interaction of the new molecule

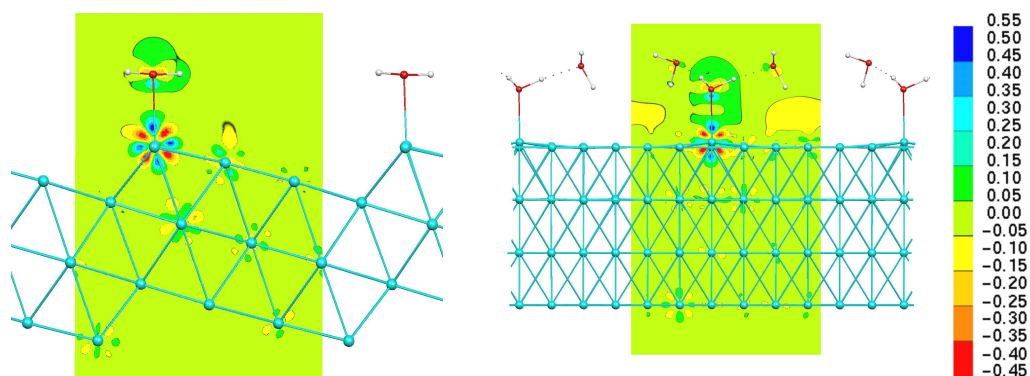


Figure 17: Geometries of a water monomer on a stepped nickel surface (left) and a water trimer on a flat surface (right). The computational unit cell has been partly replicated. In the background of the central unit cell, the electronic density difference between the isolated surface and the isolated adsorbate and the compound system is plotted. The colorscale is in units of $e/\text{\AA}^2$.

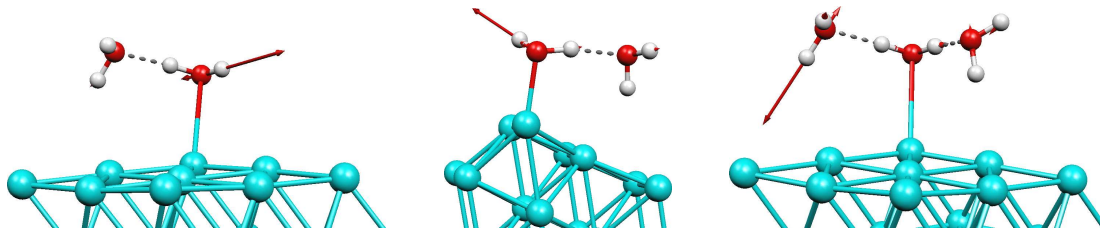


Figure 18: Pictogram of selected OH vibrations for the water dimer adsorbed on the ideal flat and stepped Ni surface (left and middle, respectively) and for a water trimer on the flat Ni surface (right). A single unit cell is shown, to which the same periodic continuation could be applied as done in figure 17. Only the first surface layer of nickel atoms is shown.

with the surface. Instead, it appears that the link between the surface and the first water molecule is enhanced. This can be seen in figure 17, where calculated electron density difference maps for selected energetically favorable configurations are presented. They show the rearrangement of the density between the surface-adsorbed $\text{Ni} \cdot (\text{H}_2\text{O})_n$ complex and the fragments. The color-coding of these maps represents the projected electron density differences $\delta\rho(x, z)$ defined as

$$\delta\rho(x, z) = \int dy \rho_{(\mathbf{r})}^{\text{Ni} \cdot (\text{H}_2\text{O})_n} - \rho_{(\mathbf{r})}^{\text{Ni}} - \rho_{(\mathbf{r})}^{(\text{H}_2\text{O})_n}. \quad (5)$$

One of the protons of the second and third molecule points towards the surface. In this area, the yellow color coding in figure 17 represents the removal of electronic density upon adsorption. This indicates that the electronic interaction of the additional two molecules with the surface actually is repulsive. In contrast to this, the electronic density in the dark green areas which surround the central water molecule is somewhat enhanced. This is the manifestation of an increased strength of the Ni–O bonding, which is also reflected in the increased total binding energies of the trimer.

An complementary confirmation of this result is found in the change of the frequencies of the normal modes of the adsorbed water oligomers. In figure 18, some of these modes are illustrated for the water dimer and trimer on the flat and stepped surfaces. Generally, both in experiment and in the ab-initio calculations, a redshift is found for many of the IR frequencies. The detailed values are given in tables 1 and 3 of ref. [25].

Several interesting trends can be extracted from these calculations. First,

the Ni–O modes at the step adsorption site are about 100cm^{-1} blueshifted with respect to the flat surface, which confirms the enhanced attraction due to the defect. A second point is that the hydrogen bonds between the water molecules are weaker in the adsorbed complex than for a dimer in vacuum. This can be seen in a strong redshift of the corresponding OH stretch mode of the H-bond donor.

The Ni–O modes of the central water molecule in the adsorbed trimer vibrate more than 100cm^{-1} higher than for the dimer. This indicates that the Ni–O bond of the first adsorbed water is strengthened due to the arrival of the third molecule (in agreement with a decrease of the Ni–O bond length: 2.26\AA for the monomer, 2.12\AA for dimer and 2.08\AA for trimer). The electronic density which constitutes the weak bond between the surface nickel atom and the oxygen of the adsorbed water is mostly taken from the bonded nickel atom, which is strongly polarized due to the adsorption, and its first Ni neighbors. This bonding mechanism remains essentially the same for all small water clusters.

3.4 Nanotubes as host/guest systems

3.4.1 Hydrogen-bonded molecular nanotubes from calixhydroquinone building blocks

The concepts of supramolecular self-assembly phenomena have attracted considerable interest as a means to create structures on the nanoscale without actually having to build them manually. A particularly active field of research is concerned with organic and inorganic nanotubes. Besides the research carried out on covalently bonded systems, recent work is devoted to supramolecular nanotubes which offer template functionalities for the design of nanoscale materials. One representative for this class of systems and the basic elements of its self-assembling via hydrogen bonds is shown in figure 19. The individual components of these tubes are calix[4]hydroquinone (CHQ, molecular structure shown in figure 20), which adopt a bowl-shaped conformation, and are stabilised by the four inner hydroxyl groups forming a circular proton tunneling resonance of hydrogen bonds at the bottom of each bowl. The tubes are built from stacks of CHQ molecules which are tied together at their upper rims through extended one-dimensional arrays of $\text{O}-\text{H}\cdots\text{O}$ hydrogen bonds. Each of these arrays consists of a well-

defined sequence of water and the hydroxyl groups. Due to this arrangement, the CHQ bowls are open towards the inner part of the tubes, and one proton per bridging water molecule is potentially available for additional hydrogen bonding. Experimentally, the CHQ nanotubes are grown from a mixture of water and acetone [142, 143].

Organic nanotubes are well-known host molecules with a pronounced capability of including small guest molecules. Therefore, the question arises whether the CHQ tubes are actually hollow or whether another species is trapped inside the bowls. X-ray data, however, cannot provide clear evidence for the presence of guests such as acetone and water, because disordered or mobile species are difficult to observe. However, solid-state NMR experiments and ab-initio calculations of NMR parameters are in principle able to characterize such mobile molecules.

The results are shown in figure 21 and presented in detail in ref. [15]. The calculation of the ^1H NMR chemical shifts of an empty CHQ nanotube could not reproduce the experimental findings, while for the acetone-filled tube, each experimental NMR line could be assigned unambiguously. In particular, the experimental peak at -0.5ppm was initially not understood, since a regular liquid acetone signal would be expected at about 2.2ppm. Via the explicit calculation of acetone molecules contained inside the tubes, an acetone resonance of about 0ppm was found, thus explaining the experimental position.

This unusually low frequency of the host molecule is due to the proximity of

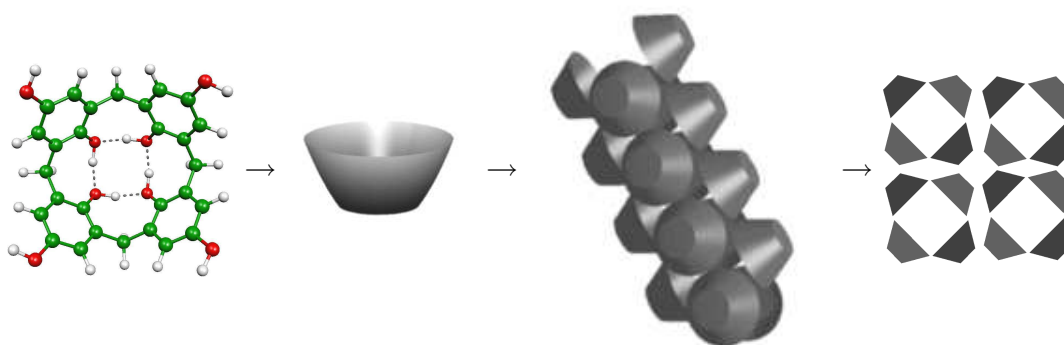


Figure 19: From left to right: A calixhydroquinone molecule, its bowl-shaped form, the nanotube made out of those bowls, and the packing of the tubes relative to each other.

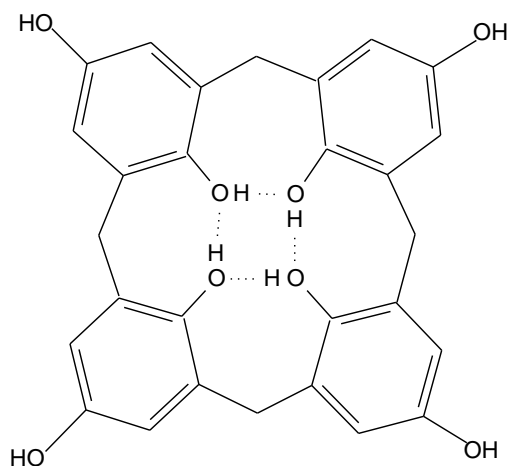


Figure 20: The structure of a single calix-hydroquinone molecule.

the acetone methyl groups to the aromatic moieties of the CHQ nanotubes. It is known that aromatic molecules are able to change the magnetic shielding in their local environment by a few ppm – for an example of this, see section 3.1.3 about the homoaromaticity of barbaralane molecules. This effect can be captured by

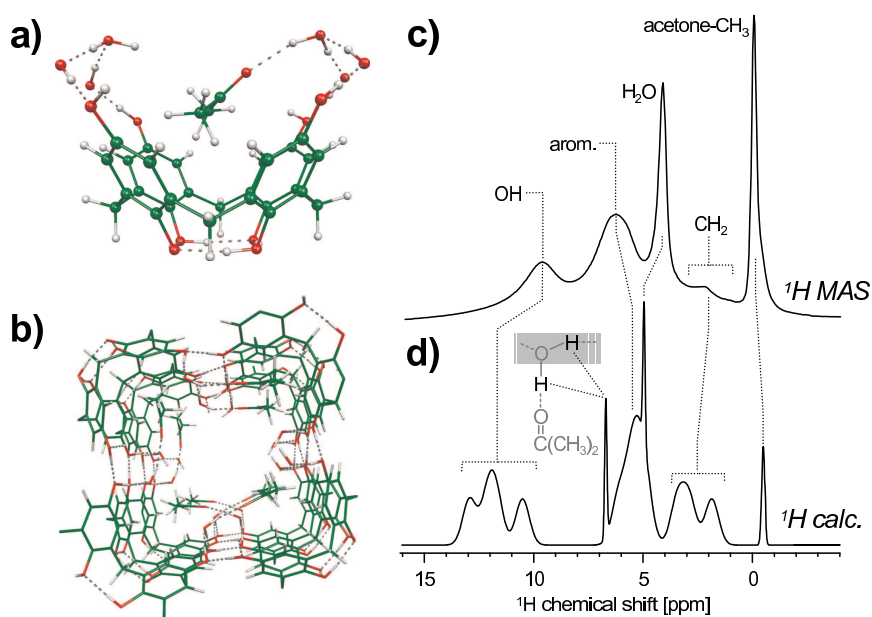


Figure 21: (a) Representation of a bowl-shaped CHQ with a hosted acetone molecule, whose carbonyl oxygen hydrogen-bonded to an available water proton. (b) Representation of a unit cell of the CHQ nanotube filled with acetone molecules. (c) Experimental and (d) calculated ^1H solid-state NMR spectrum of the acetone-filled CHQ nanotube crystal.

calculating the *change* in the local shielding at positions *around* the responsible molecule. For this kind of calculations, it is not necessary to actually place a test atom with a nuclear spin at the desired position; the calculation is done in a *nucleus independent* way. Hence, such displacements are called Nucleus Independent Chemical Shifts (NICS), an acronym introduced and pioneered by the group of Schleyer [116, 113]. The principles of these calculations, including an extension to periodic boundary conditions, are documented in ref. [24] and briefly outlined in section A. This technique has also been applied to CHQ molecules and nanotubes [24], providing a clear explanation of the unusual displacements in the NMR signals in these systems.

3.4.2 Carbon nanotubes

Carbon nanotubes (CNT) are a similar class of systems. While the CHQ nanotubes, as presented in the previous section, are composed of independent molecules which are mutually connected only by a one-dimensional hydrogen-bond network, CNTs represent single large molecules. They consist of graphene sheets that are “rolled up” along a certain direction in the graphene plane. The chirality and the diameter of a CNT are characterized by a vector (n, m) , which defines the so-called chiral vector $n\mathbf{a}_1 + m\mathbf{a}_2$ (with \mathbf{a}_1 and \mathbf{a}_2 being the lattice vectors of the graphene sheet). This vector links those two carbon atoms (in graphene) which will be overlaid on each other upon rolling [144, 145, 146].

Even more than CHQ nanotubes, CNTs are possible storage containers for guest molecules [147]. A popular example is the storage of hydrogen molecules, which was hoped to be very efficient in CNTs. While this transport functionality has not yet reached the stage of industrial applicability, it would nevertheless be interesting to be able to characterize the location of guest molecules with a simple technique. For this purpose, NMR spectroscopy can be of great use, especially in combination with the first-principles prediction of the expected spectra. While the calculation of the expected NMR chemical shifts of a guest molecule would be straightforward, there is a more general way of calculating the relevant quantities. Using nucleus independent chemical shift maps (NICS, see also appendix A for a more detailed documentation), it is possible to provide more physical insight into the expected change in NMR frequency of a guest molecule when it enters a nanotube. These maps show how the NMR signal of a spin would be modified

at any position in space due to the presence of the nanotube [24].

One component of the nucleus-independent chemical shift tensor and the full NICS map of a (11,0) carbon nanotube are shown in figure 22. On the left, a magnetic field is applied orthogonally to the tube (from left to right), and the component of the induced field along the same direction is plotted. The CNT responds to the external horizontal field with strong currents out of and into the paper plane on the upper and lower edges of the tube, respectively. These in turn induce a field shown in the picture. Particularly remarkable are the large ppm-scale, but also the homogeneity of the field inside the nanotube. The red and yellow areas are not closed due to the periodicity of the calculation (i.e. the overlaying induced field from neighboring unit cells).

On the right, the trace of the NICS tensor is presented. This plot shows that the NICS field outside the tube is quasi zero, while the values inside are of the order of 45-50 ppm and very homogeneous. This indicates that a guest molecule outside the CNT should essentially have the same NMR shift as before, while a penetration inside the tube would result in a very pronounced low-frequency shift.

As shown in ref. [24], the actual value of this low-frequency NICS shift depends on the diameter of the nanotube; but also the presence of defects has an influence on this value. A simple transition from a (11,0) to a (12,0) CNT, for instance, modifies the perfect conjugation of the aromatic rings and hence

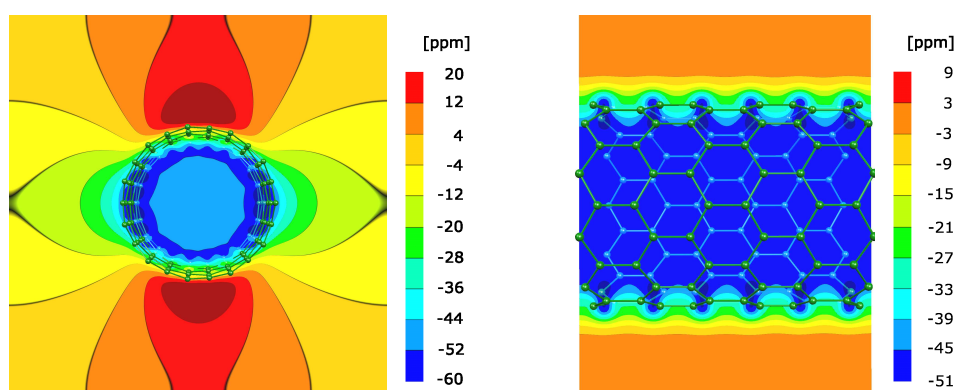


Figure 22: Left: The horizontal component of the induced magnetic field (in ppm) for a horizontal external field (i.e. the (x,x) -component of the NICS tensor field, $\delta_{x,x}$) of the (11,0) CNT. Right: The isotropic NICS field (in ppm) for the (11,0) CNT.

reduces the NICS values in the tube by about 10-20%. This property could be exploited further as a measure of the quality of the nanotube: the more perfect the nanotube, the larger the low-frequency shifts.

While further work is necessary to get a better understanding how a defect changes the NICS field, it seems possible to conclude already at this stage that the first-principles calculation of nucleus independent chemical shift maps of extended systems opens interesting new perspectives for the analysis of functional molecules and materials.

3.5 Liquids and solutions

3.5.1 Hydrochloric acid: signatures of H_3O^+ and Cl^- solvation from ^1H NMR chemical shift spectra

Liquids are disordered systems whose (instantaneous) short- and long-range structure is strongly fluctuating with time. While most of the systems presented in the previous sections were structurally ordered, at least to a certain degree, low-viscosity liquids are characterized by almost unrestricted rotational and translational degrees of freedom of the constituting molecules. On timescales that exceed a certain threshold (in low viscosity liquids usually below or around a nanosecond), every particle has essentially traveled through the entire available phase space. If an experimental measurement has a duration longer than this time, its result will be rotationally and translationally averaged over the accessible phase space.

Note also that this particular property of liquid systems is what causes the “white spot” in figure 1, where no entry is found for the combination of liquids/solutions with static calculations. The calculation of properties obtained by neglecting any statistical averaging over the thermally induced motion of the particles would result in an only partially correct picture of the experimental situation.

Hence, it is necessary to combine calculations of structural and spectroscopic properties of liquids with a sampling technique that is capable of delivering a realistic description of the quickly varying local molecular structure [148, 149]. For successful theoretical predictions, this should include intramolecular motion,

but the incorporation of intermolecular interactions as well as their influence on the intramolecular structure is even more important. A simplified example for this last point is a water dimer. The atoms of an isolated water molecule will perform a thermal motion similar to that of a harmonic oscillator – for which a calculation at the equilibrium geometry is often a good approximation. In a water dimer, however, the OH-distance of the hydrogen-bond donator proton will be significantly elongated and the vibrational motion will be more anharmonic, causing a change in many molecular properties.

A exceptionally powerful approach to this problem is the Car-Parrinello molecular dynamics scheme [46], which efficiently combines explicit atomistic molecular dynamics simulations with density functional theory for the calculation of energies and atomic forces. This approach has already been used in section 3.2.4 to obtain the temperature dependence of nuclear quadrupole couplings in benzoic acid crystals. Here, it shall be used to obtain an image of the solvation structure of an aqueous HCl solution.

Liquid water has a dense hydrogen bonding network which is subject to very fast fluctuations. The exact nature of this network is being studied with experimental and theoretical methods since many years [150, 151, 152, 153, 154, 81, 155, 156, 76, 77] and still gives rise to heated debates [157, 158, 159, 160, 161, 162, 163]. A special behavior is found for water under supercritical conditions [164, 165, 166], where the nature of the hydrogen bond network changes, as seen in several experiments and the corresponding theoretical simulations [167, 168, 169, 164, 165, 166]. This modification induces new unexpected properties, such as the ability to oxidize organic waste [170, 171].

Yet, even water under standard ambient conditions is not fully understood. A currently very active field of research is the solvation of molecules and ions, where the combination of theoretical predictions with spectroscopic methods provides improved understanding of the experimental findings.

In the following, a combined experimental and ab-initio study of the ^1H NMR chemical shift resonance of aqueous hydrochloride (HCl) solution as a function of acid concentration is presented [27]. Apart from pure water as a reference system, HCl solutions at two concentrations ($c=2.6\text{M}$ and $c=4.9\text{M}$) were considered. A snapshot from the molecular dynamics trajectory of the acid is shown in figure 23. After dissociation of the HCl molecule into H^+ and Cl^- ions, the H^+ can associate

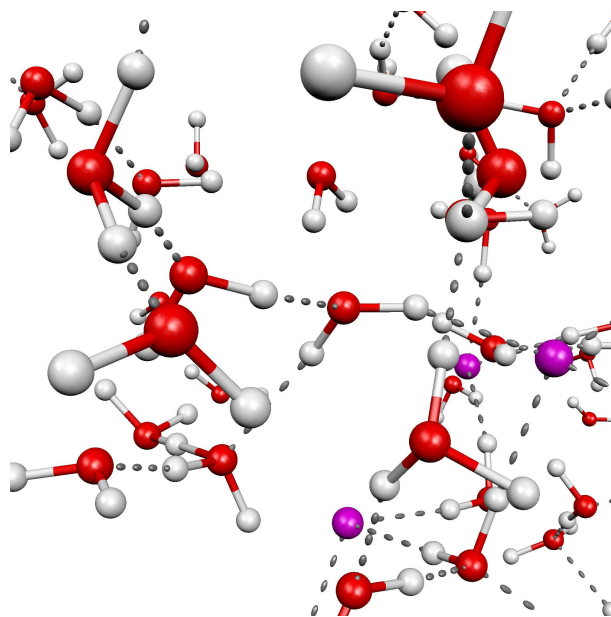


Figure 23: Geometry of a snapshot taken from the MD-simulations at 4.9M HCl concentration. Apart of the normal hydrogen bonding network of water, the solvation of some of the chlorine ions (right) as well as a Zundel ion (bottom left) and two hydronium ions (top left and bottom right) are visible.

to a water molecule (hydronium ion, H_3O^+), which is strongly hydrogen bonded by three surrounding waters. This complex is called Eigen cation. Alternatively, the charged proton can be shared by two waters, yielding a Zundel complex. Similarly, the Cl^- ion is surrounded by three to five water molecules, which screen its negative charge.

Due to the very fast molecular motion at ambient conditions, there is a steady exchange between the water molecules from the hydronium ion, from the chlorine solvation shell, and the regular water. Hence, the NMR experiment only shows a single resonance, which is the statistical average over the water molecules in these three categories. From the first-principles calculations, however, the individual ^1H NMR signatures of the different complexes are available. It can be seen that the contributions of Eigen and Zundel ions, regular water molecules and the chlorine solvation shell to the ^1H NMR resonance line are actually very distinct (presented in detail in ref. [27]), and almost independent on the acid concentration. From the computed instantaneous NMR distributions, it is further possible to characterize the average variation in hydrogen bond strength of the different complexes.

The comparison of the averaged NMR shifts from the ab-initio calculations

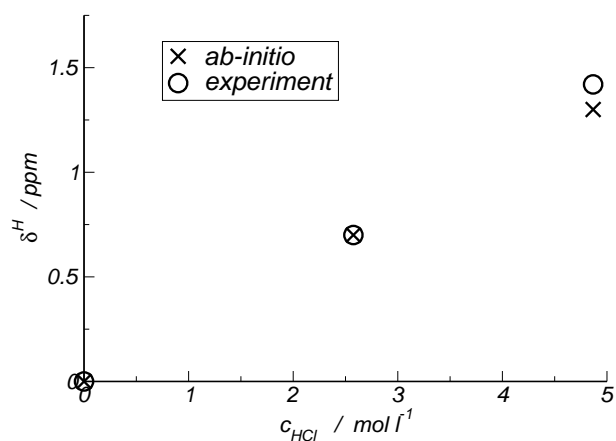


Figure 24: Dependence of the experimental and calculated NMR chemical shifts on the HCl concentration. The nuclear shieldings are referenced to liquid water, such that $\delta(\text{pure H}_2\text{O})=0\text{ppm}$.

with measured liquid-state ^1H NMR spectra of the HCl acids at the two concentrations is presented in figure 24. Both the calculated and experimental shifts were referenced to pure liquid water by using $\delta(X) = \sigma^{\text{pure H}_2\text{O}} - \sigma(X)$. The agreement is complete for the low concentration and still very good for the sample at 4.9M. The very good agreement also provides support that, despite the computational difficulties involved in these calculations, the description of disordered and highly fluctuating liquids and solutions are possible by means of Car-Parrinello molecular dynamics simulations. They provide realistic ensemble averages for the subsequent calculation of spectroscopic parameters, yielding a detailed picture of microscopic structures in complex solutions.

4 Conclusion

This Habilitation Thesis presents first principles studies of a variety of molecular and supramolecular systems with different intrinsic complexities: molecules, molecular crystals, surfaces, nanotubes, and solutions. The ab-initio calculations are always done under explicit consideration of the actual chemical environment of the systems in the condensed phase.

In many of these supramolecular systems, there is an interplay – often also a direct competition – between different structural driving forces. The most prominent one is hydrogen bonding, which is present in most of the examples shown here. Frequently, this H-bonding has to compete with sterical constraints, but also with entropic driving forces, yielding a specific equilibrium state. In such situations, a reliable incorporation of temperature effects, in combination with a realistic modeling of the chemical environment, is essential for the success of simulations.

The different complexities of the considered systems further imply different degrees of detail in the data extracted from the respective simulations. While in simple systems, accurate bond distances and angles can be computed, other more disordered samples allow only for the determination of trends and structural preferences. The same holds for the properties that can be extracted from calculations: the more complex the molecular configurations, the less accurate are computed spectral and structural parameters.

One of the more general purposes of computer simulations is the capability to invalidate structural features. While a direct *validation* is not possible in principle, it could be illustrated on several examples that tempting intuitive arguments which seem plausible do not always hold. For the temperature dependence of the nuclear quadrupole couplings (section 3.2.4), the simple anharmonic model failed, and in the HCl solutions (section 3.5.1), it could be shown that the ^1H NMR signal of the hydronium and Cl^- solvation shells is surprisingly independent on the acid concentration.

All the calculations presented in this work have been performed within a single computational approach, namely density functional theory under periodic boundary conditions. Notably, spectroscopic parameters from nuclear magnetic resonance and other spectroscopic techniques have been determined. The direct

comparison of computed and real systems facilitates a reliable interpretation of experimental results. Finally, also fundamental conceptual questions, like the notion of aromaticity in extended systems and at finite temperature, have been successfully addressed with this versatile approach.

Appendix

A Nucleus independent chemical shift maps

This appendix introduces the method for the calculation of nucleus independent chemical shift maps (NICS maps). Its concept was mentioned as early as 1958 by Johnson and Bovey [115], while its implementation and application in quantum chemistry was pioneered by the group of Schleyer [116, 113]. There is a number of further developments and applications of NICS values in literature. They are dominantly used for the characterization of global and local aromaticity of hydrocarbons [172, 173, 174, 175, 176, 177, 178, 179, 12, 180]. Some articles show how the magnetic response properties can be decomposed in contributions of individual orbitals [181, 182, 183] and the effect of particular functional groups [184]. Onother studies describes how the individual components of the NICS tensor can be interpreted [185, 186]. Several articles exploit the generalized NICS maps to describe numerically and visually particular aspects of the electronic structure of molecules [187, 188]. Another branch of publications focuses on the quantitative calculation of the induced ring currents [189] and the investigation of their topological aspects [190, 191, 192, 193]/ There seem to be cases where the prediction of aromaticity through NICS is not straightforward and may lead to an inaccurate characterization,[194, 195] but so far, these possible failures can rather be considered exceptions. Finally, there are also review articles on the topic [196, 197].

The calculations are done for extended condensed-matter systems, which implies the use of periodic (Born-von-Karmann) boundary conditions. As for the NMR chemical shifts, the framework for all calculations is density functional perturbation theory. From the electronic response of the system to the perturbation Hamiltonian due to an external magnetic field, the electronic current density and the NICS map are obtained from inverse Fourier transformations from reciprocal space (G space). Due to its intrinsically periodic description, the method is suitable for isolated molecules (by using a supercell technique) and for condensed-phase systems like solids, liquids and solutions. Via the approach described in refs. [2, 24], it is possible to compute the magnetic field which is induced in the system due to the current created by the electronic linear response to the external

field. The calculation of all relevant quantities is done in their reciprocal-space representation. Once this is achieved, the induced field is available at all points in the unit cell. At the nuclear positions, its value represents one row of the nuclear shielding tensor for a given direction of the external field:

$$\sigma_{\alpha\beta}(\mathbf{R}) = -\frac{\partial B_{\alpha}^{\text{ind}}(\mathbf{R})}{\partial B_{\beta}^{\text{ext}}}. \quad (6)$$

Experimentally, the trace of this tensor is quoted relative to that of a reference molecule to yield the isotropic NMR chemical shift

$$\delta(\mathbf{R}) = \frac{1}{3} \text{Tr} (\sigma_{\alpha\beta}^{\text{ref}} - \sigma_{\alpha\beta}(\mathbf{R})). \quad (7)$$

On the other hand, since the induced field $\mathbf{B}^{\text{ind}}(\mathbf{r})$ is well-defined at all positions of space \mathbf{r} , it is possible to calculate $\delta(\mathbf{r})$ according to eq. (7) also at coordinates where no atom is located. For special points, usually the centers of molecular symmetry, these values are known as nucleus independent chemical shift indices. Using traditional quantum chemical methods with localized basis sets, the calculation of NICS indices for a large number points on a three-dimensional mesh (e.g. 100^3 points) within a certain region of space around a molecule is computationally relatively expensive. However, with this reciprocal-space approach, the induced magnetic field (and therefore a map of NICS indices) is automatically available at all points of the considered periodic unit cell. The computational effort required to obtain these three-dimensional maps for all points \mathbf{r} is essentially equal to that of a single regular chemical shift calculation. The only difference with respect to equation (7) is that NICS maps are referenced to vacuum (with $\sigma=0\text{ppm}$) because they do not refer to any specific nucleus:

$$\delta^{\text{NICS}}(\mathbf{r}) = -\frac{1}{3} \text{Tr} \sigma_{\alpha\beta}(\mathbf{r}). \quad (8)$$

This definition means that positive values of $\delta^{\text{NICS}}(\mathbf{r})$ correspond to a locally increased total magnetic field (“downfield shifts” or high-frequency resonances) while negative ones represent areas of decreased total magnetic field (“upfield shifts”, low-frequency resonances) [24, 198].

The meaning of these NICS indices and NICS maps shall be outlined in the following, starting from the basic ideas of magnetic resonance theory. Consider a

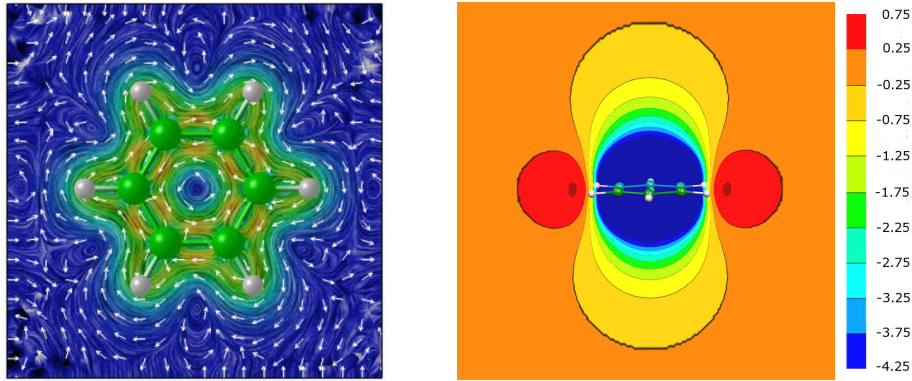


Figure 25: The induced electronic current density (left) and the NICS field (right) for a benzene molecule in a magnetic field perpendicular to the ring plane. The color scale of the current is in arbitrary units, while the NICS map is coded in ppm.

free molecule, with its nuclei as immobile point charges and its electrons following the Schrödinger equation. The presence of an external magnetic field changes the electronic Hamiltonian via a vector potential. This in turn results in small changes of the electronic orbitals, which can be described via perturbation theory. The novel electronic state creates a nonzero current density, which finally induces an additional magnetic field, which is superimposed to the external one. Both the electronic perturbation orbitals and the created electronic current density are proportional to the strength of the external magnetic field. The current can formally be defined as:

$$\mathbf{j}(\mathbf{r}) = \frac{\partial}{\partial \mathbf{B}^{\text{ext}}} \left\langle \Psi^{(\mathbf{B})} \left| \hat{\mathbf{j}} \right| \Psi^{(\mathbf{B})} \right\rangle, \quad (9)$$

where the superscript in $\Psi^{(\mathbf{B})}$ means that the electronic wavefunction has to be taken in the presence of the external magnetic field \mathbf{B}^{ext} , and α denotes the cartesian components. As an example, the ring currents in a benzene molecule upon application of a magnetic field perpendicular to the ring are shown on the left of figure 25. From the current density, the expressions of the induced magnetic field and the derived NICS field are straightforward:

$$\mathbf{B}_{\alpha}^{\text{ind}}(\mathbf{r}) = \frac{\mu_0}{4\pi} \frac{\partial}{\partial \mathbf{r}_{\alpha}} \int d^3r' \frac{\mathbf{j}(\mathbf{r}')}{|\mathbf{r} - \mathbf{r}'|} \quad (10)$$

$$\text{NICS}(\mathbf{r}) = - \sum_{\alpha} \frac{\partial}{\partial \mathbf{B}_{\alpha}^{\text{ext}}} \mathbf{B}_{\alpha}^{\text{ind}}(\mathbf{r}). \quad (11)$$

The exact expressions of the operator $\hat{\mathbf{j}}$ and of the functional form of the induced magnetic field $\mathbf{B}^{\text{ind}}(\mathbf{r})$ can be found in refs. [24], where also the computational approach used to obtain these quantities is described in detail.

For illustration, the induced NICS field of a benzene molecule is shown on the right of figure 25. While the interpretation of the current density is rather intuitive, the meaning of the NICS values according to eq. (11) is a bit more complex. Since $\mathbf{B}^{\text{tot}} = \mathbf{B}^{\text{ext}} + \mathbf{B}^{\text{ind}}$, the value plotted in the right part of figure 25 describes by how much the external magnetic field has been changed due to the reaction of the electrons. For molecules and insulators, this effect is relatively small, of the order of 10^{-6} to 10^{-4} . Hence, the proportionality factor is given in ppm (10^{-6}).

The relatively large area in blue, green and yellow above and below the benzene molecule are a typical sign of strong induced fields due to delocalized aromatic electrons. Those are able to create ring currents which cover a large surface area, which in turn increases the magnetic dipole induced by the currents. Another typical sign of aromaticity is the presence of positive NICS values (red in figure 25) in areas coplanar with the ring. These are a consequence of the closure of the magnetic field lines: The field of a dipole is inversely oriented in regions along the dipole direction, compared to regions orthogonal to it.

B Published Habilitation work

The scientific articles which constitute the written part of this Habilitation are explicitly mentioned below. Further, a detailed description of the contribution of each of the authors is given. At the end of this work, a reprint of each of these articles is added.

- Ref. [10]: G. Goward, D. Sebastiani, I. Schnell, H.W. Spiess, H.D. Kim and H. Ishida:

Benzoxazine Oligomers: Evidence for a helical structure from solid-state NMR spectroscopy and DFT-based dynamics and chemical shift calculations;

J. Am. Chem. Soc. **125**, 5792 (2003)

In this work, G. Goward, I. Schnell and H.W. Spiess were responsible for the experimental solid-state NMR spectra, and H.D. Kim and H. Ishida for the synthetic part of the work. I was responsible for all theoretical aspects.

- Ref. [18]: B. Kirchner and D. Sebastiani:

Visualizing degrees of aromaticity for different barbaralane systems;

J. Phys. Chem. A **108**, 11728 (2004)

In this work, B. Kirchner provided the structures and the initial geometries of the barbaralane molecules, and also provided bibliographic aspects for these molecules. My contribution were the molecular dynamics simulations and the calculation of the nucleus independent chemical shift maps.

- Ref. [26]: J. Schmidt, A. Hoffmann, H.W. Spiess and D. Sebastiani:

Bulk chemical shifts in hydrogen bonded systems from first principles calculations and solid-state-NMR;

J. Phys. Chem. B, submitted (2006)

In this work, A. Hoffmann and H.W. Spiess were responsible for the experimental solid-state NMR spectroscopy. J. Schmidt worked as Ph.D. student under my supervision on the calculation of structure and spectroscopic parameters.

- Ref. [7]: G. Goward, M. F. Schuster, D. Sebastiani, I. Schnell, and H.W. Spiess:

High-Resolution Solid-State NMR Studies of Imidazole-Based Proton Conductors: Structure Motifs and Chemical Exchange from ^1H NMR;

J. Phys. Chem. B **106**, 9322 (2002)

In this work, G. Goward, I. Schnell and H.W. Spiess were responsible for the experimental solid-state NMR spectra, and M. F. Schuster for the synthetic part of the work. I was responsible for all theoretical aspects.

- Ref. [23]: J. Schmidt and D. Sebastiani:

Anomalous temperature dependence of nuclear quadrupole interactions in strongly hydrogen bonded systems from first principles;

J. Chem. Phys. **123**, 074501 (2005)

In this work, J. Schmidt worked as Ph.D. student under my supervision on the molecular dynamics simulations and the calculations of the electric field gradients.

- Ref. [20]: D. Sebastiani and L. Delle Site:

Adsorption of water molecules on flat and stepped nickel surfaces from first principles;

J. Chem. Theory Comput. **1**, 78 (2005)

In this work, L. Delle Site performed the geometry optimizations of the surface-adsorbed water molecules. My contribution was the electronic analysis of the adsorption by means of density difference plots.

- Ref. [25]: T. Murakhtina, L. Delle Site and D. Sebastiani:

Vibrational frequencies of water adsorbed on (111) and (221) nickel surfaces from First Principle calculations;

ChemPhysChem **7**, 1215-1219 (2006)

In this work, T. Murakhtina worked as Ph.D. student under my supervision on the calculation of the geometric structure and the vibrational spectra of the adsorbates, and L. Delle Site provided computational assistance.

- Ref. [15]: A. Hoffmann, D. Sebastiani, E. Sugiono, K.S. Kim, H.W. Spiess and I. Schnell:

Solvent molecules trapped in supramolecular organic nanotubes: a

combined solid-state NMR and DFT study;

Chem. Phys. Lett. **388**, 164 (2004)

In this work, A. Hoffmann, I. Schnell and H.W. Spiess were responsible for the experimental solid-state NMR spectra, and E. Sugiono and K.S. Kim for the synthetic part of the work. I was responsible for all theoretical aspects.

- Ref. [24]: D. Sebastiani:

Current densities and nucleus independent chemical shift (NICS) maps from reciprocal space density functional perturbation theory calculations;

ChemPhysChem **7**, 164-175 (2006)

- Ref. [27]: T. Murakhtina, J. Heuft, E.J. Meijer and D. Sebastiani:

Ab-initio and experimental ^1H NMR signatures of solvated ions: the case of HCl(aq) ;

ChemPhysChem , submitted (2006)

In this collaboration, the molecular dynamics simulations of the hydrochloric acids were done by E.J. Meijer and his Ph.D. student J. Heuft, while T. Murakhtina worked as Ph.D. student under my supervision on the calculation and measurements of the NMR spectra of the HCl solutions.

C Acknowledgements

This Habilitation Thesis would not have been possible without the continuous support of many people, and I wish to express my gratitude to them:

Prof. H.W. Spiess for his very active and friendly encouragements, his valuable hints and suggestions regarding science and personal development.

Prof. J. Gauss and Priv.-Doz. G. Diezemann for integrating me into the regular teaching activities in the physical and theoretical chemistry department at the University of Mainz.

My Ph.D. students S. Komin, T. Murakhtina and J. Schmidt for their scientific contributions, their hard work with (or against?) the computers, and their patience with me.

C. Kautz for her patient support, as well as for the numerous candies from her desk.

My scientific collaborators from the experimental side, Dr. P. Blümle, Dr. G. Brunklaus, Dr. G. Goward, Dr. R. Graf, Prof. G. Jeschke, Dr. U. Jonas, Dr. A. Koch, Dr. J. Schmiedeskamp, Priv.-Doz. I. Schnell, and Prof. M. Wilhelm, for very interesting excursions into actual experiments.

My scientific colleagues and collaborators from the computational chemistry community, Dr. T. Alam, Prof. R. Car, Dr. L. Delle Site, Priv.-Doz. I. Frank, Prof. J. Hutter, Priv.-Doz. B. Kirchner, Prof. K. Kremer, Dr. A. von Lilienfeld, Prof. M. Parrinello, Prof. U. Röthlisberger, Dr. I. Tavernelli, for interesting discussions about the mysteries of electronic structure calculations.

All the former and present members of the Spiess group, who taught me what polymers are and what the city of Mainz and its environment can offer.

References

- [1] A. Putrino, D. Sebastiani and M. Parrinello, *J. Chem. Phys.* **113**, 7102 (2000).
- [2] D. Sebastiani and M. Parrinello, *J. Phys. Chem. A* **105**, 1951 (2001).
- [3] S. Piana, D. Sebastiani, P. Carloni and M. Parrinello, *J. Am. Chem. Soc.* **122**, 123 (2001).
- [4] D. Benoit, D. Sebastiani and M. Parrinello, *Phys. Rev. Lett.* **87**, 226401 (2001).
- [5] D. Sebastiani, G. Goward, I. Schnell and M. Parrinello, *Comput. Phys. Comm.* **147**, 707 (2002).
- [6] D. Sebastiani and M. Parrinello, *ChemPhysChem* **3**, 675 (2002).
- [7] G. Goward, M. F. Schuster, D. Sebastiani, I. Schnell and H. W. Spiess, *J. Phys. Chem. B* **106**, 9322 (2002).
- [8] A. H. Romero, D. Sebastiani, R. Ramírez and M. Kiwi, *Chem. Phys. Lett.* **366**, 134 (2002).
- [9] D. Sebastiani, G. Goward, I. Schnell and H. W. Spiess, *J. Mol. Struct. (THEOCHEM)* **625**, 283 (2003).
- [10] G. Goward, D. Sebastiani, I. Schnell and H. W. Spiess, *J. Am. Chem. Soc.* **125**, 5792 (2003).
- [11] T. M. Alam, T. Friedmann, P. A. Schultz and D. Sebastiani, *Phys. Rev. B* **67**, 245309 (2003).
- [12] A. Rapp, I. Schnell, D. Sebastiani, S. P. Brown, V. Percec and H. W. Spiess, *J. Am. Chem. Soc.* **125**, 13284 (2003).
- [13] D. Sebastiani, *Mod. Phys. Lett. B* **17**, 1301 (2003).
- [14] D. Sebastiani and U. Rothlisberger, *J. Phys. Chem. B* **108**, 2807 (2004).
- [15] A. Hoffmann, D. Sebastiani, E. Sugiono, K. S. Kim, H. W. Spiess and I. Schnell, *Chem. Phys. Lett.* **388**, 164 (2004).

- [16] L. Delle Site and D. Sebastiani, *Phys. Rev. B* **70**, 115401 (2004).
- [17] A. von Lilienfeld-Toal, I. Tavernelli, U. Rothlisberger and D. Sebastiani, *Phys. Rev. Lett.* **93**, 153004 (2004).
- [18] B. Kirchner and D. Sebastiani, *J. Phys. Chem. A* **108**, 11728 (2004).
- [19] A. von Lilienfeld-Toal, I. Tavernelli, U. Rothlisberger and D. Sebastiani, *J. Chem. Phys.* **122**, 014113 (2005).
- [20] D. Sebastiani and L. Delle Site, *J. Chem. Theory Comp.* **1**, 78 (2005).
- [21] D. Sebastiani, *Int. J. Quantum Chem.* **101**, 849 (2005).
- [22] A. von Lilienfeld-Toal, I. Tavernelli, U. Rothlisberger and D. Sebastiani, *Phys. Rev. B* **71**, 195119 (2005).
- [23] J. Schmidt and D. Sebastiani, *J. Chem. Phys.* **123**, 074501 (2005).
- [24] D. Sebastiani, *ChemPhysChem* **7**, 164 (2006).
- [25] T. Murakhtina, L. Delle Site and D. Sebastiani, *ChemPhysChem* **7**, 1215 (2006).
- [26] J. Schmidt, A. Hoffmann, H. W. Spiess and D. Sebastiani, *J. Phys. Chem. B* (2006), submitted.
- [27] T. Murakhtina and D. Sebastiani, *ChemPhysChem* (2006), submitted.
- [28] J.-M. Lehn, **67**, 249 (2004).
- [29] U. Dusek, G. P. Frank, L. Hildebrandt, J. Curtius, J. Schneider, S. Walter, D. Chand, F. Drewnick, S. Hings, D. Jung, S. Borrmann and M. O. Andreae, *Science* **312**, 1375 (2006).
- [30] J. R. Vossing HJ, *Atm. Res.* **49**, 199 (1998).
- [31] A. Szabo and N. S. Ostlund, *Modern Quantum Chemistry*, Dover Publications Inc., Mineola, New York, 1996.
- [32] R. M. Martin, *Electronic Structure: Basic Theory and Practical Methods*, Cambridge University Press, 2004.

-
- [33] J. Cízek, *J. Chem. Phys.* **45**, 4256 (1966).
- [34] J. Cízek, *Adv. Chem. Phys.* **14**, 35 (1969).
- [35] J. Cízek, *Int. J. Quantum Chem.* **5**, 359 (1971).
- [36] Y. J. Bomble, J. F. Stanton, M. Kállay and J. Gauss, *J. Chem. Phys.* **123**, 054101 (2005).
- [37] C. Møller and M. S. Plesset, *Phys. Rev.* **46**, 618 (1934).
- [38] P. Knowles, M. Schütz and H.-J. Werner, Ab initio methods for electron correlation in molecules, in *Modern Methods and Algorithms of Quantum Chemistry*, edited by J. Grotendorst, pages 97–179, John von Neumann Institute for Computing, Jülich, NIC Series, Vol. 3, 2000.
- [39] S. Saebo and P. Pulay, *J. Chem. Phys.* **115**, 3975 (2001).
- [40] M. Schutz, G. Hetzer and H. Werner, *J. Chem. Phys.* **111**, 5691 (1999).
- [41] G. Hetzer, M. Schutz, H. Stoll and H. Werner, *J. Chem. Phys.* **113**, 9443 (2000).
- [42] R. G. Parr and W. Yang, *Density functional theory of atoms and molecules*, Oxford Science Publications, 1989.
- [43] Ashcroft, *Solid state physics*, Saunders, Philadelphia, 1976.
- [44] W. A. L. Jr., editor, *Recent advances in quantum Monte Carlo methods*, World Scientific, 1997.
- [45] R. Q. Hood, M.-Y. Chou, A. J. Williamson, G. Rajagopal, R. J. Needs and W. M. C. Foulkes, *Phys. Rev. Lett.* **78**, 3350 (1997).
- [46] R. Car and M. Parrinello, *Phys. Rev. Lett.* **55**, 2471 (1985).
- [47] M. Parrinello, *Solid State Comm.* **102**, 107 (1997).
- [48] T. Christen, P. Hunenberger, D. Bakowies, R. Baron, R. Burgi, D. Geerke, T. Heinz, M. Kastenholtz, V. Krautler, C. Oostenbrink, C. Peter, D. Trzesniak and W. van Gunsteren, *J. Comp. Chem.* **26**, 1719 (2005).

- [49] B. Isralewitz, M. Gao and K. Schulten, *Curr. op. struct. biol.* **11**, 224 (2001).
- [50] D. Lu, A. Aksimentiev, A. Y. Shih, E. Cruz-Chu, P. L. Freddolino, A. Arkhipov and K. Schulten, *Phys. Biol.* **3**, 40 (2006).
- [51] K. Kremer, *Macromol. chem. phys.* **204**, 257 (2003).
- [52] J. Baschnagel, K. Binder, P. Doruker, A. A. Gusev, O. Hahn, K. Kremer, W. L. Mattice, F. Muller-Plathe, M. Murat, W. Paul, S. Santos, U. W. Suter and V. Tries, *Adv. polym. sci.* **152**, 41 (2000).
- [53] A. Laio, J. VandeVondele and U. Roethlisberger, *J. Chem. Phys.* **116**, 6941 (2002).
- [54] Q. Cui and M. Karplus, *J. Chem. Phys.* **112**, 1133 (2000).
- [55] R. Z. Deng, G. J. Martyna and M. L. Klein, *Phys. Rev. Lett.* **71**, 267 (1993).
- [56] J. Kastner, H. M. Senn, S. Thiel, N. Otte and W. Thiel, *J. Chem. Theory Comp.* **2**, 452 (2006).
- [57] B. E. Warren, *X-Ray Diffraction*, Dover, Mineola, 1990.
- [58] S. W. Lovesey, editor, *Theory of Neutron Scattering from Condensed Matter*, Oxford University Press, 1988.
- [59] U. Kolb and G. Matveeva, *Z. Kristallogr.* **218**, 259 (2003).
- [60] B. Ruckert and U. Kolb, *Micron* **36**, 247 (2005).
- [61] N. B. Colthup, L. H. Daly and S. E. Wiberley, *Introduction to infrared and Raman spectroscopy*, Academic Press, New York, 1975.
- [62] R. R. Ernst, G. Bodenhausen and A. Wokaun, *Principles of Nuclear Magnetic Resonance in One and Two Dimensions*, Clarendon Press Oxford, 1987.
- [63] K. Wüthrich, *NMR of Proteins and Nucleic Acids*, Wiley, New York, 1986.
- [64] S. Sharif, G. Denisov, M. Toney and H. Limbach, *J. Am. Chem. Soc.* **128**, 3375 (2006).

-
- [65] B. Grunberg, T. Emmeler, E. Gedat, J. Shenderovich, G. H. Findenegg, H. H. Limbach and G. Buntkowsky, *Chem. Eur. J.* **10**, 5689 (2004).
- [66] S. Brown and H. W. Spiess, *Chem. Rev.* **101**, 4125 (2001).
- [67] D. Sakellariou, S. P. Brown, A. Lesage, S. Hediger, M. Bardet, C. A. Meriles, A. Pines and L. Emsley, *J. Am. Chem. Soc.* **125**, 4376 (2003).
- [68] L. Duma, S. Hediger, B. Brutscher, A. Bockmann and L. Emsley, *J. Am. Chem. Soc.* **125**, 11816 (2003).
- [69] G. Wulff, B. O. Chong and U. Kolb, *Angew. Chem. Int. Ed. Engl.* **45**, 2955 (2006).
- [70] P. M. Tolstoy, P. Schah-Mohammedi, S. N. Smirnov, N. S. Golubev, G. S. Denisov and H. H. Limbach, *J. Am. Chem. Soc.* **126**, 5621 (2004).
- [71] M. Wanko, M. Hoffmann, P. Strodet, A. Koslowski, W. Thiel, F. Neese, T. Frauenheim and M. Elstner, *J. Phys. Chem. B* **109**, 3606 (2005).
- [72] I. Schnell, *Curr. anal. chem.* **1**, 3 (2005).
- [73] H. W. Spiess, *Macromol. Chem. Phys.* **204**, 340 (2003).
- [74] H. W. Spiess, *J. Polym. Sci. A* **42**, 5031 (2004).
- [75] H. W. Spiess, *J. Polymer Sci. Part A* **42**, 5031 (2004).
- [76] B. Hetényi, F. D. Angelis, P. Giannozzi and R. Car, *J. Chem. Phys.* **120**, 8632 (2004).
- [77] B. Hetenyi, F. D. Angelis, P. Giannozzi and R. Car, *J. Chem. Phys.* **124**, 099901 (2006).
- [78] U. Kolb, D. Nihtianova and J. Li, *Electron Crystallography*, volume 211, pages 411–420, Weirich et al. (eds.), Kluwer Academic Publishers, Netherlands, NATO ASI Series E: Applied Sciences, 2005.
- [79] A. V. Yakimanski, U. Kolb, G. N. Matveeva, I. G. VoigtMartin and A. V. Tenkovtsev, *Acta Crystallogr. Section A* **53**, 603 (1997).
- [80] P. Umari and A. Pasquarello, *Diam. rel. mat.* **14**, 1255 (2005).

- [81] P. L. Silvestrelli, M. Bernasconi and M. Parrinello, *Chem. Phys. Lett.* **277**, 478 (1997).
- [82] W. Thiel, *Chimia* **58**, 276 (2004).
- [83] A. Abragam, *Principles of Nuclear Magnetism*, Oxford University Press, 1961.
- [84] C. Ochsenfeld, S. P. Brown, I. Schnell, J. Gauss and H. W. Spiess, *J. Am. Chem. Soc.* **123**, 2597 (2001).
- [85] M. Bühl, M. Kaupp, O. L. Malkina and V. Malkin, *J. Comput. Chem.* **20**, 91 (1999).
- [86] C. J. Jameson and A. C. de Dios, *Nuc. Mag. Res.* **33**, 47 (2004).
- [87] M. Kaupp, M. Bühl, M. Malkin and G. Vladimirov, editors, *Calculations of NMR and EPR parameters*, Wiley-VCH, Weinheim, 2004.
- [88] J. R. Yates, T. N. Pham, C. J. Pickard, F. Mauri, A. M. Amado, A. M. Gil and S. P. Brown, *J. Am. Chem. Soc.* **127**, 10216 (2005).
- [89] C. Gervais, R. Dupree, K. J. Pike, C. Bonhomme, M. Profeta, C. J. Pickard and F. Mauri, *J. Phys. Chem. A* **109**, 6960 (2005).
- [90] M. Schulz-Dobrick, T. Metzroth, H. W. Spiess, J. Gauss and I. Schnell, *ChemPhysChem* **6**, 315 (2005).
- [91] K. Laasonen, M. Sprik, M. Parrinello and R. Car, *J. Chem. Phys.* **99**, 9080 (1993).
- [92] P. Silvestrelli and M. Parrinello, *J. Chem. Phys.* **111**, 3572 (1999).
- [93] M. Sharma, R. Resta and R. Car, *Phys. Rev. Lett.* **95**, 187401 (2005).
- [94] A. Putrino and M. Parrinello, *Phys. Rev. Lett.* **88**, 176401 (2002).
- [95] B. Pfrommer, F. Mauri and S. Louie, *J. Am. Chem. Soc.* **122**, 123 (2000).
- [96] M. A. Henderson, *Surf. Sc. Rep.* **46**, 1 (2002).
- [97] R. Ludwig, *Angew. Chem. Int. Ed. Engl.* **42**, 3458 (2003).

-
- [98] R. P. Sijbesma, F. H. Beijer, L. Brunsveld, B. J. B. Folmer, J. H. K. K. Hirschberg, R. F. M. Lange, J. K. L. Lowe and E. W. Meijer, *Science* **278**, 1601 (1997).
- [99] P. Szalay, L. Thogersen, J. Olsen, M. Kallay and J. Gauss, *J. Phys. Chem. A* **108**, 3030 (2004).
- [100] B. Flowers, P. Szalay, J. Stanton, M. Kallay, J. Gauss and A. Csaszar, *J. Phys. Chem. A* **108**, 3195 (2004).
- [101] J. Gauss and J. Stanton, *J. Chem. Phys.* **102**, 251 (1995).
- [102] J. Gauss and J. Stanton, *J. Chem. Phys.* **103**, 3561 (1995).
- [103] A. Dreuw and M. Head-Gordon, *J. Am. Chem. Soc.* **126**, 4007 (2004).
- [104] L. Fritsche, J. Koller and T. Reinert, *Int. J. Quantum Chem.* **100**, 681 (2004).
- [105] G. A. Jones, M. N. Paddon-Row, M. S. Sherburn and C. I. Turner, *Org. Lett.* **4**, 3789 (2002).
- [106] Z. L. Cai, K. Sendt and J. R. Reimers, *J. Chem. Phys.* **117**, 5543 (2002).
- [107] H. D. Kim and H. Ishida, *J. Appl. Polym. Sci.* **79**, 1207 (2001).
- [108] J. A. Macko and H. Ishida, *J. Polym. Sci.* **38**, 2687 (2000).
- [109] H. Ishida and Y. Rodriguez, *Polymer* **36**, 3151 (1995).
- [110] J. Dunkers, E. A. Zarate and H. Ishida, *J. Phys. Chem.* **100**, 13514 (1996).
- [111] I. Schnell, S. P. Brown, H. Y. Low, H. Ishida and H. W. Spiess, *J. Am. Chem. Soc.* **120**, 11784 (1998).
- [112] V. I. Minkin, M. N. Glukhovtsev and B. I. A. Simkin, *Aromaticity and antiaromaticity : electronic and structural aspects*, Wiley, New York, 1994.
- [113] P. v. R. Schleyer, editor, *Aromaticity*, volume 101 (5) of *Chem. Rev.*, 2001.
- [114] Z. F. Chen, A. Hirsch, S. Nagase, W. Thiel and P. v. R. Schleyer, *J. Am. Chem. Soc.* **125**, 15507 (2003).

- [115] C. E. Johnson and F. A. Bovey, *J. Chem. Phys.* **29**, 1012 (1958).
- [116] P. v. R. Schleyer, C. Maerker, A. Dransfeld, H. Jiao and N. J. R. v.E. Hommes, *J. Am. Chem. Soc.* **118**, 6317 (1996).
- [117] S. Winstein, *J. Am. Chem. Soc.* **81**, 6524 (1959).
- [118] C. Kittel, *Introduction to Solid State Physics*, Wiley, New York, 1995.
- [119] C. Kittel, *Quantum Theory of Solids*, Wiley, New York, 1987.
- [120] D. M. Pepper, J. Feinberg and N. V. Kukhtarev, *Sci. Am.* **263**, 62 (1990).
- [121] M. F. Singleton, J. F. Cooper, B. D. Andresen and F. P. Milanovich, *Appl. Phys. Lett.* **52**, 857 (1988).
- [122] H. Limbach, M. Pietrzak, S. Sharif, P. Tolstoy, I. Shenderovich, S. Smirnov, N. Golubev and G. Denisov, *cej* **10**, 5195 (2004).
- [123] H. H. Limbach, *Magn. Res. Chem.* **39**, 1 (2001).
- [124] K. D. Kreuer, *Ann. rev. mater. res.* **33**, 333 (2003).
- [125] K. D. Kreuer, S. J. Paddison, E. Spohr and M. Schuster, *Chem. Rev.* **104**, 4637 (2004).
- [126] K. D. Kreuer, *J. membr. sci.* **185**, 29 (2001).
- [127] T. J. Kushida, *Sci. Hiroshima Univ., Ser. A* **19**, 327 (1955).
- [128] T. J. Kushida, G. B. Benedek and N. Bloembergen, *Phys. Rev.* **104**, 1364 (1956).
- [129] T. C. Wang, *Phys. Rev.* **99**, 566 (1955).
- [130] V. R. Jensen, M. Graf and W. Thiel, *ChemPhysChem* **6**, 1929 (2005).
- [131] A. Michaelides, A. Alavi and D. A. King, *Phys. Rev. B* **69**, 113404 (2004).
- [132] H. Over and A. P. Seitsonen, *Science* **297**, 2003 (2002).
- [133] M. Mermin, *Phys. Rev.* **137**, A1441 (1965).

-
- [134] A. Alavi, J. Kohanoff, M. Parrinello and D. Frenkel, *Phys. Rev. Lett.* **73**, 2599 (1994).
- [135] P. L. Silvestrelli, A. Alavi, M. Parrinello and D. Frenkel, *Europhys. Lett.* **33**, 551 (1996).
- [136] P. L. Silvestrelli, A. Alavi, M. Parrinello and D. Frenkel, *Phys. Rev. B* **53**, 12750 (1996).
- [137] H. J. Monkhorst and J. D. Pack, *Phys. Rev. B* **13**, 5188 (1973).
- [138] V. Termath, F. Haase, J. Sauer, J. Hutter and M. Parrinello, *J. Am. Chem. Soc.* **120**, 8512 (1998).
- [139] J. Dobler, M. Pritzsche and J. Sauer, *J. Am. Chem. Soc.* **127**, 10861 (2005).
- [140] J. Weissenrieder, S. Kaya, J. Lu, H. Gao, S. Shaikhutdinov, H. Freund, M. Sierka, T. Todorova and J. Sauer, *Phys. Rev. Lett.* **95**, 076103 (2005).
- [141] M. H. Abu, S. Guimond, Y. Romanyshyn, A. Uhl, H. Kuhlenbeck, T. K. Todorova, M. V. Ganduglia-Pirovano, J. Dobler, J. Sauer and H. J. Freund, *Surf. Sc.* **600**, 1497 (2006).
- [142] B. H. Hong, J. Y. Lee, C.-W. Lee, J. C. Kim, S. C. Bae and K. S. Kim, *J. Am. Chem. Soc.* **123**, 10748 (2001).
- [143] K. S. Kim et al., *J. Am. Chem. Soc.* **124**, 14268 (2002).
- [144] R. Saito, G. Dresslhaus and M. S. Dresselhaus, *Physical Properties of Carbon Nanotubes*, Imperial College Press (London), 1998.
- [145] P. J. F. Harris, *Carbon Nanotubes and Related Structures*, Cambridge University Press, 1999.
- [146] V. V. Ivanovskaya, N. Ranjan, T. Heine, G. Merino and G. Seifert, *Small* **1**, 399 (2005).
- [147] G. Seifert, *Solid State Ionics* **168**, 265 (2004).
- [148] A. Laio and M. Parrinello, *Proc. Natl. Acad. Sci. USA* **99**, 12562 (2002).

- [149] J. Kastner and W. Thiel, *J. Chem. Phys.* **123**, 144104 (2005).
- [150] G. E. Walrafen, *Water. A Comprehensive Treatise*, volume 1, Editor: F. Franks; Plenum Press, New York, 1972.
- [151] A. Soper and P. Rossky, *Chem. Phys.* **258**, 107 (2000).
- [152] D. Eisenberg and W. Kauzmann, *The Structure and Properties of Water*, Clarendon, Oxford, 1969.
- [153] Y. Tu and A. Laaksonen, *Chem. Phys. Lett.* **329**, 283 (2000).
- [154] F. H. Stillinger, *Science* **209**, 451 (1980).
- [155] P. L. Geissler, C. Dellago, D. Chandler, J. Hutter and M. Parrinello, *Science* **291**, 2121 (2001).
- [156] M. Sprik, J. Hutter and M. Parrinello, *J. Chem. Phys.* **105**, 1142 (1996).
- [157] J. C. Grossman, E. Schwegler, E. W. Draeger, F. Gygi and G. Galli, *J. Chem. Phys.* **120**, 300 (2003).
- [158] I.-F. W. Kuo, C. J. Mundy, M. J. McGrath, J. I. Siepmann, J. VandeVondele, M. Sprik, J. Hutter, B. Chen, M. L. Klein, F. Mohamed, M. Krack and M. Parrinello, *J. Phys. Chem. B* **108**, 12990 (2004).
- [159] J. VandeVondele, F. Mohamed, M. Krack, J. Hutter, M. Sprik and M. Parrinello, *J. Chem. Phys.* **122**, 014515 (2005).
- [160] P. Wernet, D. Nordlund, U. Bergmann, M. Cavalleri, M. Odelius, H. Ogasawara, L. Naslund, T. Hirsch, L. Ojamae, P. Glatzel, L. G. M. Pettersson and A. Nilsson, *Science* **304**, 995 (2004).
- [161] J. D. Smith, C. D. Cappa, K. R. Wilson, B. M. Messer, R. C. Cohen and R. J. Saykally, *Science* **306**, 851 (2004).
- [162] A. Nilsson, P. Wernet, D. Nordlund, U. Bergmann, M. Cavalleri, M. Odelius, M. Cavalleri, M. Odelius, H. Ogasawara, L.-Å. Naslund, T. K. Hirsch, L. Ojamae, P. Glatzel and L. G. M. Pettersson, *Science* **308**, 793a (2005).

-
- [163] J. D. Smith, C. D. Cappa, K. R. Wilson, B. M. Messer, R. C. Cohen and R. J. Saykally, *Science* **308**, 793b (2005).
- [164] J. W. Tester, H. R. Holgate, F. J. Armellini, P. A. Webley, W. A. Kililea, G. T. Hong and H. E. Barner, *Emerging Technologies in Hazardous Waste Management III*, volume 518, chapter 3, American Chemical Society, Washington DC, USA, 1993.
- [165] L. W. Flanagan, P. B. Balbuena, K. P. Johnston and P. J. Rossky, *J. Phys. Chem.* **99**, 5196 (1995).
- [166] D. M. Pfund, J. G. Darab, J. L. Fulton and Y. Ma, *J. Phys. Chem.* **98**, 13102 (1994).
- [167] M. M. Hoffmann and M. S. Conradi, *J. Am. Chem. Soc.* **119**, 3811 (1997).
- [168] N. Matubayashi, C. Wakai and M. Nakahara, *Phys. Rev. Lett.* **78**, 2573 (1997).
- [169] N. Matubayashi, C. Wakai and M. Nakahara, *J. Chem. Phys.* **107**, 9133 (1997).
- [170] D. M. Harradine, S. J. Buelow, P. C. Dell'Orco, R. B. Dyer, R. B. Foy, J. M. Robinson, J. A. Sanchez, T. Spontarelli and J. D. Wander, *Haz. Waste Haz. Mater.* **10**, 233 (1993).
- [171] W. R. Kililea, K. C. Swallow and G. T. Hong, *J. Supercrit. Fluids* **5**, 72 (1992).
- [172] J. I. Aihara, *Chem. Phys. Lett.* **365**, 34 (2002).
- [173] C. Corminboeuf, T. Heine and J. Weber, *Phys. Chem. Chem. Phys.* **5**, 246 (2003).
- [174] G. V. Lier, P. W. Fowler, F. D. Proft and P. Geerlings, *J. Phys. Chem. A* **106**, 5128 (2002).
- [175] B. Kovacevic, D. Baric, Z. B. Maksic and T. Muller, *ChemPhysChem* **5**, 1352 (2004).
- [176] P. Lazzeretti, *Phys. Chem. Chem. Phys.* **6**, 217 (2004).

- [177] Y. Ruiz-Morales, *J. Phys. Chem. A* **108**, 10873 (2004).
- [178] J. Poater, X. Fradera, M. Duran and M. Sola, *Chem. Eur. J.* **9**, 400 (2003).
- [179] J. Poater, X. Fradera, M. Duran and M. Sola, *Chem. Eur. J.* **9**, 1113 (2003).
- [180] Z. F. Chen and W. Thiel, *Chem. Phys. Lett.* **367**, 15 (2003).
- [181] T. Heine, P. v. R. Schleyer, C. Corminboeuf, G. Seifert, R. Reviakine and J. Weber, *J. Phys. Chem. A* **107**, 6470 (2003).
- [182] E. Steiner and P. W. Fowler, *Phys. Chem. Chem. Phys.* **6**, 261 (2004).
- [183] P. v. R. Schleyer, M. Manoharan, Z.-X. Wang, B. Kiran, H. Jiao, R. Puchta and N. J. R. v. E. Hommes, *Org. Lett.* **3**, 2465 (2001).
- [184] N. H. Martin, J. D. Brown, H. Kimberly, H. Nance, H. F. Schaefer III, P. v. R. Schleyer, Z. X. Wang and H. L. Woodcock, *Org. Lett.* **3**, 3823 (2001).
- [185] C. Corminboeuf, T. Heine, G. Seifert, P. v. R. Schleyer and J. Weber, *Phys. Chem. Chem. Phys.* **6**, 273 (2004).
- [186] C. Corminboeuf, T. Heine, G. Seifert, P. v. R. Schleyer and J. Weber, *Phys. Chem. Chem. Phys.* **6**, 273 (2004).
- [187] G. Merino, T. Heine and G. Seifert, *Chem. Eur. J.* **10**, 4367 (2004).
- [188] D. Moran, F. Stahl, H. F. Bettinger, H. Schaefer and P. v. R. Schleyer, *J. Am. Chem. Soc.* **125**, 6746 (2003).
- [189] J. Juselius, D. Sundholm and J. Gauss, *J. Chem. Phys.* **121**, 3952 (2004).
- [190] S. Klod and E. Kleinpeter, *J. Chem. Soc., Perkin Trans.* **2**, 1893 (2001).
- [191] P. Lazzeretti, *Chem. Phys. Lett.* **401**, 164 (2005).
- [192] E. Steiner and P. Fowler, *Org. Biomolec. Chem.* **2**, 34 (2004).
- [193] E. Steiner, P. W. Fowler, L. W. Jenneskens and R. W. A. Havenith, *Eur. J. Org. Chem.* **365**, 163 (2002).

- [194] J. I. Aihara, *Bull. Chem. Soc. Jap.* **77**, 101 (2004).
- [195] J. Poater, M. Sola, R. G. Viglione and R. Zanasi, *J. Org. Chem.* **69**, 7537 (2004).
- [196] P. W. Fowler, E. Steiner, R. W. A. Havenith and L. W. Jenneskens, *Magn. Reson. Chem.* **42**, S68 (2004).
- [197] P. W. Fowler and A. Soncini, *Chem. Phys. Lett.* **383**, 507 (2004).
- [198] T. Heine, C. Corminboeuf and G. Seifert, *Chem. Rev.* **105**, 3889 (2005).

Benzoxazine Oligomers: Evidence for a Helical Structure from Solid-State NMR Spectroscopy and DFT-Based Dynamics and Chemical Shift Calculations

Gillian R. Goward,^{†,§} Daniel Sebastiani,[†] Ingo Schnell,[†] Hans Wolfgang Spiess,^{*,†}
Ho-Dong Kim,[‡] and Hatsuo Ishida[‡]

Contribution from the Max-Planck-Institut für Polymerforschung, Postfach 3148,
D-55021 Mainz, Germany, and Department of Chemistry, Case Western Reserve University,
10900 Euclid Avenue, Cleveland, Ohio 44106-7078

Received October 23, 2002; E-mail: spiess@mpip-mainz.mpg.de

Abstract: A combination of molecular modeling, DFT calculations, and advanced solid-state NMR experiments is used to elucidate the supramolecular structure of a series of benzoxazine oligomers. Intramolecular hydrogen bonds are characterized and identified as the driving forces for ring-shape and helical conformations of trimeric and tetrameric units. In fast MAS ¹H NMR spectra, the resonances of the protons forming the hydrogen bonds can be assigned and used for validating and refining the structure by means of DFT-based geometry optimizations and ¹H chemical-shift calculations. Also supporting these proposed structures are homonuclear ¹H–¹H double-quantum NMR spectra, which identify the local proton–proton proximities in each material. Additionally, quantitative ¹⁵N–¹H distance measurements obtained by analysis of dipolar spinning sideband patterns confirm the optimized geometry of the tetramer. These results clearly support the predicted helical geometry of the benzoxazine polymer. This geometry, in which the N···H···O and O···H···O hydrogen bonds are protected on the inside of the helix, can account for many of the exemplary chemical properties of the polybenzoxazine materials. The combination of advanced experimental solid-state NMR spectroscopy with computational geometry optimizations, total energy, and NMR spectra calculations is a powerful tool for structural analysis. Its results provide significantly more confidence than the individual measurements or calculations alone, in particular, because the microscopic structure of many disordered systems cannot be elucidated by means of conventional methods due to lack of long-range order.

Introduction

Supramolecular structures often suffer from a lack of long-range crystallinity, due to the comparatively weak interactions that determine their structures, for example, hydrogen bonding^{1–7} and π -stacking.^{8–10} Solid-state NMR, however, does not require long-range ordering to provide structural details of these fascinating systems. Hydrogen bonding and π -stacking are

building blocks of supramolecular interactions and show up clearly in high-resolution solid-state ¹H NMR studies.^{11–13} The powerful combination of quantum chemical calculations with experimental NMR studies has been used previously to elucidate structural details of other supramolecular systems.^{14–16} Here we apply a combination of molecular modeling, density functional theory (DFT) calculations, and experimental measurements to obtain insight into the structure of a series of benzoxazine oligomers and to show that hydrogen bonds have a strong influence on the structural conformation that is adopted.

Supramolecular structures influenced by self-assembly and hydrogen bonding are also frequently observed in polymeric architectures.^{17–21} Polybenzoxazines are a classic example of

[†] Max-Planck-Institut für Polymerforschung.

[‡] Case Western Reserve University.

[§] Current address: Department of Chemistry, McMaster University, Hamilton ON, Canada.

- (1) Jeffery, G. A.; Saenger, W. *Hydrogen Bonding in Biological Structures*; Springer-Verlag: New York, 1991.
- (2) Sijbesma, R. P.; Beijer, F. H.; Brunsveld, L.; Folmer, B. J.; Hirschberg, J. H.; Lange, R. F.; Lowe, J. K.; Meijer, E. W. *Science* **1997**, *278*, 1601–1604.
- (3) Lehn, J. M. *Science* **1993**, *260*, 1762–1763.
- (4) Brunsveld, L.; Folmer, B. J.; Meijer, E. W.; Sijbesma, R. P. *Chem. Rev.* **2001**, *101*, 4071–4098.
- (5) Schmuck, C. W. W. *Angew. Chem., Int. Ed.* **2001**, *40*, 4363.
- (6) Brunsveld, L.; Vekemans, J. A.; Hirschberg, J. H.; Sijbesma, R. P.; Meijer, E. W. *Proc. Natl. Acad. Sci. U.S.A.* **2002**, *99*, 4977–4982.
- (7) Yamauchi, K.; Lizotte, J. R.; Hercules, D. M.; Vergne, M. J.; Long, T. E. *J. Am. Chem. Soc.* **2002**, *124*, 8599–8604.
- (8) Ajayaghosh, A.; George, S. J. *J. Am. Chem. Soc.* **2001**, *123*, 5148–5149.
- (9) Lahiri, S.; Thompson, J. L.; Moore, J. S. *J. Am. Chem. Soc.* **2000**, *122*, 11315–11319.
- (10) Brown, S. P.; Schnell, I.; Brand, J. D.; Müllen, K.; Spiess, H. W. *J. Am. Chem. Soc.* **1999**, *121*, 6712–6718.

- (11) Percec, V.; Glodde, M.; Bera, T. K.; Miura, Y.; Shivanovskaya, I.; Singer, K. D.; Balagurusamy, V. S.; Heiney, P. A.; Schnell, I.; Rapp, A.; Spiess, H. W.; Hudson, S. D.; Duan, H. *Nature* **2002**, *419*, 384–387.
- (12) Brown, S. P.; Spiess, H. W. *Chem. Rev.* **2001**, *101*, 4125–4156.
- (13) Wei, Y.; McDermott, A. *ACS Symp. Ser.* **1999**, *732*, 177–193.
- (14) Ochsenfeld, C.; Head-Gordon, M. *Chem. Phys. Lett.* **1997**, *270*, 399–405.
- (15) Ochsenfeld, C. *Phys. Chem. Chem. Phys.* **2000**, *2*, 2153–2159.
- (16) Ochsenfeld, C.; Brown, S. P.; Schnell, I.; Gauss, J.; Spiess, H. W. *J. Am. Chem. Soc.* **2001**, *123*, 2597–2606.
- (17) Percec, V.; Ahn, C. H.; Ungar, G.; Yeardley, D. J. P.; Moller, M.; Sheiko, S. S. *Nature* **1998**, *391*, 161–164.
- (18) Berl, V.; Schmutz, M.; Krichshe, M. J.; Khoury, R. G.; Lehn, J. M. *Chemistry* **2002**, *8*, 1227–1244.
- (19) Chino, K.; Ashiura, M. *Macromolecules* **2001**, *34*, 9201–9204.

such a structure. Polybenzoxazines exhibit a number of unusual properties, including low volumetric shrinkage or expansion upon curing,²² lack of water absorption and excellent resistance to chemicals and UV light,^{23,24} as well as surprisingly high T_g values given the low cross-linking density,²⁵ all of which make them attractive candidates for many commercial applications. These properties have been attributed to the unique hydrogen-bonding structure found in these materials, and therefore this property has been the focus of recent investigation. In particular, extensive crystallographic, NMR, and IR studies of the dimer precursors have provided much insight.^{26,27} However, the benzoxazine dimers organize themselves in a highly regular, paired lattice; hence the model cannot be extended to account for the unique properties of the parent polymer. Therefore, synthetic efforts were made to procure other oligomers of the benzoxazine material and thereby bridge the gap between the fully determined dimer structure and the unknown polymer structure.²⁸ The objective here is to improve our understanding of the polymer architecture, through studies of the hydrogen bonding in the oligomers, and thereby understand the remarkable physical characteristics of the polymers. In this paper, we focus on the methyl-substituted benzoxazine trimer and tetramer, which cannot be investigated by conventional X-ray diffraction techniques, because suitable crystals could not be prepared. From the trimer, it might be possible to obtain crystallites which can be studied by electron crystallography. Work along this line is in progress.

A critical feature of these materials is their propensity to form both intra- and intermolecular hydrogen bonds. The relative number and strength of such interactions may influence the supramolecular geometry adopted by the system. In particular, we note the different structures observed among dimer pairs, which differ only in the substitution at the nitrogen center. A methyl group results in an exclusive dimer–dimer geometry, whereas ethyl, propyl, and butyl substituents cause a twist about the central nitrogen, resulting in an extended ladder structure. These differences were first elucidated using double quantum solid-state NMR²⁷ and later confirmed using X-ray diffraction.²⁹ An unanswered question is the effect of substituents on the extended structures — both their packing geometries and their physical properties. We begin to explore possible answers in this paper, focusing on the methyl-substituted oligomers and polymer. The influence of hydrogen bonding on the structural and physical properties of the benzoxazine family can be considered in the more general category of supramolecular structures, and a particular challenge is to determine the hydrogen-bonded structure in systems whose heavy-atom structure is *not* known. Here we combine advanced solid-state NMR with advanced computational strategies to meet this challenge.

Applying fast magic-angle spinning (MAS), we have successfully demonstrated that high-resolution solid-state NMR is able to provide detailed structural information about the hydrogen-bonding arrangements in benzoxazines. Both qualitative descriptions of packing geometries, based on 2D ^1H double quantum (DQ) spectra,²⁷ and quantitative analysis of the N–H distance in the methyl benzoxazine dimer³⁰ derived from heteronuclear ^1H – ^{15}N dipolar sideband patterns, have been presented. Here we demonstrate a powerful combination of solid-state NMR and DFT-based calculations, which enables us to characterize essential structural features of the methyl benzoxazine oligomers and to propose molecular structures that are based on energy minimization, hydrogen-bond measurement, and chemical-shift evaluation.

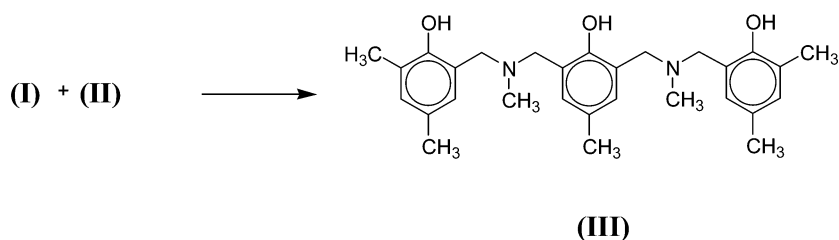
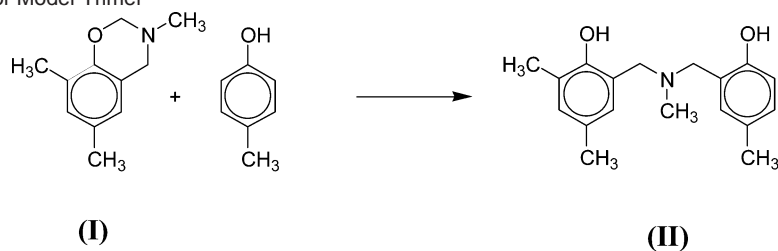
Homonuclear DQ NMR methods provide an excellent, facile route to qualitative structural evaluation, based on the proton–proton proximities evidenced in these spectra. The method relies on the generation of double quantum coherences between proximal ^1H spins, covering a ^1H – ^1H distance range of up to approximately 3.5 Å, thereby probing the spatial arrangement of protons based on the strength of the through-space dipolar coupling.^{31–34} Heteronuclear ^1H – ^{15}N recoupled polarization transfer (REPT) is a complementary method for both correlations and quantitative distance measurements, which uses rotor-encoding of dipolar couplings via sideband patterns recorded in the indirect dimensions.³⁵ Other methods for heteronuclear recoupling of the dipolar coupling have been demonstrated and used for N–H distance measurements;^{36,37} however, we selected REPT here for its robust performance under fast MAS conditions. An enhancement of the signal intensity provided by this method can be achieved both through the use of inverse detection^{30,38} and, moreover, through the addition of spoil-gradients (G_z) at appropriate positions in the pulse sequence, as described recently by Saalwächter and Schnell.³⁹ This method has been successfully used to precisely measure N–H bond lengths (on the order of 110 pm) with ^{15}N in natural abundance. However, for the longer distances relevant in the benzoxazines, we were unable to excite a strong enough signal under natural abundance conditions. Therefore, the ^{15}N – ^1H distance measurements described here were performed on a ^{15}N -enriched (>95%) methyl benzoxazine tetramer and are compared with the optimized structure.

We have performed geometry optimizations and NMR chemical shift calculations in the framework of density functional theory (DFT).⁴⁰ In recent years, it has become possible to calculate NMR chemical shifts not only for isolated molecules, but also for extended systems such as amorphous or crystalline solids and liquids. Here, we use a recently developed

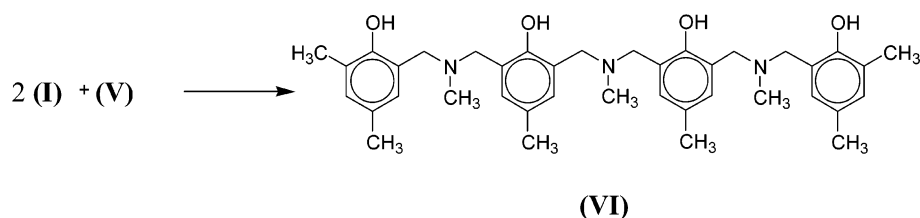
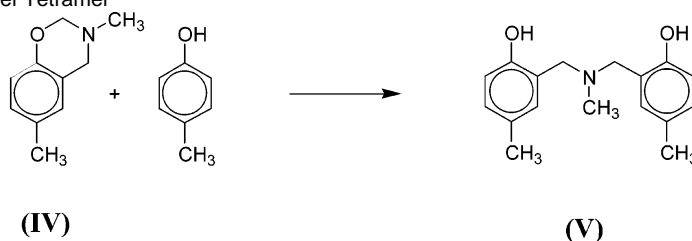
- (20) Monkman, A. P.; Palsson, L. O.; Higgins, R. W.; Wang, C.; Bryce, M. R.; Batsanov, A. S.; Howard, J. A. *J. Am. Chem. Soc.* **2002**, *124*, 6049–6055.
- (21) Ezuhara, T.; Endo, K.; Aoyama, Y. *J. Am. Chem. Soc.* **1999**, *121*, 3279–3283.
- (22) Ishida, H.; Low, H. Y. *Macromolecules* **1997**, *30*, 1099–1106.
- (23) Kim, H. D.; Ishida, H. *J. Appl. Polym. Sci.* **2001**, *79*, 1207–1219.
- (24) Macko, J. A.; Ishida, H. *J. Polym. Sci., Part B: Polym. Phys.* **2000**, *38*, 2687–2701.
- (25) Ishida, H.; Rodriguez, Y. *Polymer* **1995**, *36*, 3151–3158.
- (26) Dunkers, J.; Zarate, E. A.; Ishida, H. *J. Phys. Chem.* **1996**, *100*, 13514–13520.
- (27) Schnell, I.; Brown, S. P.; Low, H. Y.; Ishida, H.; Spiess, H. W. *J. Am. Chem. Soc.* **1998**, *120*, 11784–11795.
- (28) Ishida, H.; Moran, C. *Macromolecules* **1998**, *31*, 2409.
- (29) Kim, H.-D.; Ishida, H. *J. Macromol. Chem. Macromol. Symp.* **2003**, accepted.

- (30) Goward, G. R.; Schnell, I.; Brown, S. P.; Spiess, H. W.; Kim, H. D.; Ishida, H. *Magn. Reson. Chem.* **2001**, *39*, S5–S17.
- (31) Schnell, I.; Spiess, H. W. *J. Magn. Reson.* **2001**, *151*, 153–227.
- (32) Lee, Y. K.; Kurur, N. D.; Helmle, M.; Johannessen, O. G.; Nielsen, N. C.; Levitt, M. H. *Chem. Phys. Lett.* **1995**, *242*, 304–309.
- (33) Brinkmann, A.; Edén, M.; Levitt, M. H. *J. Chem. Phys.* **2000**, *112*, 8539–8554.
- (34) Hohwy, M.; Jakobsen, H. J.; Edén, M.; Levitt, M. H.; Nielsen, N. C. *J. Chem. Phys.* **1998**, *108*, 2686–2694.
- (35) Saalwächter, K.; Graf, R.; Spiess, H. W. *J. Magn. Reson.* **2001**, *148*, 398–418.
- (36) Brinkmann, A.; Levitt, M. H. *J. Chem. Phys.* **2001**, *115*, 357–384.
- (37) Zhao, X.; Sudmeier, J. L.; Bachovchin, W. W.; Levitt, M. H. *J. Am. Chem. Soc.* **2001**, *123*, 11097–11098.
- (38) Schnell, I.; Langer, B.; Söntjens, S. H. M.; van Genderen, M. H. P.; Sijbesma, R. P.; Spiess, H. W. *J. Magn. Reson.* **2001**, *150*, 57–70.
- (39) Schnell, I.; Saalwächter, K. *J. Am. Chem. Soc.* **2002**, *124*, 10938–10939.
- (40) Jones, R. O.; Gunnarsson, O. *Rev. Mod. Phys.* **1989**, *61*, 689–746.

Scheme 1. Synthesis of Model Trimer



Scheme 2. Synthesis of Model Tetramer



method for extended systems⁴¹ for the benzoxazine dimer in its crystal structure, and we use a supercell technique for the benzoxazine trimer and tetramer in vacuo.

The isolated structures of both trimer and tetramer have strong intramolecular OH...N and weak OH...O hydrogen bonds that keep them in a closed-ring like geometry. In the condensed phase, it would be further stabilized by packing effects such as van der Waals interactions between phenyl rings of neighboring molecules. However, because the material does not form large crystals, these effects are assumed to be of moderate strength. So far, there is little evidence for intermolecular hydrogen bonds, but we are currently investigating the possibility of a competing arrangement which would form ladderlike microstructures.

Experimental Section

Synthesis of 2,6-Bis[*N*-(3,5-dimethyl-2-hydroxybenzyl)-*N*-methylamino-methyl]-*p*-cresol (III, Scheme 1, Methyl-trimer). The starting monomer, 3,4-dihydro-3,6,8-trimethyl-2*H*-1,3-benzoxazine, **I**, was pre-

pared by the procedure described by Dunkers and Ishida.⁴² To obtain the intermediate dimer **II**, equimolar portions of the monomer **I** and *p*-cresol were heated at 80 °C for 12 h, and the resulting yellow product was recrystallized from *n*-hexane. This intermediate dimer **II** was reacted again with an equimolar portion of the monomer **I** without reaction solvent at 80 °C for 48 h. The resulting yellow product was cooled and was subsequently purified by column chromatography with silica gel using hexane/acetone (20:1) as the eluent. The product was fine white crystalline powder. ¹H NMR (200 MHz, CDCl₃, 298 K) δ: 2.20, 2.21 (15H, Ar-CH₃), 2.22 (6H, N-CH₃), 3.68 (8H, Ar-CH₂-N), and 6.70, 6.84, 6.86 (6H, Ar-H). ¹³C NMR (50.1 MHz, CDCl₃, 298 K) δ: 15.81, 20.27 (5C, Ar-C), 40.95 (2C, N-CH₃), 58.78, 59.59 (4C, Ar-C-N), and 122.14–154.05 (18C, Ar). Anal. Calcd for C₂₉H₃₈N₂O₃: C, 75.29; H, 8.28; N, 6.06. Found: C, 75.09; H, 8.30; N, 6.11. Mass spectrometry (MS-FD) exp., 462.4; calcd. for C₂₉H₃₈N₂O₃, 462.3.

Synthesis of *N,N*-Bis{2-hydroxyl-5-methyl-3-[(*N*-3,5-dimethyl-2-hydroxyl-benzyl)-*N*-methylaminomethyl]}-methylamine (VI, Scheme 2, Methyl-tetramer). The model tetramer for polybenzoxazine was synthesized according to the following procedure using 2,4-dimeth-

(41) Sebastiani, D.; Parrinello, M. *J. Phys. Chem. A* **2001**, *105*, 1951–1958.

(42) Dunkers, J.; Ishida, H. *Spectrochim. Acta, Part A* **1995**, *51*, 855–867.

ylphenol, *p*-cresol, formaldehyde, and methylamine. The starting monomer, 3,4-dihydro-3,6-dimethyl-2*H*-1,3-benzoxazine, **IV**, was prepared by the procedure described by Dunkers and Ishida.⁴² The intermediate dimer **V** was synthesized by heating equimolar portions of the monomer **IV** and *p*-cresol at 80 °C for 12 h, and the resulting yellow product was recrystallized from *n*-hexane. The mixture of intermediate dimer **V** and monomer **I** (1:2 mole ratio) was refluxed in chloroform for 48 h. After the reaction mixture was cooled to room temperature, chloroform was removed with a rotary evaporator, and the resulting yellow solid was subsequently purified by column chromatography with silica gel using hexane/acetone (20:1) as the eluent. ¹⁵N-enriched methyl-tetramer was prepared by the same method as the methyl-tetramer with the exception of methylamine-¹⁵N hydrochloride. The product was a fine white powder. ¹H NMR (200 MHz, CDCl₃, 298 K) δ : 2.19, 2.21 (18H, Ar-CH₃), 2.23 (9H, N-CH₃), 3.63, 3.66 (12H, Ar-CH₂-N), and 6.66, 6.84, 6.86 (8H, Ar-H). ¹³C NMR (50.1 MHz, CDCl₃, 298 K) δ : 15.81, 20.27 (6C, Ar-C), 40.95 (3C, N-CH₃), 57.57, 58.38, 59.59 (6C, Ar-C-N), and 121.84–153.65 (24C, Ar). Anal. Calcd for C₃₉H₅₁N₃O₄: C, 74.85; H, 8.21; N, 6.71. Found: C, 74.66; H, 7.99; N, 6.84. Mass spectrometry (MS-FD) exp., 627.6; calcd. for C₃₉H₅₁N₃O₄ (with 100% ¹⁵N isotope), 628.4.

NMR Methods. All experiments were carried out on a Bruker Avance 700 solid-state NMR spectrometer running at Larmor frequencies of 700.13 and 70.93 MHz for ¹H and ¹⁵N, respectively. The measurements were performed using a 2.5 mm MAS probe with typical rotor frequencies of 30 kHz, $\pi/2$ pulse lengths of 2–2.5 μ s for both ¹⁵N and ¹H pulses, and recycle delays of 2 s. ¹H double-quantum experiments were performed using the compensated BaBa pulse sequence.³¹ The heteronuclear recoupling sequence used to probe dipolar couplings was ¹⁵N–¹H indirectly detected REPT-HDOR, with selection of the ¹H–¹⁵N coupling supported by spoil gradients (*G*_s) of 100 μ s duration and 100–200 G/cm strength (pulse sequence given in ref 39); rotor-encoded sideband patterns were acquired applying dipolar recoupling for 20 rotor periods (τ_r) during both excitation and reconversion. The *t*₁ dimension was incremented in steps of 1.67 μ s (corresponding to $\tau_r/20$), and 40 *t*₁ slices were collected, which were subsequently catenated over 40 rotor periods prior to Fourier transformation (as described in ref 43).

Computational Details. To calculate the minimum energy geometries for all systems, we used the Car-Parrinello Molecular Dynamics simulation package, a density functional theory code based on a plane wave representation of the electronic structure.⁴⁴ Because of its known ability to reproduce reliably the character and strength of hydrogen bonds, the Becke–Lee–Yang–Parr (BLYP)⁴⁵ exchange-correlation functional was used, together with Goedecker-type pseudopotentials.⁴⁶ A plane wave cutoff of 70 Ry was chosen for all calculations, and the sampling of the Brillouin zone was restricted to the Γ -point. In all systems, the atomic positions were subsequently optimized until the maximum component of the energy gradient dropped below 5×10^{-4} au.

As the starting point for the benzoxazine dimer, we used the known crystal structure.²⁶ The geometry optimization was performed under periodic boundary conditions, taking into account the monoclinic crystal lattice. For the isolated benzoxazine trimer and tetramer molecules, we started from geometries generated by simulated annealing calculations with a standard all-atom force-field using point charges fitted by the restricted electrostatic potential method (RESP).⁴⁷ All atoms were subsequently relaxed at the DFT/BLYP level of theory in a sufficiently

large unit cell to simulate isolated molecules. The simulation boxes were chosen such as to leave a distance of approximately 5 Å of empty space between the molecules to exclude interactions between its images in neighboring cells. Possibilities for packing effects are the focus of ongoing simulations and will be presented in a further work. The use of simulated annealing with molecular dynamics can be more efficient than a standard geometry optimization. Further, an MD simulation shows less tendency to get stuck in a local minimum or a saddle point of the potential energy surface, thus avoiding the necessity of performing a calculation of the second derivatives.

A recently developed method for calculating NMR chemical shielding tensors in DFT under periodic boundary conditions⁴¹ that is implemented in CPMD was used to obtain the NMR resonance frequencies. It bears some resemblance to the IGLO approach,⁴⁸ but is actually a variant of the CSGT formulation⁴⁹ extended to periodic systems in a pseudopotential plane wave formulation.⁴⁴ The method has been shown to yield a very good agreement with experiment, in particular, concerning the effects of hydrogen bonding.^{50–52} To compare to experimental results, the shieldings were referenced to tetramethylsilane (TMS) according to $\delta(H) = \sigma(TMS) - \sigma(H)$ with $\sigma(TMS)$ being the shielding calculated for an isolated TMS molecule at the same level of theory. A Gaussian broadening with a half-width of 0.15 ppm was applied to the individual proton shift values, yielding the spectra shown below.

We estimate the error in the DFT calculation of the chemical shieldings to be in the range of about ± 0.5 ppm. It has two independent origins. First, the description by DFT as such can give rise to a maximum deviation of ± 0.5 ppm in the NMR parameters, when compared to quasi-exact methods such as coupled-cluster approaches. In most situations, however, relative shifts and trends are much better reproduced. The second origin is the geometry obtained from the DFT energy minimization, which does not include finite temperature effects and can thus be intrinsically wrong by about 0.05 Å. With a typical slope of 5 ppm/Å for ¹H shifts as a function of its location within a hydrogen bond, the geometric error could lead to a shift deviation of another ± 0.3 ppm.

For all calculations, we used a self-built Beowulf-cluster of 16 Pentium-4 machines with a MyriNet interconnect, running under the Linux operating system. The computational time was typically 1000–2000 processor-hours per system for the geometry optimization and the NMR calculations. This corresponds to a big total of roughly 10^{16} floating point operations.

Results and Discussion

Figure 1 shows the DFT/BLYP-optimized structures of the methyl benzoxazine trimer and tetramer together with the paired-dimer structure.²⁶ While the dimer forms pairs of molecules through *intermolecular* hydrogen bonding, the trimer and tetramer exhibit *intramolecular* hydrogen bonding, such that a single oligomer is self-contained in its geometry. Supporting data from solution state IR dilution studies show that, in both the trimer and the tetramer, the hydrogen bonds persist unchanged even in extremely dilute solution and are thus attributed to *intramolecular* hydrogen bonds.²⁹ The question then arises whether these structures are also present in the solid, where packing effects can lead to the formation of ladder-type arrangements, based on both intra- and intermolecular H-bonds.^{27,29}

- (43) Saalwächter, K.; Spiess, H. W. *J. Chem. Phys.* **2001**, *114*, 5707–5728.
 (44) Hutter, J.; Ballone, P.; Bernasconi, M.; Focher, P.; Fois, E.; Goedecker, S.; Parrinello, M.; Tuckerman, M. CPMD Computer Code, 1995, MPI für Festkörperforschung, Stuttgart, Germany, and IBM Zürich Research Lab.
 (45) (a) Becke, A. D. *Phys. Rev. A* **1988**, *38*, 3098. (b) Lee, C.; Yang, W.; Parr, R. G. *Phys. Rev. B* **1988**, *37*, 785.
 (46) Goedecker, S.; Teter, M.; Hutter, J. *Phys. Rev. B* **1996**, *54*, 1703–1710.
 (47) Bayly, C. I.; Cieplak, P.; Cornell, W. D.; Kollman, P. A. *J. Phys. Chem.* **1993**, *97*, 10269–10280.

- (48) Kutzelnigg, W. *Isr. J. Chem.* **1980**, *19*, 193–200.
 (49) Keith, T. A.; Bader, R. F. W. *Chem. Phys. Lett.* **1993**, *210*, 223–231.
 (50) Sebastiani, D.; Goward, G.; Schnell, I.; Parrinello, M. *Comput. Phys. Commun.* **2002**, *147*, 707–710.
 (51) Sebastiani, D.; Parrinello, M. *ChemPhysChem* **2002**, *3*, 675–679.
 (52) Goward, G. R.; Schuster, M. F. H.; Sebastiani, D.; Schnell, I.; Spiess, H. W. *J. Phys. Chem. B* **2002**, *106*, 9322–9334.

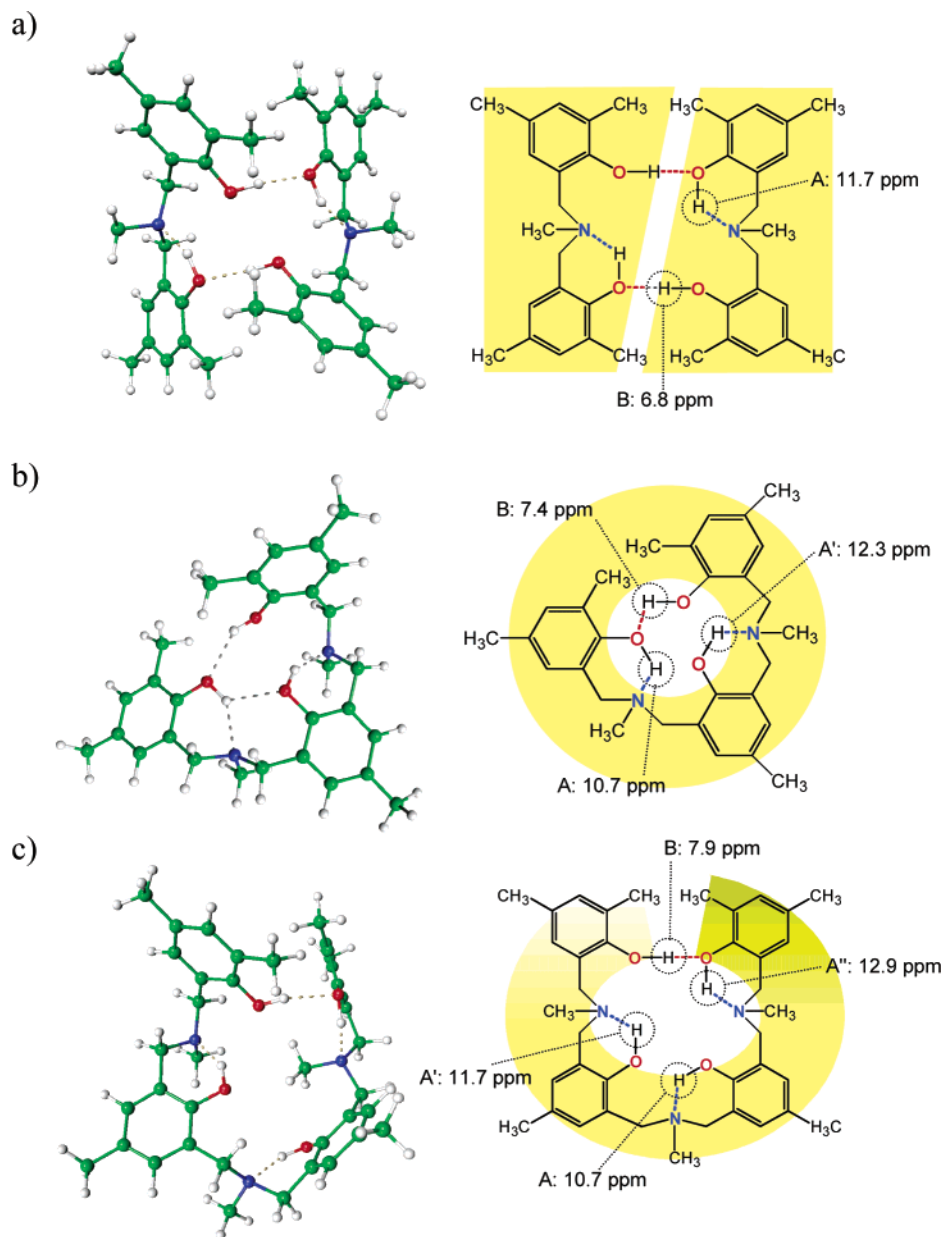


Figure 1. Methyl benzoxazine dimer, trimer, and tetramer structures in their ab initio optimized geometries. The dimer (a) forms pairs of molecules via double intermolecular N–H···O···H–O hydrogen bonds. The trimer structure (b) comprises a nearly planar ring, while in the tetramer, (c), the fourth monomer unit overlaps the start of the ring geometry, depicting the beginning of a helix. The experimental ^1H chemical shifts are assigned to the protons forming hydrogen bonds.

A comparison of the experimental ^1H MAS NMR spectra and the calculated ^1H NMR spectra is given in Figure 2. The latter were obtained from DFT-based calculations of a periodic structure built up from the models shown in Figure 1, while the MAS spectra were obtained from 10 mg of each sample, packed in a 2.5 mm rotor which was spun at 30 kHz. First, we consider the experimental ^1H MAS NMR spectra of the series of oligomers, the top traces in Figure 2. The spectra are interpreted according to an alphabetical assignment, beginning with the H-bonded resonances. N–H's at the highest resonance frequency are labeled “A” and differentiated with primes for increasing number of resolved N–H resonances. O–H's are labeled “B”, aromatic resonances are labeled “C,D”, and aliphatic resonances are labeled “E,F”. Qualitatively, it is evident that the hydrogen-bonding structures are different for the dimer, trimer, and tetramer. The clearest difference among the spectra

is the increasing number of resolved N–H resonances with increasing oligomer length, from one to two, to three. The chemical shifts are listed in Table 1. The N–H resonances begin at 11.7 ppm in the dimer and spread around this central frequency, as more resonances are added in the oligomers. Considering the O–H resonances, we see in this case a trend toward higher resonance frequency with increasing oligomer length.

The agreement between the experimental and calculated spectra is striking. Most satisfying is the correlation between the number and position of the resonances in the N–H region (10–15 ppm). In the dimer, only one N–H resonance is determined at 11.7 and 12.2 ppm by experiment and calculation, respectively. In addition, the dimer's O–H resonance is found at 6.9 ppm experimentally and at 7.0 ppm by calculation. In the trimer, two N–H resonances are found, at 10.7 and 12.3

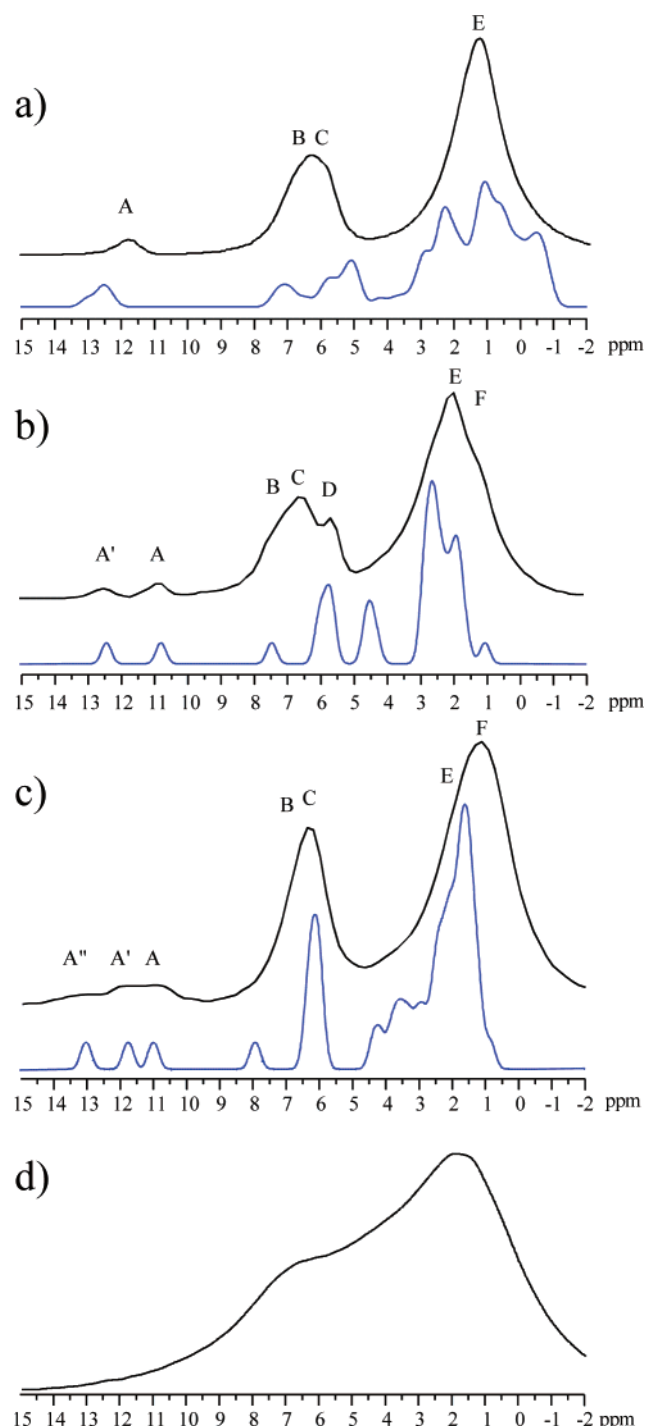


Figure 2. Comparison of calculated (blue) and experimental ^1H MAS NMR spectra for the dimer (a), trimer (b), and tetramer (c). ^1H DQ MAS spectrum of cross-linked polybenzoxazine based on methylamine (d). Resolved resonances are labeled according to the following pattern; A, N–H protons; B, O–H protons; C,D, aromatic protons; E,F, aliphatic protons. A, A', and A'' indicate the increasing number of N–H resonances observed with increasing oligomer length.

ppm in the experimental spectrum and at 10.7 and 12.2 ppm in the calculated spectrum. In contrast, the tetramer shows three N–H resonances in both experimental and calculated spectra, in the range from 10.0 to 13.5 ppm. The reduced resolution in the experimental spectrum of the tetramer demonstrates that the material is not as highly ordered as the trimer. Nevertheless, on the basis of the similarity between our experimental and calculated data, we are confident in the validity of the three-

Table 1. Calculated and Experimental ^1H Chemical Shifts of Benzoxazine Dimer, Trimer, and Tetramer^a

chemical shifts in ppm	N–H resonances			O–H	aromatic	aromatic	aliphatic	aliphatic
	A''	A'	A	B	C	D	E	F
dimer, expt.			11.7	6.8	6.5–5.5	N/A	3–0 ppm	N/A
dimer, calc.			12.2	7.0	6.0–5.0	N/A	3–0 ppm	N/A
trimer, expt.		12.3	10.7	7.4	7.0–5.0	6.0–5.5	3.0–1.5	1.5–1.0
trimer, calc.		12.2	10.7	7.4	6.2–5.5	4.8–4.2	3.0–1.5	1.5–1.0
tetramer, expt.	12.9	11.7	10.9	7.9	7.2–5.5	N/A	3.5–1.0	2.0–0.0
tetramer, calc.	13.1	11.8	11.1	7.0	6.5–5.8	N/A	4.2–2.0	2.0–0.5

^a We note that the spectral resolution within the aromatic and aliphatic regions is poor, due to significant overlap, and thus ranges of resonance frequencies are given.

dimensional structural conformations proposed. Further support for these molecular geometries is found in the 2D homonuclear DQ NMR spectra of the materials, discussed below.

To investigate the relative strength of the intramolecular hydrogen bonds in more detail, we have performed further calculations on the benzoxazine trimer and tetramer. First, the OH...O hydrogen bond that is responsible for the ring closure was opened by imposing an O...O distance of about 3 Å, while allowing the rest of the molecule to relax completely. This resulted in an increase in total energy of 10–12 kJ/mol for both molecules. Furthermore, a variety of alternative geometries were generated with the combined force-field and DFT geometry optimization approach. In all alternative geometries, the OH...N intramolecular hydrogen bonds remained intact, thus always imposing an internal curvature on the molecule. The outer OH...O bond was conserved in the majority of the structures obtained, yielding approximately the same overall geometry and a similar NMR pattern. In the cases where the ring-closing did not take place, other OH...O bonds were formed, but the total energies of the systems were always more than 25 kJ/mol higher than that in the helical arrangement. In addition, the calculated NMR spectra showed no resemblance to the experimentally observed spectrum. Thus, there is conclusive evidence that the trimer and tetramer form ring-shaped and helical structures, respectively, which are held together by a sufficiently strong intramolecular OH...O hydrogen bond.

With respect to the dimer, we need to add that the result of the geometry optimization of the periodic structure resulted in a N–H distance of 1.70 Å, which is significantly shorter than the previously determined value of (1.96 ± 0.05) Å.³⁰ Remarkably, the chemical shift of the NH proton occurs at 11.7 ppm in the nonlabeled sample (spectrum shown in Figure 2), which differs from that observed at 11.2 ppm in both the labeled material on which the distance measurement was made and a previously prepared sample.^{27,30} We also note that the sample examined in ref 27 was not uniform, but also contained a fraction of the ladder-type packing arrangement, as was observed in the 2D ^1H DQ spectrum of that material. Therefore, we attribute the difference not to an inaccuracy in the measurement or the geometry optimization, but rather to an imperfect crystal packing, which results in the longer-than-optimal N–H distance. This conclusion is based primarily on the extreme sensitivity of the proton chemical shift to the NH distance. To test this hypothesis, a NH distance was fixed, and the geometry optimization was performed under the constraint of 1.9 Å. The energy difference per dimer pair (i.e., 4 H-bonds) was small, approximately 3 kJ/mol, and the resulting ^1H chemical shift for the NH resonance was less than 11 ppm, in agreement with the

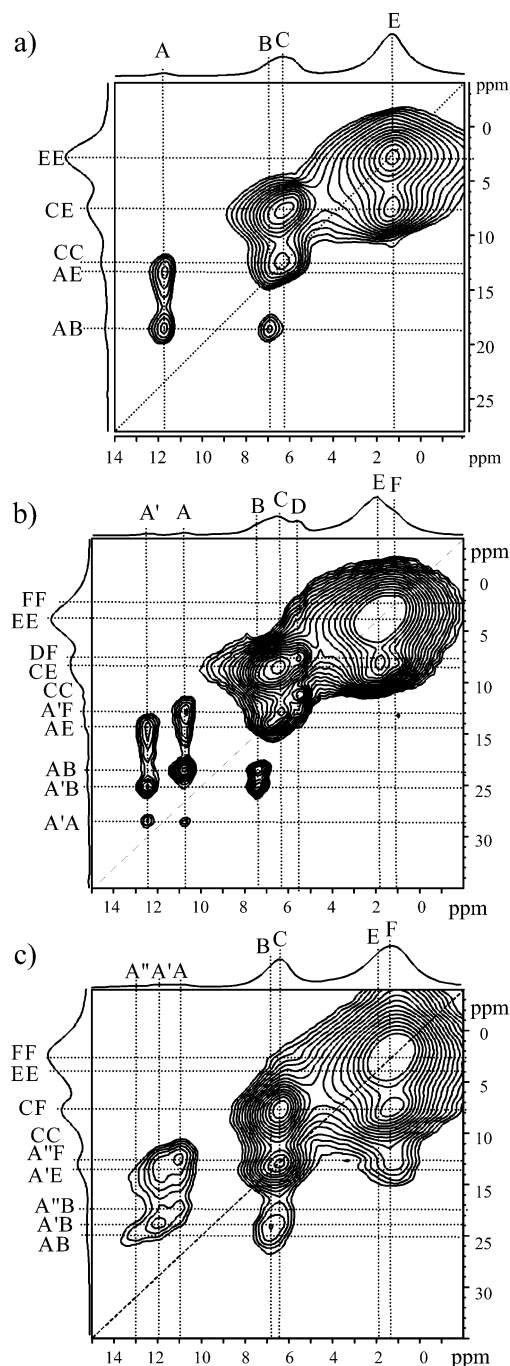


Figure 3. ^1H 2D DQ NMR spectra for the dimer (a), trimer (b), and tetramer (c), obtained at ambient temperature, under 30 kHz MAS with one rotor period of dipolar recoupling. $\pi/2$ pulse lengths of $2\ \mu\text{s}$ and recycle delays of 2 s were implemented. Sixty-four transients were averaged for each of 32 slices acquired in the indirect dimension. Labels correspond to those used in Figure 2.

trend we describe. Apparently, the position of the N–H can be adjusted to cope with packing requirements. At this point, we return to considering the trimer and tetramer structures, which are the primary focus of this paper.

The 2D ^1H – ^1H DQ NMR spectra obtained for the dimer, trimer, and tetramer are shown in Figure 3. The reader is referred to previous publications for analogous spectra obtained for the methyl dimer.^{27,30} As in the case of the dimer, strong resonances in the aliphatic and aromatic regions are observed as expected along the diagonal of the 2D spectrum and arise from self-

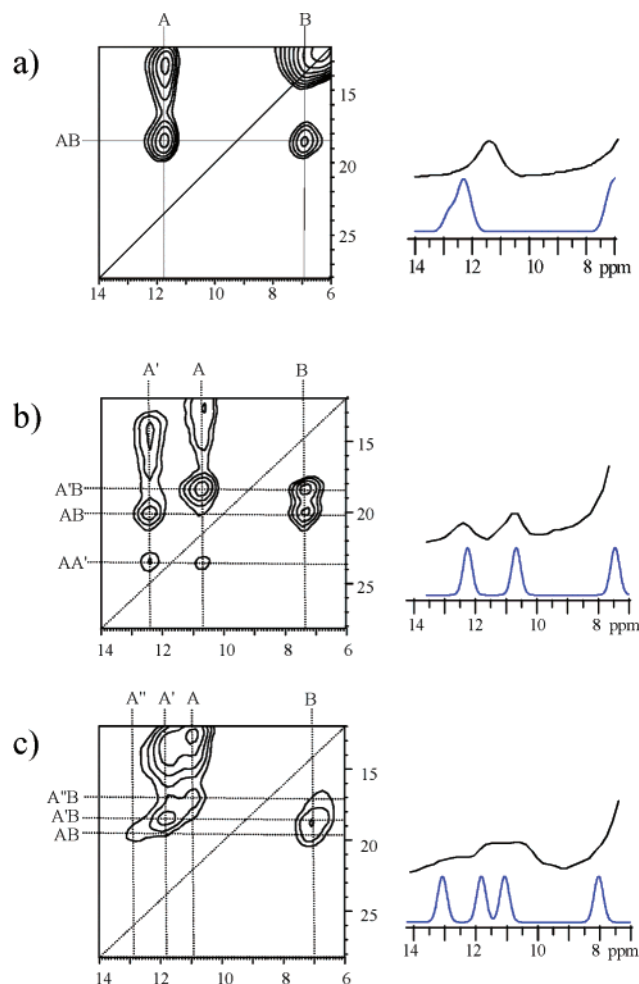


Figure 4. Regions of the ^1H 2D DQ NMR spectra (shown in Figure 2) relevant for the hydrogen bonds of the dimer (a), trimer (b), and the tetramer (c). On the right, experimental spectra are compared to calculated ^1H shifts (blue).

correlations of like methyl (E), methylene (F), and phenyl protons (C and D) in both oligomers. As well, various contacts are observed between the resonances C, D, E, and F, all of which, however, are of no significance with respect to the hydrogen-bonding scheme, but merely reflect proton–proton proximities that are obvious from the molecular structure.

More significant in terms of probing the structures are the correlations among the hydrogen-bonded protons, whose resonances occur in the lower left quadrant of the DQ spectrum. An expansion of this region is given in Figure 4. The OH resonances, labeled B, are evident in all three spectra, at 6.9 ppm in the dimer, 7.4 ppm in the trimer, and 8.0 ppm in the tetramer. The N–H resonances, labeled A in the dimer, A and A' in the trimer, and A, A', and A'' in the tetramer, distinguish the oligomers both molecularly, in the number of N–H resonances present, and structurally, in the nature of the correlations present. In the methyl benzoxazine dimer, trimer, and tetramer, one, two, and three N–H resonances, respectively, are observed. However, none of these N–H protons shows an “auto” correlation of the type A–A, A'–A', or A''–A'', which means that the N–H protons are spatially separated from each other. For the trimer, however, a correlation between A and A' is found at 23.8 ppm in the DQ dimension, which indicates that these two NH protons are in close proximity to each other

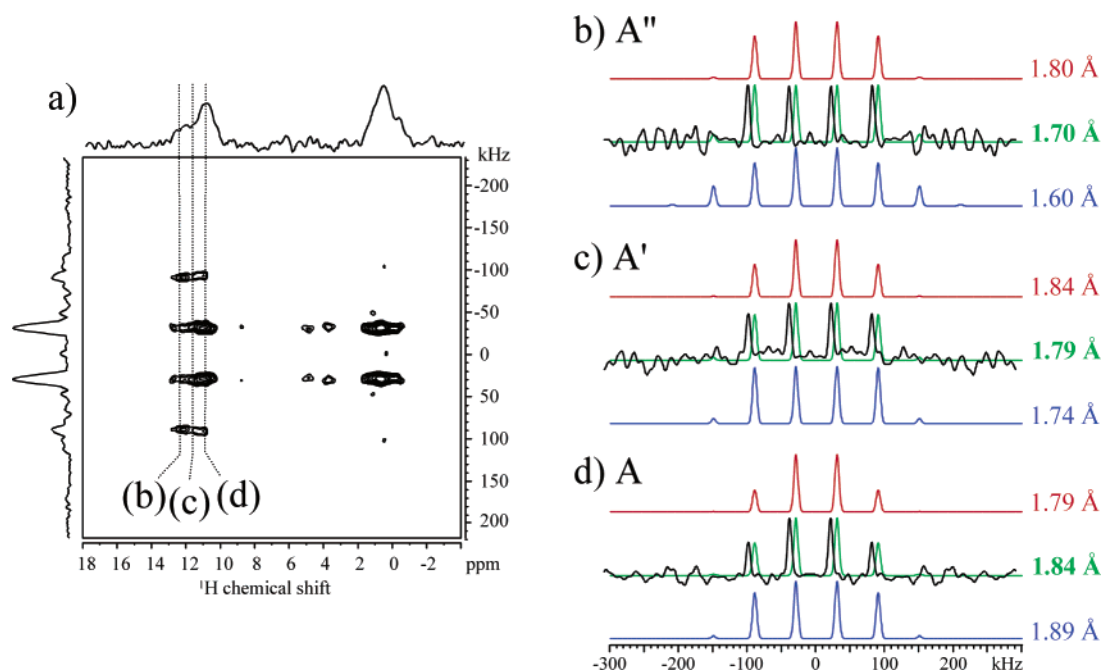


Figure 5. (a) ^{15}N - ^1H inverse CP-REPT-HDOR spectra for the benzoxazine tetramer with ^{15}N enrichment, collected using $\tau_{\text{exc}} = 20 \tau_r$ under MAS at 30 kHz. The experimental 1D patterns shown in (b, c, d) were taken from the 2D spectrum shown in (a) at the resonance positions of the NH protons A'', A', and A, respectively. The colored patterns in (b, c, d) are calculated using the N-H distances given on the right. The red and blue patterns represent the upper and lower limits of the error margin, while the green pattern fits best to the experimental data.

in the ring structure. In contrast, in the spectrum of the tetramer, no such A-A' or A-A'' contacts are observed, which is consistent with an increase in the spatial separation between the nitrogens in the larger oligomer. The A-B correlations present in all spectra are consistent with intramolecular contacts between the protons in the two types of hydrogen-bonded (N-H and O-H) protons. Similarly, expected contacts between the NH resonances and the methyl protons of the methyl at the amine position are always present.

These data are in good agreement with the molecular conformations illustrated in Figure 1. In particular, the quasi-planar ring-shaped geometry of the trimer brings the NH protons into spatial proximity with each other and is consistent with the observed A-A' contact. The respective proton-proton distance in the molecular DFT model is 2.74 Å. Furthermore, the quasi-helical tetramer structure occupies comparatively more free volume, such that the N-H protons are separated from each other by greater than 4.0 Å and therefore fall outside the range of H-H distances observable via DQ NMR under these conditions.^{27,31}

A ^1H 1D DQ MAS spectrum obtained for cross-linked, high molecular weight polybenzoxazine based on methylamine is shown in Figure 2d and clearly does not afford sufficient spectral resolution for a full structure determination due to the overlap among different types of hydrogen-bonded resonances, and generally broadened spectral features. The trend toward an increasingly complex hydrogen-bonding structure, with individually resolved resonance lines observed for the small oligomers, accounts for the broad ^1H resonances observed in the polymer, where a superposition of spectra for different H-bonded structures is expected.

Turning to the chemical properties of the polybenzoxazine polymers, we find supporting evidence for the structures described here. The overlapped ring geometry of the tetramer leads us to hypothesize a helical geometry as the most likely

conformation of the polymer. In such a geometry, the hydrogen bonds are found on the inner side of the helix, where they are protected from chemical attack. Such a geometry is consistent with the properties such as lack of water absorption and lack of contraction or expansion upon curing, the industrially favorable properties of these polymers.

^{15}N - ^1H Distance Measurements. In our previous investigation of the N-H...O distance in the methyl benzoxazine dimer, a distance of (1.96 ± 0.05) Å was measured in the ^{15}N -labeled sample prepared for that study. Here, we present distance measurements for the N-H contacts in the ^{15}N -labeled tetramer, using an improved variant of the pulse sequence.³⁹ The new pulse sequence again makes use of ^1H detection, with the added advantage of pulsed field gradients (PFGs), or, alternatively, ^1H R^3 pulses, which dephase unwanted ^1H magnetization. The measurements of N-H distances in the tetramer are in good agreement with the calculated structure. Figure 5 shows the rotor-encoded ^1H - ^{15}N dipolar sideband pattern (Figure 5a), together with the 1D patterns taken from the respective regions of the 2D spectrum and corresponding calculated patterns (Figure 5b-d). We note that, while three ^1H (N) resonances could clearly be resolved in the ^1H MAS and DQ spectra, the resolution in the ^1H dimension of the sideband experiment is somewhat hampered due to the poorer signal-to-noise which results from the extremely long recoupling time required to generate the higher order sidebands necessary for accurate measurements of these relatively long distances. Therefore, the sideband patterns (in the F_1 dimension) have been extracted from the 2D spectrum at exactly those ^1H resonance positions (in the F_2 dimension) which are known from the ^1H MAS experiment. A comparison with calculated sideband patterns (colored patterns in Figure 5b-d) yields N-H distances of (1.84 ± 0.05) , (1.79 ± 0.05) , and (1.70 ± 0.10) Å for the NH protons A, A', and A'', respectively. In Figure 5b-d, the red and blue patterns represent the upper and lower limits of the error margin,

while the green pattern fits best to the experimental data. The measured distances are in excellent agreement with the values found in the optimized geometry of the tetramer, that is, 1.89, 1.78, and 1.72 Å, and also concur with the calculated and experimental ^1H chemical shifts of the respective protons. The longest N–H distance is found for proton A, which has the smallest chemical shift (at 10.7 ppm) and forms a hydrogen bond to the central N-atom in the tetramer. The relative weakness of the hydrogen bond indicates that the central part of the tetramer experiences the most strain due to the helical geometry. For the two other NH-protons, A' and A'', shorter N–H distances as well as larger chemical shifts (of 11.7 and 12.9 ppm) are found. These observations correspond to stronger hydrogen bonds, suggesting that the more peripheral parts of the tetramer experience less conformational strain. These data therefore confirm our proposed structure of the tetramer – the first twist of a helix.

The trend to shorter N–H distances with increasing proton resonance frequency also supports our earlier discussion of the N–H distances in the slightly differing structures of the benzoxazine dimer, where the experimentally measured N–H distance of greater than 1.9 Å correlated to a ^1H resonance frequency of 11.2 ppm, whereas the distance of 1.7 Å determined via geometry optimization correlated to the calculated resonance frequency of 12.4 ppm. These data show the extreme sensitivity of the ^1H chemical shift to its environment – particularly in the presence of hydrogen bonding. Moreover, the differences noted among the dimer samples in the solid state were undetectable by other analysis methods including solution-

state NMR and FT-IR. Solid-state NMR is particularly suited to detect fine-tuning of structures via the adjustment of the $\text{NH}\cdots\text{O}$ hydrogen bond.

Conclusions

In summary, we have presented a case study in which the accord between DFT-based chemical shift calculations and high-resolution solid-state ^1H MAS NMR spectra provides ample confirmation of a supramolecular hydrogen-bonding structure. Moreover, we have established a structural motif for the methyl benzoxazine trimer and tetramer, which, in contrast to the methyl dimer pairs, are characterized exclusively by intramolecular hydrogen bonds. Extrapolating from the trends found among these oligomers, we conclude that the polybenzoxazines form helices in the solid state: such a structural conformation accounts for their favorable chemical properties.

In conclusion, this study demonstrates the remarkable success of the combination of cutting-edge experimental and computational NMR methods in the investigation of structural driving forces of supramolecular hydrogen-bonded systems.

Acknowledgment. H.I. acknowledges support from the von Humboldt Fellowship program. G.R.G. is grateful to NSERC (Canada) for support in the form of a postdoctoral fellowship. Financial support through the Deutsche Forschungsgemeinschaft (SFB 625 in Mainz) is gratefully acknowledged. We thank M. Hehn and H. Raich for their technical expertise and patience required to modify the 2.5 mm probe to incorporate gradients.

JA029059R

Visualizing Degrees of Aromaticity for Different Barbaralane Systems

Barbara Kirchner^{*,†} and Daniel Sebastiani^{*,‡}*Theoretical Chemistry, University of Bonn, Wegelerstraße 12, 53115 Bonn, Germany, and Max-Planck Institute for Polymer Research, Ackermannweg 10, 55128 Mainz, Germany**Received: July 21, 2004; In Final Form: October 4, 2004*

Aromaticity and homoaromaticity of a parent barbaralane and a tetraphosphabarbaralane of C_{2v} -symmetry are visualized by means of three-dimensional nucleus-independent chemical shift maps, showing the characteristic response properties of the electronic structure of these molecules. We combine this analysis with Car–Parrinello molecular dynamics simulations to incorporate the fluxional character of the tetraphosphabarbaralane and to show that atomistic motion at room temperature does not alter the aromaticity in this case.

Introduction

Aromaticity has a longstanding history as a fundamental concept in chemistry.¹ Its idea is taught in first year chemistry. The consequences range from elementary effects such as resonance stabilization up to structural driving forces of supramolecular or template assemblies and biological macromolecules. Aromaticity is often used in an intuitive way to describe electronic and structural properties of molecules. This rather cloudy use of the term aromaticity has been seeking supplementary clarification and further investigation since its first appearance.¹ After the discovery of benzene in 1825 by M. Faraday, the notion emerged roughly with the determination of its cyclic structure by Loschmidt in 1862 and Kekulé in 1865. Since then, a lot of effort has been devoted to the investigation of possible definitions of aromaticity, as well as chemical and physical properties of aromatic molecules. A vast collection of literature is available on the subject; see, for example, refs 1 and 2.

The term “homoaromaticity” was first introduced in 1959 by Winstein³ in an attempt to describe molecules which exhibit aromatic properties while one or several common criteria of aromaticity are not satisfied, such as, for example, the need for planarity.^{4,5} Many later works have used this expression to describe partly aromatic molecules. Just recently, a multidimensional aromaticity concept was suggested in this context; for further references, see refs 6–14.

Barbaralanes^{15,16} are a class of polycyclic molecules (**1** in Figure 1) that undergo a degenerate Cope rearrangement reaction. The transition state (TS) between the two reactants is a conformation that has a higher symmetry (C_{2v}) than the reactants (C_s). Many extended studies^{5,17–23} could confirm that an appropriate description of this transition state is homoaromatic **1***, rather than biradicaloid or radicaloid. Several experimental as well as theoretical studies have aimed at finding a possible candidate for which the double-minimum ground-state potential energy surface is turned into a single-minimum potential with the molecule exhibiting higher symmetry,^{21,24,25} that is, reducing the barrier of the transition state such that it

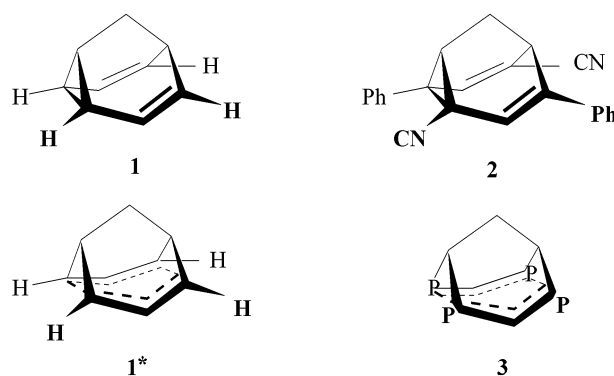


Figure 1. First column: barbaralane **1** and the symmetrical transition state **1***. Second column: diphenyl-dicyano-barbaralane **2** and tetraphosphabarbaralane **3**.

becomes a stable state. Whereas so far no gas-phase stable nondegenerate ground-state barbaralane could be determined in experiment, Seefelder and Quast received such a candidate employing different solvents.²⁰ They showed that dipolarity/polarizability and the electron pair donation ability of the solvents play the predominant role. Furthermore, very interesting extended barbaralanes giving rise to through-space interactions were suggested by Tantillo et al.²⁶ Additionally, barbaralanes and the thermochromic properties of similar molecules were investigated with respect to their use as molecular switches.^{20,27} Recently, one of the present authors (B.K.) suggested a homoaromatic barbaralane (**3**) in a theoretical work¹⁹ using an isolated molecule ansatz. Applying static quantum chemistry geometry optimization, the tetraphosphabarbaralane (**3**) displayed C_{2v} -symmetry, that is, a nondegenerate minimum structure instead of C_s -symmetry, which is a degenerate minimum structure. The barrier for the Cope rearrangement of the corresponding parent-barbaralane (**1**) agreed very well with experiment in the previous study,¹⁹ supporting the applicability of the chosen methods.

In the present investigation, we are aiming at a further characterization of **3**. The focus is three-dimensional nucleus-independent chemical shift (NICS) maps.²⁸ Here, we study NICS maps of aromatic, nonaromatic, and homoaromatic compounds to contribute to the characterization of homoaromaticity in general. We use this study then as a basis for a discussion of

* Corresponding authors. E-mail: kirchner@thch.uni-bonn.de (B.K.); sebastiani@mpip-mainz.mpg.de (D.S.).

[†] University Bonn.

[‡] Max-Planck Institute for Polymer Research.

the characteristics of the previously proposed C_{2v} -symmetrical barbaralane **3**.¹⁹ Additionally, we expose this barbaralane to a dynamical ansatz to model finite temperature effects. In particular, we will investigate the question of whether NICS maps can help to characterize the fluxional character of **3** at room temperature by combining NICS with a Car–Parrinello molecular dynamics (CPMD) simulation.²⁹ In CPMD simulations, the electronic structure of a system is calculated “on the fly” along a molecular dynamics trajectory. Polarization effects are explicitly included, and the pairwise additivity as used in almost all force field based molecular dynamics simulations is circumvented. The access to the electronic structure during a CPMD simulation allows the calculation of averaged electronic properties. Through an appropriate transformation of the Kohn–Sham orbitals, maximally localized Wannier functions can be calculated. Wannier orbitals³⁰ are the condensed phase analogues of localized molecular orbitals known from quantum chemistry. They give insight into the nature of chemical bonds and aid in the understanding of chemical concepts (e.g., nonbonding electron pairs or valency). Recent applications of the maximally localized Wannier functions are the calculations of IR absorption,^{31–33} of Raman spectra,³⁴ and of NMR chemical shifts.³⁵

Methods

Nucleus-independent chemical shift is a generalization of the atom-specific chemical shift, defined as the trace of the shielding tensor relative to a reference molecule.²⁸ NICS shows how much the chemical shift of a fictitious nuclear spin, located at a specific position in the neighborhood of the investigated molecule, would be changed. It was first introduced by Schleyer as a “simple and efficient aromaticity probe”²⁸ in 1996. Schleyer and co-workers proposed to use the absolute magnetic shielding calculated at ring centers to determine aromaticity. Negative “nucleus-independent shifts” (NICSs) indicate aromaticity, while positive NICS values denote antiaromaticity. Recently, this quantity was applied to investigate possible neutral bishomoaromatic semibullvalenes and barbaralanes.¹⁷ One of the present authors (D.S.) applied three-dimensional NICS maps, that is, by means of isosurface plots or slices, to a supramolecular assembly of dendritic polymers.³⁶ This approach which has been previously examined^{28,37,38} has the advantage that the NICS values are computed at every point in space, as opposed to a discrete set of isolated special points.

In all calculations, the framework of density functional theory employing the BP86 functional was used.^{39,40} For the molecular dynamics calculations as well as the geometry optimizations, we applied the CPMD code.⁴¹ We used Troullier–Martins norm-conserving pseudopotentials⁴² in the Kleinman–Bylander scheme⁴³ together with a 70 Ryd plane wave cutoff. To enable the study of isolated systems, the inherent periodicity of the plane-wave calculations was circumvented by applying an appropriate Poisson solver designed for nonperiodic boundary conditions.⁴⁴ The cell size was set to 14 Å³, which was found to be sufficient to converge the energies and geometries with respect to the cell parameters. We equilibrated the system for about a picosecond at 320 K with a chain of Nosé–Hoover thermostats coupled to the ionic degrees of freedom,^{45,46} before starting a production run of another picosecond at the same temperature. A 3.0 au time step (1 au = 0.0242 fs) in combination with a 400 au fictitious electron mass was chosen. These values recently were shown to be carefully chosen for obtaining good structural and dynamical properties.⁴⁷

The calculation of NICS maps was done by density functional perturbation theory⁴⁸ as implemented in the CPMD code,⁴¹

which is an extension to the NMR chemical shift module.⁴⁹ Technically, we calculate the electronic current density, which is the linear response to an external magnetic field applied to the system.⁵⁰

This quantum current induces an additional inhomogeneous magnetic field in the environment of the charge distribution. We compute this inhomogeneous field at all points of space. The resulting three-dimensional plot is visualized by a color scheme (see Figures 2, 3, and 5) in which the blue to yellow color means that the external field is attenuated, whereas it is reinforced in red regions. The delocalized character of typical aromatic electrons is translated into particularly large blue/yellow areas above and below the aromatic plane. This is due to the extended flexibility of the electrons; metaphorically speaking, they can create more extended “ring currents” than if they were aliphatic. Another feature of aromatic electron systems is a small area of opposite effect, that is, where the external field is increased (red color code). The shape of both of these effects can be seen in the nucleus-independent chemical shifts. The color scheme in the figures is gauged in parts per million (ppm), which designates the dimensionless proportionality coefficient between the induced and the external magnetic field. A charge-free test spin located at a given position in space would experience a displacement in its NMR chemical shift of the corresponding NICS value at that position. Working with a plane wave basis set, the calculation of all relevant quantities in the entire supercell is straightforwardly done by means of fast Fourier transformations.

Results: NICS Maps for Aromatic Molecules

In the original work of Schleyer and co-workers,²⁸ several test molecules were examined to assess the NICS method. For instance, a calculation employing a 6-31+G* basis set and the functional B3LYP²⁸ gave a value of −9.7 for benzene and −2.2 for cyclohexane, marking therefore a simple characteristic of distinguishing nonaromaticity from aromaticity. In our calculations, the aromatic systems exhibit large and long-ranged π -shifts in the neighborhood of the electrons, whereas the nonaromatic systems show restricted areas as can be seen in Figure 2, where the (aromatic) ring of atoms lies perpendicular to the plane.

In Figure 2, we have depicted NICS maps for representative aromatic, homoaromatic, and nonaromatic molecules: cyclopropane and dihydroxy-cyclopropenone (nonaromatic), the cyclopropenyl cation (aromatic), and the tris-homocyclopropenyl cation (homoaromatic). The maps of these molecules exhibit a very characteristic shape, which can be associated in a straightforward way with their aromaticity classification. As expected, the characteristic π -shifts (to lower frequencies, indicated in blue and yellow areas) are seen above and below an aromatic moiety, whereas the inverse effect can be found in a small localized region (a torus) beside the ring (indicated in orange/red areas). Note the remarkable spatial extension of the shielding effect. Even at a distance of about 3 Å, there is still a NICS displacement of more than 0.5 ppm. Regarding cyclopropane, we see that the aliphatic compound exposes significantly smaller shielding zones than the aromatic molecule. In addition, there is no deshielding effect next to the cyclopropane ring.

For the homoaromatic tris-homocyclopropenyl cation, we are able to pin down a sizable difference to the nonaromatic compound by means of the larger π -shifted area. Thus, we can assign a more aromatic behavior to this system. However, we cannot unequivocally assign the aromatic behavior to one of the rings, because there is a yellow cone below and above each

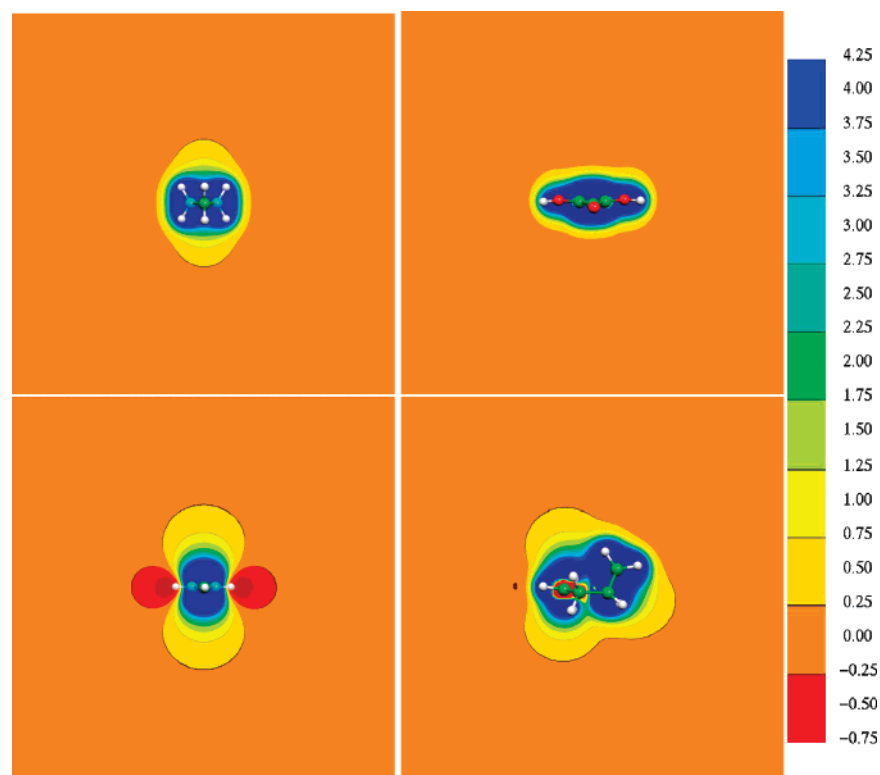


Figure 2. NICS maps for non-, homo-, and aromatic molecules. Top: cyclopropane (left) and dihydroxy-cyclopropenone (right). Bottom: cyclopropenyl cation (left) and tris-homocyclopropenyl cation (right). The spatial extension of the positive shift regions (yellow) is significantly larger for the homoaromatic (bottom right) and aromatic (bottom left) molecules than for the aliphatic ones. Note also the negative shift areas (red) outside the ring of the aromatic cyclopropenyl cation. Units in the color scheme are ppm (parts per million).

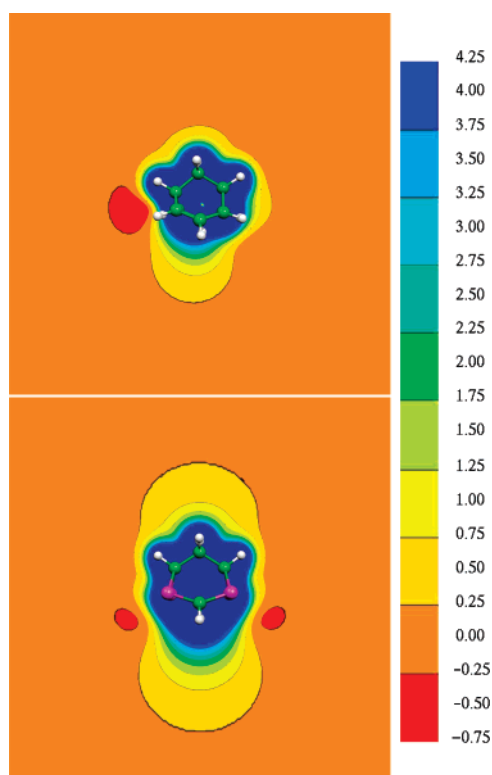


Figure 3. NICS maps for the two barbaralanes in their ground-state minimum structure. Top: **1**. Bottom: **3** (see Figure 1).

ring. Furthermore, our calculations do not display a chair structure as suggested by the Lewis formula (one 6-ring with alternating sp^2 – sp^3 carbon atoms, the sp^2 carbons forming a homoaromatic 3-ring submoiety). Instead, we get one three-membered ring (with tetragonally coordinated carbons) sharing

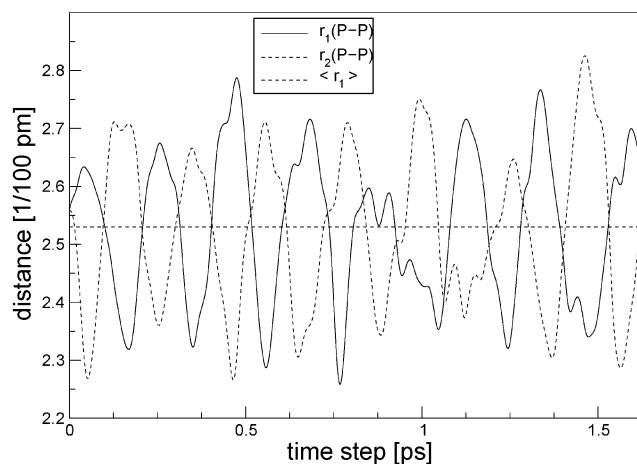


Figure 4. The evolution of the phosphorus–phosphorus atom distances of compound **3** with simulated time in picoseconds (ps).

one bond with a 5-ring, which is long known to be the right structure; see, for example, the NMR measurements by Winstein.⁵¹ These adjustments to aromatic and nonaromatic test molecules are also in accordance with the very recent work of Merino et al.,³⁸ which was published after submission of this Article. These authors compared, for example, benzene with cyclohexane among other molecules.

Turning now to NICS maps for the two barbaralane molecules (**1** and **3**) in their optimized geometry (Figure 3), we find that barbaralane **1** has only one small characteristic area under the cage, and nothing is observed above. This region concentrates beneath the two localized double bonds in the ring and reflects the more asymmetrical structure (C_s) of **1** as compared to the tetraphosphabarbaralane **3** (C_{2v}). The NICS map of the latter is found to be very similar to that of the aromatic cyclopropenyl

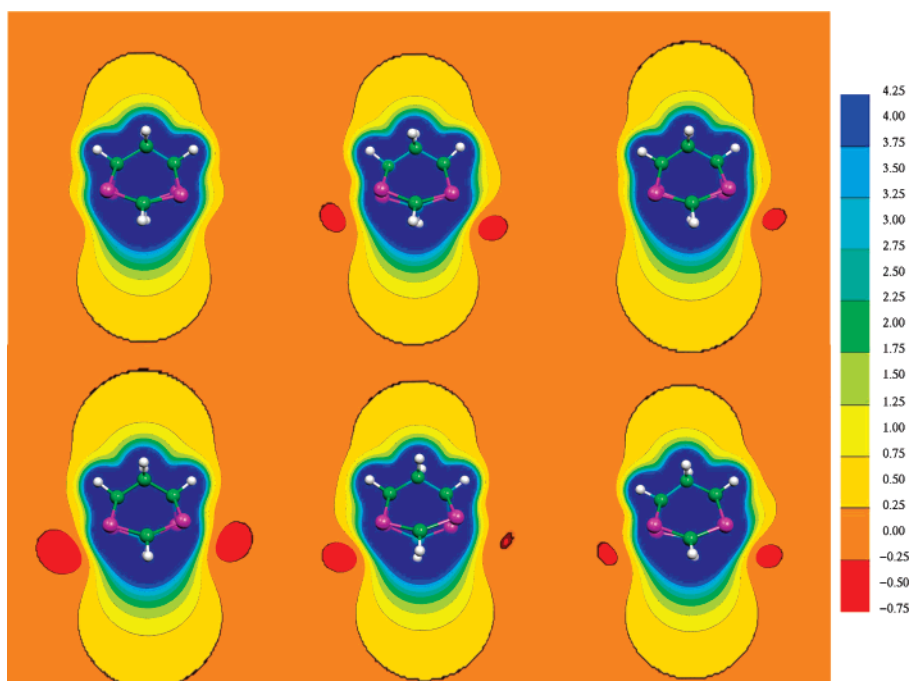


Figure 5. Time evolution of the NICS maps of **3** during a Car-Parrinello molecular dynamics trajectory. The geometries are selected configurations characteristic for the different stages of the Cope rearrangement (order: from top left to top right, then bottom left to bottom right). Note the motion of the red areas, which are typical for aromatic molecules, from one P–P bond to the other. A large aromaticity which disappears again, corresponding to extended red areas, is found when the P–P distance is below 2.6 Å.

cation shown in Figure 2 with long-ranged π -shifts below and above the cyclic structure. Also, the typical red features on the lateral sides are present. Thus, the tetraphosphabarbaralane possesses more aromatic character than the parent barbaralane **1** and the tris-homocyclopropenyl cation, and it is thus a better candidate to study homoaromaticity. These results are in accordance with Schleyer's work about semibullvalenes, barbaralanes, and bullvalenes.¹⁷ Comparing the ground-state (C_s) NICS = -8.3 ppm with the transition state (C_{2v}) NICS = -21.5 ppm for barbaralane **1**, clearly a more aromatic character for a C_{2v} minimum structure is to be expected.

In extension to the static picture, we also studied the dynamical behavior of **3**. Figure 4 shows the evolution of P–P distances, of the phosphorus atoms which are next to each other, of **3** in the Car-Parrinello simulation at finite temperature ($T = 320$ K). We see that the structure changes from the form with C_s -symmetry over the geometry of C_{2v} -symmetry to the mirrored structure of C_s -symmetry. During 1 ps of molecular dynamics (MD), nine Cope rearrangement analogous vibrations of **3** are observed. On average, one such event takes about 0.22 ps, so that the estimated wavenumber of this mode is roughly 150 cm^{-1} . The harmonic frequency analysis of the geometry-optimized molecules shows modes at about 162 cm^{-1} , which move in line with the Cope rearrangement.¹⁹ Thus, it appears justified to characterize this process as a vibrational mode, rather than a proper chemical reaction between two well-defined reactants which are separated by a significant energy barrier.

Further clarification is given by the time evolution of the NICS maps for the tetraphosphabarbaralane that are shown in Figure 5.

Although the geometric parameters undergo large changes during the Cope rearrangement-like vibration, no significant change in the NICS maps is observed. The central features, that is, the large aromaticity-indicating cones above and below the molecule, are conserved during the CPMD simulation. The inversely π -shifted regions are small and disappear temporarily, which is an indication for the somewhat weaker aromatic

character of the system. However, the comparison with non-aromatic species, as shown in Figure 2, proves the undoubtedly aromatic properties of the tetraphosphabarbaralane at ambient temperature. We thus conclude that the term homoaromaticity can definitively be applied to this molecule. In particular, its homoaromaticity is not altered when switching from the $T = 0$ K description to the more realistic finite temperature simulation.

Conclusion

We presented in this Article calculations with our NICS implementation in a CPMD framework for different test molecules. We confirmed the applicability of so-called NICS maps for distinguishing between nonaromatic, homoaromatic, and aromatic molecules. Our results are in excellent agreement with previous suggested mapping schemes.^{28,37,38} For the problem of determining aromaticity and homoaromaticity, we could show gradual differences by depicting static NICS maps for a C_s -symmetrical barbaralane and a C_{2v} -symmetrical barbaralane. These results are in accordance with the work of Schleyer and co-workers on this subject.¹⁷

With the present implementation at hand, we were able to study the aromaticity issue for molecules at finite temperature, instead of at zero temperature as in previous studies. Our approach thus resembles the experimental situation much better than static quantum chemical calculations. Thus, the major point of this study is that we extended the NICS maps to a dynamical regime and applied this option to the previously suggested tetraphosphabarbaralane with C_{2v} -symmetry. We were able to characterize its behavior under finite temperature. Because the tetraphosphabarbaralane undergoes large geometrical changes in the phosphorus atom–phosphorus atom distance (30–40 pm) under the influence of temperature and these movements are in line with a Cope rearrangement, the question arose as to whether this molecule exhibiting time-dependent C_s -symmetry also changes its aromatic character largely. With the help of NICS maps, we could confirm that it stays aromatic, and we can thus

appraise that the term homoaromatic for the C_{2v} -state of barbaralanes is appropriate.

Acknowledgment. D.S. acknowledges financial support from the Deutsche Forschungsgesellschaft (DFG) under research grant SE 1008/2 and wishes to thank the Otto-Röhm foundation for the allocation of a generous research support. B.K. acknowledges financial support from the Deutsche Forschungsgemeinschaft (DFG) of the Sonderforschungsbereich 624 and the Forschungskredit of the University of Zürich.

References and Notes

- (1) Minkin, V. M. N. G.; Simkin, B. Y. *Aromaticity and Antiaromaticity: Electronic and Structural Aspects*; Wiley-Interscience: New York, 1994.
- (2) von Ragué Schleyer, P., Ed. *Aromaticity* **2001**, 101.
- (3) Winstein, S. *J. Am. Chem. Soc.* **1959**, *81*, 6524–6525.
- (4) Williams, R. V.; Kurtz, H. *Adv. Phys. Org. Chem.* **1994**, *29*, 273.
- (5) Williams, R. V. *Chem. Rev.* **2001**, *101*, 1185–1204.
- (6) Jemmis, E. D.; von Ragué Schleyer, P. *J. Am. Chem. Soc.* **1982**, *104*, 4781–4788.
- (7) Haddon, R. C. *Acc. Chem. Res.* **1988**, *21*, 243–249.
- (8) Katritzky, A. R.; Barczynski, P.; Musumarra, G.; Pisano, D.; Szafran, M. *J. Am. Chem. Soc.* **1989**, *111*, 7–15.
- (9) Jug, K.; Köster, A. M. *J. Phys. Org. Chem.* **1991**, *4*, 163–169.
- (10) Krygowski, T. M.; Ciesielski, A.; Bird, C. W.; Kotschy, A. *J. Chem. Inf. Comput. Sci.* **1995**, *35*, 203–210.
- (11) Neus, J. *Studies in History and Philosophy of Chemistry*; HYLE Publications: Karlsruhe, 2002; Vol. 2, www.hyle.org/publications.
- (12) Chen, Z.; Jiao, H.; Hirsch, A.; von Ragué Schleyer, P. *Angew. Chem.* **2002**, *114*, 4485–4488.
- (13) Chen, Z.; Jiao, H.; Hirsch, A.; von Ragué Schleyer, P. *Angew. Chem., Int. Ed.* **2002**, *41*, 4309–4312.
- (14) Reiher, M.; Hirsch, A. *Chem.-Eur. J.* **2003**, *9*, 5442–5452.
- (15) v. E. Doering, W.; Roth, W. R. *Angew. Chem.* **1963**, *75*, 27–35.
- (16) v. E. Doering, W.; Roth, W. R. *Angew. Chem., Int. Ed. Engl.* **1963**, *2*, 115–122.
- (17) Wu, H.; Jiao, H.; Wang, Z.; v. R. Schleyer, P. *J. Am. Chem. Soc.* **2003**, *125*, 10524–10525.
- (18) Staroverov, V. N.; Davidson, E. R. *J. Am. Chem. Soc.* **2000**, *122*, 186–187.
- (19) (a) Reiher, M.; Kirchner, B. *Angew. Chem., Int. Ed.* **2002**, *41*, 3429–3583 (b) Reiher, M.; Kirchner, B. *Angew. Chem.*, **2002**, *114*, 3579–3583.
- (20) Seefelder, M.; Quast, H. *Angew. Chem., Int. Ed.* **1999**, *38*, 1068–1072.
- (21) Jackman, L. M.; Fernandes, E.; Heubes, M.; Quast, H. *Eur. J. Org. Chem.* **1945**, *10*, 2209–2227.
- (22) Gompper, R.; Nöth, H.; Spes, P. *Tetrahedron Lett.* **1988**, *29*, 3639–3642.
- (23) Dewar, M. J. S.; Lo, D. H. *J. Am. Chem. Soc.* **1971**, *93*, 7201–7207.
- (24) Chen, Y.; Hartmann, M.; Diedenhofen, M.; Frenking, G. *Angew. Chem., Int. Ed.* **2001**, *40*, 2051–2055.
- (25) Chen, Y.; Hartmann, M.; Diedenhofen, M.; Frenking, G. *Angew. Chem.* **2001**, *113*, 2107–2112.
- (26) Tantillo, D. J.; Hoffmann, R.; Houk, K. N.; Warner, P. M.; Brown, E. C.; Henze, D. K. *J. Am. Chem. Soc.* **2004**, *126*, 4256–4263.
- (27) Dohle, M.; Manz, J.; Paramonov, G. K.; Quast, H. *Chem. Phys.* **1995**, *197*, 91–97.
- (28) v. R. Schleyer, P.; Maerker, C.; Dransfeld, A.; Jiao, H.; v. E. Hommes, N. J. R. *J. Am. Chem. Soc.* **1996**, *118*, 6317–6318.
- (29) Car, R.; Parrinello, M. *Phys. Rev. Lett.* **1985**, *55*, 2471–2474.
- (30) Wannier, G. *Phys. Rev.* **1937**, *52*, 191.
- (31) Bernasconi, M.; Silvestrelli, P.-L.; Parrinello, M. *Phys. Rev. Lett.* **1998**, *81*, 1235–1238.
- (32) Gaigeot, M.-P.; Sprik, M. *J. Phys. Chem. A* **2003**, *107*, 10344–10358.
- (33) Kirchner, B.; Hutter, J. *J. Chem. Phys.* **2004**, *121*, 5133–5142.
- (34) Putrino, A.; Parrinello, M. *Phys. Rev. Lett.* **2002**, *88*, 176401.
- (35) Sebastiani, D.; Parrinello, M. *ChemPhysChem* **2002**, *3*, 675.
- (36) Rapp, A.; Schnell, I.; Sebastiani, D.; Brown, S. P.; Percec, V.; Spiess, H. W. *J. Am. Chem. Soc.* **2003**, *125*, 13284–13297.
- (37) Klot, S.; Koch, A.; Kleinpeter, E. *J. Chem. Soc., Perkin Trans. 2002*, *2*, 1506–1509.
- (38) Merino, G.; Heine, T.; Seifert, G. *Chem.-Eur. J.* **2004**, *10*, 4367–4371.
- (39) Becke, A. D. *Phys. Rev. A* **1988**, *38*, 3098–3100.
- (40) Perdew, J. P. *Phys. Rev. B* **1986**, *33*, 8822–8824.
- (41) “CPMD V3.8 Copyright IBM Corp. 1990–2003, Copyright MPI für Festkörperforschung Stuttgart 1997–2001”, see also www.cmpd.org.
- (42) Troullier, N.; Martins, J. L. *Phys. Rev. B* **1991**, *43*, 1993.
- (43) Kleinman, L.; Bylander, D. M. *Phys. Rev. Lett.* **1982**, *48*, 1425.
- (44) Martyna, G.; Tuckerman, M. *J. Chem. Phys.* **1999**, *110*, 2810.
- (45) Nosé, S. *Mol. Phys.* **1984**, *5*, 255.
- (46) Hoover, W. G. *Phys. Rev. A* **1985**, *31*, 1695.
- (47) Marx, D.; Hutter, J. *Ab initio Molecular Dynamics: Theory and Implementation. Modern Methods and Algorithms in Quantum Chemistry*; Forschungszentrum Juelich: 2000; Vol. 1.
- (48) Putrino, A.; Sebastiani, D.; Parrinello, M. *J. Chem. Phys.* **2000**, *113*, 7102.
- (49) Sebastiani, D.; Parrinello, M. *J. Phys. Chem. A* **2001**, *105*, 1951.
- (50) Sebastiani, D.; Goward, G.; Schnell, I.; Spiess, H.-W. *J. Mol. Struct. (THEOCHEM)* **2003**, *625*, 283–288.
- (51) Lowry, T. H.; Richardson, K. S. *Mechanism and theory in organic chemistry*; Harper: New York, 1986.

Bulk Chemical Shifts in Hydrogen Bonded Systems from First Principles Calculations and Solid-State-NMR

J. Schmidt[†], A. Hoffmann[‡], H. W. Spiess[†] and D. Sebastiani^{†*}

[†] Max-Planck-Institute for Polymer Research,
Ackermannweg 10, D-55128 Mainz, Germany

[‡]Institut für Makromolekulare Chemie, Freiburg University,
Stefan-Meier-Str. 31, D-79104 Freiburg, Germany

June 12, 2006

*Email: sebastia@mpip-mainz.mpg.de, Fax: +49-6131-379-100

Abstract

We present an analysis of bulk ^1H NMR chemical shifts for a series of biochemically relevant molecular crystals in analogy to the well-known solvation NMR chemical shifts. We call bulk shifts the change in NMR frequency of a gas-phase molecule when it undergoes crystallization. We compute NMR parameters from first principles electronic structure calculations under full periodic boundary conditions and for isolated molecules, and compare them to the corresponding experimental fast magic-angle spinning solid-state NMR spectra. The agreement between computed and experimental lines is generally very good. The main phenomena responsible for bulk shifts are packing effects (hydrogen bonding and π -stacking) in the condensed phase.

1 Introduction

The determination of local structural properties, intra- and intermolecular conformations of molecular systems and supramolecular assemblies has always been and still is a challenge for modern physics and chemistry. Many advanced techniques are capable of contributing to this quest, some of the most prominent being X-ray¹ and neutron scattering,² infrared (IR) spectroscopy³ and nuclear magnetic resonance (NMR) spectroscopy.^{4,5}

In crystalline systems, scattering experiments can provide very accurate atomic coordinates. Many systems, however, lack the required long-range order, which limits the applicability of these scattering techniques. Complementary to this, NMR experiments are able to probe local structure without the need of long-range order. While magnetic resonance techniques cannot provide the full structure in terms of three-dimensional atomic coordinates, the sensitivity to the local chemical environment of an atom is one of the key advantages of this method. NMR is well suited to investigate biological systems and their mechanisms of structure formation.⁶⁻⁹

The dependence of NMR chemical shifts of a molecule on its chemical environment is well-established for solutions, where the change in the NMR resonance is called solvent shift. It is due to the interaction of the solvent molecules with the solute, which may be hydrogen bond networks, van-der-Waals forces, or other non-bonded interactions. In solid phases, these packing effects are frozen out, due to the lack of fast diffusive atomic motion. In analogy to solvation shifts, we call bulk chemical shift the change in the NMR resonance due to the condensation of a molecule. Since packing effects are more stable in the solid state, their spectroscopic signatures are usually stronger than in solution. In crystalline systems, the packing is also very well-defined, as opposed to amorphous systems. Hence, the study of structure-property relation-

ships in crystals enables us to understand also effects which are seen in much more complex non-crystalline systems. Bulk chemical shifts are particularly large in the proton NMR spectra, where they can easily reach up to 100% of the normal hydrogen NMR chemical shift range.

It has become increasingly common to supplement the experimental data with adequate numerical simulations. Classical molecular dynamics (MD) techniques are performed for structures obtained via X-rays in order to test their conformational stability; quantum chemical calculations of vibrational frequencies can often help interpreting IR spectra. In NMR, dihedral angles are probed by spin-spin coupling constants and cross-relaxation rates due to dipole-dipole interactions provide distance constraints for MD simulations. For magnetic resonance experiments, accompanying ab-initio calculations have become standard for isolated molecules,^{10–12} and are becoming increasingly popular also for the solid state,^{13–17} as well as for liquids and solutions.

A particular case in point is the ab-initio simulation of structure and properties of liquid water, where the dynamically fluctuating hydrogen bond network is the central structural driving force. Important progress has been achieved in the direct simulation of the molecular structure in the liquid phase,^{18,19} the understanding of its IR spectrum,^{20,21} the Raman spectrum of ice,²² the NMR parameters in the liquid and supercritical phases,^{23,24} and last not least the hydrogen bond network of water on surfaces.^{25–27}

Realistic molecular biological systems are extremely complex, both in structure and dynamics – not to mention their functionality. In order to investigate such systems with magnetic resonance methods, a great deal of knowledge regarding the relationships between structure, atomistic dynamics and spectroscopic properties is crucial.²⁸ This is particularly true if magnetic parameters such as chemical shifts or spin-spin couplings^{4,5} are to be used as sources of information. Therefore, a clear validation

of the signatures of condensed phase packing effects both in NMR experiment and in quantum-chemical calculations is essential for a real understanding of complex systems. Such a validation is best done on systems which have known structures and a limited complexity. Thus, we focus on packing effects (hydrogen bonding, π -stacking) in crystals of small biologically relevant molecules, which we want to analyze with a combined experimental and ab-initio approach.

In this work, we present computed NMR bulk shifts of L-Alanine, L-Tyrosine, L-Histidine-hydrochloride-monohydrate, and Adenine-hydrochloride-monohydrate. We analyze the contributions to the bulk shift from hydrogen bonding, π -stacking and changes in the intramolecular structure. For one of the crystals, we replace the Cl^- ion with F^- and Br^- in order to study the effect of the radius and electronegativity of the anion. All spectra thus obtained are compared to fast (30kHz) magic-angle-spinning (MAS) solid-state NMR experiments to validate the approach.

2 Computational and experimental methods

It is well-known that for the reliable calculation of NMR parameters, in particular for chemical shifts, the chemical environment of the considered atoms is of crucial importance. Highly accurate electronic structure methods on the explicitly correlated level of theory are available for the calculation of structure^{29,30} and magnetic resonance properties,^{31,32} small molecular systems, but not for the condensed phase. Density functional theory (DFT) represents a compromise between accuracy and computational efficiency, and has been proven many times to yield good agreement with experimental data. Although DFT based methods are sometimes erratic for particularly difficult cases of electronic structure,^{33–36} they allow for a parameter-free prediction of structural and spectroscopic properties in complex systems, well beyond isolated

gas-phase molecules.^{10, 11, 17, 37} In turn, the much less expensive implicit models for solvation effects have been shown to have limits in the description of explicit hydrogen bonding.³⁸ Therefore, we believe that the density functional theory approach is a reasonable tool for obtaining the structural and spectroscopic information we need.

The recent advent of parallel supercomputers enables a routinely simulation of crystalline and amorphous solids, liquids, and solutions from first principles.³⁹ For such systems, cluster models do not always yield satisfactory results, and even embedded models seem to have a questionable accuracy. Therefore, we study our crystals within a plane-wave-based DFT approach under periodic boundary conditions in order to overcome the limits of cluster calculations. We use the CPMD code⁴⁰ with Goedecker-type pseudopotentials,^{41, 42} the BLYP exchange-correlation functional,^{43, 44} and a plane-wave cutoff of 70-90Ry depending on the atomic species present in the crystals.

In all cases, crystallographic data was taken from the Cambridge Structural Database (CSD)⁴⁵ and subsequently relaxed within the computational setup described above, keeping the crystal lattice fixed at the experimentally determined values. In particular, the position of hydrogen atoms changed significantly (up to about 0.15Å), while the bond distances for the heavier atoms changed only by small amounts. In view of the experimental uncertainties – in particular for X-ray experiments dated from the middle of the 20th century – we believe that it is justified to relax also the heavier atoms, although this is an ongoing matter of debate.⁴⁶ The NMR chemical shifts were calculated fully from first principles in the optimized periodic crystal structure.^{47, 48} The computed nuclear shieldings were referenced directly to computed shieldings of tetramethylsilane. For a better comparison with experimental spectra, we convolute the computed shift values with Gaussians, using a spread of $\Delta=0.2$ ppm.

It is possible to perform direct ab-initio simulations of the effect of molecular mo-

tion on magnetic resonance spectra.¹⁶ However, this requires a series of Car-Parrinello molecular dynamics simulations and property calculations for each involved system, which is beyond the scope of this work. Thus, we restrict ourselves to static observations of the molecular geometries in the condensed phase.

Solid-state MAS NMR experiments were performed on a Bruker DRX Avance spectrometer operating at a Larmor frequency of 700.12MHz and using 2.5mm rotors. Magic-angle spinning was applied at 30kHz to enhance spectral resolution. The NMR resonances were referenced to the chemical shift of liquid water (such that $\delta_{\text{liq}}(\text{H}_2\text{O})=4.8\text{ppm}$).

3 Results and Discussion

3.1 L-Alanine

Alanine is the second smallest amino acid after Glycine. Its structure-determining groups are the amino and carboxy-groups. In the crystal, the nitrogen is threefold protonated and thus forms one strong and two weaker hydrogen bonds to neighboring carbonyl-oxygens. In our static geometry optimization, we found $\text{H}\cdots\text{O}$ distances of 1.51Å, 1.84Å and 1.89Å (see figure 1). The NH bond of the proton involved in the strongest H-bond is elongated by as much as 0.05Å compared to the two other hydrogens.

The experimental and computed ^1H NMR chemical shift spectra are shown in figure 2. In the static calculation, the asymmetry of the three NH_3 protons is reflected in very different NMR chemical shifts at 14.3, 6.4 and 5.6ppm, illustrating the high sensitivity of the NMR line to the geometry of hydrogen bonds. In reality, the NH_3^+ group is rotating, resulting in a single experimental NMR line for the amino protons at 8.6ppm. About the same value (8.8ppm) is obtained when averaging the calcu-

lated chemical shifts. The agreement with experiment is very good, especially for the hydrogen-bonded protons. The only significant deviation of about 1ppm is obtained for the CH proton.

Comparing to the NMR parameters of an isolated Alanine molecule in the same conformation, this hydrogen bonding effect is even more pronounced. Using the same computational setup, we found shifts changes of 7.9, 1.5 and 0.5ppm, respectively.

A direct comparison to an optimized isolated molecule is more difficult because the molecule tautomerizes into a regular $\text{NH}_2\cdots\text{COOH}$ structure. Naturally, the ^1H NMR chemical shifts of this geometry are very different from that in the crystalline state. The modeling of the structure in solution is in principle also possible, but significantly exceeds the scope of this work. For solutions, a full ab-initio molecular-dynamics simulation with subsequent NMR calculations of many individual conformations is required. Further, the results would strongly depend on the chosen solvent. For this reason, we only show the NMR signals of the $\text{NH}_2\cdots\text{COOH}$ arrangement, in which the carboxy-proton forms a hydrogen bond to the nitrogen (see figure 2).

3.2 L-Tyrosine

As in alanine, the protons in the amino group of tyrosine are strongly hydrogen bonded. In our optimized geometry, one of them creates a bifurcated H-bond to a carbonyl and a phenol oxygen, while the two remaining ones are H-bonded to carbonyl oxygens. Similarly, the phenolic OH is H-bonded to a carbonyl oxygen.

The amino protons are likely to rotate at ambient temperatures, which results in an averaged chemical shift resonance. The strong hydrogen bonding is reflected in the downfield chemical shifts 8.9 and 9.8ppm in the experimental and 9.0 and 9.7ppm in the computed spectra (see figure 4). The phenolic OH proton shows up as a shoulder of the larger amino peak.

With respect to alanin, the tyrosine molecule contains a phenol group instead of a methyl (see figure 3). This additional group thus provides a further structural driving force, namely delocalized π -electrons. The effect of this unpolar group can be seen in the crystal packing, where phenylic and polar atoms arrange in a sheet-like topology. However, the aromatic interactions are not strong enough to form columnar structures, which are only seen in larger polyaromatic hydrocarbons.⁴⁹ Instead, the somewhat tilted configuration of the phenyl rings leads to an orientation of the aromatic protons in the direction of neighboring rings.

This proximity yields several different upfield shifts of the aliphatic and aromatic protons. According to our calculated shifts, the following assignment of the two experimental main peaks (at 4.6 and 6.6ppm) can be made: The aliphatic CH₂ protons (“C”) and the aromatic hydrogens close to the OH group (“F”, “G”) constitute the most upfield resonance at 4.6ppm, while the two remaining aromatic protons (“E”, “H”) and the CH hydrogen (“B”) are responsible for the more downfield one at 6.6ppm.

The agreement between experimental and computed shifts is very good for the hydrogen-bonded protons, while the aromatic and aliphatic hydrogens are somewhat too upfield shifted in our calculated spectrum. This effect is due to the proximity of these protons to the aromatic moieties. In our static conformation, no molecular and atomic motion is taken into account, only the optimized geometry (corresponding to a temperature T=0K) is used. The incorporation of such motion could significantly weaken the through-space upfield shift of these packing effects, which would bring the average shifts closer to the experimental values. Molecular dynamics could also slightly weaken the hydrogen bonds of the amide groups, which would lead to less downfield shifted proton peaks. As in the case of alanine, both effects, could only be realistically described via a combined molecular dynamics/spectroscopy calculation.

The expected tendency, however, are readily seen in the computed NMR resonance

lines for the isolated molecule in the crystal geometry, which are shown in the bottom of figure 4. The aromatic protons converge at 5.5ppm, while the aliphatic ones return to 2.6 and 3.8ppm. This represents an aromatic upfield shift – as a purely intermolecular through-space effect – of up to 4ppm due to crystallization, which is an unusually large value. As discussed above, temperature effects weaken this extreme displacement, but it is still clearly visible in the experimental NMR spectrum.

As expected, the absence of intermolecular hydrogen bonding can also be seen from the NH_3 peak at about 5.5ppm and the phenolic OH at 4.7ppm. Upon condensation, they hence experience downfield shifts of 3.5-5ppm.

3.3 L-Histidine-hydrochloride-monohydrate

Histidine is a slightly more complex molecule than alanine, containing an additional imidazole ring. The structure of its $\text{HCl}\cdot\text{H}_2\text{O}$ modification in the crystalline phase is shown in figure 5.

The experimental and calculated NMR chemical shift spectra are shown in figure 6. The overall agreement is excellent, with the exception of the crystal water, where a difference of about 1.4ppm is found. This discrepancy could be due to temperature effects: At ambient temperature, the water protons will significantly oscillate, and the whole water molecule will occasionally undergo 180-degree-flips. This increased motion will weaken its hydrogen bonds, yielding an upfield chemical shift. Using a computed dependence of about 6ppm/Å of the ^1H NMR chemical shift for a water dimer on the $\text{H}\cdots\text{O}$ distance as an estimation, the observed 1.4ppm would correspond to an effective increase of the average $\text{H}\cdots\text{O}$ distance of about 0.23Å between the crystal water and the carboxyl oxygen. This seems a reasonable value for the difference in temperature between experiment and calculation.

In the hydrochloride modification, both the imidazole and the amino nitrogens are

protonated, with the COO^- and Cl^- as counterions. The imidazole protons form H-bonds to carbonyl oxygens of 1.90Å and 1.58Å length, respectively. The resulting chemical shifts appear at unusually large values, at 11.6 and 16.16ppm.

For the NH_3 protons, of which two are hydrogen bonded to a chlorine ion and the remaining one to a water molecule, the NMR resonances show up at 7.3, 8.3 and 9.5ppm, respectively. This is about the same region as the alanine NH_3 protons, but the spread of the shifts is much smaller. Taking into account the size of the chlorine ion, this can be explained by the more similar H-bond distances of 2.25Å and 2.17Å ($\text{H}\cdots\text{Cl}$) and 1.72Å ($\text{H}\cdots\text{OH}_2$).

A comparison to the isolated histidine molecule in the geometry found in the crystal is shown in figure 6. The most striking feature is the downfield shift of the imidazole hydrogens in the condensed phase. While the proton with the weaker H-bond is shifted by only 1.8ppm, the other proton experiences a downfield shift of about 6ppm. A more subtle, but nevertheless very characteristic change is seen in the CH proton, which is upfield shifted by 2.3ppm. This strong displacement can be explained by the vicinity of its neighboring molecules: in the crystal structure, this hydrogen is located only 2.7Å above an imidazole ring of another molecule. For the NH_3 peak, we observe a crystallization shift of 3.1ppm, which is due to the hydrogen bonds.

We have further investigated the effect of the size of the anion on the hydrogen shifts. To this purpose, we have replaced the Cl^- by F^- and Br^- . Since we keep the crystal lattice unchanged, this setup does not represent the physically correct system, in which the lattice would be altered. However, we want to focus on the direct electronic effect of such a substitution, and explicitly ignore its structural effect.

We have plotted the dependence of the chemical shifts of the two NH_3 protons pointing towards the anion as a function of the ionic radius⁵⁰ of the latter in figure 7. Surprisingly, the NMR line is predicted to move *downfield* with increasing size of the

ion – somewhat counterintuitive to the rule of thumb that a higher electron density at the position of a nuclear spin causes a higher shielding (i.e. an upfield shift).

We believe that the reduced shielding for Br^- may be due to the stronger repulsive effect of the bromine electrons on those of the NH_3 group – which would in turn satisfy the rule of thumb. However, this explanation is highly speculative, and a full investigation of this phenomenon is beyond the scope of this work. Also the structural effect of the variation of the anion’s size has been ignored here. From our calculation, we can only conclude that a bigger electronic cloud effectively *reduces* the nuclear shielding of a H-bonded proton.

An alternative view of this phenomenon can be based on the electronegativity differences of the counterions. Tabulated values⁵⁰ are approximately (negatively) proportional to the ionic radius. An increased electronegativity in the series $\text{Br} \rightarrow \text{Cl} \rightarrow \text{F}$ yields almost linearly decreasing chemical shifts. This indicates that the more electronegative anions donate less electronic density to the hydrogen bond, or in other words, they pull stronger on the electronic density in the $\text{H} \cdots \text{X}^-$ region.

3.4 Adenine hydrochloride monohydrate

The last molecule of our study is adenine, which is a basic building block of nucleic acids. A view on the crystal structure of adenine hydrochloride monohydrate is presented in figure 8. The crystalline packing is sheet-like, with a parallel arrangement of the rings. However, they are not aligned in the conventional $\pi - \pi$ -stacked arrangement; instead, the layers are laterally displaced with respect to each other. The water molecules and the Cl^- anions are placed at interstitial positions, providing hydrogen bond acceptors for the NH protons of adenine.

Since in this salt, the adenine molecule acquires the proton from the HCl, there are four hydrogen bond donator sites (two NH and one NH_2). The NH hydrogen of the

six-ring is H-bonded to the crystal water, while the NH in the five-ring is linked to the Cl^- anion. The NH_2 protons finally are H-bonded to the unprotonated nitrogen in the five-ring and the Cl^- , respectively.

The experimental and computed NMR spectra are shown in figure 9. The agreement between the theoretical and experimental resonances is generally good. The chemical shift of the strongly hydrogen-bonded NH protons (“B” and “D”) are found at about 13.5-14ppm. As seen in the comparison to the isolated molecule (also shown in figure 9), this represents a strong downfield shift of 3.5-4.5ppm, which is characteristic for the strong hydrogen bonds.

The hydrogens of the amino group appear at 8.7ppm, together with the aromatic CH proton and the crystal water. This value is relatively large for an aromatic proton, but can be explained by the positive charge carried by the six-ring. The amino hydrogens are shifted downfield by 2-3ppm with respect to the isolated molecule, which indicates a weaker, yet clearly nonvanishing hydrogen bonding state. The surprisingly strong shift for the water molecule – which would be at 4.8ppm in the liquid state – actually compares very well to the (experimental and computed) value for crystalline ice Ih,²⁴ which is around 8ppm. This provides evidence for a very tight confinement of the crystal water, since large vibrational amplitudes would weaken the H-bonding and bring the chemical shift closer to that of liquid water.

We have also optimized the geometry of the isolated molecule, keeping the charge at +1. The calculated NMR spectrum of the resulting geometry is also shown in figure 9. The results reveal that there is an almost constant upfield shift of the whole spectrum, mainly due to shortened covalent bonds with respect to the crystal geometry.

4 Conclusions

We have presented an investigation of packing effects in strongly hydrogen-bonded molecular crystals of amino acids using periodic first-principles calculations and solid-state MAS NMR experiments.

The agreement of our first-principles calculations of NMR chemical shifts with the corresponding experimental values is in general very good. This means that solid-state ^1H NMR combined with quantum chemical calculations can indeed be used to yield valuable structural information of hydrogen-bonded systems, including packing effects.¹⁷ The largest deviations was found for the NMR chemical shift of the strongly hydrogen bonded crystal water in the histidine system, where the ab-initio results are off by about 1.4ppm. A similar discrepancy has been found previously by Yates et al.⁴⁶ for the HNMR chemical shift of a carboxylic acid dimer within the fluriprofen crystal. In both cases, the calculations were done without considering atomic motion, i.e. at zero temperature. Realistic calculations of NMR spectra and related properties at finite temperature do exist,^{16,23,24,51} but are still rare due to the computational cost involved in such calculations.

Our combined computational and experimental study shows that already very simple model systems exhibit packing effects which are characteristic for much larger biological and biomimetic systems.^{52,53} Their molecular building blocks feature hydrogen bonding and aromatic π -stacking, which are clearly visible in the ^1H NMR pattern, and much easier to study than the real target systems which are present in nature.

Last not least, the direct benchmarking of computed magnetic resonance spectra against experimental data shows to which degree property calculations from first principles are capable of realizing the sometimes subtle details in real spectra. This is

highly important in situations where the theoretical support regarding the interpretation of spectroscopic data is needed, in particular when only little experimental expertise exists from previous studies on similar and related systems.^{13,53} The growing importance of direct simulations of chemical processes and the increasing complexity of today's atomic structures in realistic systems will give rise to more of such combined experimental/theoretical investigations. This holds also for other spectroscopic properties like EPR g-tensors, scalar spin-spin-couplings (J-couplings) or nuclear quadrupolar coupling constants.¹² In addition, further developments on the experimental side – e.g. for resolution enhancement in NMR⁷ – will pave the way for substantially better descriptions of the more and more complex disordered systems of modern chemistry.

5 Acknowledgments

This work was funded by the DFG grants SE 1008/2 (J.S.) and SFB 625 (A.H.).

References

- [1] Warren, B. E. *X-Ray Diffraction*. Dover, Mineola, 1990.
- [2] Lovesey, S. W., Ed. *Theory of Neutron Scattering from Condensed Matter*. Oxford University Press, 1988.
- [3] Colthup, N. B.; Daly, L. H.; Wiberley, S. E. *Introduction to infrared and Raman spectroscopy*. Academic Press, New York, 1975.
- [4] Ernst, R. R.; Bodenhausen, G.; Wokaun, A. *Principles of Nuclear Magnetic Resonance in One and Two Dimensions*. Clarendon Press Oxford, 1987.
- [5] Wüthrich, K. *NMR of Proteins and Nucleic Acids*. Wiley, New York, 1986.

- [6] Brown, S.; Spiess, H. W. *Chem. Rev.*, **2001**, *101*, 4125.
- [7] Sakellariou, D.; Brown, S. P.; Lesage, A.; Hediger, S.; Bardet, M.; Meriles, C. A.; Pines, A.; Emsley, L. *J. Am. Chem. Soc.*, **2003**, *125*, 4376–4380.
- [8] Duma, L.; Hediger, S.; Brutscher, B.; Bockmann, A.; Emsley, L. *J. Am. Chem. Soc.*, **2003**, *125*, 11816–11817.
- [9] Spiess, H. W. *J. Polym. Sci.*, **2004**, *A 42*, 5031–5044.
- [10] Bühl, M.; Kaupp, M.; Malkina, O. L.; Malkin, V. *J. Comput. Chem.*, **1999**, *20*, 91–105.
- [11] Jameson, C. J.; de Dios, A. C. *Nuc. Mag. Res.*, **2004**, *33*, 47–75.
- [12] Kaupp, M.; Bühl, M.; Malkin, M.; Vladimir, G., Eds. *Calculations of NMR and EPR parameters*. Wiley-VCH, Weinheim, 2004.
- [13] Goward, G.; Sebastiani, D.; Schnell, I.; Spiess, H. W. *J. Am. Chem. Soc.*, **2003**, *125*, 5792–5800.
- [14] Yates, J. R.; Pham, T. N.; Pickard, C. J.; Mauri, F.; Amado, A. M.; Gil, A. M.; Brown, S. P. *J. Am. Chem. Soc.*, **2005**, *127*, 10216–10220.
- [15] Gervais, C.; Dupree, R.; Pike, K. J.; Bonhomme, C.; Profeta, M.; Pickard, C. J.; Mauri, F. *J. Phys. Chem. A*, **2005**, *109*, 6960–6969.
- [16] Schmidt, J.; Sebastiani, D. *J. Chem. Phys.*, **2005**, *123*, 074501.
- [17] Schulz-Dobrick, M.; Metzroth, T.; Spiess, H. W.; Gauss, J.; Schnell, I. *ChemPhysChem*, **2005**, *6*, 315–327.
- [18] Laasonen, K.; Sprik, M.; Parrinello, M.; Car, R. *J. Chem. Phys.*, **1993**, *99*, 9080–9089.

- [19] Silvestrelli, P.; Parrinello, M. *J. Chem. Phys.*, **1999**, *111*, 3572.
- [20] Silvestrelli, P. L.; Bernasconi, M.; Parrinello, M. *Chem. Phys. Lett.*, **1997**, *277*, 478–482.
- [21] Sharma, M.; Resta, R.; Car, R. *Phys. Rev. Lett.*, **2005**, *95*, 187401.
- [22] Putrino, A.; Parrinello, M. *Phys. Rev. Lett.*, **2002**, *88*, 176401.
- [23] Sebastiani, D.; Parrinello, M. *ChemPhysChem*, **2002**, *3*, 675.
- [24] Pfrommer, B.; Mauri, F.; Louie, S. *J. Am. Chem. Soc.*, **2000**, *122*, 123–129.
- [25] Sebastiani, D.; Delle Site, L. *J. Chem. Theory Comp.*, **2005**, *1*, 78–82.
- [26] Henderson, M. A. *Surf. Sc. Rep.*, **2002**, *46*, 1–308.
- [27] Ludwig, R. *Angew. Chem. Int. Ed. Engl.*, **2003**, *42*, 3458–3460.
- [28] Sijbesma, R. P.; Beijer, F. H.; Brunsveld, L.; Folmer, B. J. B.; Hirschberg, J. H. K. K.; Lange, R. F. M.; Lowe, J. K. L.; Meijer, E. W. *Science*, **1997**, *278*, 1601–1604.
- [29] Szalay, P.; Thogersen, L.; Olsen, J.; Kallay, M.; Gauss, J. *J. Phys. Chem. A*, **2004**, *108*, 3030–3034.
- [30] Flowers, B.; Szalay, P.; Stanton, J.; Kallay, M.; Gauss, J.; Csaszar, A. *J. Phys. Chem. A*, **2004**, *108*, 3195–3199.
- [31] Gauss, J.; Stanton, J. *J. Chem. Phys.*, **1995**, *102*, 251–253.
- [32] Gauss, J.; Stanton, J. *J. Chem. Phys.*, **1995**, *103*, 3561–3577.
- [33] Dreuw, A.; Head-Gordon, M. *J. Am. Chem. Soc.*, **2004**, *126*, 4007–4016.

- [34] Fritsche, L.; Koller, J.; Reinert, T. *Int. J. Quantum Chem.*, **2004**, *100*, 681–694.
- [35] Jones, G. A.; Paddon-Row, M. N.; Sherburn, M. S.; Turner, C. I. *Org. Lett.*, **2002**, *4*, 3789–3792.
- [36] Cai, Z. L.; Sendt, K.; Reimers, J. R. *J. Chem. Phys.*, **2002**, *117*, 5543–5549.
- [37] Sebastiani, D. *Mod. Phys. Lett. B*, **2003**, *17*, 1301–1319.
- [38] Klein, R. A.; Mennucci, B.; Tomasi, J. *J. Phys. Chem. A*, **2004**, *108*, 5851–5863.
- [39] Hutter, J.; Curioni, A. *ChemPhysChem*, **2005**, *6*, 1788–1793.
- [40] Hutter, J. et al. Computer code CPMD, version 3.10, 1990-2005. Copyright IBM Corp. and MPI-FKF Stuttgart, <http://www.cpmd.org>.
- [41] Goedecker, S.; Teter, M.; Hutter, J. *Phys. Rev. B*, **1996**, *54*, 1703.
- [42] Hartwigsen, C.; Goedecker, S.; Hutter, J. *Phys. Rev. B*, **1998**, *58*, 3641.
- [43] Becke, A. D. *Phys. Rev. A*, **1988**, *38*, 3098.
- [44] Lee, C.; Yang, W.; Parr, R. G. *Phys. Rev. B*, **1988**, *37*, 785–789.
- [45] Allen, F. H. *Acta Crystallogr.*, **2002**, *B58*, 380–388.
- [46] Yates, J. R.; Dobbins, S. E.; Pickard, C. J.; Mauri, F.; Ghi, P. Y.; Harris, R. K. *Phys. Chem. Chem. Phys.*, **2005**, *7*, 1402–1407.
- [47] Sebastiani, D.; Parrinello, M. *J. Phys. Chem. A*, **2001**, *105*, 1951.
- [48] Sebastiani, D.; Goward, G.; Schnell, I.; Spiess, H. W. *J. Mol. Struct. (THEOCHEM)*, **2003**, *625*, 283–288.

- [49] Ochsenfeld, C.; Brown, S. P.; Schnell, I.; Gauss, J.; Spiess, H. W. *J. Am. Chem. Soc.*, **2001**, *123*, 2597–2606.
- [50] Atkins, P. W. *Physical Chemistry*, 3rd edition. Oxford University Press, 1986.
- [51] Rossano, S.; Mauri, F.; Pickard, C. J.; Farnan, I. *J. Phys. Chem. B*, **2005**, *198*, 245–7250.
- [52] Hoffmann, A.; Sebastiani, D.; Sugiono, E.; Kim, K. S.; Spiess, H. W.; Schnell, I. *Chem. Phys. Lett.*, **2004**, *388*, 164–169.
- [53] Rapp, A.; Schnell, I.; Sebastiani, D.; Brown, S. P.; Percec, V.; Spiess, H. W. *J. Am. Chem. Soc.*, **2003**, *125*, 13284–13297.

List of Figures

- 1 Structure of Alanine in the periodic crystal lattice. The $\text{NH}\cdots\text{O}$ hydrogen bond distances are shown for one of the molecules (in Ångstroms). The labeling A-C of the protons is introduced. 22
- 2 Experimental solid-state MAS and computed first principles proton NMR chemical shift spectra for Alanine in the condensed phase. Top: experimental spectrum; middle: computed spectrum in the fully periodic crystal; bottom: computed spectrum of an isolated molecule in the crystalline molecular geometry and in the optimized geometry (see text). In the computed solid-state spectra, the CH_3 and NH_3 shifts have been averaged (see text). For the labeling see figure 1. 22
- 3 Structure of Tyrosine in its periodic crystal lattice. The distances of some of the aromatic protons to neighboring aromatic moities as well as $\text{NH}\cdots\text{O}$ and $\text{OH}\cdots\text{O}$ hydrogen bond distances are shown for one of the molecules (in Ångstroms). The labeling A-G of the protons is introduced. 23
- 4 Experimental solid-state MAS and computed first principles proton NMR chemical shift spectra for Tyrosine in the condensed phase. Top: experimental spectrum; middle: computed spectrum in the fully periodic crystal; bottom: computed spectrum of an isolated molecule in the crystalline molecular geometry. In the computed solid-state spectrum, the three NH_3 proton chemical shifts have been averaged (see text). For the labeling see figure 3. 23

5	Structure of crystalline Histidine-Cl-H ₂ O. The NH···O hydrogen bond distances are shown for one of the molecules (in Ångstroms).The labeling A-G of the protons is introduced.	24
6	Experimental solid-state MAS and computed first principles proton NMR chemical shift spectra for Histidine-Cl-H ₂ O in the condensed phase. Top: experimental spectrum; middle: computed spectrum in the fully periodic crystal; bottom: computed spectrum of an isolated molecule in the crystalline molecular geometry.For the labeling see figure 5.	24
7	NMR chemical shift of the NH ₃ proton of histidine which is strongly H-bonded to the halogenid, plotted as a function of the relative electronegativity of the anion (taken from ⁵⁰).	25
8	View on the periodic structure of the adenine hydrochloride monohydrate crystal, with selected hydrogen bonds and their distances in Ångstroms. The labeling A-E of the protons is introduced.	26
9	Experimental solid-state MAS and computed first principles proton NMR chemical shift spectra for Alanine in the condensed phase. Top: experimental spectrum; middle: computed spectrum in the fully periodic crystal; bottom: computed spectrum of an isolated molecule in the crystalline molecular geometry. For the labeling see figure 8. . . .	26

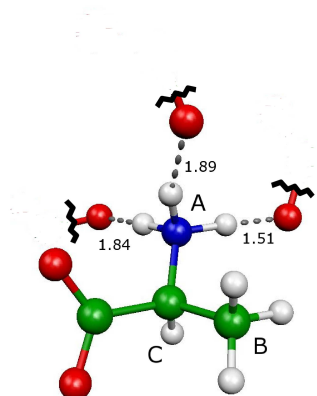


Figure 1: Structure of Alanine in the periodic crystal lattice. The $\text{NH}\cdots\text{O}$ hydrogen bond distances are shown for one of the molecules (in Ångstroms). The labeling A-C of the protons is introduced.

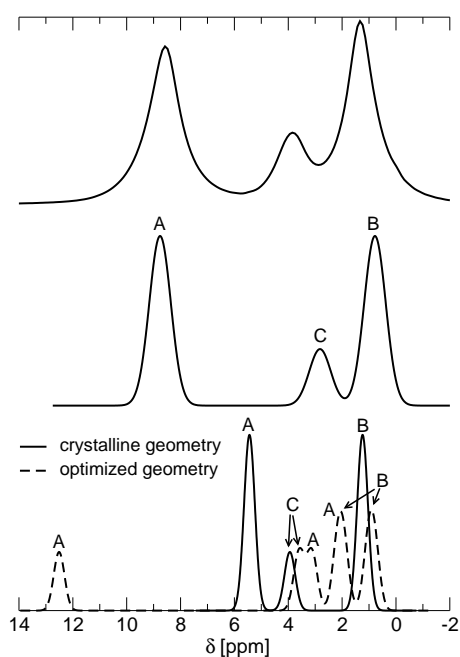


Figure 2: Experimental solid-state MAS and computed first principles proton NMR chemical shift spectra for Alanine in the condensed phase. Top: experimental spectrum; middle: computed spectrum in the fully periodic crystal; bottom: computed spectrum of an isolated molecule in the crystalline molecular geometry and in the optimized geometry (see text). In the computed solid-state spectra, the CH_3 and NH_3 shifts have been averaged (see text). For the labeling see figure 1.

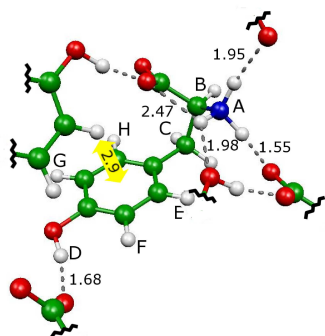


Figure 3: Structure of Tyrosine in its periodic crystal lattice. The distances of some of the aromatic protons to neighboring aromatic moieties as well as $\text{NH}\cdots\text{O}$ and $\text{OH}\cdots\text{O}$ hydrogen bond distances are shown for one of the molecules (in Ångstroms). The labeling A-G of the protons is introduced.

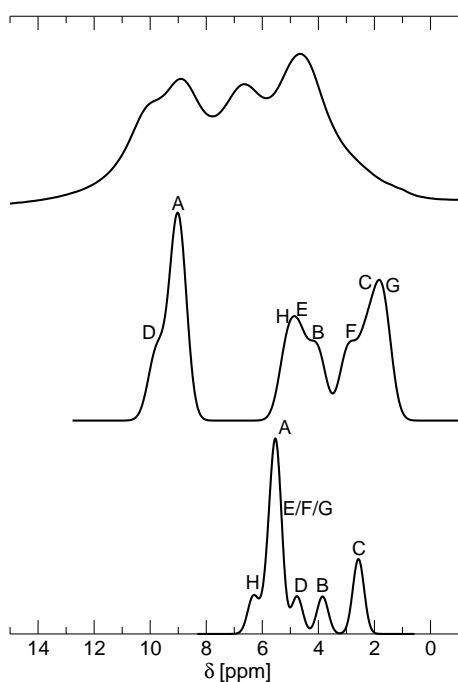


Figure 4: Experimental solid-state MAS and computed first principles proton NMR chemical shift spectra for Tyrosine in the condensed phase. Top: experimental spectrum; middle: computed spectrum in the fully periodic crystal; bottom: computed spectrum of an isolated molecule in the crystalline molecular geometry. In the computed solid-state spectrum, the three NH_3 proton chemical shifts have been averaged (see text). For the labeling see figure 3.

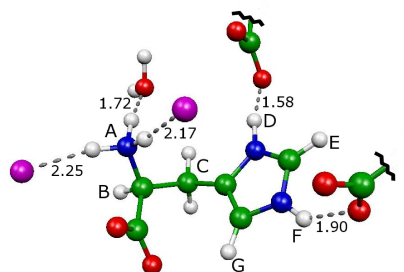


Figure 5: Structure of crystalline Histidine-Cl-H₂O. The NH...O hydrogen bond distances are shown for one of the molecules (in Ångstroms). The labeling A-G of the protons is introduced.

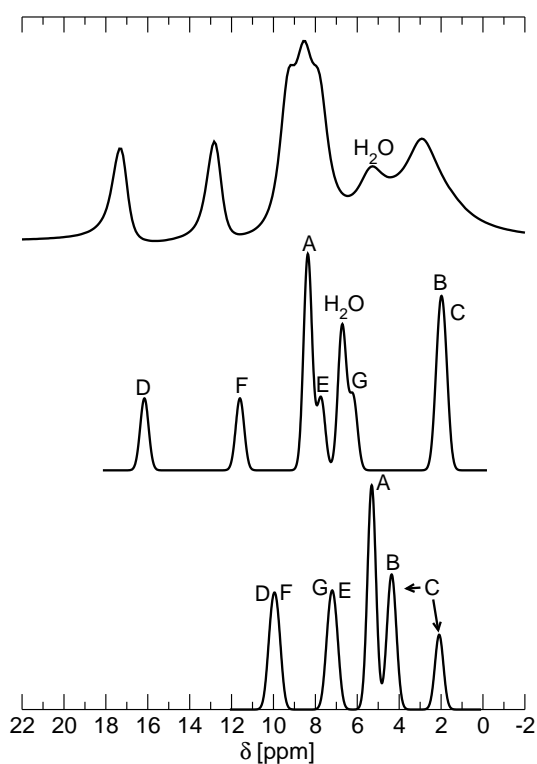


Figure 6: Experimental solid-state MAS and computed first principles proton NMR chemical shift spectra for Histidine-Cl-H₂O in the condensed phase. Top: experimental spectrum; middle: computed spectrum in the fully periodic crystal; bottom: computed spectrum of an isolated molecule in the crystalline molecular geometry. For the labeling see figure 5.

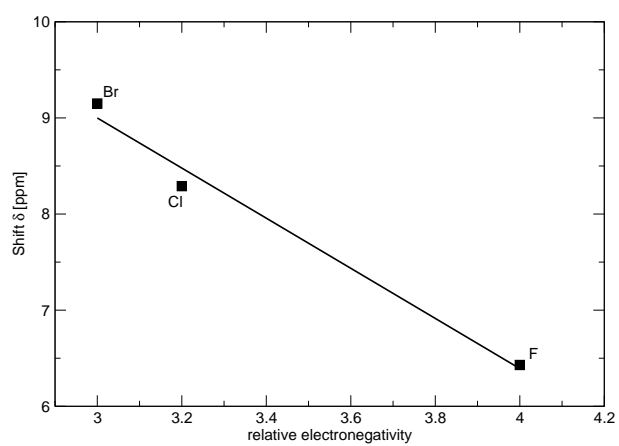


Figure 7: NMR chemical shift of the NH_3 proton of histidine which is strongly H-bonded to the halogenid, plotted as a function of the relative electronegativity of the anion (taken from⁵⁰).

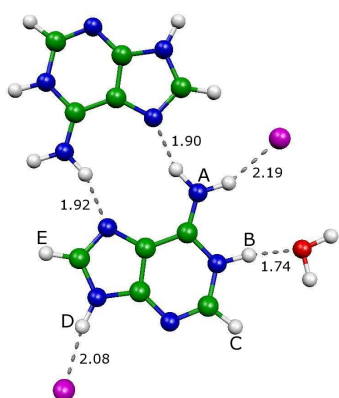


Figure 8: View on the periodic structure of the adenine hydrochloride monohydrate crystal, with selected hydrogen bonds and their distances in Ångstroms. The labeling A-E of the protons is introduced.

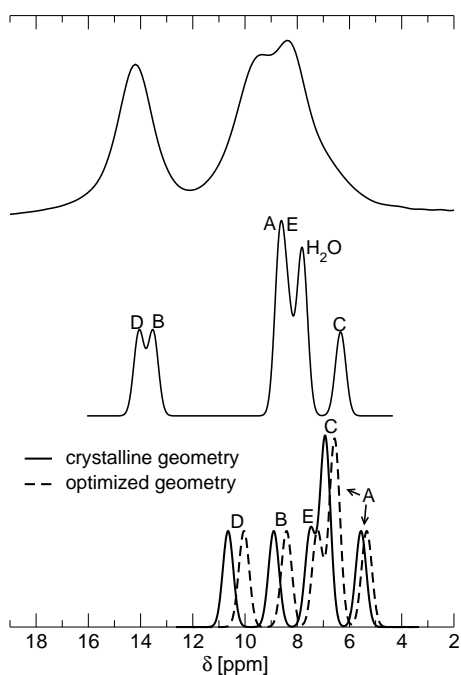


Figure 9: Experimental solid-state MAS and computed first principles proton NMR chemical shift spectra for Alanine in the condensed phase. Top: experimental spectrum; middle: computed spectrum in the fully periodic crystal; bottom: computed spectrum of an isolated molecule in the crystalline molecular geometry. For the labeling see figure 8.

High-Resolution Solid-State NMR Studies of Imidazole-Based Proton Conductors: Structure Motifs and Chemical Exchange from ^1H NMR

Gillian R. Goward, Martin F. H. Schuster, Daniel Sebastiani, Ingo Schnell, and Hans Wolfgang Spiess*

Max-Planck-Institut für Polymerforschung, Postfach 3148, D-55021 Mainz, Germany

Received: April 16, 2002; In Final Form: July 8, 2002

High-resolution solid-state ^1H NMR under fast magic angle spinning is used for the first time to study proton conductivity. The materials of interest, ethylene oxide tethered imidazole heterocycles (Imi-*n*EO), are characterized by variable temperature experiments, as well as 2D homonuclear double quantum (DQ) NMR and 2D exchange spectroscopy. Quantum chemical calculations provide a full assignment and understanding of the ^1H chemical shifts, based on a single-crystal structure obtained for Imi-2EO. Three types of hydrogen-bonded N- ^1H resonances are observed by ^1H MAS NMR at 30 kHz. Double quantum NMR experiments identify those hydrogen-bonded protons that are mobile on the time scale of the experiment, and thereby, those which are able to participate in charge transport. Characterized by their spin–spin relaxation (T_2^*) behavior, the local mobility of these protons as a function of temperature is compared to the conductivity of the materials. Homonuclear ^1H 2D DQ MAS spectra provide evidence for locally ordered domains within all the Imi-*n*EO materials. Disordered (mobile) and ordered components in Imi-2EO dramatically differ in their ^1H spin–lattice relaxation times. 2D NOESY spectra show no evidence of chemical exchange processes between the ordered and disordered domains. These results indicate that the highly ordered regions of the materials do not (or only poorly) contribute to proton conductivity, which is rather taking place in the disordered regions. Molecules in the disordered domains are in a state of dynamic or fluctuating hydrogen-bonding, allowing for Grotthuss mechanism proton transport, while molecules in the ordered domains do not experience exchange, and do not participate in long-range proton conductivity. At the interface between these regimes a small number of molecules undergo slow exchange. With increasing temperature, this exchange becomes fast on the NMR time scale, and the final chemical shift of 12.5 ppm in Imi-5EO implies the persistence of strongly and weakly hydrogen-bonded domains, which reorganize rapidly to support the proton transport process.

1. Introduction

The quest for clean portable energy sources has focused in the past decade on fuel cell technologies. In particular, the successful development of polymer electrolyte membrane fuel cells (PEM-FC) has garnered widespread interest in these types of fuel cells as a clean source of energy, potentially viable for automotive applications.^{1–3} Nevertheless, many hurdles remain, in particular, meeting the demands placed on the proton exchange membrane, which is traditionally a hydrated perfluorosulfonic polymer. To gain more flexibility with respect to the fuel source (ideally hydrogen gas, and alternatively other hydrogen-rich fuels such as methanol) or the operating temperature of the cell, and to avoid poisoning of the fuel cell catalyst by CO ,⁴ various alternatives have been proposed. These include membrane modification with inorganic particles, complexation of basic polymers with oxoacids, e.g., H_3PO_4 ,⁵ or the replacement of water with alternative choices of proton solvents, for example imidazole, pyrazole, or benzimidazole.⁶ The proton conductivity remains high in polymers saturated with such heterocycles; however, in a functioning fuel cell, which is an open system, the operating temperature must still be maintained below the boiling point of the solvent.

Motivated by this evaporation issue, a new class of materials has been designed in which proton-conducting units are tethered to a polymer backbone, yielding materials capable of operating at intermediate temperatures. In such membranes, the mechanism of proton transport must involve structural diffusion, also known as the Grotthuss mechanism, in which proton transfer between heterocycles and their reorganization dominates the proton conductivity. In hydrated polymers, by contrast, rapid proton transport occurs via the hydrogen-bonded liquid water network, i.e., by vehicle transport,⁶ which is not possible in the tethered systems due to the immobilization of the heterocycles within the membrane. The latter concept was recently demonstrated for model compounds composed of heterocycles linked pairwise to ethylene oxide oligomers.^{7,8} The chemical structure of these Imi-*n*EO materials is shown in Figure 1. These model compounds are of much smaller molecular weight than the envisaged polymeric membrane materials, but their successful synthesis and characterization demonstrated that the concept is viable, and moreover, allowed for a thorough characterization of these well-defined materials.

In this paper, we characterize the Imi-*n*EO materials by means of high-resolution solid-state ^1H NMR spectroscopy, which allows us to directly probe the protons as the nuclei responsible for conduction – the ‘workhorse’ ions in these materials. A comparison to the parent compound, pure imidazole, provides

* Corresponding author: Prof. Dr. H. W. Spiess, Tel.: +49 6131 379 120, Fax: +49 6131 379 100, E-mail: spiess@mpip-mainz.mpg.de.

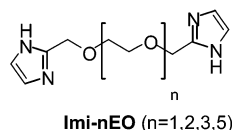


Figure 1. Chemical structure of the Imi-*n*EO compounds.

confirmation of the processes observed in the Imi-*n*EO materials. For imidazole, anisotropic conductivity has been reported and attributed to the directional H-bonding in the crystalline material.⁹ A recent ¹⁵N solid-state NMR study of this material concluded, however, that no reorientation of the imidazole rings occurs, and that therefore the previous ideas concerning ¹H conductivity in this material were poorly founded.¹⁰ Our results provide a clearer picture of these controversial findings.

2 Methods

2.1. ¹H NMR. Solid-state ¹H NMR spectroscopy exhibits attractive features for studying proton conductivity. First, the nuclei of interest can be observed directly in the NMR spectra with excellent sensitivity and resolution, because the ¹H chemical shift is indicative of the electronic environment of the individual protons (in particular, the presence of hydrogen bonds). Second, molecular mobility can be readily probed by measuring the relative strength of the ¹H–¹H dipolar interactions, which are either present at full strength in rigid molecules or reduced as a consequence of molecular motion occurring on time scales of 10 to 100 μs.¹³ To achieve spectral resolution in solid-state ¹H NMR, magic angle spinning (MAS) is applied, with the spinning frequency requirements depending on the strength of the (residual) ¹H–¹H dipolar interactions encountered in the material.¹³ For rigid ¹H systems, usually MAS frequencies of 30 kHz are used.

Initial insight into the structure as well as into the nature of the dipolar interactions present in the materials is provided by variable temperature ¹H MAS spectra, providing a snapshot of the number and comparative strength of the H-bonding interactions present. In systems where local motion is fast on the NMR time scale the spin–spin relaxation times (*T*₂), as reflected in the proton line widths,^{11,12} are related to the correlation time for the local mobility in question, in this case, proton hopping. Motional processes that are slow with respect to the NMR time scale can be detected via a coalescence phenomenon involving the resonances of the sites in slow exchange. These processes are discussed in more detail in the results section. Saturation–recovery experiments yielding longitudinal or spin–lattice relaxation (*T*₁) times further quantify the nature of the H-bonded domains and the degrees of molecular mobility.

To investigate ¹H–¹H dipole–dipole couplings more directly and specifically, two alternative experimental approaches are available, depending on the strengths of the dipolar interactions in question. Strong couplings can be used for the generation of dipolar double-quantum (DQ) coherences between pairs of protons, whose signals can then be correlated with their individual resonance signals (i.e., single-quantum, SQ, coherences) in terms of a two-dimensional DQ spectrum.¹³ Weak couplings, in contrast, tend to give rise to incoherent processes, such as dipolar cross relaxation that forms the basis for NOE experiments.¹⁴ Thus, exploiting either coherent (having a nonzero time-averaged value) or incoherent (arising from the time-dependent part of the interactions) dipolar phenomena, it is possible to distinguish between signals arising from strongly and weakly coupled nuclei, i.e., from rigid and mobile molecules in the material. Consequently, we have applied DQ experiments

to select relatively rigid components, while simple 2D NOESY-type exchange spectroscopy under MAS based on a three-pulse sequence has been used to investigate the mobile parts as well as potential interactions between mobile and rigid components.

¹H–¹H DQ MAS spectroscopy combines ¹H chemical-shift resolution and information on ¹H–¹H dipolar interactions by employing dipolar recoupling pulse sequences (such as “back-to-back”¹⁵) for DQ generation in conjunction with fast MAS for ¹H resolution enhancement.^{15,13} In such DQ spectra, the observation of individual DQ signals implies the existence (or persistence) of a dipole–dipole coupling, *D*_{ij}, between the pair of nuclei on the time scale of the experiment (typically 10 to 100 μs). Conversely, the absence of a DQ signal indicates a lack of the respective dipole–dipole coupling (approximately meaning that *D*_{ij}/2π < 2 kHz), which can either be due to long ¹H–¹H distances (typically > 0.4 nm) in the structure or due to molecular motions on time scales < 100 μs.

2.2. Molecular Dynamics and DFT-Based Calculations of NMR Chemical Shifts. Quantum chemical calculations of the ¹H chemical shift spectra of perfect single crystals of both imidazole and Imi-2EO are presented which allow a full assignment and interpretation of our experimental ¹H NMR data. The calculations are based on a recently developed formalism for NMR chemical shifts in periodic systems in the density functional theory framework.^{16,17} This method is implemented in CPMD (Car–Parrinello molecular dynamics),^{18,19} a pseudopotential-based electronic structure program using a plane-wave basis for the electronic orbitals. All calculations were done with the BLYP gradient-corrected density functional²⁰ and a plane-wave cutoff of 70 Ry. The pseudopotentials were of Martins–Trouiller type, in the Kleinman–Bylander form.²¹

For the ab initio calculation of NMR chemical shifts, it is important to have very good local geometries of the system. Initially, the ionic positions were taken from single crystal X-ray spectra. Since the positions of the hydrogen atoms are difficult to determine from X-ray scattering experiments, and also the position of the heavy atoms is subject to a finite uncertainty, a full geometry optimization was performed. All atoms were relaxed, in a fully periodic prescription, until the ionic forces decreased below 5 × 10^{−4} atomic units. As expected, the heavy atoms moved only slightly (<2 pm) with respect to their initial X-ray determined coordinates, whereas the protons shifted their positions significantly (up to 9 pm) during the optimization, showing an increase in the distances between heavy atoms and attached protons in all cases.

The calculations presented here are unique in two ways. First, the molecules of interest represent a new family of proton-conducting materials, first presented by Schuster et al. in 2001.⁷ Second, the methods developed by Sebastiani and Parrinello give calculated values of the proton chemical shifts, which can be used for direct comparison with the experimental results. Many groups, however, are engaged in probing proton mobility and hydrogen bonding using a variety of calculational methods. In particular, imidazole and imidazole-based systems have attracted a great deal of attention due their biological and technological relevance. Münch et al. have reported preliminary results of an investigation of imidazole reorientation using CPMD calculations.²²

3. Results and Discussion

Here we describe a series of experimental findings which, when combined, provide a description the microscopic processes that give rise to proton transport in the Imi-*n*EO materials. A comparison of single pulse ¹H MAS spectra to double quantum

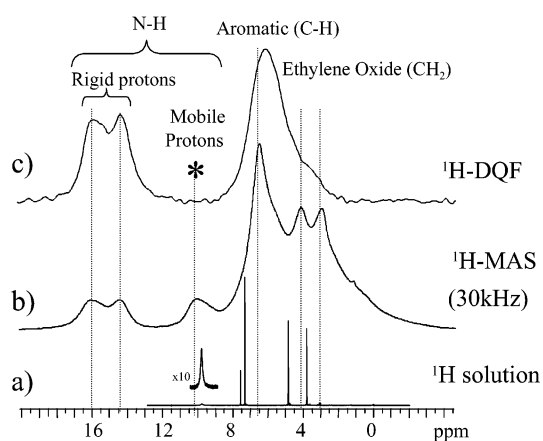


Figure 2. Comparison of ^1H spectra of Imi-1EO (a) in solution, and (b) in the solid-state, using single-pulse ^1H MAS, and (c) in the solid-state, using a 1D double quantum filtered pulse sequence.

filtered ^1H spectra allows us to distinguish mobile and rigid domains with different hydrogen bond characteristics. Variable temperature ^1H MAS spectra are used to characterize the local proton mobility via the observed line narrowing, which is compared to the macroscopic conductivity measurements in crystalline (Imi-1EO) and glassy (Imi-5EO) samples. Possible exchange between mobile and rigid domains is probed via spin-lattice relaxation, 2D exchange NMR, and ^1H chemical shifts as a function of the temperature.

Crystalline Imi-2EO and imidazole are more thoroughly studied, including DFT-based chemical shift calculations, to fully assign the ^1H resonances of the ordered and disordered domains.

3.1. ^1H MAS and DQ Spectra of Imi-*n*EO. It is well-established that the structures of materials in the solid state can differ dramatically from solution conformations, and moreover, that these differences have marked effects on the NMR spectra of the materials.²³ Such effects are particularly notable for structures that include aromatic groups and hydrogen bonds, where π - π packing effects and hydrogen-bonding arrangements may be manifest exclusively in the solid state. Because ^1H chemical shifts are very sensitive to hydrogen bonding and ring current effects, high resolution ^1H MAS NMR is well suited to detect such structural change.²³ Due to the imidazole substituents, the Imi-*n*EO materials under investigation are capable of exhibiting both these phenomena. Three ^1H NMR spectra of Imi-1EO are shown in Figure 2: a solution-state spectrum, a solid-state MAS spectrum obtained at 30 kHz MAS, and a 1D DQ-filtered spectrum. Immediately apparent are the differences between the N-H resonances observed in the region of hydrogen-bonded protons, above 9 ppm. In dilute solution, a single N-H resonance at 9 ppm is found (Figure 2a), indicating very weak, if any, hydrogen bonding. In the solid-state, in contrast, three N-H resonances occur, two of which are shifted significantly downfield to 14.5 and 16 ppm. In principle, such a change in resonance frequency is expected for molecules forming multiple types of hydrogen bonds in the solid polycrystalline material.²⁴ Two such low-field N-H peaks in the range of 12 to 16 ppm are found for all Imi-*n*EO samples investigated in this study. More remarkable, however, is the comparison of the MAS and DQ-filtered spectra, because in the latter, one of the three N-H resonances is eliminated by the DQ-filtration procedure. Therefore, the resonance at 10 ppm is attributed to "mobile" protons, whose dipolar interactions are significantly reduced by molecular motions, while the reso-

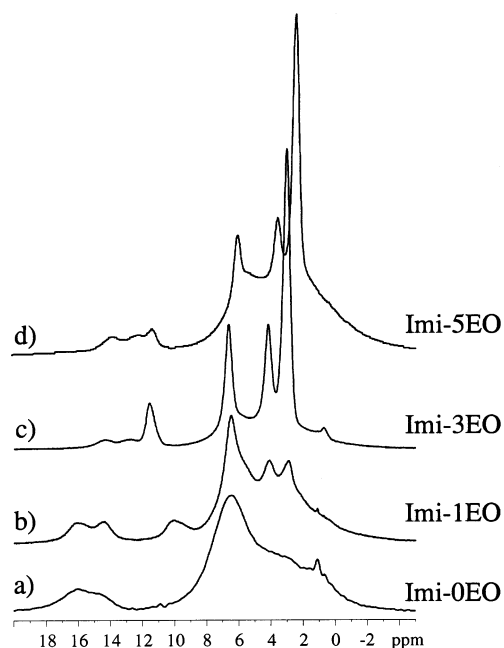


Figure 3. ^1H MAS spectra of Imi-*n*EO: (a) Imi-0EO, (b) Imi-1EO, (c) Imi-3EO, (d) Imi-5EO, acquired at 30 kHz spinning, and averaged over 16 transients.

nances at higher frequency (14.5 and 16 ppm) are assigned to "rigid" protons involved in strong hydrogen bonds. This interpretation is confirmed by quantum-chemical NMR shift calculations based on single-crystal structural data (*vide infra*). The resonance attributed to mobile N-H protons occurs at a frequency much closer to that of the solution state N-H resonance than the "rigid" N-H resonances, which suggests that this proton is in a more "free" state of fluctuating hydrogen bonding, as opposed to participating in a strong hydrogen bond. Apart from this N-H resonance, the relatively narrow features in the aromatic and aliphatic regions of the MAS spectrum (Figure 2b) are also removed by the DQ filter (Figure 2c), while the broader underlying features remain. It thus appears that the mobile protons are associated with mobile molecules, whose entire ^1H signal is removed using the DQF experiment. The Imi-1EO material therefore consists of, at least, two components with significantly different motional properties.

Similar behavior is observed for all of the Imi-*n*EO materials investigated in this study. Figure 3 provides the 1D ^1H spectra of the Imi-*n*EO materials acquired under 30 kHz MAS. At ambient temperature, the relative line width of the ethylene oxide ^1H resonances decreases with increasing oligomer chain length. This demonstrates the increasing mobility of the chains, as the influence of the hydrogen-bonded imidazole rings is reduced with a proportionally increased concentration of the ethylene oxide. Congruent results were obtained from differential scanning calorimetry (DSC) measurements, which showed that the T_g decreases with increasing *n*.²⁵ The presence of the "mobile" resonance is found to be temperature dependent (*vide infra*), but in all cases, when present, it is removed by the DQ sequence. This illustrates that its mobility is maintained, even when small concentrations of the mobile species are present. The time scale of the DQ experiment used here is two rotor periods, or 66 μs , thus the local proton motion must occur at least that rapidly in all cases.

3.2. ^1H MAS Variable Temperature Studies and Correlation to Conductivity. To investigate the temperature dependence of the hydrogen-bonded ^1H resonances, variable temperature (VT) studies were carried out in the temperature range

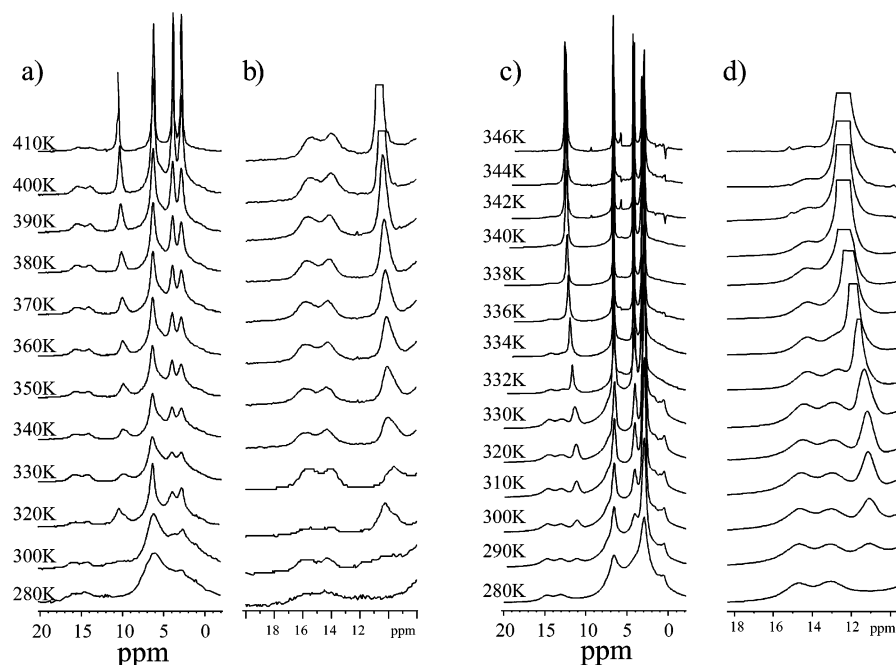


Figure 4. ^1H variable temperature MAS spectra for (a) Imi-1EO and (c) Imi-5EO acquired at 30 kHz spinning, and averaged over 64 transients. Expansions of the hydrogen-bonding regions for Imi-1EO and Imi-5EO are given in (b) and (d), respectively.

280–410 K under MAS at 30 kHz (corrected from the bearing gas temperature, to account for heating induced by high-speed MAS).²⁶ The VT ^1H NMR spectra of Imi-1EO and Imi-5EO are shown in Figures 4a and c, respectively. As expected, a continuous narrowing of the resonance lines is observed as the temperature is increased. For polycrystalline Imi-1EO ($T_m = 425$ K), the melted phase is not quite reached at 410 K, but melting is clearly expected right above the range accessible with our MAS NMR experiments. The melting process is accompanied by the disappearance of the signals of the strongly hydrogen-bonded N–H protons at 14.5 and 16 ppm. The presence of the third N–H resonance around 10 ppm is temperature dependent, indicating that the mobility of the proton is induced by temperature and that this mobile species is frozen out at low temperatures. This effect was also observed for Imi-0EO, in which case the mobile N–H proton signal did not appear until 350 K, and subsequently increased in relative intensity with increasing temperature.

Considering the temperature-dependent behavior of the N–H resonance at 10 ppm in the polycrystalline material, Imi-1EO, (Figure 4a), several trends are observed. First, the line narrows with increasing temperature, and second, the chemical shift of this proton resonance trends toward higher frequency with increasing temperature, exhibiting an overall shift difference of 0.8 ppm between 330 and 410 K. The gradual shift and the high-temperature limit of this resonance at 10.8 ppm indicate the formation of a hydrogen-bonding network in the disordered, mobile phase, since the respective signal occurs at only 9 ppm in dilute solution. The intensity of the strongly hydrogen-bonded N–H proton signals remains relatively unchanged between $T = 290$ and $T = 400$ K, but is then reduced on going to the highest temperature investigated (410 K). Although this is still below the melting point at 425 K, molecular mobility already increases in the material at this temperature and the line width of the N–H resonance is subsequently reduced. This interpretation is corroborated by the analogous study of Imi-5EO discussed below, where the melting temperature falls within the range of accessible temperatures. Closer examination of the N–H line width reveals a linear temperature dependence of the spin–

spin relaxation time (characterized by the effective transverse relaxation time, T_2^*), as plotted versus $1/T$ in Figure 5a. The observed N–H resonance therefore arises from molecules in the fast exchange limit, such that the line shape is described by a Lorentzian, centered at ω , with $\Delta\nu_{\text{fwhm}} = 1/\pi T_2^*$. The fast exchange limit is defined as $\tau_C < 10^{-7}$ s, and $\Omega^2 \gg \Delta^2$, where τ_C is the correlation time of the motion, Ω is the exchange rate ($\tau_C = 1/2\Omega$), and Δ is the frequency difference between the two sites undergoing exchange.²⁷ To estimate the jump rate we assume a simple two-site exchange process, with a maximum Δ of 3.5 kHz, or 5 ppm (the difference between the solution state N–H resonance and the average strongly hydrogen-bonded ^1H resonance frequencies), although we were unable to resolve the slow-exchange limit due to the broadening and overlap of the aromatic resonance at low temperature. The line narrowing as a function of temperature for spins in fast exchange is correlated with the exchange rate, or equivalently, the inverse of the correlation time.

Accurately described by Arrhenius activation,

$$\frac{1}{\tau_C} \propto \Omega = \frac{1}{\pi T_2^*} = \Omega_0 \exp\left(-\frac{E_A}{RT}\right) \quad (1)$$

the behavior of T_2^* as a function of temperature follows an Arrhenius relation in the temperature range investigated. From this relation of the correlation time to temperature, we obtain an activation energy of 48 kJ/mol for proton mobility on a local scale. The exchange rate, Ω , for this process increases by an order of magnitude in the temperature range investigated here.

The temperature dependence of the conductivity in a polycrystalline pellet of Imi-1EO is also described by the Arrhenius relation,

$$\sigma = \sigma_0 \exp\left(-\frac{E_A}{RT}\right) \quad (2)$$

with σ , in S/cm replacing Ω , obtained from NMR. Conductivity data for a pressed pellet of Imi-1EO is plotted in Figure 5b.

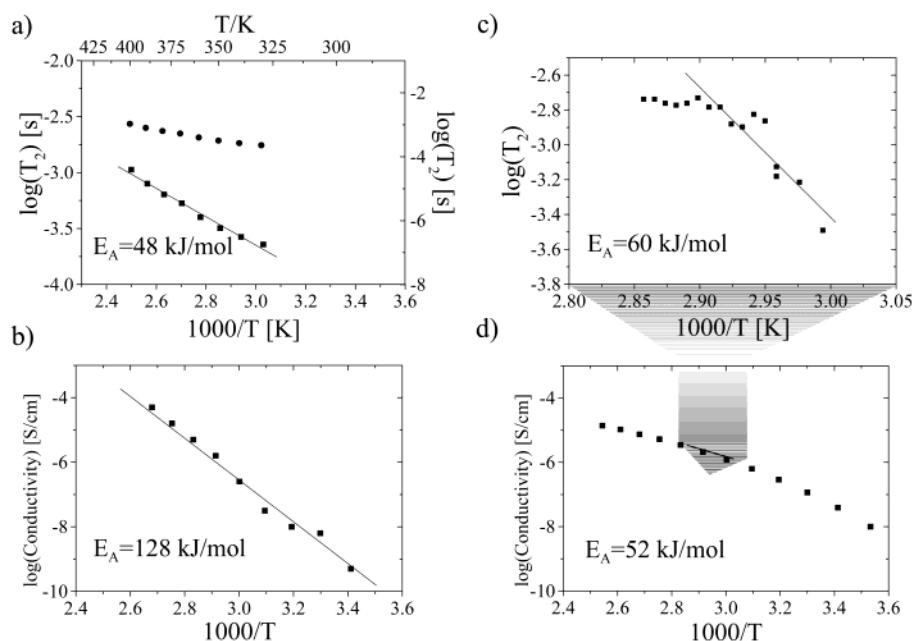


Figure 5. Comparison of temperature-dependent transverse relaxation behavior of mobile ^1H resonance, T_2^* , and conductivity measurements. (a) T_2^* data for polycrystalline Imi-1EO, plotted on two y axes: the left axis corresponds to the squares, and the right axis to the circles. The right axis is chosen for ease of comparison with the corresponding conductivity data, shown below in (b). (c) T_2^* data for glassy Imi-5EO and (d) corresponding conductivity data. Activation energies were determined by fitting the data to Arrhenius functions, as described in the text.

Such data represents a macroscopic measure of charge transport in this polycrystalline material. A much higher activation energy of 128 kJ/mol is obtained.

The Arrhenius-type temperature dependence of the microscopic scale proton mobility exhibits the same trend as that observed for the conductivity of Imi-1EO. That these processes follow the Arrhenius relation is consistent with the polycrystalline nature of the Imi-1EO sample. The respective activation energies, however, differ by roughly a factor of 3. This difference in micro- and macroscopic activation energies for proton mobility is addressed again below, where we determine that only the disordered, mobile fraction of the samples contributes to proton conductivity. The lower activation energy determined for proton hopping within this fraction of the sample is consistent with our picture of proton transport, which is facile in the disordered, mobile domains, but inhibited in strongly hydrogen-bonded domains. The significantly larger activation energy for macroscopic proton transport in this polycrystalline sample clearly demonstrates that processes in addition to the local mobility described by T_2 contribute to the conductivity measurements. This gives rise to two intriguing questions. First, what is the local exchange process detected by NMR, and second, what additional processes influence macroscopic conductivity?

In the case of the glassy material, Imi-5EO ($T_g = 249$ K, $T_m = 341$ K), more substantial changes in the VT ^1H MAS NMR spectra, shown in Figure 4c, are observed. Here, the temperature is varied initially in 10 degree steps, and then in fine increments of 2 K between 326 and 350 K. This range covers the melting process, which occurs at 341 K and is clearly indicated (i) by the variation of the line widths of the aliphatic and aromatic C–H resonances toward a final narrow limit and (ii) by the disappearance of the ^1H resonances at high frequency (at 13 and 15 ppm), assigned to strongly hydrogen-bonded protons. Hence, strong hydrogen bonds are absent in the disordered phase, but present at low temperature, regardless of the glassy (Imi-5EO) or polycrystalline (Imi-1EO) nature of the material. Furthermore, the low-field N–H resonances are affected neither

by the thermal history of the sample nor by the EO chain length (indicated by n in Imi- n EO), because an analogous pair of strongly hydrogen-bonded ^1H resonances has been observed for all Imi- n EO materials. This indicates that the pure materials achieve a local ordering of their H-bonds, irrespective of their thermal history or their ethylene oxide chain length. At low temperatures, the third resonance, assigned to the mobile proton species, is broadened and disappears under the two high-frequency N–H resonances of the glassy Imi-5EO. With increasing temperatures, however, the resonance clearly emerges, corresponding to the increasing degree of mobilization while approaching the melting temperature. In principle, the same behavior was observed for the polycrystalline Imi-1EO, though spread over a broader temperature range. Interestingly, the resonance of the mobile proton shifts again toward higher frequency with increasing temperature, beginning at 11.5 ppm and reaching a plateau at 12.5 ppm, at a temperature of 345 K. The final shift of this resonance is higher than that observed in solution, indicating again that a degree of hydrogen-bonding character is retained in this phase, which can be envisaged as mobile molecules that rapidly break and reform hydrogen bonds. Such a mechanism is well known also from other liquid systems, in particular liquid water.²⁸ With respect to proton conduction, this residual hydrogen bonding provides a means by which structural diffusion may take place.

In Figure 5c, the spin–spin relaxation times of the weakly hydrogen-bonded protons are plotted as a function of temperature. The data are compared to the conductivity measurements for this sample (Imi-5EO), shown in Figure 5d. In this case, the conductivity is not described by an Arrhenius activated process, but rather exhibits a Vogel–Fulcher–Tamman (VFT)-type temperature dependence, indicating that segmental motion plays a role in charge transport.^{3,7,29} This temperature dependence is described by the following equation:

$$\sigma = A_T \exp\left(-\frac{B}{T - T_0}\right) \quad (3)$$

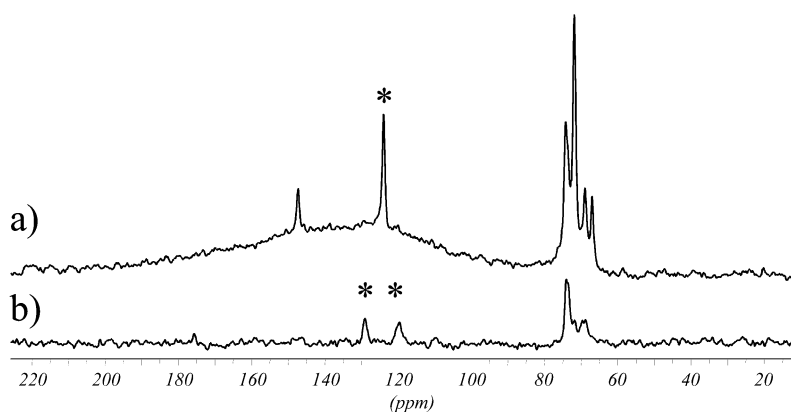


Figure 6. Imi-3EO (a) ^{13}C 1D MAS and (b) ^1H - ^{13}C CP-MAS: contact time = 3 ms, spinning speed = 30 kHz. Peak positions of basal ^{13}C resonances are marked with asterisks – the motionally averaged position observed in (a), and the two resolved resonances, observed for rigid molecules in (b).

in which the glass transition, T_g , is an empirically determined factor, generally $T_g + 50$ °C. This parameter takes into account the cooperative motion of the chain segments that influence the molecular-scale mobility. In the limited temperature range accessible for our NMR experiments we observe an initial narrowing of the line shape with increasing temperature, followed by a plateau value, reached at high temperature, which represents the inherent line width of this ^1H resonance, beyond which point the line shape is no longer dominated by anisotropic broadening that would be averaged by molecular motions. Analysis of the initial slope using a simple Arrhenius relation provides a rough estimate of the activation energy of approximately 60 ± 10 kJ/mol. In the narrow temperature range accessible by NMR, the conductivity data is accurately estimated by a linear Arrhenius function, with a corresponding activation energy of 52 ± 5 kJ/mol. The determined energies for the macroscopic proton transport and microscopic proton mobility are in much closer agreement in this glassy sample; considering the experimental accuracy, essentially identical. This points to the conclusion that large, ordered domains significantly impede long range proton transport in the polycrystalline material while having less influence in the glassy material, where locally ordered domains are presumed to be much smaller.

In answer to the first question posed, we assign the local exchange process in the weakly hydrogen-bonded domains to rapidly fluctuating hydrogen bonds among mobile molecules. This assignment is supported both by the chemical shift of the protons in these disordered domains, which is significantly downfield relative to the solution state resonance, and by the line narrowing as a function of temperature, which is consistent with a fast exchange process. The trend of this N–H resonance toward higher frequency with increasing temperature is, however, unaccounted for, and is inconsistent with a single fast exchange process. In the case of a single fast exchange process between a “free” and “bonded” state, above coalescence, the chemical shift should tend to lower frequency, as the concentration of free molecules is favored by higher temperatures.³⁰ The fact that the opposite trend is observed in both Imi-1EO and Imi-5EO necessitates a more thorough understanding of the processes at play. We will probe this feature in more detail in section 4.1.

Additional evidence that the Imi-*n*EO materials comprise a mixture of ordered and disordered components was obtained from a ^{13}C study of Imi-3EO. In the imidazole rings, the two (nonapical) carbons have inequivalent chemical shifts, because

only one of the two nitrogens is protonated. ^1H - ^{13}C cross-polarization (CP) MAS as well as conventional single-pulse MAS spectra were recorded (Figure 6). The CP MAS technique requires ^1H - ^{13}C dipolar interactions to persist in order for the polarization transfer from the protons to the carbons to occur. Thus, the signal of ordered molecules dominates in the CP MAS spectra and, as expected from the molecular structure, a pair of resonances was observed at 117 and 127 ppm. Standard single-pulse ^{13}C NMR spectra, in contrast, gave rise to a single resonance in the aromatic region at 122 ppm, which represents the average resonance frequency of the signals at 117 and 127 ppm. This coalescence phenomenon is due to a rapid reorientation of the imidazole rings taking place in the disordered component of the sample. In the single-pulse spectra, the ^{13}C signal of the rigid component is suppressed due to its unfavorably long spin–lattice relaxation time.

The 1D ^{13}C and ^1H NMR spectra indicate the presence of both rigid, ordered and mobile, disordered domains, and the ^1H line shapes of the mobile protons can be correlated with the conductivity measurements. No evidence is yet available to indicate whether the ordered domains participate in charge transport. This fundamental question refers back to the issue of charge transport in crystalline imidazole, and it is therefore highly relevant. We address this possibility later using 2D NMR measurements.

3.3. Studies of Crystalline Imi-2EO. To establish a thorough understanding of solid-state ^1H MAS NMR spectra of proton conductors and to provide a basis for the investigations, we proceed with the assignment and a more detailed interpretation of the spectra recorded on a crystalline sample of Imi-2EO. This particular material was chosen because it is the only one among the Imi-*n*EO samples where a single crystal could be successfully prepared and studied by X-ray diffraction. Figure 7 schematically depicts the critical features of the crystal structure, together with an excerpt from the crystal structure, showing two pairs of Imi-2EO molecules. Crystalline Imi-2EO is composed of pairs of molecules, linked to each other and to other pairs via N–H–N hydrogen bonds. Correspondingly, two types of hydrogen-bonding protons are identified, namely intrapair and interpair protons. By comparing the experimental ^1H MAS spectrum of crystalline Imi-2EO (shown in Figure 8a) to a calculated ^1H spectrum based on the crystal structure (Figure 8c), these two types of protons are assigned to the pair of low field ^1H NMR resonances occurring in this sample at shifts of 16.4 and 15.0 ppm. The calculation was performed after a

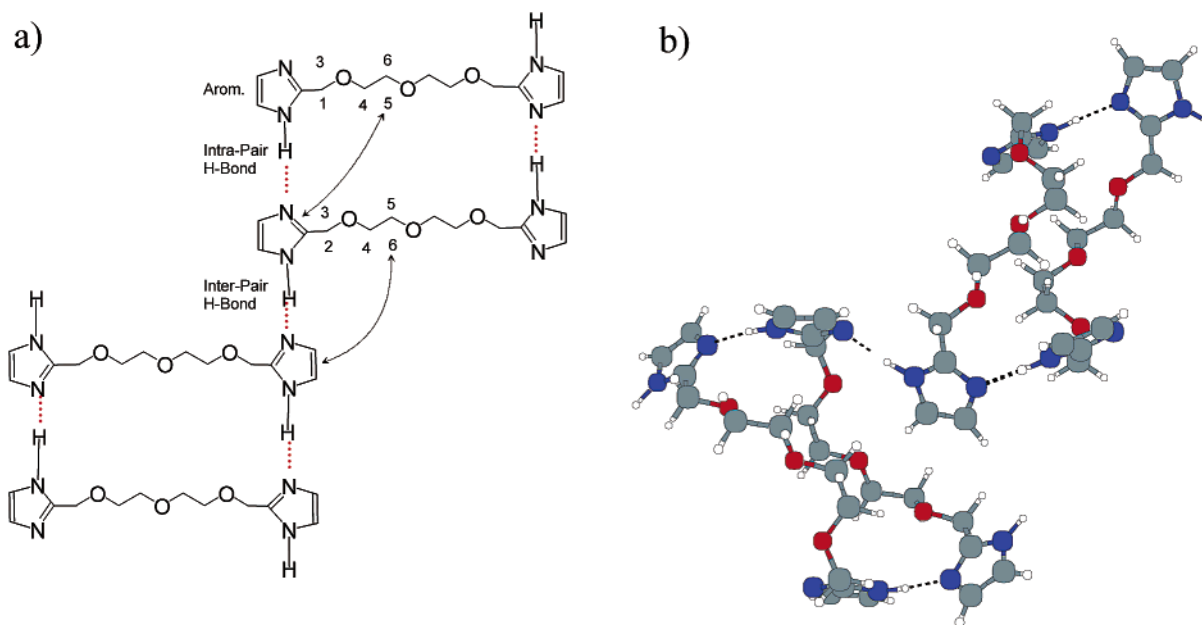


Figure 7. (a) Molecular structure of paired Imi-2EO molecules and (b) segment of crystal structure of Imi-2EO. Labels are placed in crystal structure to depict the positions of the protons according to the assignments determined from the CPMD-DFT calculations of the ^1H resonance frequencies.

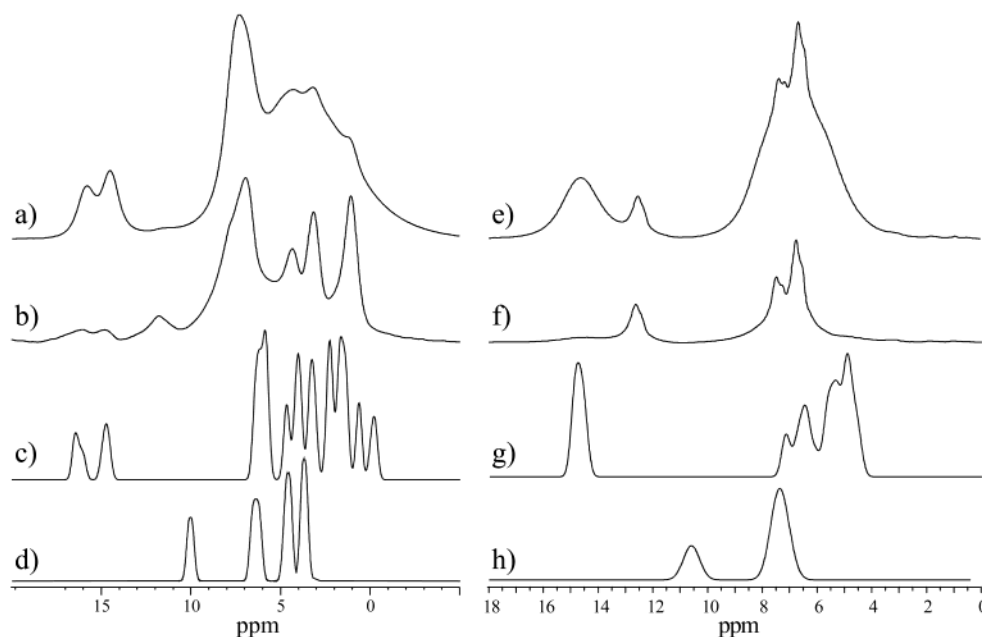


Figure 8. Experimental and calculated ^1H NMR spectra of Imi-2EO (a–d) and imidazole (e–h). Panels (a, e) give ^1H MAS spectra at 30 kHz MAS, 60 s and 5400 s recycle delays, respectively. Panels (b, f) give experimental ^1H MAS spectra at 30 kHz MAS, 3 s recycle delays. Panels (c, g) give CPMD-DFT calculated ^1H NMR spectra for periodic structures, and panels (d, h) give CPMD-DFT calculated ^1H NMR spectra for single molecules.

geometry optimization of the atomic positions using a simulated annealing technique within a Car–Parrinello molecular dynamics simulation. The subsequent chemical shift calculations were done using these relaxed geometries, maintaining the full periodic structure.

Calculations were performed in two ways, namely with all atoms of the fully relaxed crystal, and with only protons fully relaxed, which gave rise to chemical shifts that agree up to a maximum difference of 0.5 ppm. In addition to the resonance assignments, the simulated spectrum provides many detailed insights into the correlation between molecular structure and the ^1H spectrum. The differences between the chemical shifts of the strongly hydrogen-bonded protons, for example, are

attributed to the differing N–H distances for the two interactions ($N-N_{\text{intra}} = 2.83 \text{ \AA}$ and $N-N_{\text{inter}} = 2.87 \text{ \AA}$) with the shorter distance corresponding to the higher frequency ^1H resonance. Furthermore, the broad resonances at high field in the experimental spectrum are also present in the calculated spectrum and arise from protons on the ethylene oxide backbone which experience ring-current effects due to their orientation with respect to the imidazole rings. This effect has been observed before in aromatic systems, for example hexabenzocorenes,³¹ and molecular tweezers.³² Table 1 classifies the experimental and calculated ^1H chemical shifts for solid Imi-2EO, according to their positions in the Imi-2EO molecule as indicated in Figure 7a, and in their 3D packing geometry. Also, the absence of any

TABLE 1: Comparison of Calculated and Experimental ^1H Chemical Shifts in Crystalline Imi-2EO, Assigned According to the 3D Packing Geometry, and Labelled as In Figure 7

	proton description	calcd ^1H shift (ppm)	expt. ^1H shift (ppm)
	H-bonded intrapair N—H \cdots N	16.5	16.0
	H-bonded interpair N—H \cdots N	15.0	14.7
	Aromatic protons	6.0–6.7	7.1
	Ethylene-oxide protons		
1	Bonded to first carbon after the imidazole ring with intrapair H-bond and in-plane with the ring	5	4.2
2	Bonded to first carbon after either imidazole ring, pointing “away” from molecule	4	3.0–4.0
3	Bonded to first carbon after the imidazole ring with inter-pair H-bond, in-plane with the ring	3.3	
4	Bonded to second carbon after the imidazole ring in-plane with the ring and pointing in the same direction as the NH of that ring	3.3	
5	Bonded to third carbon after the imidazole ring, pointing into the partner molecule’s ring, but not exactly centered relative to that other ring	1.0	1.0 and 0.0–1.0 (broad)
6	Bonded to third carbon after the imidazole ring, pointing into a ring of the other dimer. The proton is located <i>directly</i> in the center of the ring	0.0	

^1H resonance in the region of 9–12 ppm in the computed perfect single crystal confirms the conclusion that this resonance in the experimental spectrum arises from disordered, mobile protons. The X-ray structure was collected at low temperature (120 K), where any motion would be frozen out. A comparison to the calculated ^1H spectrum of a single molecule of Imi-2EO in the gas phase (Figure 8d) clearly demonstrates that the resonance of the mobile protons occurs at an intermediate chemical shift consistent with the persistence of weak, fluctuating H-bonds in the disordered mobile phase.

In the following sections we demonstrate that this hydrogen-bonding motif is recurrent among the various Imi-*n*EO materials. The pattern is characterized structurally by linked pairs of Imi-EO molecules, associated through intrapair and interpair hydrogen bonds between the imidazole rings, and spectroscopically by pairs of high-frequency ^1H NMR resonances.

3.4. Relaxation Behavior: Imi-*n*EO and Imidazole. For Imi-2EO, Imi-5EO, and imidazole itself, a dramatic difference between the spin–lattice relaxation behavior of the ordered and disordered components was observed. Shown in Figure 8a and 8b are experimental single-pulse ^1H spectra of crystalline Imi-2EO, averaged over 16 transients, with recycle delays of 3 and 60 s. A saturation recovery experiment at 330 K yielded T_1 values of 0.75 and 140 s for the mobile and rigid component of Imi-2EO, respectively. The spin–lattice relaxation times in a typical glassy sample of Imi-5EO also differ greatly between the ordered and disordered components. This was quantified for a sample that had been thermally tempered in the same manner as that used to prepare the materials for conductivity studies, namely heating into the melt state, and then cooling at a rate of approximately 1 K/min. While this treatment did not result in a crystallization process that was detectable via DSC,²⁵ nevertheless, strongly hydrogen bonded moieties are formed, as identified by their distinctive ^1H chemical shifts. Spin–lattice relaxation times of 0.7 and 25 s were determined for the mobile and rigid components, respectively. Using these values to calculate the corrected relative intensities, it is found that only a small portion of the materials exist in the free or mobile state at 330 K. The relative proportions are 5% disordered, 95% ordered in Imi-1EO and 10% disordered, 90% ordered in Imi-5EO at ambient temperature. As is clear from the variable temperature ^1H NMR data, this ratio is strongly temperature dependent. This can be seen from the dramatic change in relative

populations of mobile and rigid components induced by a temperature increase. In Imi-5EO, assuming a negligible change in T_1 , following equilibration after a small temperature change of two degrees, 62% of the molecules are disordered.

In a parallel study of imidazole itself, it was established that a high purity sample, packed in an inert atmosphere, and measured at 330 K (significantly below the melting point of 363 K), comprised both mobile, or disordered and ordered components, as well. These disordered and ordered components are similarly characterized by differing $^1\text{H}(\text{N})$ chemical shifts and differing spin–lattice relaxation times. Figures 8e and 8f show the ^1H spectra for two recycle delays, of 1.5 and 5400 s. A comparison of the calculated spectra of a periodic structure based on the imidazole crystalline lattice versus a single imidazole molecule (Figure 8g and 8h respectively) supports this finding.¹⁷ The percentage of the disordered component is more substantial in this sample at ambient temperature (18%), and the T_1 values are similarly disparate, with a rapid relaxation time of 0.5 s for the disordered component, compared to an extremely slow relaxation time with a minimum value of 90 s for the ordered component.

This T_1 data for crystalline imidazole sheds light on the results of a previous ^{15}N 2D exchange NMR study, in which a lack of reorientation of the imidazole rings was observed. This observation led to the conclusion that proton conductivity could not take place via the broadly purported Grotthus mechanism, since the rings do not reorient on a time scale of up to several seconds.¹⁰ However, the cross polarization pulse sequence employed necessarily selected only ordered molecules capable of transferring magnetization from ^1H to ^{15}N via a sustained dipolar coupling. As we have demonstrated in the Imi-*n*EO and other samples, the dipolar couplings of the disordered, mobile molecules are averaged on the time scale of a cross polarization or a double quantum filtering sequence. Thus, by their nature, the experiments chosen did not lend themselves to successful observation of proton conductivity in imidazole. Our ^1H spin–lattice relaxation data together with preliminary ^{15}N direct detection experiments demonstrate that mobile species, most likely defects present in the crystalline material, must be invoked to account for the unusual conductivity of these materials. Proof of the nature of the interaction between the ordered and disordered domains has been elusive, primarily due to their

disparate spin–lattice relaxation times; however, further ^{15}N studies together with calculations are ongoing.

An early study of charge transport in crystalline imidazole established that anisotropic conductivity is observed. In a large single crystal of imidazole a conductivity of 10^{-11} S/cm was measured in the *c* direction, parallel to the hydrogen-bonding direction, which is a factor of 10^3 greater than the conductivity measured in the orthogonal directions. Therefore, this anisotropic conductivity has been attributed to the Grotthus mechanism of charge transport, with the rate limiting step being the ring reorientation. While the observed conductivity is indeed anisotropic, the absolute value of the conductivity is very low and could plausibly be attributed to defects that migrate through the structure along the hydrogen bonded network. A significantly higher macroscopic conductivity of 10^{-6} S/cm at the equivalent temperature is achieved in a polycrystalline pressed pellet sample.^{9,29} Recalling that the conductivity is related to the number of charge carriers (*n*), their charge (*q*), and their mobility (μ),

$$\sigma = nq\mu \quad (4)$$

and surmising that the number of charge carriers is directly related to the number of defects, this discrepancy between the conductivity of a single crystal compared to a polycrystalline sample confirms the hypothesis that defects facilitate the charge transport.

3.5. 2D DQ NMR Spectra: Evidence for Local Order in Imi-*n*EO Samples. The strongly hydrogen-bonded portions of crystalline or glassy samples, of the Imi-*n*EO materials can be selectively investigated using ^1H – ^1H DQ NMR spectroscopy, since the generation of dipolar DQ coherences requires the existence (or persistence) of relatively strong ^1H – ^1H dipole–dipole couplings. Such DQ spectra are shown in Figure 9 for three Imi-*n*EO materials (*n* = 1, 2, 5). The dominant features in the upper right corners of these spectra arise from the dipolar couplings among the CH_2 groups of the ethylene oxide units, and therefore provide little relevant information. The relative intensity of this region increases in the sequence *n* = 1, 2, 5, corresponding to the increasing length of the EO bridge. The lower left corner of the DQ spectra sheds light onto the hydrogen bonds formed by the Imi-*n*EO molecules. The absence of peaks along the diagonal at the N–H resonance (i.e., between 12 and 16 ppm in the SQ dimension, and between 24 and 32 ppm in the DQ dimension) indicates that the strongly hydrogen-bonding NH protons are not close in space to each other in any of the materials. Rather, these two types of NH protons only show DQ signals with aromatic CH protons (between 17 and 23 ppm in the DQ dimension), which are clearly expected due to the proton–proton distance of 0.25 nm at the imidazole ring. In addition, there are no DQ signals indicating spatial proximities between NH protons and the protons of the EO linking chain. These observations confirm that, within this family of materials, the imidazole rings form a hydrogen-bonded structure that is based on single and spatially separated $\text{N–H}\cdots\text{N}$ bridges, as found in the crystal structure of Imi-2EO and shown schematically in Figure 7. The NH protons of the imidazole rings do not interact closely with the EO linker units, but rather form a hydrogen-bonded structure among themselves. These structural features are clearly evident in the crystal structure of Imi-2EO,³³ which strongly supports the interpretation of the DQ spectra. Since all DQ spectra acquired for the other Imi-*n*EO samples (*n* = 0, 1, 3, 5) exhibit the same principal features, although no crystal structures are available, the same basic structure can be assumed. This demonstrates that, even in the absence of long-

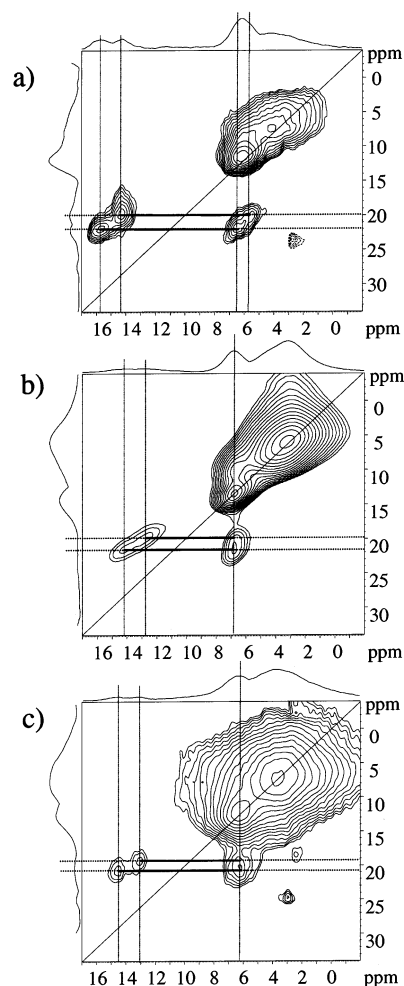


Figure 9. 2D Double quantum filtered spectra of (a) Imi-1EO at RT, (b) Imi-2EO at 250 K, and (c) Imi-5EO at 250 K.

range order in glassy Imi-*n*EO materials, the highly ordered arrangement of hydrogen bonds is adopted as a local structure in short-range ordered domains. Such local order is already evidenced in the ^1H NMR spectra of all of the samples studied, in which the presence of a pair of resonances at high frequency is observed that is assigned to the strongly H-bonded protons.

3.6. 2D Exchange Spectroscopy. After an investigation of the structure of the strongly hydrogen-bonded crystalline components using dipolar DQ NMR, we now turn to a more general experiment which probes both the ordered and disordered mobile components, and possible interactions between the two. Here we apply the straightforward three-pulse ^1H – ^1H exchange experiment.¹⁴ For Imi-2EO at 330 K, such a 2D exchange spectrum with a mixing time of 50 ms, shown in Figure 10, exhibits various off-diagonal peaks. None of these, however, can be attributed to exchange processes occurring between the ordered and the disordered portions of the material; rather, the contacts are restricted to the ordered or disordered portions, respectively. This demonstrates that there is minimal contact between the two components of the material, and is consistent with the vastly differing T_1 relaxation times established for these components.

Focusing on the disordered portions, the ^1H – ^1H exchange spectrum shows a number of cross-peaks among the protons of the EO chain, the imidazole CH proton and, most importantly, the “mobile” NH proton at 10 ppm. The low-field resonances of the strongly hydrogen-bonding NH protons as well as the resonance at 0.5 ppm, which has been assigned to a proton

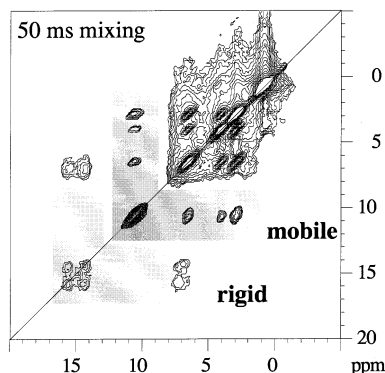


Figure 10. 2D ^1H exchange spectrum of Imi-2EO for mixing time of 50 ms.

within the ordered domains, that experience a marked π -electron high-field shift (Table 1) do not take part in the exchange with the protons belonging to the disordered portions. The involvement of the weakly hydrogen-bonded NH protons (while the strongly hydrogen-bonded NH protons are excluded) and the relatively narrow line widths confirm the assignment of the resonances to the disordered, mobile portion of the material. Note that the relatively narrow lines can be clearly distinguished from the broader signals of the ordered portions, which lie underneath the narrow peaks in the EO and CH resonance region.

The build-up of cross-peak intensity (I_{AB}) for dipolar-driven contacts is described by the following equation, where R_C denotes the rate of cross-relaxation and R_L denotes the leakage rate according to the terminology of Ernst, Bodenhausen, and Wokaun.¹⁴

$$I_{AB}(\tau_m) = I_{BA}(\tau_m) = -\frac{M_0}{2} W(1 - e^{-R_C\tau_m})e^{-R_L\tau_m} \quad (5)$$

We neglect R_L in our analysis, and R_C is defined as

$$R_C = \frac{1}{5} D_{ij}^2 \tau_c \quad (6)$$

where D_{ij} is the dipolar coupling constant and τ_c is the correlation time for molecular motion, or tumbling, and is related to the correlation described by the transverse relaxation times. This correlation time for molecular tumbling, τ_c for mobile Imi-2EO molecules at 335 K, is determined to be approximately 30 ns and is therefore in the slow motion regime relative to the inverse Larmor frequency of 1.43 ns. Nevertheless, this is rapid compared to inverse dipolar frequencies and again indicates their high degree of local mobility.

The contacts between the disordered NH and the EO protons have significant structural implications, as they are not found in the ordered portions. Hence, the signals indicate that the disordered molecules have “slipped” out of the crystalline lattice, and are now able to interact with the ethylene oxide moieties. Since these molecules have been proposed to be the ones active in the proton conduction mechanism, their interactions are the most intriguing in this study. The lack of interaction between the ordered and disordered protons in the 2D exchange protons was observed for all mixing times utilized [10 μs – 1 s]. Our interpretation of these results is that molecules that exhibit local or long range order, as indicated by their NH resonances and DQF signals, are not able to participate in proton transport, and that very few molecules, at the interfaces between the ordered and disordered domains, are able to participate in exchange but

are not observed due to their low relative concentration. This model is further developed in section 4.1.

4. Model of Proton Conductivity

4.1. At the Microscopic Level. In this section we bring together the key finding of this study and develop a model for describing proton mobility in the Imi-*n*EO family. This model and the accompanying exchange processes are shown schematically in Figure 11.

The resonance of the weakly hydrogen-bonded protons in both Imi-1EO and Imi-5EO was found to narrow with increasing temperature, consistent with a fast motional process. The disordered portion of the material can be viewed as a bath of molecules that rapidly break and reform their hydrogen bonds. This fast motional process, with a rate constant of k_1 , results in an averaged chemical shift, ν_{AV} , between the “free” resonance frequency, ν_F , and the “hydrogen-bonded” frequency, ν_H . The value of ν_F is taken from the calculated spectrum (9 ppm) of a free molecule in the gas phase, while the value of ν_H is ill-defined but cannot be larger than that of a strong hydrogen bond at 15 ppm. From this information we can calculate the relative concentration of the two species in the fast exchange domains, according to¹²

$$\nu_{AV} = n_H\nu_H + n_F\nu_F \quad (7)$$

where n_H and n_F represent the concentration of bonded and free molecules, respectively, and the sum of ($n_H + n_F$) = 1. At 330 K this results in a ratio $n_H/n_F = 1/6$. Since the value of ν_H is likely overestimated in this description, because the hydrogen bonding strength is certainly weaker than in the ordered domains, the ratio represents the minimum number of bonded molecules. Nevertheless, the presence of hydrogen bonds in this disordered phase is consistent with a Grotthus mechanism in proton transport in this phase, which is supported by the local mobility of the molecules. As yet, we have included only the line narrowing phenomena in our model. Now we turn to the interaction between ordered and disordered domains.

For both Imi-1EO and Imi-5EO, a trend toward higher chemical shift values is observed for the weakly hydrogen-bonded protons with increasing temperature. The chemical shifts of the all NH resonances in Imi-5EO as a function of temperature are shown in Figure 12a. The chemical shift of the weakly hydrogen-bonded NH resonance trends smoothly to higher frequency with increasing temperature, and in Imi-5EO a plateau is reached once the sample is molten. The chemical shift at this plateau, of 12.5 ppm, is equal to the weighted average of the two strongly and one weakly hydrogen-bonded resonances, as also plotted in Figure 12a. In Imi-1EO, the chemical shift changes more slowly and the plateau value is not reached within the temperature range sampled. Nevertheless, we infer that a similar pretransitional process is taking place, with a temperature offset relative to Imi-5EO of approximately 70 degrees. As mentioned in section 2.2, this change of the chemical shift cannot be explained by a single, fast exchange process between two species, since the trend is in the opposite direction to that predicted by such a model. We interpret this result, therefore, as evidence for a *slow* exchange process, which occurs at grain boundaries between ordered and disordered regions and involves a very small fraction of the sample, i.e., that at the interfaces. We furthermore note a qualitative correlation between the relative intensity of the mobile ^1H resonance, as well as its tendency toward higher chemical shift value, and the corresponding increase in conductivity with

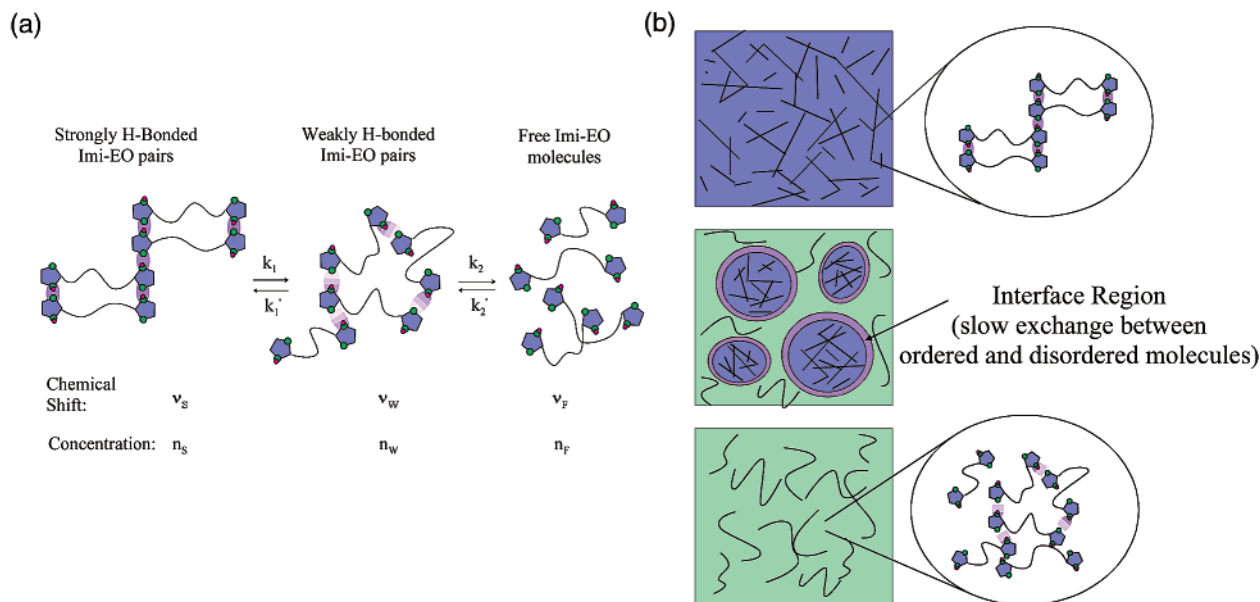


Figure 11. (a) Pictorial representation of proposed exchange processes, described by two rate constants, k_1 and k_2 , and three chemical shifts (ν_S , ν_W , ν_F) and concentrations (n_S , n_W , n_F). Strong H-bonds represented by solid purple ellipses, and fluctuating H-bonds represented by shaded ellipses. (b) Visualization of (i) ordered domains (blue) in which no exchange occurs found at low temperature, (ii) disordered domains in fast exchange (green) separated by interfaces (purple) at which slow exchange is proposed to occur at intermediate temperature, and (iii) bath of mobile molecules (green) with rapidly breaking and reforming H-bonds, found at high temperature.

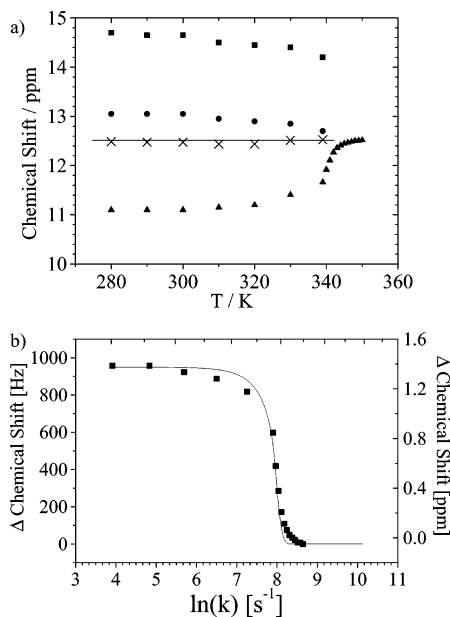


Figure 12. (a) Chemical shift of mobile N—H resonances in Imi-5EO plotted as a function of the sample temperature. Squares and circles represent the chemical shifts of the two strongly hydrogen-bonded NH resonances, triangles represent the mobile NH resonance, and X's represent the weighted average chemical shift. The solid line is included as a guide for the eye and indicates that the chemical shift of the weakly hydrogen-bonded resonance trends toward the constant weighted average as coalescence occurs. (b) Relative change in chemical shift of peak maximum for coalescing resonances as a function of the temperature. Calculated data are shown as solid line and experimental data are represented by black squares. Data are fit to an activated exchange process, with an activation energy of 55 ± 10 kJ/mol.

increasing temperature, found in both Imi-1EO and Imi-5EO. Therefore, it appears that the intensity of the disordered fraction can be taken as a qualitative estimate of the number of charge carriers present in the material. The slow exchange process, (i.e., exchange prior to coalescence) is typically described by shift effects, associated with line broadening, as a function of

temperature, which ultimately results in coalescence, and the onset of fast exchange. The effect on the line-shape is obscured by the dominant line narrowing effect in the more prominent fast exchanging regimes. Nevertheless, the position of this resonance is correlated with the slow exchange process, according to the following equation.¹²

$$g(\nu) = \frac{2\tau_A(\nu_S - \nu_W)^2}{[\nu - (1/2)(\nu_S + \nu_W)]^2 + \pi^2 \tau_A^2 (\nu - \nu_S)^2 (\nu - \nu_W)^2} \quad (8)$$

Here, $g(\nu)$ is the calculated line shape as a function of frequency, τ_A is the lifetime in seconds, and ν_S and ν_W represent the strongly and weakly hydrogen-bonded ^1H resonance frequencies, respectively. In Figure 12b we have plotted the changing position of the peak maximum obtained by evaluating the derivative of $g(\nu)$ at $g(\nu)' = 0$ in the calculated coalescing line shapes, $g(\nu)$, for a series of exchange rates, $k = 1/\tau_A$, spanning the coalescence process from slow exchange to fast exchange. The relative change in the experimentally observed chemical shift, as a function of temperature, is overlaid on the calculated peak positions. The maximum change in peak position of just more than 1.0 ppm corresponds to a change in the exchange rate, τ_A , of 1 order of magnitude. The fit of the experimental data corresponds to an activation energy of approximately 55 ± 10 kJ/mol. The concentration of ordered molecules undergoing exchange is assumed to be significantly smaller than the total number of ordered molecules at low temperature, consistent with the lack of cross-peaks between these domains in the 2D NOESY spectra. The relative concentration increases with increasing temperature, as the grain boundaries infringe on the ordered domains, as indicated in Figure 11b. Therefore, we assign the slow exchange process, and the associated energy, to that required for the strongly hydrogen-bonded molecules to break free of their ordered domains into the disordered, regions. The final chemical shift of these disordered domains implies the continued coexistence of both strongly and weakly hydrogen bonded species, in rapid exchange. We note that these studies

do not allow us to distinguish two possible processes active within the weakly hydrogen-bonded, disordered regions. First, the observed fast exchange process could represent solely rapid proton motion within and among the fluctuating hydrogen bonds, or second, a longer length scale rapid reorganization of the ordered and disordered domains could be occurring. The nature and length scale of any possible structural reorganization have not yet been identified.

4.2. Comparing the Microscopic Picture with Macroscopic Properties. We have presented a model for the microscopic processes that govern proton conductivity in Imi-*n*EO materials. Now, returning to the known trends in charge transport, we check the consistency of the model with those data and with other known properties of the materials. Considering Imi-1EO, a polycrystalline material with strongly temperature-dependent proton conductivity ($E_A = 128$ kJ/mol), we find that the local proton mobility described by NMR significantly underestimates the activation energy for charge transport. Therefore, to accurately describe charge transport on the microscopic scale, a second process must be invoked. In answer to the second question posed above in section 2.2, we have identified a secondary process which may account for this discrepancy. If we include the influence of large, ordered domains, which do not participate in long-range charge transport, we can justify the large activation energy of charge transport in this sample.

Imi-5EO, in contrast, is a disordered sample, with a glass transition temperature and a much more weakly temperature dependent proton conductivity. At first inspection, it appears that because the activation energies determined by NMR and conductivity are comparable with the given error margins, no secondary process need be considered in this case. However, analysis of all the available data, and in particular the chemical shift of the weakly hydrogen-bonded resonance, indicated that indeed a second pretransitional process is active. Imi-5EO is a glassy sample, with comparatively small locally ordered domains, therefore long range proton mobility is influenced to a much lesser extent by the presence of these locally ordered domains, and the similar activation energies for local and long-range proton mobility are consistent with the nature of the material. Within the temperature ranges investigated, the conductivity of Imi-1EO changes by several orders of magnitude, whereas that of Imi-5EO changes by less than 1 order of magnitude, again supporting our interpretation that the secondary reorganizational process is more influential in the crystalline material. The details of the conductivity studies are discussed elsewhere;⁷ however, for completeness we note that the maximum conductivity achieved at high temperature is greater in Imi-1EO than in Imi-5EO due to the higher relative concentration of imidazole moieties, which are able to act as charge carriers.

As a general comment on the comparison between NMR and conductivity measurements, we note here several important features that made this study challenging. First, conductivity measurements are able to detect a much broader range of time scales of molecular motion, and in particular, detect extremely small fraction of particles participating in charge transport. NMR, however, is less sensitive, and a significant fraction of molecules must participate in order for successful experimental observation. This fact prevented the observation of a cross-peak between ordered and disordered NH resonances in the 2D NOESY experiments. Nevertheless, the rate of the exchange is slow on the NMR time scale in the pristine samples, thus it was detected through the coalescence process, which caused the changing chemical shift.

4.3. The Effect of Doping with Acid. Doping Imi-*n*EO materials with small amounts of triflic acid has been shown to enhance the conductivity of these materials by providing an excess of protons.⁷ Our preliminary ¹H NMR studies of Imi-2EO doped with 5–10% triflic acid show a single narrow NH resonance, with a chemical shift of 12.5 ppm. The behavior is unchanged, as compared to the pristine materials, apart from the appearance of an averaged NH resonance at ambient temperature. The chemical shift of this resonance is similar to the averaged chemical shift in the pristine materials, achieved following the coalescence process. We therefore infer that the proton mobility is increased by doping, such that exchange occurs in the fast motional regime. The primary effect is not a structural change, but possibly a change in the rate of proton mobility. Such an effect of increasing the rate of exchange by changing the pH is known from the influence of a small pH change on the conductivity of H₂O, where the question of the number of charge carriers is also critical.^{28,34} Our detailed studies of the pristine materials form a good basis for continuing studies of these doped materials, in which the time scale of proton mobility is comparable to that required in a viable proton-conducting membrane.

5. Conclusions

We have shown for the first time that microscopic and macroscopic proton transport processes can be related through a comparison of the temperature dependence of the conductivity and the effective spin–spin relaxation time (T_2^*). The latter is a measure of the correlation times for molecules undergoing motion in the fast exchange regime, and the proton hopping of these disordered, mobile molecules is thus correlated with charge transport via proton mobility measured macroscopically.

DFT methods were used to calculate the ¹H chemical shifts for crystalline Imi-2EO and found to be in excellent agreement with the experimental results. In particular, these calculations provided a structurally specific assignment of the strongly hydrogen-bonded N–H resonances, as well as the protons in the ethylene oxide backbone that are shifted to lower frequency due to their orientation with respect to the aromatic rings. Moreover, comparison of the calculated chemical shifts for the periodic structures versus the single molecules of both Imi-2EO and imidazole itself supports the assignment of the lower frequency NH resonances to weakly hydrogen-bonded molecules. The hydrogen-bonding motif present in crystalline Imi-2EO and characterized spectroscopically by a pair of high-frequency NH resonances is common among the Imi-*n*EO materials, because this characteristic fingerprint is present regardless of the thermal history, we conclude that local ordering is present, even in the glassy materials, below the melt temperature.

Mobile molecules are present in all Imi-*n*EO materials and in imidazole itself below the glass transition or melting point, respectively. These molecules represent disordered domains and are proposed to be responsible for the charge transport observed in the materials below the melt temperature. The 2D ¹H exchange study showed no cross-peak between ordered and disordered domains, therefore no large scale exchange between these components occurs. The chemical shift of the disordered fraction shows, however, a slow exchange process that we propose is occurring at interfacial regions; a pretransitional process, which, together with local proton mobility, govern the observed conductivity. Within the disordered domains, the chemical shift is consistent with the presence of fluxional

hydrogen bonds, which allow for charge transport via the Grotthuss mechanism, or structural diffusion.

6. Experimental Section

Sample Preparation. The materials were synthesized as described in ref 7 and handled such that exposure to moisture was excluded.

Solid-State NMR. Data were collected on a 16.4 T magnet with a Bruker DRX spectrometer, using a double resonance MAS probe supporting rotors of 2.5 mm outer diameter. The resonance frequency of ^1H is 700 MHz. The samples were spun at 30 kHz. The $\pi/2$ pulse lengths were set to 2 μs . A recycle delay of 3 s was used. The spectra are referenced to adamantane (1.63 ppm, ^1H).

Variable temperature experiments were performed in the range of 250–380 K, bearing gas temperature, and the sample temperature was correct to include heating effects arising from the high-speed MAS.²⁶ Five minutes were allowed following each temperature change to allow for equilibration of the sample.

Spin–lattice relaxation measurements were acquired using a saturation recovery sequence, with variable delay values ranging from 0.001 to 5400 s. Twenty-five data points were acquired in the indirect dimension, and 16 transients were averaged per slice. The saturation recovery method allowed us to use a short recycle delay of 2 s because, in contrast to inversion–recovery experiments, complete relaxation was not required prior to the next saturation sequence. 2D NOESY exchange spectra were acquired using mixing times between 0.001 and 3 s. The rotor-synchronized 2D ^1H – ^1H DQ spectra were recorded using a five-pulse sequence with $\tau_{\text{exc}} = 1/2\tau_{\text{R}}$ or a full back-to-back sequence, with $\tau_{\text{exc}} = \tau_{\text{R}}$.¹³ States-TPPI was applied for phase sensitive detection³⁵ in t_1 , and 64 slices were detected in the indirect dimension, with 16 transients averaged per slice. The experimental time was about 1 h.

Acknowledgment. G.R.G. thanks NSERC (Canada) for financial support in the form of a postdoctoral fellowship. The authors thank Wolfgang Meyer and Burkhard Doliwa for several helpful discussions.

References and Notes

- (1) Carrette, L.; Friedrich, K. A.; Stimming, U. *Fuel Cells* **2001**, *1*, 5–39.
- (2) Kreuer, K.-D. *Chem. Mater.* **1996**, *8*, 610–641.
- (3) *Proton Conductors: Solids, Membranes, and Gels – Materials and Devices*; Colomban, Ph., Ed.; Cambridge University Press: Cambridge, 1992.
- (4) Kreuer, K.-D. *Solid State Ionics*, **1997**, *97*, 1–15.
- (5) Savadogo, O. *J. New Mater. Electrochem. Syst.* **1998**, *1*, 47.
- (6) Kreuer, K.-D.; Fuchs, A.; Ise, M.; Spaeth, M.; Maier, J. *Electrochim. Acta*, **1998**, *43*, 1281.
- (7) Schuster, M.; Meyer, W. H.; Wegner, G.; Herz, H. G.; Ise, M.; Schuster, M.; Kreuer, K. D.; Maier, J. *Solid State Ionics* **2001**, *145*, 85–92.
- (8) Schuster, M. F. H.; Meyer, W. H.; Schuster, M.; Kreuer, K. D. *Chem. Mater.* **2002**, submitted.
- (9) Kawada, A.; McGhie, A. R.; Labes, M. M. *J. Chem. Phys.* **1970**, *52*, 3121.
- (10) Hickman, B. S.; Mascal, M.; Titman, J.; Wood, I. *J. Am. Chem. Soc.* **1999**, *121*, 11490.
- (11) Becker, E. D. *High-Resolution NMR Theory and Chemical Applications*, 3rd ed.; Academic Press: San Diego, 2000; p 30–32.
- (12) Harris, R. K. *Nuclear Magnetic Resonance Spectroscopy A Physicochemical View*; Pitman Books Ltd.: London, 1983; p 122.
- (13) Schnell, I.; Spiess, H. W. *J. Magn. Reson.* **2001**, *151*, 153–227.
- (14) Ernst, R. R.; Bodenhausen, G.; Wokaun, A. *Principles of Nuclear Magnetic Resonance in One and Two Dimensions*; Clarendon Press: Oxford, 1987. p 516–520.
- (15) Schnell, I.; Brown, S. P.; Lee, H. L.; Ishida, H.; Spiess, H. W. *J. Am. Chem. Soc.* **1998**, *120*, 11784–11795.
- (16) Sebastiani, D.; Parrinello, M. *J. Phys. Chem. A* **2001**, *105*, 1951.
- (17) Sebastiani, D.; Goward, G.; Schnell, I.; Parrinello, M. *Comput. Phys. Commun.*, in press.
- (18) Hutter, J.; Ballone, P.; Bernasconi, M.; Focher, P.; Fois, E.; Goedecker, S.; Parrinello, M.; Tuckerman, M. CPMD Computer code, MPI für Festkörperforschung, Stuttgart, and IBM Zürich Research Lab (1995–2002).
- (19) Car, R.; Parrinello, M. *Phys. Rev. Lett.* **1985**, *55*, 2471.
- (20) Becke, A. D. *Phys. Rev. A* **1988**, *38*, 3098.
- (21) Trouiller, N.; Martin, J. L. *Phys. Rev. B* **1991**, *43*, 1943.
- (22) Münch, W.; Kreuer, K.-D.; Silvestri, W.; Maier, J.; Seifert, G. *Solid State Ionics* **2001**, *145*, 437.
- (23) Brown, S. P.; Spiess, H. W. *Chem. Rev.*, **2001**, *101*, 4125.
- (24) Schnell, I.; Langer, B.; Soentjens, S. H. M.; van Genderen, M. H. P.; Sijbesma, R. P.; Spiess, H. W. *J. Magn. Reson.* 2001; in press.
- (25) Schuster, M. F. H. *Dissertation*, Mainz, Germany, 2002; chapter 3.
- (26) Langer, B.; Schnell, I.; Spiess, H. W.; Grimmer, A.-R. *J. Magn. Reson.* **1999**, *138*, 182–186.
- (27) Spiess, H. W. *Adv. Polym. Sci.* **1985**, *66*, 24.
- (28) Marx, D.; Tuckerman, M. E.; Hutter, J.; Parrinello, M. *Nature* **1999**, *397*, 601.
- (29) Schuster, M. F. H. *Dissertation*, Mainz, Germany, 2002; Ch. 5.
- (30) Brown, S. P.; Schnell, I.; Brand, J. D.; Müllen, K.; Spiess, H. W. *Phys. Chem. Chem. Phys.* **2000**, *2*, 1735.
- (31) Brown, S. P.; Schaller, T.; Seelbach, U. P.; Koziol, F.; Ochsenfeld, C.; Klärner, F. G.; Spiess, H. W. *Angew. Chem.* **2001**, *40*, 717.
- (32) Ochsenfeld, C.; Brown, S. P.; Schnell, I.; Gauss, J.; Spiess, H. W. *J. Am. Chem. Soc.* **2001**, *123*, 2597–2606.
- (33) Schuster, M. F. H. *Dissertation*, Mainz, Germany, 2002; chapter 10.
- (34) Kreuer, K. D. *Solid State Ionics* **2000**, *136/137*, 149.
- (35) Marion, D.; Ikura, M.; Tschudin, R.; Bax, A. *J. Magn. Reson.* **1989**, *85*, 393.

Anomalous temperature dependence of nuclear quadrupole interactions in strongly hydrogen-bonded systems from first principles

J. Schmidt^{a)} and D. Sebastiani^{b)}*Max Planck Institute for Polymer Research, Ackermannweg 10, D-55128 Mainz, Germany*

(Received 8 February 2005; accepted 21 June 2005; published online 19 August 2005)

We present an analysis of the effect of finite temperatures on the deuteron nuclear quadrupole coupling constants in a strongly hydrogen-bonded molecular crystal by means of first-principles Car-Parrinello molecular-dynamics simulations. Our findings agree well with experiments and provide a microscopic explanation of the anomalous increase of the quadrupole coupling in this class of systems. We show that a simple model based on the anharmonicity of the hydrogen bond potential fails to describe the temperature dependence of the couplings even qualitatively. Instead, the inclusion of fluctuations and disorder in terms of atomic motion of the surrounding molecules turns out to be important to obtain the correct magnitude of the temperature effect.

© 2005 American Institute of Physics. [DOI: [10.1063/1.2000241](https://doi.org/10.1063/1.2000241)]

I. INTRODUCTION

The determination of local structural properties, such as intramolecular conformation as well as intermolecular interactions, has always been and still is a challenge for modern physics and chemistry. A variety of advanced techniques have emerged that are capable of contributing elements to this quest, some of the most prominent being x-ray and neutron scattering, IR spectroscopy, and nuclear-magnetic-resonance (NMR) spectroscopy.

NMR experiments are able to probe a local structure without the need of long-range order as required for diffraction techniques, which is one of the key advantages of this method. Therefore, it is well suited to investigate biological systems and their mechanisms of structure formation. Besides NMR chemical shifts, nuclear quadrupole coupling constants (NQCCs) are a powerful tool to probe local structures, especially hydrogen bonds, which are essential for the secondary and even tertiary conformations of bio-organic assemblies. This work concentrates on benzoic acid, a dicarboxylic acid, which is used as a model system for hydrogen bonding.

The dependence of the nuclear quadrupole resonance frequency on temperature in solids has been studied theoretically and experimentally in the past for many compounds and the problems in determining this dependence have been pointed out in literature. A theory based on modes of oscillation has first been developed by Bayer.¹ Kushida² and Wang³ generalized this work to a theory which was able to describe experimental trends analytically. According to this theory, the average internal field gradient at the nucleus decreases with increasing temperature because of the increase in the amplitude of the thermal vibrations.⁴ Therefore this theory would not explain any increase of the NQCC with

increasing temperature, which is observed in some compounds in the solid state (e.g., potassium hydrogen maleate⁵). The temperature dependence of the NQCC has also been studied both experimentally and theoretically in liquid methanol and ethanol.^{6,7} Within quantum cluster equilibrium theory, the theoretical model that was used in that work, temperature-dependent properties are calculated by weighting these properties by the appropriate population of molecular clusters. In principle, this model could also be used in the solid state.

Our approach instead is based on a direct on-the-fly calculation of NQCCs along a finite-temperature Car-Parrinello molecular-dynamics trajectory. Since the NQCC depends on the electric-field gradient (EFG), a ground-state property, it can easily be computed from the knowledge of the electronic density alone, at essentially no additional computational cost. This enables us to apply the predictive power of *ab initio* and density-functional calculations, which is nowadays a well-established and widely used tool, to NQCCs. We show that a simple model based on the anharmonicity of the potential curve of a hydrogen-bonded deuteron returns the incorrect trend of the temperature dependence, while our direct calculation agrees well with the experimental results.

It is known that for a reliable calculation of EFGs, the chemical environment of the considered atoms is of crucial importance, since the EFG is very sensitive to electrostatic effects which may arise from molecular charges and dipoles even at larger distances. Cluster models do not always yield satisfactory results, and even embedded models seem to have a questionable accuracy.⁸ Therefore, in this work, the system is studied within a plane-wave-based density-functional theory (DFT) approach under periodic boundary conditions in order to overcome the limits of such calculations.

^{a)}Electronic mail: schmidt@mpip-mainz.mpg.de^{b)}Fax: +49-6131-379-100; electronic mail: sebastia@mpip-mainz.mpg.de

II. THEORY

Starting from the classical expression for the energy of an electric quadrupole in an external electrical potential $\phi(\mathbf{r})$, we find the quantum-mechanical Hamiltonian,

$$\mathcal{H}_Q = \frac{1}{6} \sum_{ij} \phi_{ij} Q_{ij}, \quad (1)$$

with the electric-field gradient (EFG),

$$\phi_{ij} \equiv \left. \frac{\partial^2 \phi(\mathbf{r})}{\partial x_i \partial x_j} \right|_{\mathbf{r}=\mathbf{R}_N}, \quad (2)$$

and the nuclear quadrupole moment tensor Q_{ij} , defined as the second moment of the nuclear charge distribution centered at \mathbf{R}_N . In a NMR experiment we observe transitions between different spin eigenstates of nuclei. Therefore, it is useful to transform \mathcal{H}_Q into a function of spin operators I by using the Wigner-Eckart theorem,

$$\mathcal{H}_Q = \frac{Q}{6I(2I-1)} \sum_{ij} \phi_{ij} \left[3 \frac{I_j I_i + I_i I_j}{2} - \delta_{ij} I^2 \right]. \quad (3)$$

The constant Q is the nuclear quadrupole moment which has been measured with high accuracy for many species⁹ and I is the nuclear spin. In a measured spectrum we find a splitting due to the nuclear quadrupole coupling (3) which can be written as¹⁰

$$\Delta\nu = \frac{3}{2} \frac{qQ}{I(2I-1)} \frac{1}{2} (3 \cos^2 \theta - 1 - \eta \sin^2 \theta \cos(2\phi)), \quad (4)$$

where (θ, ϕ) are the polar and the azimuth angles of the magnetic field in the principal-axis system of the EFG tensor. Only two parameters, namely, the *field gradient* $q = \phi_{33}$ and the *asymmetry parameter* $\eta = (\phi_{11} - \phi_{22})/\phi_{33}$, are needed to describe the splitting. These can easily be computed from the total ground-state probability density, $\rho(\mathbf{r}) = \rho_{\text{el}}(\mathbf{r}) + \rho_{\text{nuc}}(\mathbf{r})$. With the convention $|\phi_{33}| \geq |\phi_{11}| \geq |\phi_{22}|$, the field gradient q is directly proportional to the measured NQCC.

In the Kohn-Sham formulation of DFT,¹¹ the ground-state probability density $\rho_{\text{el}}(\mathbf{r})$ can be found by minimizing the energy of the many-electron system, given as a functional of the density,

$$E_{\text{DFT}}[\rho_{\text{el}}] = T_s[\rho_{\text{el}}] + J[\rho_{\text{el}}] + E_{\text{xc}}[\rho_{\text{el}}] + \int \nu(\mathbf{r}) \rho_{\text{el}}(\mathbf{r}) d\mathbf{r}, \quad (5)$$

where T_s is the kinetic energy, J is the Coulomb potential energy, E_{xc} is the exchange-correlation energy, and $\nu(\mathbf{r})$ is an external potential.¹² The charge distribution of the nuclei $\rho_{\text{nuc}}(\mathbf{r})$ is modeled by Gaussians, centered at the positions of the nuclear point charges.

The electrostatic potential $\phi(\mathbf{r})$ has to fulfill the Poisson equation, which can be expressed in Fourier space as

$$\phi(\mathbf{G}) = \frac{4\pi}{G^2} \rho(\mathbf{G}), \quad (6)$$

where \mathbf{G} is a reciprocal space vector (we use atomic units throughout this paper). Since spatial derivatives transform to

multiplications with reciprocal space vectors, the EFG can be written as

$$\phi_{ij}(\mathbf{G}) = -\frac{4\pi}{G^2} \rho(\mathbf{G}) G_i G_j. \quad (7)$$

With the help of Eq. (7), the EFG in real space can easily be obtained through a single inverse Fourier transformation.

III. COMPUTATIONAL DETAILS

We incorporate atomic motion at finite temperature via Car-Parrinello molecular-dynamics (CPMD) simulations. All calculations were done using a fully periodic description of the crystal with a unit cell, which contained four crystallographically identical molecules of benzoic acid, using the pseudopotential plane-wave program package CPMD.¹³ We used the BLYP gradient-corrected exchange-correlation functional,^{14,15} pseudopotentials of the type of Goedecker *et al.*¹⁶ and a plane-wave cutoff of 80 Ry. The atomic coordinates were initially taken from x-ray data^{17,18} and subsequently relaxed. The systems were equilibrated at the target temperature for 0.5 ps (each step of the simulation corresponds to 0.1 fs) using chains of Nosé-Hoover thermostats¹⁹ attached to the nuclear degrees of freedom. Subsequently, the EFG was computed on the fly during a production run of another 1.5 ps of microcanonical MD.²⁰ During the MD simulation and the calculation of the EFG for the relaxed geometry the plane wave cutoff was set to 110 Ry. The fictitious masses μ_i were set to 800 a.u., which has been shown to be sufficiently small to yield accurate structural information for deuterated systems.^{21,22}

To check the convergence of our field gradients with respect to computational parameters and to estimate the error introduced by the use of pseudopotentials, we have compared the EFGs obtained from CPMD with those from a TURBOMOLE (Ref. 23) calculation using a cc-PV5Z basis set at the same level of theory. A convergence analysis showed that at a plane-wave cutoff of 110 Ry, the difference of deuteron EFGs is below 3%.

In principle, another possible contribution to the temperature dependence is the thermal expansion of the crystal. Within the temperature range that we considered, a typical average thermal-expansion coefficient is about $10^{-4}/\text{K}$, corresponding to a 1% change in the lattice constant for a jump of $\Delta T = 100$ K. We have checked that at a given temperature, such a 1% expansion of the cell has no significant effect on the electric-field gradients. The variations were always within the numerical noise of our calculations.

Our simulation cells contain only four molecules. Therefore, phonons with long wavelengths are not taken into account properly. To establish an estimate for the error introduced due to this finite-size effect, we approximate the case of a phonon with a very large wavelength by an appropriate variation in the lattice constant. The above-mentioned 1% change in the lattice constant resulted in an increase of the total energy of the system of about 0.3 mhartree/molecule. Assuming that such phonon modes will be thermally populated by $k_B T \lesssim 0.3$ mhartree, we expect their amplitudes to

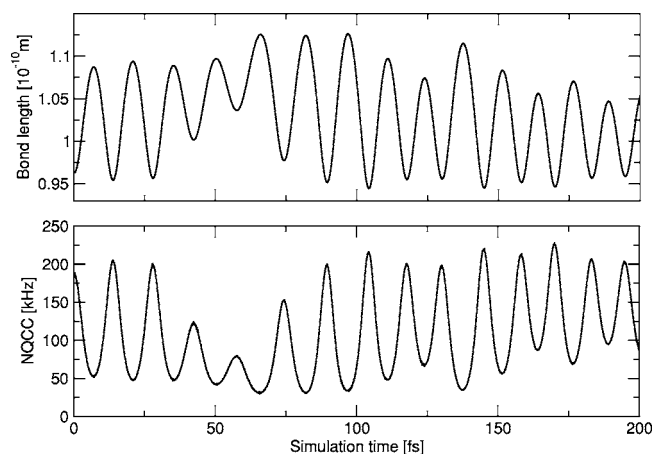


FIG. 1. Bond length d_{OD} and NQCC of the hydrogen bonded deuterons in benzoic acid during a MD simulation at 305 K.

correspond to less than this 1% lattice expansion and therefore to have no significant effect on the electric-field gradients.

The effect of zero-point motion was not taken into account explicitly, i.e., the nuclei were treated as classical particles. Their quantum nature could be included by performing path integral molecular-dynamics (PIMD) simulations.^{24,25} This technique is computationally much more expensive (by a factor of between 10 and 80) than standard Car-Parrinello MD, and the results of a PIMD simulation that is presently being prepared will be published elsewhere. The strength of this effect cannot be predicted easily without performing the actual calculation. However, at first order, the corresponding change in the EFGs will be an additional constant offset at any temperature that is close to zero at the scale of the associated nuclear vibrational modes. For wave numbers $\tilde{\nu} \approx 1000\text{--}3500\text{ cm}^{-1}$, this can safely be assumed below $T=500\text{ K}$.

IV. RESULTS AND DISCUSSION

NMR experiments on benzoic acid reveal a quadrupole splitting of 115(5) kHz for the hydrogen-bonded deuteron,²⁶ while calculations with the relaxed geometry at 0 K yield a NQCC of 101 kHz. This deviation is relatively large and above the numerical error expected for a standard DFT calculation, but it can be caused by temperature effects. Since the hydrogen bond is anharmonic, thermal vibrations at finite temperatures lead to an elongation of the average bond length of the deuteron. With the simple model of two negative charges (the oxygens) for the hydrogen bond, it is easy to show that the EFG has a minimum at the center of mass of the system due to its symmetry. Hence, on average, the larger bond length should lead to a smaller NQCC according to this model. This, however, is in contradiction to the experimental observations. The measured temperature dependence of the NQCC can therefore not be explained by this static model which correlates the EFG with an effective bond length.

A more realistic picture can be obtained with the help of a MD simulation, in which we calculate the instantaneous properties, i.e., bond length d_{OD} and EFG, during each step. Figure 1 shows the time evolution $d_{OD}(t)$ as well as the cor-

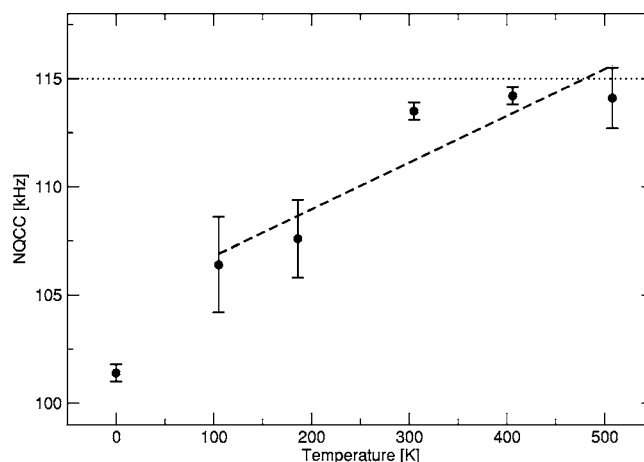


FIG. 2. Temperature dependence of the NQCC of the hydrogen-bonded deuterons in benzoic acid. The linear fit (dashed line) shows a temperature gradient of 2.2 kHz/100 K. The error bars indicate the standard deviation between the four crystallographically identical deuterons in the supercell. The dotted line represents the experimental value.

relation EFG [$d_{OD}(t)$]. The latter in fact supports the simple point-charge model above, in which the NQCC decreases as d_{OD} increases (i.e., when the $OD\cdots O$ hydrogen bond becomes more symmetric). The erroneous assumption must therefore be found in the averaging process and the mapping of the effective bond length onto the measured NQCC.

Thermal vibrations are much faster than the characteristic time of a NMR experiment and thus, the measured quantities indeed represent averaged values. A computer simulation has to incorporate this fact by averaging the instantaneous properties over all steps of the MD. This averaging procedure, however, has to be done on the level of the final properties, and not on the geometrical parameters. This means that we may not extract an effective $OD\cdots O$ bond length from the MD and deduce the NQCC from that. Instead, the full time evolution of the field gradient has to be computed and finally averaged. Following this procedure for benzoic acid, we find a NQCC of 114 kHz at 305 K, which agrees well with the experimental value.

The quantitative temperature dependence has been investigated in a series of MD simulations at different temperatures, whose results are shown in Fig. 2. The shape of the NQCC- d_{OD} correlation (Fig. 3) is very similar for all considered temperatures. The amplitudes of the bond elongation increase at higher temperatures, while the effective bond length of 1.023 Å hardly changes. This confirms that the vibrational modes related to bond stretching are essentially still in their harmonic regime.

On the one hand the NQCC is affected by the collective motion of all atoms, which causes the broadness of the line in Fig. 3. For a given distance d_{OD} , the EFG values are distributed within a certain band as a result of the different positions of the surrounding atoms. We find that this band is centered at a value higher than the $T=0\text{ K}$ value.

On the other hand, the dependence of the field gradient on the bond distance is nonlinear. Due to its curvature, larger distances of d_{OD} lead to a weaker decrease and shorter ones result in a stronger increase than a linear extrapolation of the

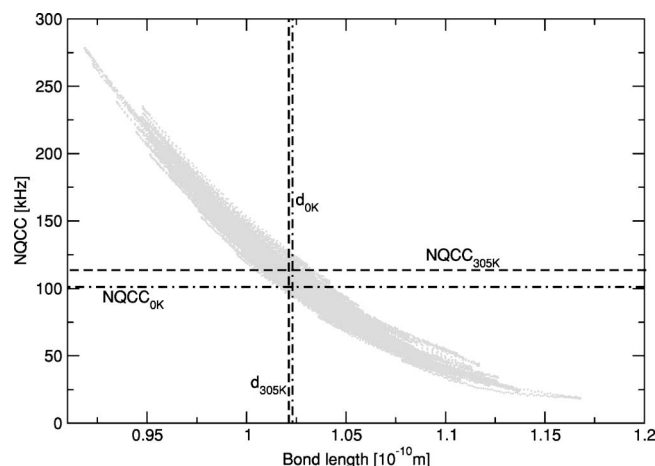


FIG. 3. Correlation of the NQCC and the bond length from each MD step of the CP trajectory at 305 K. The lines show the averaged values for 0 and 305 K.

EFG as a function of d_{OD} . Thus, the combination of both trends yields an effective increase of the field gradient for larger oscillation amplitudes.

While the NQCC increases with temperature by 2 kHz/100 K (the 0-K value has been omitted in the regression), the averaged bond length varies only by 0.002 Å (see Table I), with a slope of 3 $\mu\text{Å}/\text{K}$. The asymmetry η turns out to be constant as well. The linear behavior of the NQCC seems to hold even beyond the melting point at standard pressure ($T_m = 395$ K), even though the 500-K value shows a slight deviation. This is reasonable when considering the statistical error, but could also be an indication that the system would like to undergo a phase transition. Since the shown errors do not include systematic contributions, we expect the linearity to be better than indicated by the error bars.

V. CONCLUSIONS

In conclusion, we have investigated the temperature dependence of deuteron nuclear quadrupole coupling constants in an exemplary strongly hydrogen-bonded molecular crystal by means of first-principles Car-Parrinello molecular-dynamics simulations at various temperatures. The experimentally observed value is well reproduced by our simulations.

TABLE I. Temperature dependence of the calculated quantities. NQCC is the nuclear quadrupole coupling constant, η the asymmetry parameter, and d_{OD} the bond length of the considered deuteron. Only statistical errors are given.

T (K)	NQCC (kHz)	η	d_{OD} (Å)
0	101.4(4)	0.20(1)	1.023(1)
105	106.4(22)	0.19(1)	1.022(2)
186	107.6(18)	0.19(1)	1.023(2)
305	113.5(4)	0.18(1)	1.022(2)
406	114.2(4)	0.18(1)	1.023(1)
508	114.1(14)	0.18(1)	1.025(2)
300 (expt.)	115(5)		

A straightforward model based on the temperature-induced elongation of the hydrogen bond incorrectly predicts a smaller coupling constant due to a more symmetric $OD \cdots O$ hydrogen bond. The explicit calculation of the electric-field gradients at each step of the molecular-dynamics trajectory indeed reflects this inverse proportionality. However, the experimentally observed value of the coupling constant cannot be explained by this anharmonic model, but only by properly averaging the instantaneous values of the field gradients along the trajectory. The increase of the NQCC is thus caused by nonlinear effects and collective motion, coming into play at experimental time scales.

This work sheds light on an important aspect in the spectroscopic analysis of molecular structure, which is the necessary intermediate interpretation step between raw experimental data and desired spatial information. In our case, experiments yield effective coupling constants which cannot always be transformed directly into structural data such as bond lengths. We have shown that this is because measured data does not directly reflect geometric parameters, but rather represents the ensemble average of highly fluctuating quantities. Especially when nonlinear dependencies between geometric and spectroscopic parameters come into play, a direct *ab initio* simulation is the method of choice for the explanation of experimental features.

In complex situations, as the case presented in this work, simplified models may lead to qualitatively wrong conclusions. In such cases, the theoretical support regarding the interpretation of spectroscopic data can be crucial.

ACKNOWLEDGMENTS

This work was funded by the DFG Grant No. SE 1008/2. The authors would like to thank Professor H. W. Spiess for continuous fruitful discussions.

- ¹H. Bayer, Z. Phys. **130**, 227 (1951).
- ²T. J. Kushida, Sci. Hiroshima Univ., Ser. A 19, 327 (1955).
- ³T. Wang, Phys. Rev. **99**, 566 (1955).
- ⁴T. Kushida, G. B. Benedek, and N. Bloembergen, Phys. Rev. **104**, 1364 (1956).
- ⁵K. Miyakubo and N. Nakamura, Z. Naturforsch., A: Phys. Sci. **57**, 337 (2002).
- ⁶M. A. Wendt, M. D. Zeidler, and T. C. Farrar, Mol. Phys. **97**, 753 (1999).
- ⁷R. Ludwig, F. Weinhold, and T. C. Farrar, Mol. Phys. **97**, 479 (1999).
- ⁸M. Strohmeier, D. Stueber, and D. M. Grant, J. Phys. Chem. A **107**, 7629 (2003).
- ⁹P. Pykkö, Mol. Phys. **99**, 1617 (2001).
- ¹⁰K. Schmidt-Rohr and H. W. Spiess, *Multidimensional Solid-State NMR and Polymers* (Academic, London, 1994).
- ¹¹W. Kohn and L. J. Sham, Phys. Rev. **140**, A1133 (1965).
- ¹²R. G. Parr and W. Yang, *Density-Functional Theory of Atoms and Molecules* (Oxford University Press, New York, 1989).
- ¹³J. Hutter *et al.*, computer code CPMD, version 3.8, copyright IBM Corp. and MPI-FKF Stuttgart, 1990–2003; <http://www.cpmd.org>
- ¹⁴A. D. Becke, Phys. Rev. A **38**, 3098 (1988).
- ¹⁵C. Lee, W. Yang, and R. G. Parr, Phys. Rev. B **37**, 785 (1988).
- ¹⁶S. Goedecker, M. Teter, and J. Hutter, Phys. Rev. B **54**, 1703 (1996).
- ¹⁷The Cambridge Structural Database, F. H. Allen, Acta Crystallogr. **58**, 380 (2002).
- ¹⁸G. Bruno and L. Randaccio, Acta Crystallogr., Sect. B: Struct. Crystallogr. Cryst. Chem. **36**, 1711 (1980).
- ¹⁹G. J. Martyna, M. L. Klein, and M. Tuckerman, J. Chem. Phys. **97**, 2635 (1992).

- ²⁰This simulation time was found to be sufficient to allow a good sampling of the phase space. We checked explicitly that extraction windows at the beginning and the end of this simulation yield the same results within numerical noise. For a system in the solid state, the accessible phase space is much smaller than, e.g., for a liquid.
- ²¹I.-F. W. Kuo, C. J. Mundy, M. J. McGrath *et al.*, J. Phys. Chem. B **108**, 12990 (2004).
- ²²We have checked explicitly that the field gradients computed from Car-Parrinello orbitals do not differ significantly from fully optimized ones. Although the EFG evaluated from a single MD step using the CP orbitals deviates up to 0.5% from the calculation with fully optimized Born-

Oppenheimer orbitals, the averaged values taken from the whole MD simulation were found to differ by less than 0.02%.

- ²³R. Ahlrichs *et al.*, Computer code TURBOMOLE, University of Karlsruhe, 1988; <http://www.turbomole.de>
- ²⁴M. E. Tuckerman, in Quantum Simulations of Complex Many-Body Systems: From Theory to Algorithms, NIC series Vol. 10, edited by J. Gro-tendorst D. Marx, and A. Muramatsu (John von Neumann Institute for Computing, Jülich, 2002), pp. 269–298.
- ²⁵D. Marx and M. Parrinello, Z. Phys. B: Condens. Matter **95**, 143 (1994).
- ²⁶A. Hoffmann and I. Schnell, (private communication).

Adsorption of Water Molecules on Flat and Stepped Nickel Surfaces from First Principles

Daniel Sebastiani* and Luigi Delle Site*

Max-Planck-Institute for Polymer Research, Ackermannweg 10,
55128 Mainz, Germany

Received August 25, 2004

Abstract: We present an ab initio density functional study of the adsorption of a series of water oligomers (molecule, dimer and trimer) on nickel surfaces with and without step defects. We investigate the preferred adsorption geometries and adsorption energies and analyze the binding mechanisms by means of electronic density difference maps. Special attention is devoted to the incremental adsorption process, i.e., the way additional molecules attaches to an already adsorbed water. In agreement with recent findings, we show that the first water molecule is bound to the surface with an energy of about 0.2–0.4 eV, i.e., with up to twice the strength of a hydrogen bond. In contrast to this, subsequent water molecules increase the total adsorption energy by typically 0.5 eV. However, electron density difference considerations indicate that this additional attraction is *not* due to the interaction of the new molecule with the surface but mediated by the first water molecule. The interaction of the additional molecule with the surface appears even to be repulsive. We discuss the implications of these findings for the wetting properties of transition metal surfaces.

1. Introduction

The interaction of water with metal surfaces is of tremendous importance for industrial applications and of very high relevance in surface chemistry. The fundamental mechanisms of the initial phases of this adsorption process has been the subject of a variety of recent experimental and theoretical investigations^{1–6} and is still a matter of intense controversy.^{7–9}

There is evidence that the water molecules can approach the surfaces in both hydrogen-up and hydrogen-down orientations. Depending on the metal species, a water monolayer can be formed through simultaneous binding of all water molecules to the surface, e.g. in the case of Pt(111), or alternatively as a partially dissociated layer, which is the case for Ru(0001).^{2,4}

The deposition of isolated water molecules has already been studied on several flat metallic surfaces, such as Ru(0001), Rh(111), Pd(111), Pt(111), Cu(111), and Ag(111).^{10–12} An interesting mechanism for dimer diffusion

through a combined proton tunneling and molecular rotation scheme has been proposed recently.¹³

Most of these studies deal with the interaction of either a single water molecule on a metallic slab or the adsorption of a highly symmetric water monolayer. A high degree of order facilitates the computational modeling within periodic boundary conditions, because the unit cell can be kept small.

In this work, we study more extended systems, which allow for significantly more geometrical relaxation. Our aim is to focus on a realistic description of the initial steps of wetting, going beyond a single adsorbed molecule but without imposing a complete coverage of the surface. For this purpose, we look at the adsorption of a sequence of water oligomers on nickel. Starting from an isolated molecule, we investigate a water dimer as well as a trimer, paying particular attention to the influence of hydrogen bonding on the adsorption energy and the structure of the adsorbate. In particular, we compare the incremental adsorption energy due to the addition of a second and third molecule.

Inspired by previous studies,^{14–17} we look not only at a perfect surface but also at the simplest possible defect, a one-dimensional step. This is realized by using a surface in the

* Corresponding authors fax: +49-6131-379-100; e-mail: sebastia@mpip-mainz.mpg.de (D.S.) and fax: +49-6131-379-100; e-mail: dellsite@mpip-mainz.mpg.de (L.D.S.).

Table 1. Energetical and Structural Data for the Various Water Oligomers and Surfaces^a

	ΔE	$d_{\text{Ni-O}}$	$\Delta_{xy}(\text{O})$	$\Delta_z(\text{Ni})$	α	$d_{\text{O...O}}$
(H ₂ O) ₂	0.22					
Ni _{flat} *(H ₂ O) _{1,atop}	0.242	2.26	0.14	0.17	5	
Ni _{flat} *(H ₂ O) _{1,bridge}	0.10	3.02	0.02	0.16	-10	
Ni _{step} *(H ₂ O) _{1,atop,trans}	0.403	2.12	0.04	0.10	4	
Ni _{step} *(H ₂ O) _{1,bridge,trans}	0.249	2.46	0.03	0.08	8	
Ni _{step} *(H ₂ O) _{1,atop,cis}	0.397	2.10	0.07	0.05	2	
Ni _{step} *(H ₂ O) _{1,bridge,cis}	0.137	2.51	0.05	0.03	0	
Ni _{flat} *(H ₂ O) _{2,atop}	0.675	2.12	0.16	0.19	22	2.71
Ni _{step} *(H ₂ O) _{2,atop}	0.900	2.09	0.13	0.08	28	2.69
Ni _{flat} *(H ₂ O) _{3,atop}	1.26	2.08	0.2	0.25	34	2.72/2.81
Ni _{flat} *(H ₂ O) _{3,bridge}	1.09	2.24	0.2	0.11	72	2.69/2.7

^a Adsorption energies (ΔE) are in eV and are always computed relative to isolated water molecules according to eq 1, such as to include also the hydrogen bonding energy. The Ni–O bond lengths ($d_{\text{Ni-O}}$), the vertical displacements of the binding nickel atom ($\Delta_z(\text{Ni})$), and the lateral displacements of the binding oxygen atom from its optimal position ($\Delta_{xy}(\text{O})$) are given in Å, and the angle between the molecular plane of the adsorbing water molecule and the surface (α) is in degrees. A negative angle means that the hydrogens are pointing toward the surface. For oligomers, the distance between the oxygen atoms ($d_{\text{O...O}}$) is also shown in Å.

(221) direction. The adsorption-enhancing effect of such steps has also been shown very recently by experimental studies of germanium deposition on silicon surfaces.¹⁸

2. Computational Details

We have modeled the flat and stepped surfaces within density functional theory (DFT) as two-dimensional slabs under periodic boundary conditions. We have chosen hexagonal supercells containing 3 (111)-layers for the (221) step and 4 layers for the flat surface, with nickel supercells of 2×2 atoms for the water monomer on the flat surface, 3×3 for the water dimer and trimer on the flat, and 1×2 for the monomer and dimer on the step surface. In all cases, the slabs were separated in the third dimension by about 10 Å of vacuum. Throughout this work, a plane-wave cutoff of 60Ry has been used,¹⁹ together with Troullier-Martins pseudopotentials²⁰ in the Kleinman-Bylander scheme for hydrogen and oxygen as well as a special pseudopotential by Lee²¹ for nickel. All calculations have been done with the PBE exchange-correlation functional.²² The electronic structure has been computed using the implementation of the free energy functional of Alavi.^{23,24} In this approach, a finite-temperature propagator is diagonalized iteratively for the electronic degrees of freedom, ensuring a Fermi distribution function for the occupation levels of the Kohn–Sham orbitals. We have used a $4 \times 4 \times 1$ and a $3 \times 3 \times 1$ k -point mesh within the Monkhorst-Pack scheme²⁵ to sample the Brillouin zone for the step and flat surfaces, respectively. Using this computational setup, we could reproduce the recently published results of Michaelides et al.²⁶ for the adsorption of a highly structured water monolayer with a numerical error of less than 50 meV.

Geometry optimizations were done until the atomic forces dropped below a threshold of $2 \cdot 10^{-3}$ atomic units. This level is sufficiently strict for the considered systems; further optimization changes the total energy by negligible amounts only.²⁷ We have also computed an estimator for the artificial energy lowering due to the periodicity of our simulation cell. An isolated water molecule in our standard box has a total energy which is about 0.01 eV lower than that in a box of twice the lattice constant.

All adsorption energies have been computed with respect to single isolated water molecules in the same simulation box (thus eliminating the dipole interaction error):

$$\Delta E = E[\text{Ni}(\text{H}_2\text{O})_n] - E[\text{Ni}] - nE[\text{H}_2\text{O}] \quad (1)$$

This definition also allows to obtain directly the incremental adsorption energies for an additional water molecule, which would be more involved when considering the adsorption energy of the water cluster as an entity (i.e. when taking $E[(\text{H}_2\text{O})_n]$ instead of $nE[\text{H}_2\text{O}]$).

We have further computed electron density difference maps for selected energetically favorable configurations, showing the rearrangement of the density between the surface-adsorbed $\text{Ni}(\text{H}_2\text{O})_n$ complex and the fragments. For visualizing these maps, we plot color-coded slices with the projected electron density differences $\delta\rho$ defined as

$$\delta\rho(x, z) = \int dy (\rho^{\text{Ni}(\text{H}_2\text{O})_n}(\mathbf{r}) - \rho^{\text{Ni}}(\mathbf{r}) - \rho^{(\text{H}_2\text{O})_n}(\mathbf{r})) \quad (2)$$

Here, in contrast to the definition of the energy difference, the density plots compare the adsorbed system with the water oligomer cluster and the isolated surface. In this way, the density displacements due to the formation of hydrogen bonds between the water molecules are not plotted, while the modifications of these densities due to the adsorption become visible. The density difference maps were computed in orthorhombic cells obtained by doubling the original hexagonal unit cells and by cutting out a suitable orthorhombic subpart of at least the size of the original setup. This was necessary for a proper visualization of the densities with the program MOLEKEL.²⁸

3. Results

3.1. Monomer. The geometry for three typical adhesion sites (“top”, “bridge”, and “hollow”) of a single water molecule on a flat nickel surface was optimized as well as “top” and “bridge” sites on a 221-surface which represents a step defect. Pictograms illustrating the top and bridge geometries on the flat and stepped surfaces are shown in Figures 1 and 2. The corresponding adsorption energies for these configurations which exhibit a (local) minimum of the potential energy

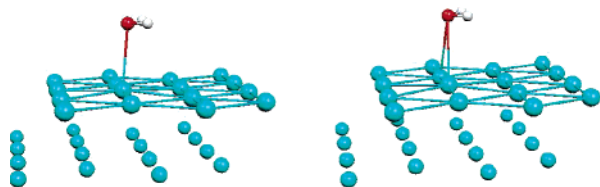


Figure 1. Pictogram of the two adsorption sites for the flat nickel surface which constitute local minima of the potential energy surface: top (left) and bridge (right). The hollow structure turns out to converge toward the top configuration. Only two layers of nickel atoms are shown: the first surface layer is drawn with bonds, the second layer as spheres only.

surface are shown in Table 1. The energies of the top site differ from those of the bridge position by typically a factor of 2 in favor of the top configuration. Since the hollow system relaxed to the top site, it was not considered further. Despite the tetrahedral location of the lone pairs of the oxygen atom, the geometry optimization yields a flat arrangement of the molecule, so that the protons are found at the same distance from the surface as the oxygen (for both flat and step cases).

We have explicitly checked a possible vertical adsorption geometry for the flat surface on the hollow site and a tilted one (with one OH-bond parallel to the surface and the other OH normal to it) on the atop site. For both initial geometries, the optimization yields a flat orientation, and in the case of the hollow site, the oxygen atom also moves over to the atop site. Intermediate adsorption energy values from the optimization process are in the area of 0.1 eV during the turning process. This indicates that when the water molecule approaches the surface vertically, the adsorption strength is roughly half as large as in the parallel orientation. These results are in full agreement with the orientations found by Ranea, Michaelides, and others^{10,11,13} for water configurations on various other metallic surfaces.

Similar to the recently studied case of an adsorbed benzene molecule,¹⁴ the adsorption of a water molecule is significantly stronger on the surface with the step defect than on the flat one. The adsorption energy for the latter is roughly one hydrogen bond (cf. the (H₂O)₂ value in Table 1), while the step provides about twice that attraction. There exists a cis and a trans orientation (both shown in Figure 2) for the step defect, but their adsorption energy is almost the same. Thus, the top position on the step surface reaches the highest energy value, which is also approximately equal to the typical hydrogen bond energy of a 4-fold-coordinated liquid water molecule.

The electron density difference according to eq 2 for both the flat and step surfaces is shown in Figure 3. The plot represents the density of the aggregate minus the sum of the densities of the isolated surface and the water molecule at the top site (trans configuration for the step).

The formation of a weak bond between the surface nickel atom and the oxygen is clearly visible through the displacement in electronic density (dark green and blue regions). To some extent, we also find additional density on top of the water molecule, while relatively little is removed from the central area around the oxygen. Most of the electronic density

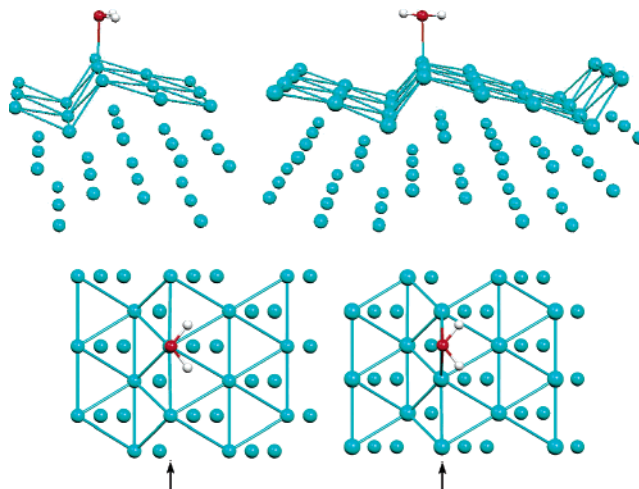


Figure 2. Pictogram of the two adsorption sites for the stepped nickel surface: top/cis (upper left), top/trans (upper right). A comparison with the bridge site is given below, from a top view: top/cis (lower left), and bridge/cis (lower right). As in Figure 1, the atoms of the top layer are drawn with bonds, those of the deeper layers as spheres only.

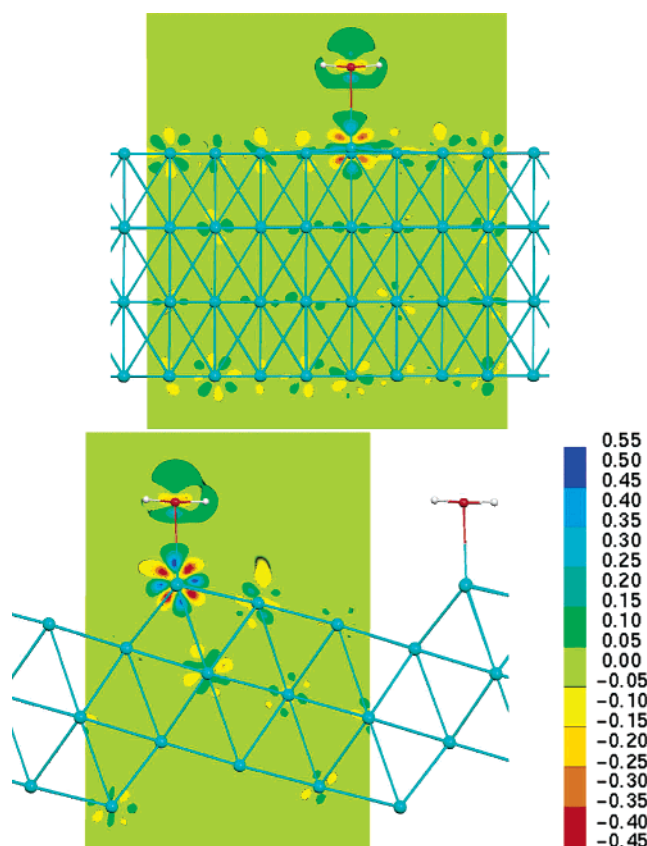


Figure 3. Density difference plots for the adsorption of a water molecule on the flat (top plot, atop configuration) and the step surfaces (bottom plot, atop trans configuration). The scale is given in units of $e/\text{\AA}^2$.

is taken from the bonding nickel atom, which is strongly polarized, and its first neighbors.

Similar to the case of an adsorbed benzene molecule,¹⁴ the polarization of the nickel atom which is bonded to the water molecule is significantly stronger on the step surface

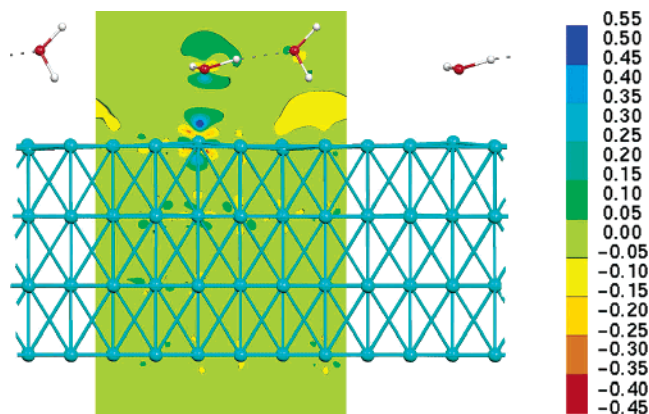


Figure 4. Electron density difference plot for the adsorption of a water dimer on the flat surface.

than on the flat one. This effect also translates into the higher adsorption energy for the latter.

3.2. Dimer. The second step in water adsorption on the surface is the attachment of a second water molecule to the first one. For this purpose, the geometries of a water dimer on the nickel surfaces (flat and with the step defect) have been optimized. Since the monomer adsorption is energetically significantly more favorable on the top site than in the bridge position, only the atop configuration has been considered.

The computed Ni–O bond distances and adsorption energies are shown in Table 1. They are taken relative to isolated water molecules in order to have a common reference for all systems. On both the flat and the step surfaces, the attachment of an additional water molecule to the first one through a hydrogen bond yields an additional 0.43 eV and 0.5 eV, respectively. These energies are about twice as large as it would be expected for a standard hydrogen bond (cf. the water dimer in Table 1), leading again to an adsorption strength that is comparable to that of a water molecule in liquid water. Especially on the step defect, two water molecules attach with an energy that is equivalent to four hydrogen bonds, while still possessing two hydrogen bond acceptor sites (one on each oxygen) and two dangling donor protons.

Thus, the dimer adsorption on the metal surface can energetically compete with the solvation of the second molecule in liquid water, even though the optimized cluster on the surface is not directly comparable to the situation in liquid water due to the high dynamics of the hydrogen bond network at finite temperature.

For the flat surface, a part of this increased energy probably stems from the decreased Ni–O bond distance compared to the water monomer, whereas the step surface does not show this effect.

The analysis of the electronic density difference for the dimer adsorption on the flat surface is shown in Figure 4. According to eq 2, the isolated water dimer is taken as reference system, to suppress the charge difference due to the water–water hydrogen bond and to show rather how much this hydrogen bond is changed due to the adsorption on the surface. The plot reveals that the bonding mechanism of the first water molecule is essentially the same as for the

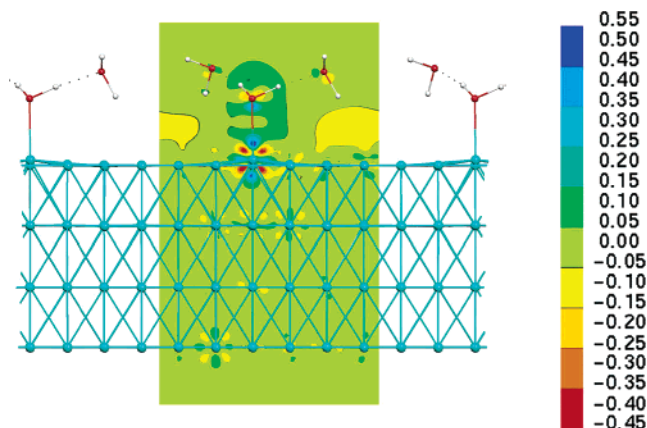


Figure 5. Electron density difference plot for the adsorption of a water trimer on the flat surface.

monomer, except that the charge displacement around the first water is now less symmetric than before. There is a region of strongly increased electron density leading to a Ni–O bond and an additional charge increase on top of the first water molecule. Furthermore, the amount of electronic charge density which is found on top of the bonding Ni atom is significantly stronger than for the water monomer (deep blue color in Figure 4 compared to light blue in Figure 3).

It is interesting to note that the second water molecule does not bind directly to the surface, it is even repelled from it. The second oxygen is not accumulating any electronic density toward the metal surface, and there is a distinguishable region of decreased electron density (yellow color coding) below the hydrogen which points toward the surface. In contrast to this, the hydrogen bond between the two water molecules becomes slightly stronger than in the isolated dimer, as seen by the polarization of the H-bond accepting oxygen.

3.3. Water Trimer on the Flat Surface. The last point in our investigation focuses on the adsorption of a third water molecule onto H₂O dimer on the flat nickel surface. As before, the energy and the bonding distance of the first water are shown in Table 1 for both the bridge and the top sites. The energy difference between bridge and top geometries is conserved upon adsorption of further molecules, implying that the secondary water molecules do not feel any significant influence from the adsorption site of the first one.

It is surprising that the third water increases the total adsorption energy by almost 0.6 eV, thus practically doubling the value of the dimer. This can be explained only in parts by the decreased Ni–O bond length directly. The density difference map of the trimer, which is shown in Figure 5 for the top site, reveals a highly increased electronic charge density in the Ni–O bond region, at the expense of the areas below the dangling protons of the secondary water molecules. Together with a very high polarization of the binding nickel atom as well as slightly stronger hydrogen bonds between the waters, this indicates a much stronger binding of the first oxygen atom.

It is interesting to note that this increased binding of the first water is practically not related to any of its geometric properties but is rather due to the mere presence of secondary water molecules, which constitute a kind of a first solvation

shell. These additional water molecules perturb and repel the electron density at the metal surface in the neighborhood of the initial molecule in such a way that the polarization of the bonding nickel is significantly increased. This phenomenon is already visible for the adsorbed dimer but even stronger in the presence of a third water molecule.

4. Conclusion

We have presented an investigation of the energetic details and the electronic mechanism of the adsorption of water oligomers on nickel surfaces with and without a step defect. The data shown indicates an increased binding strength on the step and in “top” geometries. The findings are in good agreement with previous theoretical and experimental results for similar systems,⁶ where an energetic enhancement of water adsorption was found along step defects on platinum surfaces.

Further, we could show by means of electronic density difference maps that additional water molecules tend to strengthen the nickel–oxygen bond. This effect leads to a significant stabilization of the binding of the first water molecule and to strongly increased binding energies of the dimer and trimer complexes. Not surprisingly, the adhesion of water to nickel surfaces is much weaker than of aromatic molecules such as benzene or phenol,^{14,29,30} but the adsorption energies can definitively compete with those found in liquid water. The second and third water molecule increased the total binding energy by the equivalent of more than two hydrogen bonds each, which correspond to the average binding energy per molecule of standard 4-fold coordinated water.

By means of our study, the initial steps of aqueous wetting of transition metal surfaces can be understood on the basis of electronic effects that govern molecular adsorption.

Acknowledgment. We have profited from fruitful exchange and very helpful discussions with A. Alavi. We also would like to thank P. Blümler for critically reading the manuscript.

References

- (1) Henderson, M. A. *Surf. Sc. Rep.* **2002**, *46*, 1–308.
- (2) Feibelman, P. J. *Science* **2002**, *295*, 99–102.
- (3) Menzel, D. *Science* **2002**, *295*, 58–59.
- (4) Ludwig, R. *Angew. Chem., Int. Ed. Engl.* **2003**, *42*, 3458–3460.
- (5) Mitsui, T.; Rose, M. K.; Fomin, E.; Ogletree, D. G.; Salmeron, M. *Science* **2002**, *297*, 1850–1852.
- (6) Grecea, M. L.; Backus, E. H. G.; Riedmüller, B.; Eichler, A.; Kleyn, A. W.; Bonn, M. *J. Phys. Chem. B* **2004**, *108*, 12575–12582.
- (7) Meng, S.; Xu, L. F.; Wang, E. G.; Gao, S. *Phys. Rev. Lett.* **2002**, *89*, 176104.
- (8) Feibelman, P. *Phys. Rev. Lett.* **2003**, *91*, 059601.
- (9) Meng, S.; Xu, L. F.; Wang, E. G.; Gao, S. *Phys. Rev. Lett.* **2003**, *91*, 059602.
- (10) Michaelides, A.; Ranea, V. A.; de Andres, P. L.; King, D. A. *Phys. Rev. Lett.* **2003**, *90*, 216102.
- (11) Ranea, V. A.; Michaelides, A.; Ramírez, R.; Vergès, J. A.; de Andres, P. L.; King, D. A. *Phys. Rev. B* **2004**, *69*, 205411.
- (12) Cerdá, J.; Michaelides, A.; Feibelman, M.-L. B. P. J.; Mitsui, T.; Rose, M.; Fomin, E.; Salmeron, M. *Phys. Rev. Lett.* **2004**, *93*, 116101.
- (13) Ranea, V. A.; Michaelides, A.; Ramírez, R.; de Andres, P. L.; Vergès, J. A.; King, D. A. *Phys. Rev. Lett.* **2004**, *92*, 136104.
- (14) Delle Site, L.; Sebastiani, D. *Phys. Rev. B* **2004**, *70*, 115401.
- (15) Dahl, S.; Logadottir, A.; Egeberg, R. C.; Larsen, J. H.; Chorkendorff, I.; Törnqvist, E.; Nørskov, J. K. *Phys. Rev. Lett.* **1999**, *83*, 1814.
- (16) Mavrikakis, M.; Bäumer, M.; Freund, H. J.; Nørskov, J. K. *Catal. Lett.* **2002**, *81*, 153.
- (17) Shah, V.; Li, T.; Baumert, K. L.; Cheng, H. S.; Sholl, D. S. *Surf. Sc.* **2003**, *537*, 217.
- (18) Hannon, J. B.; Copel, M.; Stumpf, R.; Reuter, M.; Tromp, R. *Phys. Rev. Lett.* **2004**, *92*, 216104.
- (19) “The plane wave cutoff convergence has been checked on a water dimer geometry optimization at 60Ry and at 100Ry. The resulting hydrogen bond energies are 0.2400eV and 0.2398eV, which represents a difference that lies within the numerical noise of the method. The OH...O distance changes by about 1%, while covalent bond lengths vary even less.”
- (20) Troullier, N.; Martins, J. L. *Phys. Rev. B* **1991**, *43*, 1993.
- (21) Lee, M. Ph.D. Thesis; Cambridge University: 1995.
- (22) Perdew, J.; Burke, K.; Ernzerhof, M. *Phys. Rev. Lett.* **1996**, *77*, 3865.
- (23) Alavi, A.; Kohanoff, J.; Parrinello, M.; Frenkel, D. *Phys. Rev. Lett.* **1994**, *73*, 2599.
- (24) Silvestrelli, P. L.; Alavi, A.; Parrinello, M.; Frenkel, D. *Europhys. Lett.* **1996**, *33*, 551–556.
- (25) Monkhorst, H. J.; Pack, J. D. *Phys. Rev. B* **1973**, *13*, 5188.
- (26) Michaelides, A.; Alavi, A.; King, D. A. *Phys. Rev. B* **2004**, *69*, 113404.
- (27) “The value of $2 \cdot 10^{-3}$ Hartree/bohr corresponding to 0.1 eV/Å for the force convergence describes the maximum component of the forces on all atoms. The commonly cited root-mean-square (rms) force was always below 10^{-3} Hartree/bohr. This remaining force usually arises from metal atoms which are moving on a highly complex (non-parabolic) potential energy hypersurface which is very difficult to optimize. Further optimization does not change the adsorption picture significantly. However, a test calculation has been performed, in which the threshold for the convergence criterion of the geometry optimization was lowered to $3 \cdot 10^{-4}$ atomic units. The resulting change in the total energy was less than 0.05eV.”
- (28) Flükiger, P.; Lüthi, H. P.; Portmann, S.; Weber, J. Molecular visualization program MOLEKEL, version 4.0, Swiss Center for Scientific Computing, Manno, Switzerland, 2000.
- (29) Delle Site, L.; Abrams, C. F.; Alavi, A.; Kremer, K. *Phys. Rev. Lett.* **2002**, *89*, 156103.
- (30) Delle Site, L.; Alavi, A.; Abrams, C. F. *Phys. Rev. B* **2003**, *67*, 193406.

CT0499550

Vibrational Frequencies of Water Adsorbed on (111) and (221) Nickel Surfaces from First Principle Calculations

Tatiana Murakhtina, Luigi Delle Site, and Daniel Sebastiani^{*,[a]}

Transition metal surfaces play a crucial role for many reactions in heterogeneous catalysis. Their catalytic functionality can be affected by a variety of factors, such as the morphology of the surface, defects, or poisoning. The most prominent example of poisoning is the adsorption of CO on platinum and similar surfaces.^[1–3] Another important issue is the co-adsorption of several species, which may have an important influence on dissociation processes.^[3,4]

More generally, the adsorption of small molecules from the environment can significantly modify the catalytic efficiency of such metal surfaces. One particular case, in this scenario, is the adsorption of water. There are many theoretical and experimental studies of the structure and properties of water layers on metal surfaces in the literature.^[5–10] Normally, the presence of a full layer is assumed in these investigations. However, the process of wetting, which is initiated by the adsorption of a single water molecule or small water clusters, is still poorly understood. From the view of an adsorbing water molecule, the surface has to compete thermodynamically with larger water clusters or simply the gas phase. Both phases provide a significantly larger entropic contribution to the free energy, which has to be compensated by a corresponding energy difference. Therefore, the theoretical investigation of the structural and energetic properties of the initial adsorption process on realistically modeled surfaces deserves particular attention.

In particular, the crucial role of surface defects on adsorption processes is not always considered, especially in theoretical studies. Recently, we showed that a simple step defect on the nickel surface has the potential to enhance the adsorption energy of the initial water molecule by as much as 40%.^[11] Also the incremental adsorption energy of an additional second water molecule is higher than at a defect-free adsorption site. In principle, these adsorption energies can be determined experimentally, but spectroscopic parameters are often easier to obtain. First-principle calculations of experimentally accessible spectra are very scarce because of the relatively high computational cost involved in realistic and accurate calculations.

Herein we want to bridge the gap between experiment and theory by providing ab initio calculations of IR peaks as a func-

tion of adsorption sites and cluster sizes, enabling for the first time a direct comparison of measurements and calculations. The initial steps of water adsorption on different nickel surfaces by means of their harmonic frequencies are characterized. The modification of the vibrational modes and frequencies of water clusters (monomer, dimer and trimer) upon adsorption are illustrated and these new vibrational modes involving the nickel-oxygen bond are described. Recent theoretical and experimental studies have shown that both the antisymmetric and the symmetric stretch vibrations can promote catalytic processes such as the chemisorption of methane on nickel,^[12] we investigate how the eigenmodes of the adsorbates can be used as a first step in modeling the dissociation of water which may eventually lead to corrosion and surface passivation.^[13]

Computational Details

We have modeled the flat and stepped surfaces within density functional theory (DFT) under periodic boundary conditions as two-dimensional slabs with a finite thickness. We have chosen hexagonal supercells containing 3 (111)-layers for the (221) step and 4 layers for the flat surface, with nickel supercells of 2×2 atoms for the water monomer on the flat surface, 3×3 for the water dimer and trimer on the flat, and 1×2 for the monomer and dimer on the step surface. The (221) surface has been chosen for modeling the step-defect as it is the smallest possible configuration. This setup ensures that the water oligomers are always separated from their lateral periodic images by at least 5 Å for the step and 7.5 Å for the flat surfaces. In the third dimension, the slabs were separated by about 10 Å of vacuum. Throughout this work, a plane-wave cutoff of 60Ry has been used^[14], together with Troullier-Martins pseudopotentials^[15] in the Kleinman-Bylander scheme. All calculations have been done with the PBE exchange-correlation functional.^[16] The electronic structure has been computed using the implementation of the free energy functional^[17,18] in the CPMD code. We have used a 4×4×1 and a 3×3×1 k-point mesh within the Monkhorst-Pack scheme^[19] to sample the Brillouin zone for the step and flat surfaces, respectively. Using this computational setup, we reproduce the recently published results of Michaelides et al.^[9] for the adsorption of a complete water monolayer within a numerical tolerance of 50 meV.

In our previous work^[11] we made an energy comparison between possible adsorption sites for the water monomer on flat and stepped Ni surfaces. We found that the top configuration is typically a factor of 2 in favor of both cases, while the adsorption energies for the two possible *trans* and *cis* water orientations on the step defect were almost the same. Thus, in this current study we consider the top adsorption site for the flat surface and the top/*trans* site for the defect surface (see Figure 1), both of which are the most energetically favorable configurations.

Geometry optimizations were done until the norm of the atomic forces dropped below a threshold of 4×10^{−4} atomic units. This level is significantly lower than in our previous study^[11] where only energies and geometries were computed. Although this further optimization changes the total energy only by negligible amounts, the accuracy of the calculated vibrational frequencies is very sensitive to the convergence norm of the atomic forces. For the sake of clarity, we did not scale any frequencies with empirical factors. The frequency calculations were done using a finite displacement

[a] T. Murakhtina, Dr. L. Delle Site, Dr. D. Sebastiani
Max-Planck-Institut für Polymer Research
Ackermannweg 10, 55128 Mainz (Germany)
Fax: (+49)6131-379-100
E-mail: murakht@mpip-mainz.mpg.de

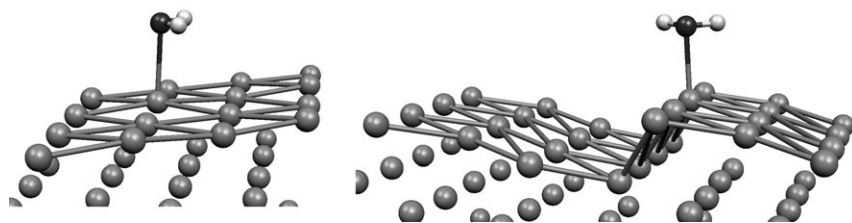


Figure 1. Illustration of the two top adsorption sites for flat and stepped Ni surfaces. All atoms on the top are drawn with bonds, those of the deeper layers are spheres only. For clarity more than one unit cell is shown for the stepped surface.

scheme with a symmetric displacement step of 0.025 Å, considering all water atoms and the nickel atom which is bonded to the first adsorbed water. The coordinates of all other nickel atoms were fixed. We checked that this scheme reproduces the frequencies of the relevant modes within our numerical accuracy, by doing a frequency calculation in which the modes of the six first neighbors of the bonding nickel atom are also included in the dynamical matrix.

fore all vibrational modes of the water clusters on the flat and stepped surfaces are compared with their counterparts of the corresponding optimized clusters in vacuo. This decreases the impact of the numerical errors from the various computational approximations involved in the calculations.

The calculations of IR intensities enable us to detect modes which are symmetry-allowed but have low intensity in the spectrum (silent modes) or those that might be hidden in ex-

Results and Discussion

Our computed harmonic frequencies for free and adsorbed water oligomers are presented in Table 1. While the numerical accuracy is not sufficient for a reliable comparison of absolute frequency values, the calculated trends and differences are more trustworthy since they profit from error cancellations in the computational scheme. There-

Table 1. Calculated vibrational frequencies (in cm^{-1}) of the water molecules illustrated in Figure 4.

Water cluster	System	Mode						
		O-H stretch H free	O-H stretch H bonded	O-H stretch H - Ni	Bending	Other internal modes	Ni-O	Coupled modes
monomer								
1st water	Free	3833a			1586			
		3724s						
	Flat Ni	3664a			1536	513	174	200, 196
		3563s				392		98
	Step Ni	3733a			1544	477	241	196, 155
		3619s				467	112	
dimer								
1st water	Free	3792	3568		1616			
		Flat Ni	3702	3092	1611	887, 607	217	297,188
					404, 318		184, 120	
	Step Ni	3728	3052	1591	990, 559	318	294, 249	
					521, 437		212, 192	
							139, 105	
2nd water	Free	3829a			1589			
		3721s						
	Flat Ni	3750		3449	1558	474, 404		297,148
						318		
	Step Ni	3742		3363	1556	521, 437	161	294, 249
							212, 192	
							139, 105	
trimer								
1st water	Free		3692a		1608			
			3610s					
	Flat Ni		3268a		1636	919, 876	368	237, 188
			3227s			674, 479	337	187, 184
						266, 248		158, 135
2nd water	Free	3842a			1614			
	Flat Ni	3729s						
		3755		3434	1555	479, 374		237, 188
						266, 248	187, 184	
							158	
3rd water	Free	3834a			1653			
	Flat Ni	3722s						
		3747		3419	1547	479, 374		237, 188
						266, 248	187, 184	
							158	

perimental spectra below other more intense peaks. However, for metallic solids (and surfaces) the calculation of IR intensities is not straightforward. This is because the dipole moment in a zero-gap system is difficult to define, even with the help of polarization theory (via maximally localized Wannier-functions) which is nowadays frequently used in insulators.^[20–23] The problem of IR intensities in metallic systems can presently not be addressed within this implementation.

Monomer

For the water monomer, both asymmetric and symmetric bond stretch modes are red shifted, showing the weakening of the OH bonds in the adsorbate when attached to the flat or stepped Ni surface. Although the stretch frequencies on the flat surface are red-shifted by 200 cm^{-1} (Table 1), which is twice as large as the shift on the step defect, the adsorption energy (and thus the Ni–O bond) is stronger for the latter (2.26 Å and 2.12 Å of Ni–O bond length for flat and step case respectively^[11]). This increased adsorption strength, which should lead to a reduced strength in the OH bonds, is also reflected in the Ni–O oscillation, which is at 174 cm^{-1} on the flat surface but at 241 cm^{-1} on top of a defect. However this is not the case, as the flat surface has a stronger repulsive effect on the hydrogens than the stepped one, in which there is more free space between the surface and the protons. This constrains the OH vibrations less than in the flat case. The bending mode is red shifted $\approx 50\text{ cm}^{-1}$, independently of the surface structure.

An interesting difference arises in Ni–H modes. The protons, which are not bonding to the surface (compare to the density difference plots in ref.[11]) may oscillate symmetrically or asymmetrically towards the surface (see Figure 2). On flat Ni, these two modes differ by 120 cm^{-1} while on the step surface, where the distance to the nearest Ni atom is larger for both protons, they are almost indistinguishably. Although this phenomenon is somewhat unexpected, it adequately discriminates the adsorption on the two surface modifications.

Dimer

In the gas-phase water dimer, each molecule has one symmetric and one asymmetric HOH-stretch mode, with slightly lowered frequencies for the hydrogen bond donor. Upon adsorption, the symmetry of these modes is broken and they transform into isolated OH vibrations some of which are illustrated in Figure 3. These vibrations still consist of two high-frequency modes and two at reduced frequency. The former appears

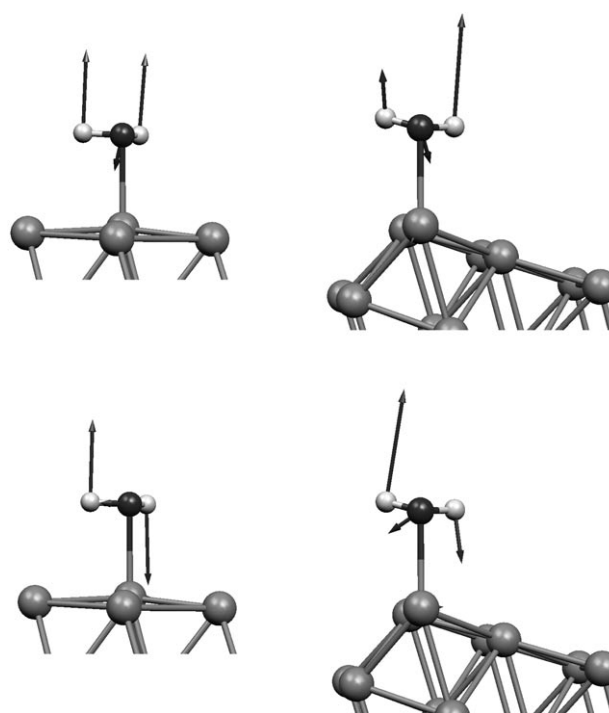


Figure 2. Pictogram of selected Ni–H modes for water monomer adsorbed on the ideal Ni surface (left) and on the Ni surface with the step defect (right). Only the first nickel layer is shown.

around the same frequency as the asymmetric stretch modes of the isolated water dimer, both on the flat surface and on the step. Also for the bending modes, only small differences are visible between the isolated dimer and the two adsorbates. In contrast to this, the four bond stretch modes of the free water dimer are transformed due to the adsorption into individual OH stretch modes, some of which are strongly red-shifted with respect to the vacuum dimer. In particular, the new OH modes of the H-bond acceptor molecule are now split by

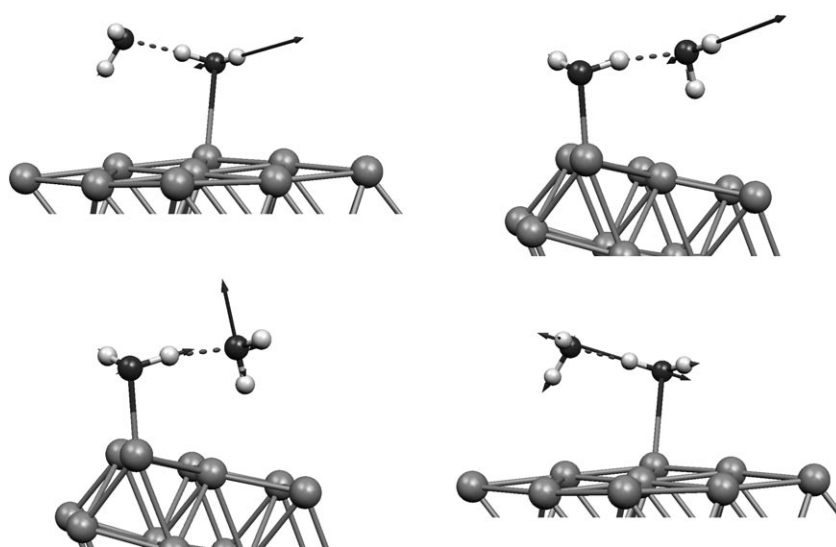


Figure 3. Pictogram of selected isolated OH vibrations for the adsorbed water dimer. Only the first layer of Ni atoms is shown.

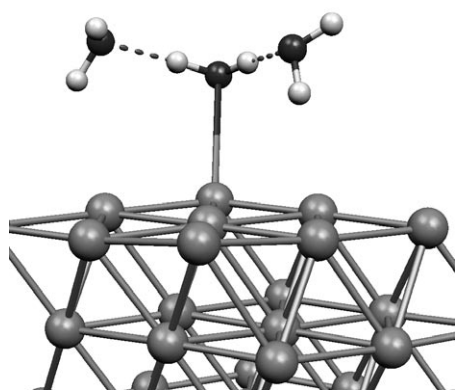


Figure 4. Configuration of the water trimer adsorbed on the flat Ni surface. 1st water (centre molecule) 2nd (left) and 3rd (right) as defined in Table 1.

almost 300 cm^{-1} (3750 cm^{-1} and 3449 cm^{-1}), while its symmetric/antisymmetric modes in vacuo are only split by 100 cm^{-1} (3829 cm^{-1} and 3721 cm^{-1}). The first adsorbed water (H-bond donor) even shows a splitting of 600 cm^{-1} between its OH bond stretches (3702 cm^{-1} and 3092 cm^{-1}), while in the isolated dimer the difference is only 220 cm^{-1} (3792 cm^{-1} and 3568 cm^{-1}). This reflects the fact that the first water molecule is more strongly bonded to the nickel surface than the second one.

All these high-frequency stretch modes, however, are not suitable to discriminate between the flat and the step adsorption site. Taking into account that our estimated numerical errors are of the order of $20\text{--}30\text{ cm}^{-1}$, the frequency differences are too small to draw reliable conclusions about the red- or blue-shift of the different adsorption sites. Only the effect of the actual adsorption is, of course, clearly visible.

This situation changes for some of the other modes involving the heavier atoms. In particular, the frequency of the motion of the protons towards the nickel surface is clearly affected by the adsorption site. The step surface yields a mode which is more than 100 cm^{-1} higher than the corresponding mode on the flat surface. The Ni-O modes at 217 cm^{-1} for the flat surface also increase to a higher frequency of 318 cm^{-1} for the stepped surface. Thus, there is a way to discriminate the two adsorption sites from these vibrations.

The comparison of the dimer adsorption to the monomer is not trivial due to the mixing of the stretch HOH modes. However, when assuming that the dimer's higher/lower-frequency modes correspond to the monomer's asymmetric/symmetric modes, respectively, a trend to lower frequencies for the symmetric vibrations of the dimer can be extracted. The asymmetric modes do not show a significant deviation.

Trimer

For the incremental adsorption of a third water molecule, we consider only the flat surface, as illustrated in Figure 3. As expected from the symmetry of the system, the second and third water molecules have very similar vibrational modes and frequencies, resulting in a quasi-degeneracy of the spectrum.

Comparing to the adsorbed dimer, the OH stretch modes of the free protons appear at about the same frequency ($3700\text{--}3750\text{ cm}^{-1}$), with the exception of those of the H-bond donor protons (3227 and 3268 cm^{-1}). Their stretching modes are about $100\text{--}150\text{ cm}^{-1}$ higher in frequency than the corresponding mode in vacuo (3092 cm^{-1}), which is very similar to the dimer adsorption shift.

The bending modes are almost unchanged, while the Ni-O modes of the central water molecule vibrate more than 100 cm^{-1} higher than for the dimer (337 cm^{-1} and 368 cm^{-1} vs 217 cm^{-1}). This clearly indicates that the Ni-O bond of the first adsorbed water is strengthened due to the arrival of the third molecule (in agreement with changes of Ni-O bond length: 2.26 Å for monomer, 2.12 Å for dimer and 2.08 Å for trimer) as previously reported in ref. [11]. The electronic density which constitutes the weak bond between the surface nickel atom and the oxygen of the adsorbed water is mostly taken from the bonded nickel atom, which is strongly polarized due to the adsorption, and its first Ni neighbors. This bonding mechanism remains essentially the same for all small water clusters that we have studied (compare the density difference plots in ref. [11]).

Comparison with Experiment

There are only few experimental IR studies in the literature about water adsorbed on nickel surfaces.^[24,25] Also, the specific configurations of the investigated adsorbates and their cluster size have a somewhat speculative character. At low coverage $\approx \theta = 0.03$, it can safely be assumed that only monomolecular clusters are formed, while at high coverage ($\theta = 0.66$), the water is found in a hexagonal close-packed structure,^[25] the so-called ice-like bilayer. The details of the water structure at intermediate coverages are not known with certainty and in experimental studies, the assignment of frequencies to modes and even to oligomers is based on experience. Thus, a direct assignment of the frequencies to our calculated IR signatures is not possible. However, a comparison of the set of computed frequencies with the experimental spectra allows the structural features about intermediate water coverages to be obtained. For the lowest coverage that presumably corresponds to adsorbed water monomers,^[25] the agreement with the experimentally observed red shift of the IR frequencies due to the adsorption is reasonably good for the flat Ni surface. In contrast to this, the experimental spectrum does not fit to the set of frequencies computed for an adsorption on the step site (Table 2).

The IR frequencies using the deuterium mass are calculated in order to compare to the IR study of refs. [24,25]. Table 3 shows the frequencies obtained for the water oligomers, to-

Table 2. Adsorption red shift of the vibrational modes (in cm^{-1}).

Mode	Flat Ni (calc)	Step Ni (calc)	Ni (exp) ^[25]
Assym. stretch	169	100	181
Symm. stretch	161	105	
Bending	50	42	18

Table 3. Comparison of calculated IR frequencies (in cm^{-1}) for the deuterated water oligomers on the flat Ni surface with experimental spectra.

D ₂ O oligomers (calculated)		D ₂ O clusters (experiment)				
		Experiment ^[24]		Experiment ^[25] coverage		
monomer	trimer	monomer	trimer	0,03	0,1	0,33
	stretching					
2684	2738	2765	2738		2701	2696
	2731	2655			2632	2638
2567	2488		2580		2562	2560
	2480			2474	2456	2460
	2400				2453	2434
	2327					
	bending					
1125	1191			1116	1186	1190
	1138				1175	
	1133					

gether with the experimental IR lines at $\theta=0.03$, $\theta=0.1$ and $\theta=0.33$ coverage. Although a perfect match is not obtained, a reasonable agreement with the calculated spectra is found. The experimental lines around 2562 cm^{-1} are not among our computed dimer and trimer frequencies, but only obtained in the monomer calculation. This might indicate that even at coverages as high as $\theta=0.33$, where most of the surface is covered by larger clusters, there are still a few isolated molecules left on the surface. On the other hand, the relatively low-lying peaks around 2430 cm^{-1} and 2460 cm^{-1} at $\theta=0.1$, provide evidence that already at low coverage, some clusters of more than one water molecule have formed on the surface. Based on the present computational and experimental studies, we cannot say with certainty whether this is a genuine phenomenon. It may be a sign of disorder in the water structure or of defects of the surface structure in the experiments, but equally well it might represent a computational artifact due to our limited cluster size. In any case, this question deserves further investigation, computationally and experimentally.

Conclusions

We have presented an investigation of vibrational properties of water oligomers adsorbed on flat and stepped Ni surfaces. We show that a step, which is the simplest possible surface defect, influences significantly the vibrational modes and frequencies of the small adsorbed clusters as well as the shift in frequencies due to the adsorption.

To our best knowledge, our study is the first direct comparison of calculated and measured IR spectra. Although the

agreement with experiment is qualitative, our accuracy is sufficient to characterize vibrational modes and distinguish between relevant adsorption sites and sizes of adsorbed clusters.

Keywords: ab initio calculations • IR spectroscopy • surface analysis • transition metals • water chemistry

- [1] T. H. M. Housman, J. M. Feliu, R. Gomez, M. T. M. Koper, *ChemPhysChem* **2005**, *6*, 1522.
- [2] D. L. S. Nieskens, D. C. Ferre, J. W. Niemantsverdriet, *ChemPhysChem* **2005**, *6*, 1293.
- [3] D. C. Ferre, A. P. van Bavel, J. W. Niemantsverdriet, *ChemPhysChem* **2005**, *6*, 473.
- [4] O. R. Inderwildi, D. Lebiez, O. Deutschmann, J. Warnatz, *ChemPhysChem* **2005**, *6*, 2513.
- [5] P. A. Thiel, T. E. Madey, *Surf. Sci. Rep.* **1987**, *7*, 211.
- [6] M. A. Henderson, *Surf. Sci. Rep.* **2002**, *46*, 1.
- [7] J. S. Filhol, M. Neurock, *Angew. Chem.* **2006**, *118*, 416; *Angew. Chem. Int. Ed.* **2006**, *45*, 402.
- [8] R. Ludwig, *Angew. Chem.* **2003**, *115*, 3580; *Angew. Chem. Int. Ed.* **2003**, *42*, 3458.
- [9] A. Michaelidis, A. Alavi, D. A. King, *Phys. Rev. B* **2004**, *69*, 113404.
- [10] S. Yamamoto, A. Beniya, K. Mukai, Y. Yamashita, J. Yoshinobu, *J. Phys. Chem. B* **2005**, *109*, 5816.
- [11] D. Sebastiani, L. Delle Site, *J. Chem. Theory Comput.* **2005**, *1*, 78.
- [12] P. Maroni, D. C. Papageorgopoulos, M. Sacchi, T. T. Dang, R. D. Beck, T. R. Rizzo, *Phys. Rev. Lett.* **2005**, *94*, 246104 and references therein.
- [13] H. Zaidi, H. Nery, D. Paulmier, *Appl. Surf. Sci.* **1993**, *70*, 180.
- [14] The plane wave cutoff convergence has been checked on a water dimer geometry optimization at 60 Ry and at 100 Ry. The resulting hydrogen bond energies are 0.2400 eV and 0.2398 eV, which represents a difference that lies within the numerical noise of the method. The OH...O distance changes by $\approx 1\%$, while covalent bond lengths vary even less.
- [15] N. Troullier, J. L. Martins, *Phys. Rev. B* **1991**, *43*, 1993.
- [16] J. Perdew, K. Burke, M. Ernzenhof, *Phys. Rev. Lett.* **1996**, *77*, 3865.
- [17] A. Alavi, J. Kohanoff, M. Parrinello, D. Frenkel, *Phys. Rev. Lett.* **1994**, *73*, 2599.
- [18] P. L. Silvestrelli, A. Alavi, M. Parrinello, D. Frenkel, *Europhys. Lett.* **1996**, *33*, 551.
- [19] H. J. Monkhorst, J. D. Pack, *Phys. Rev. B* **1973**, *13*, 5188.
- [20] N. Marzari, D. Vanderbilt, *Phys. Rev. B* **1997**, *56*, 12847.
- [21] R. Resta, *Phys. Rev. Lett.* **1998**, *80*, 1800.
- [22] R. Resta, D. Ceresoli, T. Thonhauser, D. Vanderbilt, *ChemPhysChem* **2005**, *6*, 1815.
- [23] P. L. Silvestrelli, M. Bernasconi, M. Parrinello, *Chem. Phys. Lett.* **1997**, *277*, 478.
- [24] L. Fredin, B. Nelander, G. Ribbegard, *J. Chem. Phys.* **1977**, *66*, 4065.
- [25] M. Nakamura, M. Ito, *Chem. Phys. Lett.* **2004**, *384*, 256.

Received: November 21, 2005

Revised: March 7, 2006

Published online on May 3, 2006

Solvent molecules trapped in supramolecular organic nanotubes: a combined solid-state NMR and DFT study

Anke Hoffmann^a, Daniel Sebastiani^a, Erli Sugiono^a, Sungoo Yun^b,
Kwang S. Kim^b, Hans Wolfgang Spiess^a, Ingo Schnell^{a,*}

^a Max-Planck-Institute for Polymer Research, NMR Division, Postfach 3148, 55021 Mainz, Germany

^b Division of Molecular and Life Sciences, Department of Chemistry, National Creative Research Initiative Center for Superfunctional Materials, Pohang University of Science and Technology, Pohang 790-784, South Korea

Received 24 November 2003; in final form 16 February 2004

Published online: 20 March 2004

Abstract

When crystallised from water/acetone mixtures, calix[4]hydroquinone (CHQ) forms supramolecular nanotubes which we studied by NMR spectroscopy and DFT calculations, using the ¹H and – for the first time – ²H chemical-shift resolution achievable in the solid state under fast (30 kHz) magic-angle spinning. Acetone molecules are trapped in the bowl-shaped CHQ molecules inside the tubes and hydrogen-bonded to an extended chain of hydrogen bonds, which is formed by CHQ and water molecules along the tube axis. Both water and acetone molecules occupy well-defined average positions, but undergo fast reorientation motions during which their protons interchange their positions.

© 2004 Elsevier B.V. All rights reserved.

1. Introduction

In nanotechnology, concepts of supramolecular self-assembly and self-organisation have attracted considerable interest as a means to build structures on the nanoscale. A particularly active field of research is concerned with organic and inorganic nanotubes. Besides the wealth of research carried out on covalently bonded architectures, recent work is devoted to supramolecular tubular assemblies which offer template functionalities for the design of nanoscale materials. In our work, we investigate self-assembled organic nanotubes composed of nontubular subunits of calix[4]hydroquinone (CHQ)[1,2], which combine a tubular structure with an strong electrochemical reduction potential and can therefore be used as templates for building silver nanowires [3,4].

In the nanotubes, the CHQ molecules (Fig. 1a,b) adopt a bowl-shaped conformation (Fig. 1a,c), which is well known from related calix[4]arenes [5,6]. It is stabilised

by the four inner hydroxyl groups which form a circular proton tunneling resonance of hydrogen bonds at the bottom of each bowl (Fig. 1b). The tubes (Fig. 1d,e) are built from stacks of CHQ molecules which are tied together at their upper rims through extended one-dimensional arrays of –O–H···O hydrogen bonds. Each of these arrays consists of a well-defined sequence of water and the hydroxyl groups. Due to this arrangement, the CHQ bowls are open towards the inner part of the tubes, and one proton per bridging water molecule is potentially available for additional hydrogen bonding. Experimentally, the CHQ nanotubes are grown from a mixture of water and acetone [2,4]. The needlelike crystals have been characterised by X-ray crystallography [1] (Fig. 1).

Calix[4]arenes are well-known host molecules with a pronounced capability of including small guest molecules [5,6]. Therefore, the question arises whether the tubes are actually hollow or whether another species is trapped inside the CHQ bowls. X-ray data, however, cannot provide clear evidence for the presence of guests such as acetone [7–9] and water [10,11], because disordered or mobile species cannot be observed. Therefore,

* Corresponding author. Fax: +49-613-137-9100.

E-mail address: schnelli@mpip-mainz.mpg.de (I. Schnell).

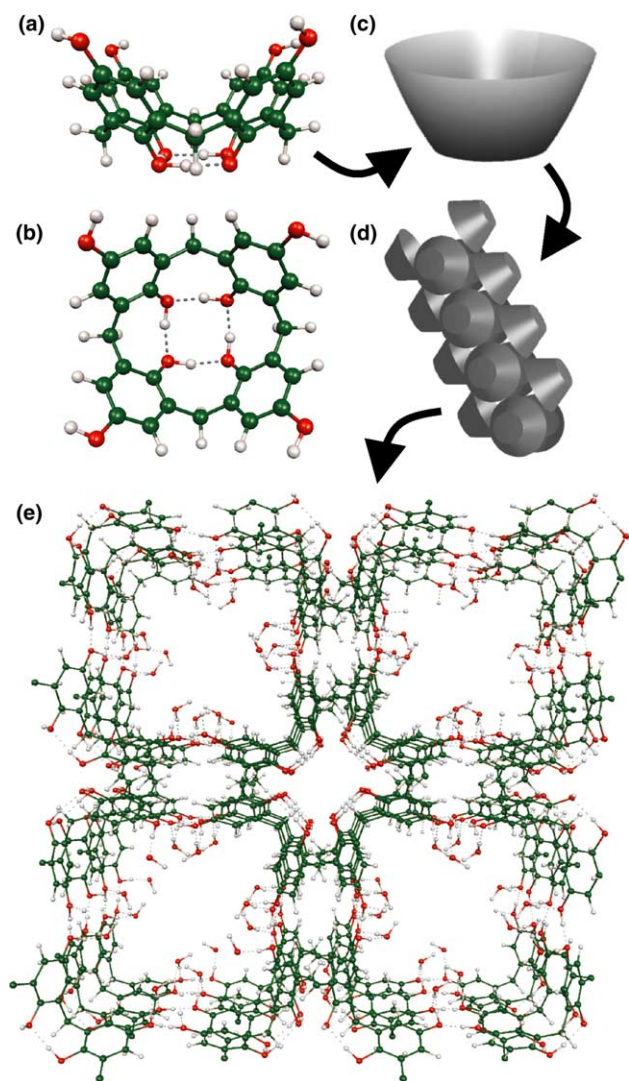


Fig. 1. (a) Bowl-shaped conformation of calix[4]hydroquinone (CHQ), (b) stabilised by a ring of four hydrogen bonds at the bottom of each bowl. (c,d) Self-assembly of the CHQ bowls into nanotubes. (e) Crystal structure of the CHQ nanotubes which have a $17 \text{ \AA} \times 17 \text{ \AA}$ cross-section with a $6 \text{ \AA} \times 6 \text{ \AA}$ pore (with the van der Waals volume excluded).

we performed ^1H and ^2H solid-state NMR experiments which were supplemented by ab initio MP2 and DFT calculations of NMR parameters [12–16].

2. Experiments, samples and computational details

All NMR spectra were recorded on a Bruker Avance spectrometer operating at Larmor frequencies of 700.12 and 107.49 MHz for ^1H and ^2H , respectively. Magic-angle spinning (MAS) was applied at 30 kHz to enhance spectral resolution, and the spin system was manipulated using $\pi/2$ radiofrequency (RF) pulses of 2.5 μs length. Dipolar ^1H – ^1H double-quantum (DQ) coherences were excited using the back-to-back pulse se-

quence [17,18]. In the two-dimensional version of the DQ experiment, the DQ coherences evolve according to the sum of the chemical shifts of the two protons involved in the coherence, while no such evolution takes place in the one-dimensional double-quantum filtered (DQF) version.

CHQ was synthesised from *p*-tert-butylphenol following the procedure given in [19–21]. Prior to reduction with $\text{Na}_2\text{S}_2\text{O}_7$, the calix[4]quinone was recrystallised from THF and purified by chromatography on silica gel using ethylacetate as solvent. Finally, the crude brownish CHQ product was purified using a soxhlet extractor and methanol as solvent. CHQ nanotubes were crystallised from mixtures of acetone and water, from acetone and deuterated water (D_2O), and from deuterated acetone (D_6 -acetone) and water.

To aid the interpretation of the experimental data, ^1H NMR spectra were calculated within DFT using a fully periodic description of the systems [15,16] within the pseudopotential plane wave programme package CPMD [22]. The atomic coordinates were initially taken from X-ray data and subsequently relaxed until the forces fell below 10^{-3} atomic units, using pseudopotentials of Goedecker type [23] and a plane wave cutoff of 70 Ry. The BLYP gradient-corrected exchange-correlation functional [24,25] was applied in all calculations. The shieldings so obtained were referenced to tetramethylsilane values calculated under the same computational conditions.

3. Results and discussion

The experimental ^1H MAS NMR spectrum of the CHQ nanotubes is shown in Fig. 2a. Based on typical values of ^1H chemical shifts, the signals at 10, 6.5 and 2 ppm can be ascribed to the CHQ hydroxyl, aromatic and methylene protons, respectively. The resonance position of the hydroxyl protons at 10 ppm is shifted downfield, which is characteristic for protons involved in hydrogen bonds. The two relatively sharp lines at 0.5 and 4.5 ppm, however, cannot be readily assigned.

The calculated spectrum shown in Fig. 2b confirms the assignment of the CHQ signals. In the case of the hydroxyl protons, the calculation yields two separated resonances for: (i) the four protons forming the strong ring-shaped hydrogen bonds at the bottom of the CHQ cones and (ii) the four hydroxyl protons at the rim which are involved in the extended chain of hydrogen bonds along the tubes. Experimentally, however, the spectral resolution does not allow for this distinction among the hydroxyl resonances. The methylene proton resonances are found to be spread over a range from about 2 up to 5 ppm, which includes considerable downfield shifts due to ‘ring current effects’ arising from the π electrons of the aromatic rings in neighbouring CHQ.

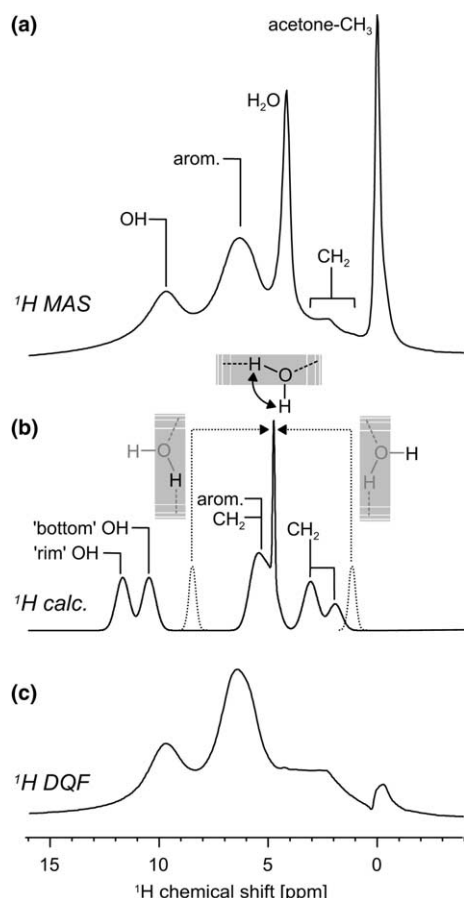


Fig. 2. ^1H solid-state NMR spectra of CHQ nanotubes. (a) Spectrum recorded under 30 kHz MAS. (b) Calculated ^1H spectrum of the CHQ nanotubes without further guest molecules. The two protons of the water molecules in the 1D hydrogen-bonded chain give rise to two separated lines which have been averaged in order to account for fast motional processes in which the two protons interchange their positions. A broadening has been applied to all resonances by means of appropriate Gaussian convolutions. (c) ^1H - ^1H double-quantum filtered (DQF) spectrum, recorded under 30 kHz MAS using one rotor period for excitation and reconversion of ^1H - ^1H DQ coherences.

Experimentally, this spread is reflected by the broad methylene line which is not resolved and cannot be assigned to a single ppm-value.

Turning to the water molecules, the calculations yield two separated ^1H resonances at 8.5 and 1 ppm, which belong to the same water molecule and arise from the proton involved in the hydrogen bonding and from the other proton dangling freely inside the tube. Experimentally, an intense resonance is observed at 0.5 ppm (Fig. 2a), which could correspond to the 'free' protons of the water molecules, but there is no counterpart resonance at around 8.5 ppm. Moreover, the thermal energy at room temperature is expected to cause fast reorientation motions of the small water molecules. Thereby, the two protons interchange their positions and average their resonance frequencies to about 4.8 ppm, which corresponds to the rather sharp signal at 4.5 ppm in the experimental spectrum.

Accidentally, about the same chemical shift would be observed for water in a liquid bulk phase. However, the tubes investigated in this study were dried under moderate conditions after crystallisation to remove residual amounts of volatile solvent. Exposing the tubes to more drastic heat and vacuum conditions, we found that signal losses at 4.5 ppm are always associated with a highfield shift of the hydroxyl signal and changes over the whole spectrum. This indicates that the network of hydrogen bonds is directly affected and, after intense heat and vacuum treatment, even destroyed. Therefore, our samples do not contain significant amounts of liquid-like bulk water inside the tubes, which could be removed without affecting the tube structure.

To take a closer look at molecular mobilities, a ^1H - ^1H DQF spectrum was recorded using a back-to-back pulse sequence with one rotor period excitation (i.e., 33 μs at 30 kHz MAS). In this experiment, signals are only observed for protons that experience strong homonuclear dipole-dipole couplings and, therefore, belong to immobile molecules, while the signals of mobile species are suppressed. As shown in Fig. 2c, the two narrow lines at 4.5 and 0.5 ppm basically disappear from the DQF spectrum, and only the signals of the (rigid) CHQ molecules remain. Firstly, this finding confirms the assumption that the water molecules in the CHQ crystals undergo fast reorientation motions. Secondly, the DQF spectrum provides evidence that the other narrow resonance line at 0.5 ppm also arises from a species with a pronounced mobility on the $<\mu\text{s}$ time-scale, as is typically encountered for solvent molecules.

To identify this second mobile species, CHQ nanotube crystals were grown from solvent mixtures with one component deuterated, i.e., D_2O /acetone and $\text{H}_2\text{O}/\text{D}_6$ -acetone. The ^1H spectra of the two samples are shown in Fig. 3a,b, respectively. When using D_2O , the narrow signal at 4.5 ppm disappears almost completely from the ^1H spectrum, which again confirms the above interpretation.

When growing the CHQ tubes from $\text{H}_2\text{O}/\text{D}_6$ -acetone, the ^1H spectrum no longer shows the intense signal at 0.5 ppm (Fig. 3b). Correspondingly, the ^2H spectrum of the same sample exhibits exactly (and only) this signal (Fig. 3c), which provides clear evidence that the peak at 0.5 ppm arises from the methyl groups of acetone. The slight shoulder at about 0 ppm indicates the presence of more than one species of acetone molecules in the crystals, which probably differ slightly in their motional properties and in the average position they occupy in the nanotube structure. Interestingly, for various samples grown from $\text{H}_2\text{O}/\text{D}_6$ -acetone mixtures, the water resonance at about 4.5 ppm was found to be strongly reduced, too. Provisionally, we ascribe this effect to chemical proton-deuteron exchange processes which are currently under further investigation.

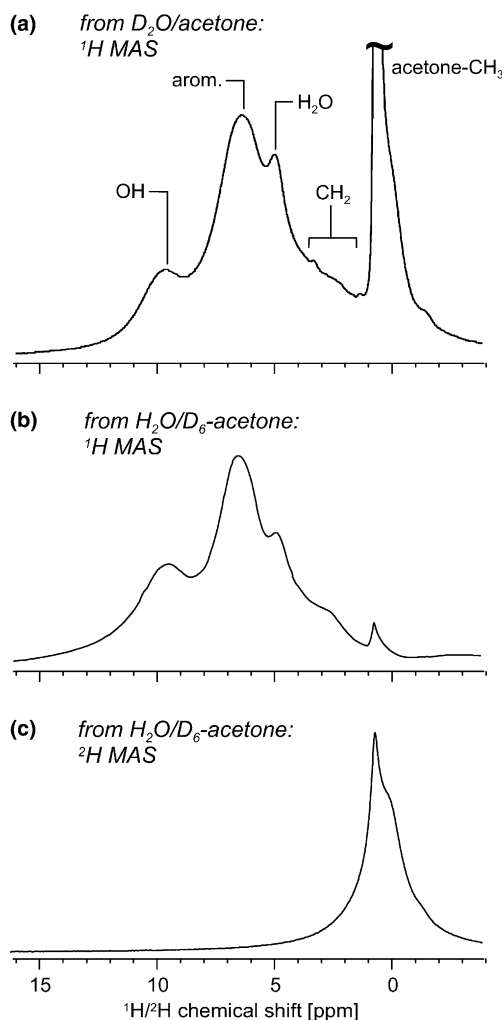


Fig. 3. The 30-kHz MAS spectra of CHQ nanotube crystals grown from solvent mixtures with one component deuterated. (a) 1H MAS spectrum of CHQ tubes grown from D_2O /acetone. (b) 1H MAS spectrum and (c) 2H MAS spectrum of CHQ tubes grown from H_2O/D_6 -acetone.

Thus, we conclude that acetone is present in the CHQ nanotube crystals. The acetone molecules are mobile, but occupy an average position at which they experience aromatic ring current effects that cause an upfield shift of their signal by about -2.5 ppm. Recalling the typical shielding effects of benzene rings, this implies a position of the acetone methyl groups above (and not beside) the aromatic ring planes, which means that the methyl groups stick inside the CHQ bowls. This calls for a spatial proximity between the acetone methyl groups and the CHQ aromatic rings which can, using solid-state MAS NMR, be readily identified from two-dimensional 1H - 1H DQ spectra. The DQ signals are indicative for proton-proton distances below 4 Å in rigid systems, when the experiment is performed under fast MAS conditions with short excitation times (i.e., \leq one rotor period) [18]. Indeed, the 1H - 1H DQ spectrum of the

CHQ tubes (Fig. 4) clearly shows a DQ signal which involves the acetone methyl protons and the CHQ phenyl protons. Thus, the acetone molecules do not form a separated phase, but are in close contact with the aromatic rings in the CHQ nanotube.

These observations show that acetone molecules are trapped inside the CHQ bowls (Fig. 5a,c) of the nanotubes. Such trapping phenomena are very well known in the context of calix[4]arenes [5–9].

Assuming such an acetone/CHQ/water arrangement, we have optimised the geometry of a CHQ/acetone complex at the MP2 level using a 6-31G basis set and computed the BSSE-corrected MP2-adsorption energy using a 6-31G(d) basis with the G98 code [26]. In order to separate the dispersion attraction from the hydrogen bonding energy, a full and a partial geometry optimization were done, the former only relaxing the intramolecular degrees of freedom of the two fragments. We found a van der Waals interaction of about 12 kJ/mol and a full adsorption energy (including a hydrogen bond between CHQ and acetone) of 68 kJ/mol. This energy is sufficiently strong to support the hypothesis of a preferential position of the acetone molecule in the center of the CHQ bowls of the nanotube, in agreement with the recent findings of [27].

The energy hypersurface is very flat and rich in local minima. Thus, for a complete analysis of the finite temperature NMR chemical shifts, one would have to

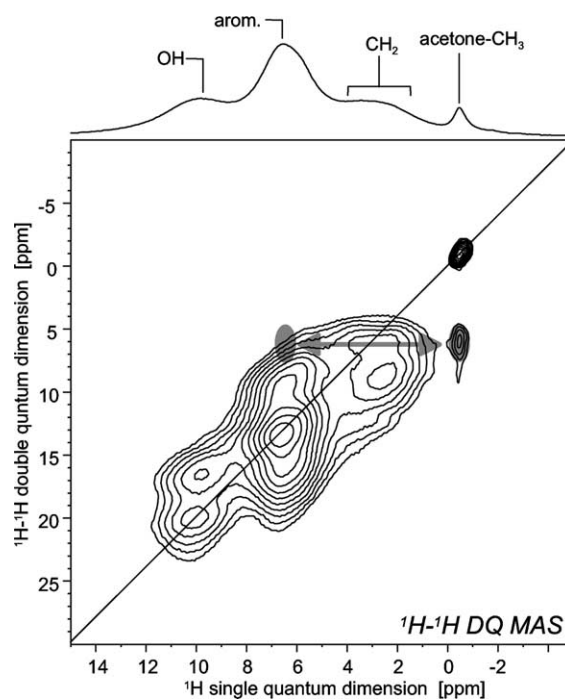


Fig. 4. 1H - 1H double-quantum (DQ) NMR spectrum of CHQ nanotube crystals, recorded under 30 kHz MAS using one rotor period of back-to-back recoupling for excitation and reconversion of the DQ coherences.

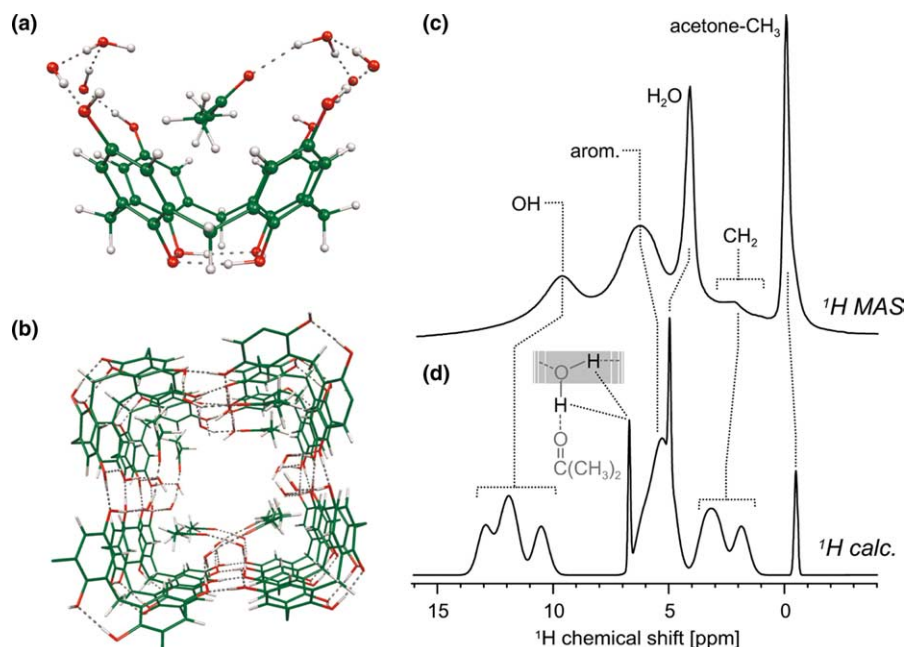


Fig. 5. (a) Representation of a bowl-shaped CHQ molecule taken out of the nanotube crystal structure (i.e., with hydrogen-bonded water molecules attached). An acetone molecule is trapped inside the CHQ bowl with its carbonyl oxygen hydrogen-bonded to an available water proton. (b) Representation of a unit cell of the CHQ nanotube filled with acetone molecules. (c) Experimental ^1H spectrum of CHQ nanotube crystals. (d) Calculated spectrum using the CHQ nanotube crystal structure filled with acetone molecules (shown in b). All chemical shifts of methyl and water protons have been averaged. Different Gaussian line broadening was applied for the signals of rigid (nanotube) and mobile (water, acetone) atoms.

resort to a statistical sampling as in [28], which is beyond the scope of this Letter. Instead, a representative acetone position was taken from the partial geometry optimization done at the MP2 level, and inserted in the periodic nanotube. Four acetone molecules were placed inside a unit cell, which corresponds to filling each CHQ bowl with one acetone molecule. Their exact positions were slightly randomised to yield a better statistics of the chemical shifts, which were subsequently averaged. Intrinsic errors in the calculations (such as the use of DFT, incomplete basis sets, pseudopotential approximation, and especially the neglect of temperature effects) may lead to an estimated error margin of 1–2 ppm.

The calculated ^1H spectrum is shown in Fig. 5d. To account for molecular mobilities, the parameters were averaged over all protons belonging to the same acetone and water molecule, respectively, and little Gaussian broadening was applied to these lines. In comparison to

the spectrum calculated without acetone (Fig. 2b), three major differences are obvious: (i) The methyl protons of acetone give rise to an additional resonance line at 0.5 ppm, which fully reproduces the experimental observation (see Fig. 5c). (ii) For water molecules with and without acetone being hydrogen-bonded to them, different average ^1H shifts of 6.8 and 5 ppm, respectively, are found. Without acetone, averaging takes place between two shifts of about 8.5 and 0.5 ppm for hydrogen-bonded and free protons, respectively, as discussed above. With acetone, both water protons have chemical shifts of 6, ..., 7.5 ppm, because the hydrogen bond of one water proton to the acetone carbonyl oxygen weakens the other two hydrogen bonds in which the water molecule is involved in the one-dimensional chain. (iii) The shifts of the hydroxyl protons are affected by the acetone through a weakening of the rim-OH network, causing a slight geometrical rearrangement and in

Table 1

Experimental and calculated values of the ^1H NMR chemical shifts of the CHQ tubes, along with those of the trapped acetone

^1H chemical shifts	Experiment (ppm)	Calculation empty tube (ppm)	Calculation tube with acetone (ppm)
CHQ tube aliphatic	2–5	1.5; 3.0; 5.0	1.5; 3.0; 5.0
CHQ tube aromatic	6.5	5.6	5.6
CHQ tube rim-OH	10.0	11.7	11.3
CHQ tube bottom-OH	10.0	10.4	11.6
H_2O	4.5	1.5; 8.3	1.5–10
Acetone CH_3	0.5	–	–0.7

The presence of several values for a single proton species indicates topologically different protons of the same molecule.

particular a strengthening of the bottom OH group (see Table 1).

4. Conclusions

In nanotube crystals grown from solutions of CHQ in water/acetone mixtures, the solvent molecules play an important role in terms of structure formation as well as composition of the materials. Fast-MAS ^1H and ^2H solid-state NMR spectra and DFT calculations confirm that water molecules link the CHQs through extended one-dimensional chains of $\cdots\text{O}-\text{H}\cdots$ hydrogen bonds. In addition, our investigations prove that acetone is trapped in the CHQ bowls inside the tubes and, moreover, attached to the extended hydrogen-bonded chain via a carbonyl-water hydrogen-bond. Both water and acetone molecules occupy well-defined average positions, but undergo fast reorientation motions in the course of which their protons interchange their positions and average their chemical shifts. A more detailed study focusing on the dynamics of the acetone and water molecules including chemical exchange processes is currently underway.

Our work shows how the combination of solid-state NMR performed under fast MAS conditions and DFT calculations can provide substantial information on the presence and properties of disordered and/or mobile species in supramolecular structures, such as crystalline nanotubes. Using ^1H and – for the first time – ^2H chemical shifts in the solid state, simple MAS NMR experiments can complement X-ray studies to elucidate both long-range order properties as well as phenomena of disorder and molecular dynamics.

Acknowledgements

The authors thank Dr. Jochen Gutmann for providing X-ray data of the nanotubes. Financial support by the DFG through the SFB 625 in Mainz is gratefully acknowledged.

References

- [1] B.H. Hong, J.Y. Lee, C.-W. Lee, J.C. Kim, S.C. Bae, K.S. Kim, *J. Am. Chem. Soc.* 123 (2001) 10748.
- [2] B.H. Hong, S.C. Bae, C.-W. Lee, S. Jeong, K.S. Kim, *Science* 294 (2001) 348.
- [3] K.S. Kim, *Cur. Appl. Phys.* 2 (2002) 65.
- [4] K.S. Kim, S.B. Suh, J.C. Kim, B.H. Hong, E.C. Lee, S. Yun, P. Tarakeshwar, J.Y. Lee, Y. Kim, H. Ihm, H.G. Kim, J.W. Lee, J.K. Kim, H.M. Lee, D. Kim, C. Cui, S.J. Youn, H.Y. Chung, H.S. Choi, C.-W. Lee, S.J. Cho, S. Jeong, J.-H. Cho, *J. Am. Chem. Soc.* 124 (2002) 14268.
- [5] A.F.D. de Amor, R.M. Cleverley, M.L. Zapata-Ormachea, *Chem. Rev.* 98 (1998) 2495.
- [6] A. Ikeda, S. Shinkai, *Chem. Rev.* 97 (1997) 1713.
- [7] R. Ungaro, A. Pochini, G.D. Andreotti, V. Sangermano, *J. Chem. Soc., Perkin Trans. 2* (1984) 1979.
- [8] G.Y. Lu, F. Liu, Y.J. Liu, W.J. He, Q. Li, L.G. Zhu, *J. Chem. Cryst.* 29 (1999) 1121.
- [9] G.Y. Lu, W. Song, X.B. Wan, *J. Chem. Cryst.* 30 (2000) 185.
- [10] P.M. Zhang, Z.T. Huang, *Acta Chem. Sin.* 50 (1992) 209.
- [11] P.C. Leverd, P. Bethault, M. Lance, M. Nierlich, *Eur. J. Org. Chem.* 1 (2000) 133.
- [12] S.P. Brown, H.W. Spiess, *Chem. Rev.* 101 (2001) 4125.
- [13] S.P. Brown, T. Schaller, U.P. Seelbach, F. Koziol, C. Ochsenfeld, F.-G. Klärner, H.W. Spiess, *Angew. Chem., Int. Ed.* 40 (2001) 717.
- [14] C. Ochsenfeld, F. Koziol, S.P. Brown, T. Schaller, U.P. Seelbach, F.-G. Klärner, *Solid-State Nucl. Magn. Reson.* 22 (2002) 128.
- [15] D. Sebastiani, M. Parrinello, *J. Phys. Chem. A* 105 (2001) 1951.
- [16] D. Sebastiani, G. Goward, I. Schnell, H.-W. Spiess, *J. Mol. Struct. (Theochem)* 625 (2003) 283.
- [17] M. Feike, D.E. Demco, R. Graf, J. Gottwald, S. Hafner, H.W. Spiess, *J. Magn. Reson. A* 122 (1996) 214.
- [18] I. Schnell, H.W. Spiess, *J. Magn. Reson. Adv. Magn. Reson.* 151 (2001) 153.
- [19] C.D. Gutsche, M. Iqbal, D. Stewart, *J. Org. Chem.* 51 (1986) 742.
- [20] C.D. Gutsche, J.A. Levine, *J. Am. Chem. Soc.* 104 (1982) 2652.
- [21] Y. Morita, T. Agawa, *J. Org. Chem.* 57 (1992) 3658.
- [22] J. Hutter et al., Computer code CPMD, version 3.8. Copyright IBM Corp. and MPI-FKF Stuttgart 1990–2003, <http://www.cpmd.org>.
- [23] S. Goedecker, M. Teter, J. Hutter, *Phys. Rev. B* 54 (1996) 1703.
- [24] A.D. Becke, *Phys. Rev. A* 38 (1988) 3098.
- [25] C. Lee, W. Yang, R.G. Parr, *Phys. Rev. B* 37 (1988) 785.
- [26] M.J. Frisch et al., Computer code GAUSSIAN 98, Revision A.7, 1998.
- [27] K.A. Udachin, G.D. Enright, C.I. Ratcliffe, J.A. Ripmeester, *Chem. Phys. Chem.* 4 (2003) 1059.
- [28] D. Sebastiani, M. Parrinello, *Chem. Phys. Chem.* 3 (2002) 675.

Current Densities and Nucleus-Independent Chemical Shift Maps from Reciprocal-Space Density Functional Perturbation Theory Calculations

Daniel Sebastiani*[a]

A method to calculate condensed-matter nucleus independent chemical shift maps (NICS maps) from first principles in the framework of density functional theory is presented. I use a pseudopotential plane-wave approach in which the electronic current density and the NICS map are obtained from an inverse Fourier transformation of the induced magnetic field represented in re-

ciprocal space (G space). Due to its intrinsically periodic description, the method is suitable for isolated molecules (by using a supercell technique) and for condensed-phase systems like solids. The periodic NICS method was applied to hydrogen-bonded calixhydroquinone nanotubes, crystalline graphite, and two carbon nanotube systems.

1. Introduction

Nuclear magnetic resonance (NMR) is a widespread analytical tool in many areas of chemistry and biology. Among the key quantities in this context are NMR chemical-shift spectra, which allow the characterization of the chemical environment of individual atoms. In particular, bond types and interatomic distances can be obtained by analyzing the nuclear spin resonance frequencies. The NMR chemical shifts are also used for measuring hydrogen-bond strength. Especially in condensed matter, where hydrogen bonding ranges from intramolecular bridges up to complicated intermolecular networks, magic-angle-spinning (MAS) solid-state NMR has emerged in the last few decades as a promising technique for the analysis of microscopic structures of molecular and supramolecular systems.^[1,2] In contrast to other spectroscopic techniques, NMR allows the determination of many local structural properties, even if the systems do not exhibit long-range order. Thus, for such materials, NMR can have advantages over conventional diffraction methods, which require order on length scales far larger than what is necessary for NMR.

The NMR chemical shift is derived from the Larmor frequency of the nuclear spin of an atom, which describes the precession of the spin when the system is placed in a magnetic field. Since the electrons also react to the external field, the total magnetic field responsible for this precession is the superposition of the external field and the field induced by the electronic response. The nuclear shielding tensor is the negative proportionality factor between the electronically induced magnetic field, taken at the atomic position, and the externally applied field. When taken relative to a reference value, the shielding is called chemical shift tensor. The trace of this tensor is the central quantity measured in magnetic resonance spectroscopy.

The induced field and thus the nuclear shielding tensor, however, are well-defined in all points of space, not only at the

positions of the nuclei. This generalization of the chemical shift into such a scalar field is called nucleus-independent chemical shift (NICS). Its concept was mentioned as early as 1958 by Johnson and Bovey,^[3] while its implementation and application in quantum chemistry was pioneered by Schleyer et al.^[4,5]

There is a number of further developments and applications of NICS values in the literature. They are predominantly used for characterization of global and local aromaticity of hydrocarbons.^[6–14] Some articles show how the magnetic response properties can be decomposed into contributions of individual orbitals^[15–17] and the effect of particular functional groups.^[18] Another study describes how the individual components of the NICS tensor can be interpreted.^[19] Several articles exploit the generalized NICS maps to describe numerically and visually particular aspects of the electronic structure of molecules.^[20,21] Another branch of publications focuses on the quantitative calculation of the induced ring currents^[22] and the investigation of their topological aspects.^[23–26] There seem to be cases where the prediction of aromaticity through NICS is not straightforward and may lead to an inaccurate characterization,^[27,28] but so far these possible failures can be considered exceptions.

Further developments of the NICS concept include a graph-theoretical interpretation of NICS maps^[29] and the derivation of stability criteria.^[30] Another recent application is the investigation of the dynamic evolution of aromaticity in combination with molecular dynamics simulations.^[31] Finally, there are also review articles on the topic.^[32,33]

[a] Dr. D. Sebastiani

Max-Planck-Institute for Polymer Research
Ackermannweg 10, 55128 Mainz (Germany)
Fax: (+49) 6131-379-100
E-mail: sebastia@mpip-mainz.mpg.de

The particular feature of the present work is that nucleus independent chemical shifts are calculated by using a periodic plane-wave basis, that is, in reciprocal space. All physical quantities are stored in Fourier space by means of their plane wave coefficients, which are defined as a three-dimensional grid of reciprocal space vectors. Operators which are defined in direct space (\mathbf{r} representation), such as the position operator itself or the exchange-correlation potential, are applied by means of forth-and-back fast Fourier transformations (FFT)^[34] of the orbitals. Other operators, such as the Coulomb propagator or the Biot–Savart law for transforming a current into a magnetic field, can be expressed and computed very efficiently in reciprocal space (\mathbf{G} representation). In this approach, a single Fourier transform is enough to obtain the desired NICS field at all points of space. In contrast to direct-space-based methods, it is not necessary to specify particular points for which the NICS is to be computed. Instead, it is available after a regular NMR calculation on all points of the direct space mesh at essentially no additional cost.

The concepts of plane-wave basis sets and the corresponding implementations have long been well established,^[35] as is the theory behind the calculation of magnetic linear response.^[36–38] The calculation of NMR parameters under periodic boundary conditions is somewhat more recent.^[39–42] By means of these relatively new approaches, it is now possible to analyze the NMR chemical shifts of many systems that could not be investigated before, such as crystalline and amorphous solids as well as liquids.^[43–52]

To document my tool for the calculation of NICS maps and its implementation in the CPMD package,^[53] I have included a somewhat detailed description of the theoretical foundations of the perturbation-theory-based calculation of the required magnetic properties. Further details about the underlying density functional and density functional perturbation theory are published elsewhere.^[54–59]

2. Theory

2.1. General

The linear response scheme is realized in reciprocal space by using a plane-wave basis set. To this purpose, the system is placed into a unit cell, which is assumed to be replicated periodically in all dimensions of space. According to the Bloch theorem, the electronic orbitals are periodic with certain lattice vectors \mathbf{R}_L , apart from a phase factor which is not considered here (Γ -point approximation). The orbitals $\psi(\mathbf{r})$ are expanded in plane waves, which are generated from \mathbf{G} -space vectors [Eq. (1)]

$$\psi(\mathbf{r}) = \sum_{\mathbf{G}} c_{\mathbf{G}} \exp[i\mathbf{G} \cdot \mathbf{r}] \quad (1)$$

where $N_{\mathbf{G}}$ is the total number of \mathbf{G} vectors. Equation (1) describes a Fourier transformation from the set of coefficients $c_{\mathbf{G}}$ to the direct-space representation $\psi(\mathbf{r})$. The \mathbf{G} vectors are characterized by Equation (2)

$$\frac{1}{2\pi} |\mathbf{G} \cdot \mathbf{R}| \in \mathbb{N}_0 \quad (2)$$

where \mathbb{N}_0 represents the set of non-negative integers and \mathbf{R} is any lattice vector. The coefficients can be obtained by means of inverse Fourier transformation [Eq. (3)].

$$c_{\mathbf{G}} = \frac{1}{N_{\mathbf{G}}} \sum_{\mathbf{r}} \psi(\mathbf{r}) \exp[-i\mathbf{G} \cdot \mathbf{r}] \quad (3)$$

Calculation of physical properties of the system such as densities and potentials within this representation is beyond the scope of this work and has already been published in detail elsewhere.^[35] Note, however, that the application of the position operator is not trivial for periodic orbitals and requires special consideration. Several ways exist to circumvent the problem that $\hat{\mathbf{r}}$ violates the periodicity of the unit cell.^[40,41,60,61] The method adopted here is a sawtooth-shaped representation of $\hat{\mathbf{r}}$, which can be applied to the orbitals in a very simple way if they have previously been transformed into maximally localized Wannier orbitals.^[41,62] In contrast, the momentum operator can be applied in reciprocal space by simply multiplying the coefficients $c_{\mathbf{G}}$ by $i\mathbf{G}$. This can be seen from the identity of Equation (4).

$$\frac{\partial}{\partial \mathbf{r}} \psi(\mathbf{r}) = \sum_{\mathbf{G}} i\mathbf{G} c_{\mathbf{G}} \exp[i\mathbf{G} \cdot \mathbf{r}] \quad (4)$$

All other operators that are required in this work, namely, the Hamiltonian, angular momentum, current density, and Biot–Savart operators, can be expressed as combinations of $\hat{\mathbf{r}}$ and $\hat{\mathbf{p}}$.

2.2. Magnetic Perturbation Theory

A magnetic field is represented by a vector potential \mathbf{A} , which must satisfy Equation (5).

$$\mathbf{B} = \nabla \times \mathbf{A}(\mathbf{r}) \quad (5)$$

The vector potential is an auxiliary quantity that has no direct physical meaning. For a given magnetic field, a whole class of vector potentials exist which fulfill the constituting Equation (5).

It contains a degree of freedom in form of an arbitrary scalar function $\Phi_g(\mathbf{r})$ whose gradient may be added to $\mathbf{A}(\mathbf{r})$ without affecting the resulting magnetic field [Eqs. (6)–(8)].

$$\mathbf{A}(\mathbf{r}) \mapsto \mathbf{A}'(\mathbf{r}) = \mathbf{A}(\mathbf{r}) + \nabla \Phi_g(\mathbf{r}) \quad (6)$$

$$\Rightarrow \mathbf{B}' = \nabla \times (\mathbf{A}(\mathbf{r}) + \nabla \Phi_g(\mathbf{r})) \quad (7)$$

$$= \nabla \times \mathbf{A}(\mathbf{r}) = \mathbf{B} \quad (8)$$

$\Phi_g(\mathbf{r})$ is called the gauge function, and its choice should not affect any physical results (gauge invariance). However, this is numerically not exactly true, and intermediate values in an actual calculation can change a lot.

A typical choice for \mathbf{A} in the case of a desired homogeneous magnetic field \mathbf{B} is given by Equation (9).

$$\mathbf{A}(\mathbf{r}) = -\frac{1}{2}\mathbf{r} \times \mathbf{B} \quad (9)$$

It obviously satisfies Equation (5). Special care must be taken in extended systems, where the position operator $\hat{\mathbf{r}}$ is ill-defined^[40,41] because of its intrinsically nonperiodic character. However, in this article I ignore this aspect and treat the system as isolated. A particular class of gauge functions is defined by Equation (10)

$$\Phi_g(\mathbf{r}) = \frac{1}{2}\mathbf{r} \cdot \mathbf{R}_g \times \mathbf{B} \quad (10)$$

with a particular position in space denoted by \mathbf{R}_g . The transformation [Eq. (6)] yields for the new vector field Equation (11).

$$\mathbf{A}'(\mathbf{r}) = -\frac{1}{2}(\mathbf{r} - \mathbf{R}_g) \times \mathbf{B} \quad (11)$$

This transformation only translates the origin of the coordinate system by \mathbf{R}_g . For this reason, the point \mathbf{R}_g is called the gauge origin of the new vector potential \mathbf{A}' . It is a cyclic variable, because it does not change the physics of the system, but it turns out that a careful choice of the gauge function is essential for ensuring good numerical accuracy.

2.3. Density Functional Perturbation Theory

The magnetic field is incorporated into the Hamilton operator by means of the so-called minimal substitution [Eq. (12)]

$$\hat{\mathbf{p}} \rightarrow \hat{\boldsymbol{\pi}} = \hat{\mathbf{p}} - e\mathbf{A}(\hat{\mathbf{r}}) \quad (12)$$

which defines a generalized momentum operator $\boldsymbol{\pi}$. This generalized momentum replaces the standard momentum operator $\hat{\mathbf{p}}$ in the Hamiltonian. Developing the latter in powers of the magnetic field (i.e., in powers of \mathbf{A}) yields a linear and a quadratic term [Eqs. (13) and (14)].

$$\hat{H}^{(1)} = -\frac{e}{m}\hat{\mathbf{p}} \cdot \mathbf{A}(\hat{\mathbf{r}}) \quad (13)$$

$$\hat{H}^{(2)} = \frac{e^2}{2m}\mathbf{A}(\hat{\mathbf{r}})^2 \quad (14)$$

These modifications of the field-free Hamiltonian are treated within perturbation theory and represent the first- and second-order perturbation Hamiltonians. I use density functional perturbation theory (DFPT), also known as the coupled perturbed Kohn–Sham (KS) method,^[59] which provides the electronic linear response $|\psi_i^{(1)}\rangle$ to the magnetic field according to Equation (15)

$$(\hat{H}^{(0)} - \varepsilon_i)|\psi_i^{(1)}\rangle = \hat{P}^n \hat{H}^{(1)}|\psi_i^{(0)}\rangle \quad (15)$$

where $|\psi_i^{(0)}\rangle$ are the unperturbed KS orbitals, ε_i their KS eigenvalues, and $\hat{P}^n = 1 - \sum_j^{\text{occ}} |\psi_j^{(0)}\rangle \langle \psi_j^{(0)}|$ the projector on the un-

occupied orbitals. In Equation (15), there is no first-order perturbation density $\rho^{(1)}(\mathbf{r})$ as in standard density functional perturbation theory,^[59] because the perturbation Hamiltonian (13) is purely imaginary in the position representation. This in turn results in a vanishing first-order density,^[41] which can be expressed as $\rho^{(1)}(\mathbf{r}) = \sum_j \bar{\psi}_j^{(1)}(\mathbf{r})\psi_j^{(0)}(\mathbf{r}) + \bar{\psi}_j^{(0)}(\mathbf{r})\psi_j^{(1)}(\mathbf{r})$. The total wavefunction is obtained as Equation (16)

$$|\psi_i\rangle = |\psi_i^{(0)}\rangle + |\psi_i^{(1)}\rangle \quad (16)$$

Equation (15) can formally be inverted by using a Green's function formalism [Eqs. (17) and (18)]

$$|\psi_i^{(1)}\rangle = (\hat{H}^{(0)} - \varepsilon_i)^{-1} \hat{P}^n \hat{H}^{(1)}|\psi_i^{(0)}\rangle \quad (17)$$

$$= \hat{G}_i \hat{H}^{(1)}|\psi_i^{(0)}\rangle \quad (18)$$

Note that the Green's function \hat{G}_i does not commute neither with position nor with the momentum operators, because it is the inverse of an operator which contains both $\hat{\mathbf{r}}$ and $\hat{\mathbf{p}}$. Equation (18) will be used in the following as a compact notation to represent the calculation of the $|\psi_i^{(1)}\rangle$. In the implementation, however, Equation (15) is solved directly by using a conjugate-gradient minimization algorithm for the second-order perturbation energy.^[59] Its computational cost is comparable to and usually less than that of a total-energy calculation. No wavefunctions of unoccupied states are required in this scheme, in contrast to sum-over-states techniques.^[63,64]

2.4. Electronic Current Density

The electronic current density at a position \mathbf{r}' is defined as the expectation value of the current operator [Eq. (19)].

$$\hat{\mathbf{j}}_{\mathbf{r}'} = \frac{e}{2m}[\hat{\boldsymbol{\pi}}|\mathbf{r}'\rangle \langle \mathbf{r}'| + |\mathbf{r}'\rangle \langle \mathbf{r}'|\hat{\boldsymbol{\pi}}] \quad (19)$$

With first-order perturbation theory, this expectation value must be taken within the perturbed orbitals $|\psi_i\rangle = |\psi_i^{(0)}\rangle + |\psi_i^{(1)}\rangle$. Note that the unperturbed orbitals $|\psi_i^{(0)}\rangle$ are real functions, while it can be shown that the first-order corrections $|\psi_i^{(1)}\rangle$ are purely imaginary.^[41] It is easy to see that the expectation value of $\hat{\mathbf{j}}_{\mathbf{r}'}$ within the unperturbed states vanishes due to the real nature of the orbitals. The expansion of the expectation value up to first order yields Equation (20)

$$j^{(1)}(\mathbf{r}') = \frac{e}{2m} \sum_j \langle \psi_j^{(0)} | (\hat{\mathbf{p}}|\mathbf{r}'\rangle \langle \mathbf{r}'| + |\mathbf{r}'\rangle \langle \mathbf{r}'|\hat{\mathbf{p}}) | \psi_j^{(1)} \rangle + \text{c.c.} \\ - \frac{e^2}{m} \sum_j \mathbf{A}(\mathbf{r}') \langle \psi_j^{(0)} | \mathbf{r}' \rangle \langle \mathbf{r}' | \psi_j^{(0)} \rangle \quad (20)$$

after backsubstitution of $\boldsymbol{\pi} = \hat{\mathbf{p}} - e\mathbf{A}(\hat{\mathbf{r}})$. In my approach, I use the so-called " $\mathbf{R}_g = \mathbf{r}$ " variant of the continuous set of gauge trans-

formations (CSGT method^[37]). For each point \mathbf{r}' in space at which the current density is calculated, the gauge origin \mathbf{R}_g is set to \mathbf{r}' . This method makes the last term of Equation (20) vanish analytically.

Inserting the vector potential [Eq. (5)] within the $\mathbf{R}_g = \mathbf{r}'$ gauge into the perturbation Hamiltonian (13) and expanding the $|\psi_i^{(1)}\rangle$ according to Equation (18), the expression for the Cartesian component α of the current density reads as Equation (21).

$$j_\alpha^{(1)}(\mathbf{r}') = \frac{e^2}{m^2} \sum_k \langle \psi_k^{(0)} | (\hat{p}_\alpha | \mathbf{r}' \rangle \langle \mathbf{r}' | + | \mathbf{r}' \rangle \langle \mathbf{r}' | \hat{p}_\alpha) [\hat{G}_k \hat{\mathbf{r}} \times \hat{\mathbf{p}} | \psi_k^{(0)} \rangle - \hat{G}_k \mathbf{r}' \times \hat{\mathbf{p}} | \psi_k^{(0)} \rangle] \cdot \mathbf{B} \quad (21)$$

To avoid ambiguities related to the vector character of the current density and the cross products involving $\mathbf{r}' \times \hat{\mathbf{p}} \cdot \mathbf{B}$ and variations thereof, this expression was formulated for the Cartesian component α of the current density.

Note that in Equation (21), $\hat{\mathbf{p}}$ and $\hat{\mathbf{r}}$ as well as \hat{G}_k are operators, whereas \mathbf{r}' is a position variable. Therefore, \mathbf{r}' in the second cross-product commutes with the Green's function \hat{G}_k and the momentum operator $\hat{\mathbf{p}}$, so that \mathbf{r}' can be replaced by a position operator acting on the position states $|\mathbf{r}'\rangle$ [Eq. (22)].

$$j_\alpha^{(1)}(\mathbf{r}') = \frac{e^2}{m^2} \sum_k \left\langle \psi_k^{(0)} \left| (\hat{p}_\alpha | \mathbf{r}' \rangle \langle \mathbf{r}' | + | \mathbf{r}' \rangle \langle \mathbf{r}' | \hat{p}_\alpha) \hat{G}_k \hat{\mathbf{r}} \times \hat{\mathbf{p}} | \psi_k^{(0)} \right\rangle \cdot \mathbf{B} - \frac{e^2}{m^2} \sum_k \left\langle \psi_k^{(0)} \left| (\hat{p}_\alpha | \mathbf{r}' \rangle \langle \mathbf{r}' | \hat{\mathbf{r}} + \hat{\mathbf{r}} | \mathbf{r}' \rangle \langle \mathbf{r}' | \hat{p}_\alpha) \times \hat{G}_k \hat{\mathbf{p}} | \psi_k^{(0)} \right\rangle \cdot \mathbf{B} \right. \quad (22)$$

Contrary to Equation (21), this new expression does not contain any explicit dependence on \mathbf{r}' except its eigenstate $|\mathbf{r}'\rangle$. It has the form of the diagonal direct-space matrix elements of an operator [Eq. (23)].

$$j_\alpha^{(1)}(\mathbf{r}') = \frac{e^2}{m^2} \left\langle \mathbf{r}' \left| \sum_k \left[\hat{G}_k \hat{\mathbf{r}} \times \hat{\mathbf{p}} | \psi_k^{(0)} \rangle \cdot \langle \psi_k^{(0)} | \hat{p}_\alpha + \hat{p}_\alpha \hat{G}_k \hat{\mathbf{r}} \times \hat{\mathbf{p}} | \psi_k^{(0)} \rangle \langle \psi_k^{(0)} | - \hat{\mathbf{r}} \times \hat{G}_k \hat{\mathbf{p}} | \psi_k^{(0)} \rangle \langle \psi_k^{(0)} | \hat{p}_\alpha + \hat{p}_\alpha \hat{G}_k \hat{\mathbf{p}} | \psi_k^{(0)} \rangle \times \langle \psi_k^{(0)} | \hat{\mathbf{r}} \right] | \mathbf{r}' \right\rangle \cdot \mathbf{B} \quad (23)$$

Although this equation looks a bit lengthy, it can be computed efficiently in a single run for the whole system. In particular, the application of position and momentum operators to any set of orbitals (unperturbed or perturbed) is straightforward in their respective representations (direct and Fourier space) with the help of fast Fourier transformations. In contrast, direct application of Equation (21) would require one inversion of the Hamiltonian per real space mesh point \mathbf{r}' , which is prohibitively expensive.

As an illustrative example, I shall describe in more detail how to compute the last term in Equation (23), that is, Equation (24).

$$\sum_k \left\langle \mathbf{r}' | \hat{p}_\alpha \hat{G}_k \hat{\mathbf{p}} | \psi_k^{(0)} \right\rangle \times \left\langle \psi_k^{(0)} | \hat{\mathbf{r}} | \mathbf{r}' \right\rangle \cdot \mathbf{B} \quad (24)$$

First, the momentum operator is applied to the unperturbed orbitals according to Equation (4). The resulting functions are transferred to the perturbation theory routines, which deliver the response orbitals by solving Equation (15). Then, \hat{p}_α is applied to these functions, followed by a Fourier transformation, which yields the left part of Equation (24) as a function on the direct-space grid. After that, the unperturbed orbitals are transformed to direct space and multiplied by $\hat{\mathbf{r}}$. Finally, the latter are multiplied with the previously obtained left part of Equation (24) on each point of the real space grid, resulting in the contribution of this term to the electronic current density [Eq. (23)].

In this way, the induced current density j_α is obtained at each point of the real space grid. It is subsequently transformed to reciprocal space by fast Fourier transformation, yielding $j_{\alpha G}$.

Note that in order to obtain a formalism that can be applied to truly periodic systems with extended Bloch orbitals, the use of the position operator in Equation (23) is not straightforward. In an extended system, the position operator is nonperiodic and can thus not be represented directly in its standard form. One possibility to circumvent this problem is to restart at Equation (9) and to assume that the external magnetic field is modulated with a cosine along its direction.^[65] This results in a periodic vector potential which is then well defined under periodic boundary conditions.^[39,40] An alternative is the transformation of the Bloch wavefunctions into maximally localized Wannier orbitals,^[62] for which a suitably modified sawtooth position operator can be defined.^[41,42] This technique renders the formulation of Equation (23) more complicated, since these Wannier orbitals are not eigenfunctions of the Hamiltonian any more and require a generalized version of perturbation theory^[59] as compared to Equation (18). However, the basic procedure remains unchanged.

2.5. Induced Magnetic Field

The electronic current density induces an additional inhomogeneous magnetic field, which can be obtained by the law of Biot–Savart [Eq. (25)].

$$\mathbf{B}^{\text{ind}}(\mathbf{r}) = \frac{\mu_0}{4\pi} \nabla \times \int d^3r' \frac{\mathbf{j}(\mathbf{r}')}{|\mathbf{r}' - \mathbf{r}|} \quad (25)$$

The integral in Equation (25) is well known as the solution of the Poisson equation for the electrostatic field. The difficulty lies in the point that the current density $\mathbf{j}(\mathbf{r})$ is a periodic function, while $\frac{1}{|\mathbf{r}' - \mathbf{r}|}$ is not. Under periodic boundary conditions, the convergence of Equation (25) is not assured generally, but with the exception of the $\mathbf{G} = 0$ component, its Fourier transform can be computed in a straightforward way [Eq. (26)]^[35]

$$\mathcal{F} \int d^3r' \frac{\mathbf{j}(\mathbf{r}')}{|\mathbf{r}' - \mathbf{r}|_{\mathcal{F}}} = \frac{4\pi}{\mathbf{G}^2} \mathbf{j}_{\mathbf{G}} \quad (26)$$

where the $\mathbf{j}_{\mathbf{G}}$ denote the 3D vectors of Fourier coefficients of the current density, defined in complete analogy to Equation (3). The curl required for Equation (25) is then very easy to apply according to the Equation (4). Eventually, the Fourier coefficient vectors $\mathbf{B}_{\mathbf{G}}^{\text{ind}}$ of the induced field can be expressed as Equation (27).

$$\mathbf{B}_{\mathbf{G} \neq 0}^{\text{ind}} = i\mu_0 \frac{\mathbf{G} \times \mathbf{j}_{\mathbf{G}}}{\mathbf{G}^2} \quad (27)$$

To obtain the complete representation of the induced magnetic field in the system, evaluation of the $\mathbf{G}=0$ component is still required, which is more involved than the $\mathbf{G} \neq 0$ case. It is defined as Equation (28)

$$\mathbf{B}_{\mathbf{G}=0}^{\text{ind}} = \frac{1}{\Omega} \int_{\Omega} d^3r \mathbf{B}^{\text{ind}}(\mathbf{r}) \quad (28)$$

where the integration runs over the entire (macroscopic) sample volume Ω . Thus, the integration can only be done analytically if the shape of the sample is known. Since the experimental standard is to assume a spherical geometry, we restrict ourselves to this special case here. Together with the Biot-Savart law [Eq. (25)], the integration can be carried out explicitly [Eqs. (29) and (30)].

$$\mathbf{B}_{\mathbf{G}=0}^{\text{ind}} = \frac{1}{\Omega} \frac{\mu_0}{4\pi} \int_{\Omega} d^3r d^3r' \frac{\mathbf{r}' - \mathbf{r}}{|\mathbf{r}' - \mathbf{r}|^3} \times \mathbf{j}(\mathbf{r}') \quad (29)$$

$$= \frac{1}{\Omega} \frac{\mu_0}{4\pi} \int_{\Omega} d^3r' \mathbf{j}(\mathbf{r}') \times \frac{\partial}{\partial \mathbf{r}'} \int_{\Omega} d^3r \frac{1}{|\mathbf{r}' - \mathbf{r}|} \quad (30)$$

The last integral can easily be evaluated in polar coordinates. For a sphere with radius R_s , it yields $2\pi(R_s^2 - r'^2/3)$, where r' is the distance of the position \mathbf{r}' to the center of the sphere. Thus, the gradient in Equation (30) gives $-4\pi/3r'$ and the induced field can be computed as Equations (31) and (32).

$$\mathbf{B}_{\mathbf{G}=0}^{\text{ind}} = \frac{\mu_0}{3\Omega} \int_{\Omega} d^3r' \mathbf{r}' \times \mathbf{j}(\mathbf{r}') \quad (31)$$

$$= \frac{2}{3} \chi_m \cdot \mathbf{B}^{\text{ext}} \quad (32)$$

where χ_m is the magnetic susceptibility tensor [Eq. (33)].

$$\chi_m = \frac{\partial}{\partial \mathbf{B}^{\text{ext}}} \frac{\mu_0}{2\Omega} \int_{\Omega} d^3r' \mathbf{r}' \times \mathbf{j}(\mathbf{r}') \quad (33)$$

In Equation (31), integration over the whole sample volume Ω can be restricted to one unit cell if the normalization factor $1/\Omega$ is changed accordingly. The integral in Equation (33) is translationally invariant, since the integral of the current densi-

ty over one unit cell must vanish. Thus, the calculation of χ_m is straightforward on the direct-space mesh.

2.6. Three-Dimensional NICS Maps

In this way, the magnetic field which is induced in the system due to the current created by the electronic linear response to the external field can be computed in its reciprocal-space representation. Once this goal is achieved, this induced field is available at all points in the unit cell. At the nuclear positions, its value represents one row of the nuclear shielding tensor for a given direction of the external field [Eq. (34)].

$$\sigma(\mathbf{R}) = -\frac{\partial \mathbf{B}^{\text{ind}}(\mathbf{R})}{\partial \mathbf{B}^{\text{ext}}} \quad (34)$$

Experimentally, the trace of this tensor is quoted relative to that of a reference molecule to give the isotropic NMR chemical shift [Eq. (35)].

$$\delta(\mathbf{R}) = \frac{1}{3} \text{Tr}[\sigma^{\text{ref}} - \sigma(\mathbf{R})] \quad (35)$$

On the other hand, since the induced field is well-defined at all positions of space, it is possible to calculate Equation (34) also in places where no atom is located. For special points, usually the centers of molecular symmetry, these values are known as nucleus independent chemical shifts (NICS).

Using traditional quantum chemical methods with localized basis sets, the calculation of NICS values for a large number of points on a fine mesh (e.g., 100^3 points) within a significant region of space around a molecule is computationally relatively expensive. However, with the reciprocal-space approach presented here, the induced magnetic field and therefore the NICS values are automatically available at all points of the considered periodic unit cell. The computational effort required to obtain these three-dimensional maps for all points \mathbf{r} in space is essentially equal to that of a single regular calculation of NMR chemical shift. The only difference with respect to Equation (35) is that NICS maps are not referenced because they do not refer to any specific nucleus. Hence [Eq. (36)]

$$\delta^{\text{NICS}}(\mathbf{r}) = -\frac{1}{3} \text{Tr} \sigma(\mathbf{r}). \quad (36)$$

This definition is kept throughout this work. Positive values of $\delta^{\text{NICS}}(\mathbf{r})$ thus correspond to locally increased magnetic fields ("upfield shifts") while negative ones represent areas of decreased magnetic field ("downfield shifts").

Computational Details

All calculations of NICS maps were carried out with the density functional perturbation theory module^[59] implemented in the Car-Parrinello Molecular Dynamics program package CPMD.^[53] This code is designed for calculations under periodic boundary conditions, where plane waves are used as basis set. NICS maps are a

generalization of nuclear magnetic shielding tensors whose calculation is implemented within the same package.^[41,42] All properties required for the calculation of NICS maps can be computed efficiently in reciprocal space (**G** space) by using fast Fourier transform techniques to switch to direct space and vice versa. All visualizations were done with the MOLEKEL program^[66] and postprocessed with the GIMP package.^[67]

The BLYP exchange and correlation functional^[68,69] and Goedecker–Teter–Hutter pseudopotentials^[70,71] were used together with a plane-wave cutoff of 60 Ry for hydrocarbons and 90 Ry in the presence of oxygen atoms. For all systems, large supercells (typically $(20 \text{ \AA})^3$ or larger) were used to isolate the molecules from their periodic images and to avoid that the NICS fields overlay each other. For the graphite crystal, I used an orthorhombic supercell of two layers of 32 carbon atoms each. To avoid convergence problems, I restricted the sampling of the Brillouin zone to the Γ point only, in which case graphite has a finite band gap. This results in a partially incorrect description of the physics of this system, but the main purpose of this example is to illustrate the potential of the method, for which I believe the Γ point to be sufficient.

Norm-conserving pseudopotentials were used to represent the ionic core and the inner electrons for non-hydrogen atoms. Therefore, the current densities and NICS fields are missing the effect of core electrons, which is very important close to the atomic positions. There are sometimes doubts whether pseudopotential-based calculations can capture the full picture of orbital magnetic response, and it was found that for uranium compounds that there are actually problems with the effective core potential approximation.^[72] A more recent article on the same class of uranium complexes, however, finds that pseudopotentials are indeed suitable for such ultraheavy systems, provided the chosen electronic core is small enough.^[73] These examples show that the effect of core electrons is limited to the immediate neighborhood of the heavy atoms. It is also known that the NMR chemical shifts of protons in organic molecules does not depend on the explicit consideration of the carbon core electrons.^[39–41] Therefore, the NICS maps can be considered to be correct everywhere except at positions closer than about 0.5 Å to heavy atoms.

The periodic NICS method presented here has specific advantages and disadvantages when compared to the well-established quantum chemical approaches using localized basis sets. In the latter, great care must be taken when choosing the gauge origin, and a whole branch of theoretical methods exists to cope with this issue, which is a consequence of the incompleteness of every finite basis set. Since plane waves are completely delocalized and thus more complete in the sense of diffuse and polarization basis functions, this problem is less significant here. In contrast, plane waves are cumbersome for an accurate description of strongly oscillating orbitals. In particular, the accuracy of properties relative to the region of core electrons is reduced due to the necessity to use pseudopotentials. However, it was already shown in the early days of the IGLO method^[36] that the effect of core electrons on NMR chemical shifts can be well represented as an additive constant.

A clear advantage of the present formulation is that all operators used in magnetic perturbation theory can be represented as a sequence of the position and momentum operators. The application of the former can be done in real space, while the latter is a simple multiplication operation in Fourier space. The transition between the two representations can be done very efficiently by using fast Fourier transforms (FFT), which typically consume about two-thirds of the total computer time. Special care must be taken for a proper periodic representation of the position operator, which vio-

lates the periodicity of the system in its trivial formulation. This issue, however, exceeds the scope of this work and has already been discussed in more detail elsewhere.^[41,42]

3. Results and Discussion

3.1. NICS of Calixhydroquinone

As a first example of a strongly aromatic moiety, I computed the NICS map of calixhydroquinone (CHQ). This molecule consists of four hydroquinone rings that are linked by CH_2 spacers. They assume the shape of a bowl, with an array of strong $\text{OH}\cdots\text{O}$ hydrogen bonds in its bottom. Molecules of CHQ have the unusual ability to crystallize as noncovalently bonded nanotubes which are linked by a hydrogen-bond network involving additional water molecules.^[74,75] This system has been investigated previously by means of solid-state ^1H MAS NMR techniques and DFT-based calculations from our group, which showed that the nanotube crystals are filled with mobile acetone molecules.^[51] Considering the available space within the nanotubes, each CHQ can host about one acetone molecule. The pronounced London dispersion attraction between the CHQ bowls and the acetone molecules led us to the assumption that the acetone molecules might preferentially occupy the site in the center of the CHQs.

In that previous study, we showed that experimentally the ^1H NMR resonance line of the methyl groups of acetone appears at an unusually upfield chemical shift. This shift could be shown to be due to the assumed proximity of the acetone to the aromatic hexagons of the CHQ molecules. Here, the NICS map of the calixhydroquinone molecule is computed (Figure 1) as well as a unit cell of the full nanotube (Figure 2).

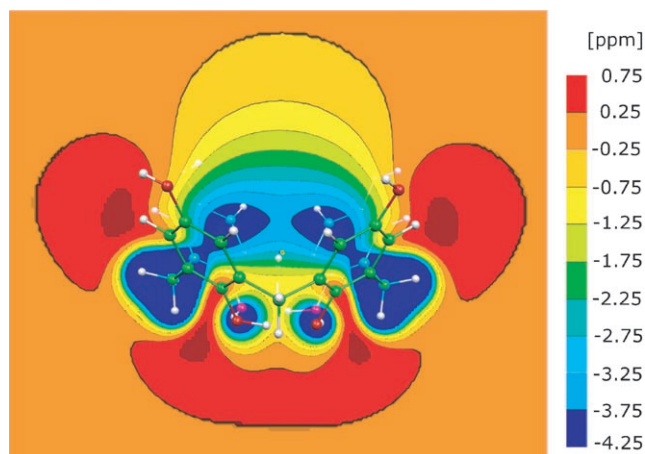


Figure 1. The NICS map of an isolated calixhydroquinone molecule.

Already for the isolated CHQ molecule, shown in Figure 1, the spatial extent of the typical aromatic NICS cone is significantly larger than for the benzene molecule. This is not surprising, since the individual cones of the four aromatic hydroquinones overlap in the center of the bowl. The strength of this

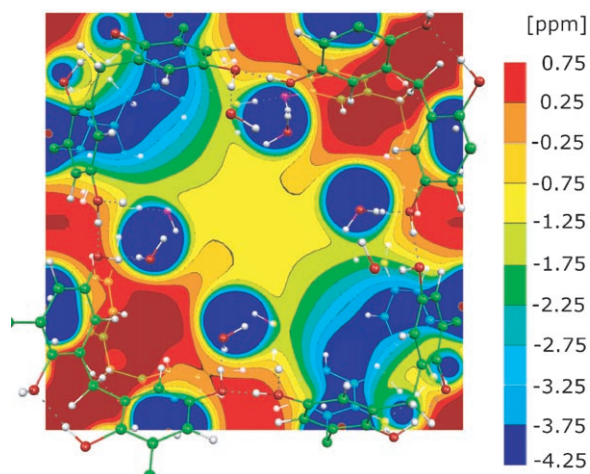


Figure 2. The NICS map of a nanotube composed of calixhydroquinone molecules and bridging water molecules.

cumulative effect results in a large NICS of about 1–2 ppm at the top of the bowl.

The CHQ nanotube in its three-dimensional structure is evidently more complex. Its NICS map is shown in Figure 2, where the plane is placed in the center of the the top-left and the bottom-right CHQ molecules. Since the top-right and bottom-left CHQ molecules are displaced by half a lattice vector along the tube, the figure contains half a molecule above the cut and half a molecule below.

The NICS map shows that even in the plain center of the CHQ nanotube, a test spin would still feel an upfield shift of at least –1 ppm due to the nearby presence of π electrons. The closer one approaches the CHQ bowl, the stronger is this effect. It eventually reaches a magnitude of about –3 ppm. Although NICS-derived predictions cannot be taken as a quantitative measure of the upfield shift of real protons (which would inherently distort the electronic structure of the CHQs, an effect that is not taken into account in the NICS scheme), it illustrates the expected strength of the displacement. Indeed, the estimation from the NICS values, that is, a range of –1 to –3 ppm, is in very good agreement with experiment,^[51] where an upfield shift of the acetone proton of about –2 ppm was found with respect to pure acetone.

3.2. NICS of Graphite

Figure 3 shows a section of the NICS field of graphite parallel to the graphene plane, about 0.5 Å below the carbon atoms. The color coding includes a significantly wider range of shifts compared to that used for the calixhydroquinone systems. Still, the actual NICS close to the atoms and bonds clearly exceeds the –20 ppm scale (dark blue regions).

When starting from the simple benzene molecule, whose NICS map has been investigated in several articles,^[3,9,17,20] and moving to large polybenzenoid hydrocarbons,^[6,21] graphite constitutes the limit of an infinitely large system of this category. So far, its NICS map could not be computed since it is a periodic system, not tractable with standard quantum chemistry codes. Previous studies indicate that even for very large polybenzenoid hydrocarbons (up to $C_{222}H_{42}$), different rings exhibit individual NICS strengths that lead to the assignment of different aromaticities to different rings.^[21] Here graphite shows—as imposed by its translational symmetry and thus not unexpectedly—a fully symmetric NICS field.

The NICS is weakest at the centers of the hexagons. This can be explained from the larger spatial distance to the bonds, where the electronic current density is stronger. This fact is also visible in Figure 4, where the plane is orthogonal to the graphite plane, in the middle of the C–C bonds. The centers of the hexagons represent local minima of the NICS field. The NICS values at the ring centers of about –6 ppm (and –8 ppm 1 Å above the plane) are only about half that of benzene (–10 and –11 ppm). Insofar, graphite would have to be considered nonaromatic. However, when graphite is thought of as the in-

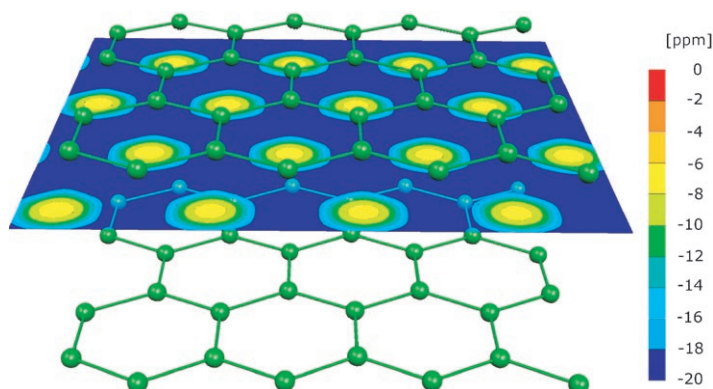


Figure 3. Section of the NICS field of graphite in the plane parallel to the sheets, taken 1 bohr below the atoms. Note the difference in the color coding with respect to the calixhydroquinone nanotube (Figure 2), which covers a significantly larger range.

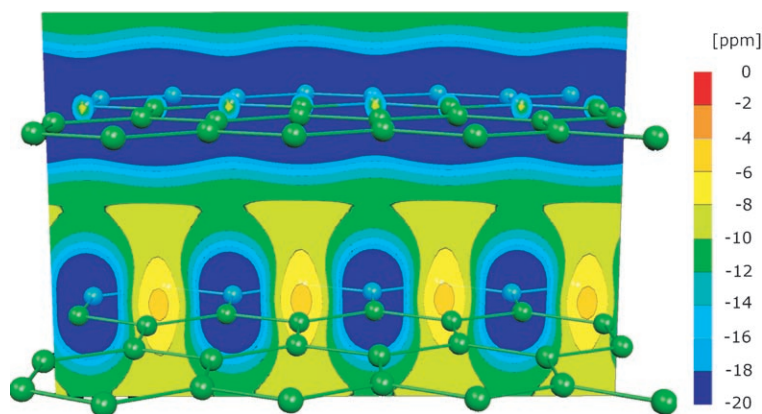


Figure 4. Section of the NICS field of graphite taken at the middle of the C–C bonds. The color code is the same as in Figure 3.

finite extension of the largest polybenzenoid system studied by Moran (i.e., $C_{222}H_{42}$, molecule **11** in ref. [21]), it could be constructed as a periodic hexagonal continuation of $C_{222}H_{42}$. Since in $C_{222}H_{42}$, the ratio of aromatic/nonaromatic rings is 1/2, a hexagon of a graphite sheet could be represented as the superposition of one aromatic and two nonaromatic rings. Taking the corresponding NICS values of approximately -15 and -4 ppm, respectively (Table 1 of ref. [21], atoms A and F), this yields an average NICS of -7.5 ppm, which is very close to my -8 ppm. Thus, it appears justified to see graphite as some kind of symmetrization of large polybenzenoid hydrocarbons.

3.3. Carbon Nanotubes

Single-wall carbon nanotubes (CNTs) exhibit a broad variety of surprising physics and chemistry and are of growing importance in industrial applications. A large amount of literature describes their structural, electronic, and thermal properties, amongst other characteristics.^[76–79] As they can be thought to be built from a wrapped graphene sheet, they are in many respects similar to the graphite system computed in the Section 3.2. In particular, they have highly delocalized electrons, despite the distortions imposed by their tubular structure.

Since, in their idealized form, they are infinite periodic systems, they are intrinsically difficult to treat with conventional quantum chemistry codes. So far, there is no investigation of the aromaticity of infinite CNTs in terms of NICS maps in the literature. Such calculations do exist, however, for finite-length tubes.^[80,81] In finite CNTs, the assignment of aromaticity/nonaromaticity of the individual rings changes as a function of the size of the CNT segment. Also the C–C bond lengths and the NICS values themselves are not constant, while in a real (infinite) CNT, all carbon atoms are equal by symmetry. For the properties of finite tubes, a real convergence in size could not yet be reached due to the required computational effort.

CNTs exist in several categories depending on the way their graphene sheets are wrapped up. Their physical and chemical properties depend on the diameter and chirality of the tube, which is characterized by a pair of numbers (n,m) . This pair defines the chiral vector $n\mathbf{a}_1 + m\mathbf{a}_2$ (where \mathbf{a}_1 and \mathbf{a}_2 are the lattice vectors of the underlying graphene sheet) which describes the chiral periodicity of the CNT.

If the difference $n-m$ is divisible by three, then the CNT is metallic; otherwise, it is a semiconductor. Since my approach is not applicable to metallic systems, I studied only a nonmetallic (11,0) nanotube. With the help of a trick, however, a (12,0) CNT could also be computed. To this end, I connected a (12,0) segment with a piece of a (11,0) CNT,^[82] which made the analysis possible.

Carbon nanotubes have two distinct directions, along the tube axis and orthogonal to it, in which their electronic response properties are naturally very different. I therefore not only studied the average induced field (the isotropic NICS field), but also the individual cases in which the external magnetic field is applied along those two directions.

3.3.1. Zig-Zag (11,0) Nanotube

The (11,0) CNT is a semiconducting tube with a diameter of about 8.6 \AA , with eleven hexagons per winding and without chirality. I took a supercell of three repeat units, containing a total of 132 carbon atoms, in a box of $25 \times 25 \times 12.78 \text{ \AA}$.

Initially, I studied the magnetic properties for an external field applied along the tube axis. Figure 5 shows an isosurface

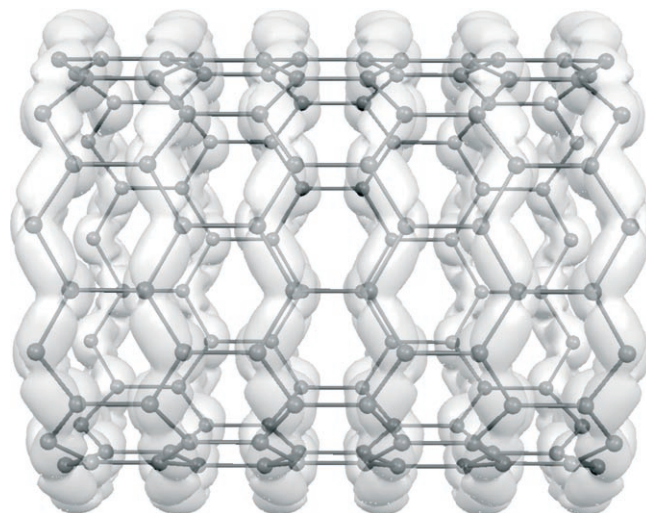


Figure 5. Isosurface map of the modulus of the induced electronic current of a (11,0) CNT when the external magnetic field is along the tube axis. Tori are formed and closely follow the zig-zag C–C bonds.

plot of the modulus of the induced current density $|\mathbf{j}(\mathbf{r})|$. The current nicely follows the carbon atoms zig-zag-wise around the tube, that is, the largest contributions arise from regions very close to the C–C bonds.

Figure 6 shows a single component $j_{\text{vert}}(\mathbf{r})$ of the same current density in the direction orthogonal to the image plane. The dominance of the near-bond areas is evident, but the presence of a large diffuse region of additional current density at about $1\text{--}2 \text{ \AA}$ outside the CNT is visible as well. Small currents with opposite orientation, located close to the atomic positions, correspond to localized ring currents around the bonds. Their magnitude, however, is significantly smaller than that of their delocalized counterpart that embraces the whole tube. The scatter which is visible in the middle of the CNT is numerical noise, which arises from the fact that the zero for the current lies at a color step. Thus, small fluctuations around zero may result in a change in the color code without physical meaning.

Another interesting view on the induced current density in an extended system is shown in Figure 7, which illustrates the particular effect of the periodicity used in the present method on the horizontal current component $j_{\text{horiz}}(\mathbf{r})$. In this calculation, the external magnetic field is applied in the direction orthogonal to the tube axis (orthogonal to the plane). Such an external field creates a current that does not circulate as a closed loop within a unit cell, but which is carried through the box. The

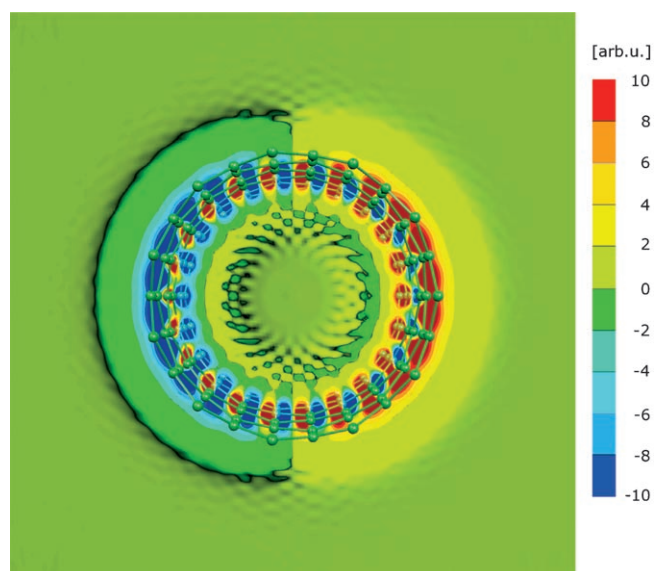


Figure 6. Vertical component of the induced current (in arbitrary units) of a (11,0) CNT for the external field along the tube axis. The section is taken in the center of a current torus (as shown in Figure 5).

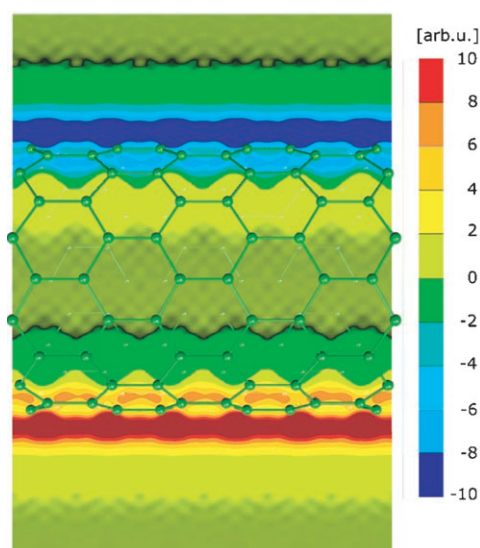


Figure 7. Horizontal current component (along the tube axis) of a (11,0) CNT for an external field perpendicular to the paper plane.

current enters the cell at the top right (and bottom left) border and leaves at the top left (and bottom right) position. In this way, two infinite "slabs" of current are created on the top and bottom of the CNT. Only if the CNT were of finite size (e.g., terminated with a suitable fullerene-type cap) would this current density be represented as a closed ring current.

Figure 8 shows the horizontal component of the magnetic field that is induced by this current density. This corresponds to a diagonal element of the NICS tensor, for instance $\sigma_{xx}(\mathbf{r})$. The current density slabs of Figure 7 would be located at the top and the bottom of the tube. They create an approximately dipolar magnetic field outside the tube, ranging from -20 to

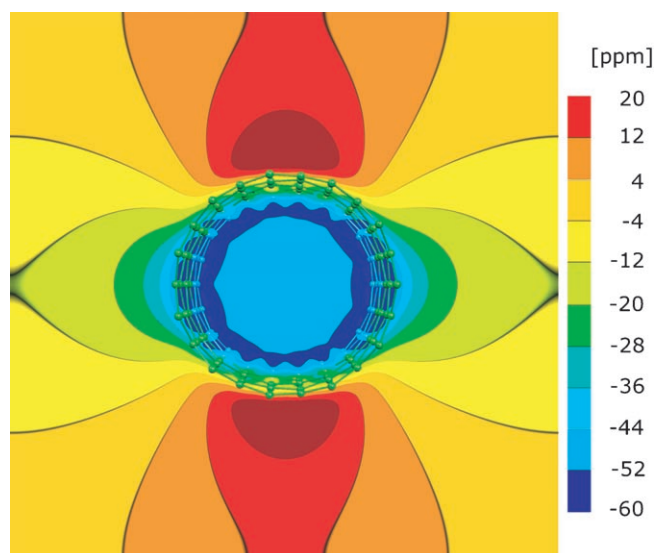


Figure 8. Horizontal component (orthogonal to the tube axis) of the induced magnetic field (in ppm) for a horizontal external field of the (11,0) CNT. Apart from the sign, this corresponds to a diagonal component of the NICS tensor (e.g., $\sigma_{xx}(\mathbf{r})$). Note the large ppm scale, but also the homogeneity of the field inside the nanotube.

$+20$ ppm. The induced field inside the CNT, however, is surprisingly homogeneous. Apart from the regions immediately adjacent to the tube wall, it varies by less than 8 ppm throughout the tube.

The superposition of this field with the other two components of the NICS tensor constitute the isotropic NICS field $\delta(\mathbf{r})$, which is shown in Figure 9. Outside the tube, the two dipole fields cancel each other when superimposed, so that the isotropically averaged shift tensor is close to zero. Inside the tube, all three components of the NICS tensor have equal signs and thus add up. They result in an isotropic NICS field that is very homogeneous in the entire nanotube.

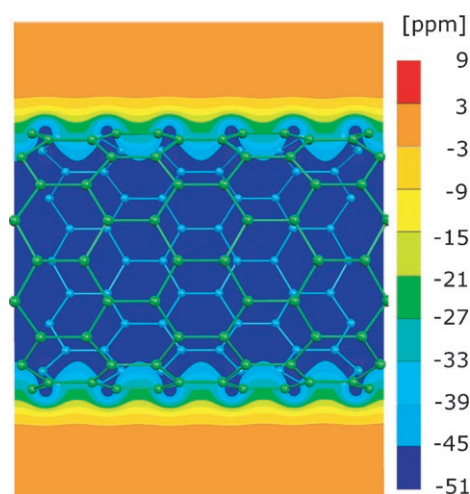


Figure 9. Isotropic NICS field (in ppm). Note that the NICS outside the tube is quasiszero, while the values inside are on the order of -45 to -51 ppm and very homogeneous.

This isotropic NICS field is not unexpected, since the nanotube is of course very symmetric with respect to rotations around its axis. This does not allow for significant asymmetries in the NICS. However, the very strong variations in the field shown in Figure 8 would lead to a large chemically induced shift anisotropy (CSA) for spins located outside the nanotube. This could be useful for determining experimentally whether a certain molecule (e.g., H_2) is physisorbed outside of the CNT, where its chemical shift would vary only relatively little.

In comparison to calculations on finite CNTs,^[80,81] the NICS values of the present infinite tubes are significantly more negative. While the finite segments yield NICS shifts similar to that of benzene (−9 to −12 ppm) for aromatic rings, I observe roughly two to three times those values (cf. Figure 9). This could be due to the position where the NICS values were taken in refs. [80,81]^[80,81] (1 Å along the normal to the hexagon plane). It appears that these locations, although very common for isolated planar molecules, are not perfectly suitable for carbon nanotubes, because their NICS fields have strong gradients in these areas (see Figure 9). Another possible explanation of the discrepancies is the mere fact of the finite size of the tube segments. The NICS field of the infinite rest of the CNT might provide a significant contribution which is not taken into account in the isolated model system. In my calculations, I also observe a much stronger difference between the regions inside and outside the tubes. Unfortunately, no information is given in refs. [80,81] concerning NICS values deeper inside or outside the CNT. Their trend (more negative NICS values inside than outside), however, agrees qualitatively with my results.

More technically, the absence of diffuse basis functions in the calculations of both articles (6–31G* at most) might be another source of numerical differences. My plane-wave basis set principally lacks accuracy in the atomic core region, but is practically converged in terms of diffuse basis functions (i.e., the possibility to represent delocalized electronic states).

3.3.2. Zig-Zag (11,0)–(12,0) Transition

My approach for the calculation of magnetic linear response properties is suitable for insulators and semiconductors (i.e., for systems with a sizeable band gap), but it is not designed for conductors. Thus, the calculation of a metallic (12,0) CNT is not possible. However, this difficulty can be partially circumvented by “interrupting” a (12,0) CNT with a piece of a (11,0) CNT as presented in the previous section.

To this end, the (11,0) and (12,0) nanotube pieces are connected with a pentagon/heptagon pair at each junction. The rest of the nanotube topology remains unchanged. The geometry for this arrangement was taken from the website of Ph. Lampin^[82] and optimized by using the plane-wave DFT methodology described above. The geometry of this hybrid CNT is shown in Figure 10, where the unit cell of the system is replicated twice in the direction of its axis.

In analogy to Figure 7, the electronic current density for an external field orthogonal to the tube axis is shown in Figure 11. Apart from the distortions due to the junction between the (11,0) and (12,0) CNT pieces, which make the current

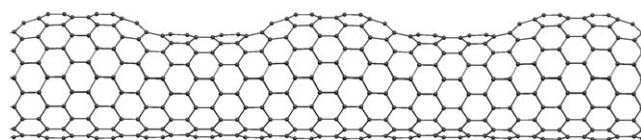


Figure 10. Geometry of the junction between a (11,0) and a (12,0) carbon nanotube. For this illustration, the unit cell is replicated twice along the tube axis.

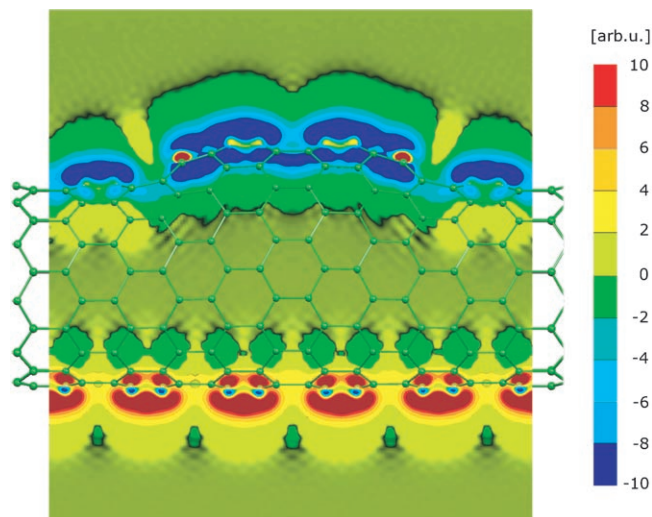


Figure 11. Horizontal current component for an external field perpendicular to the paper plane for the (11,0)–(12,0) CNT junction. The scale is the same that of Figure 7.

distribution somewhat less homogeneous, the picture is similar to Figure 7. Also in this case, the current which enters from the top right border leaves at the top left position, while the same happens with inverse orientation at the bottom of the tube.

The resulting induced magnetic field is indeed very similar to that of the (11,0) CNT in Figure 8 (data not shown). A small difference, however, appears when considering the isotropic NICS field, which is shown in Figure 12. The effect of the

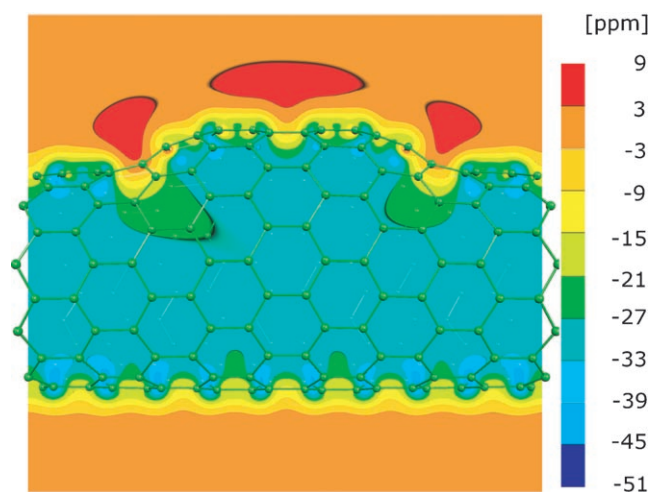


Figure 12. Isotropic NICS field (in ppm) of a CNT at a (11,0)–(12,0) defect. The scale is the same as that of Figure 9.

broken rotational symmetry of the CNT is clearly visible, both as a local weakening of the inner-tube NICS at the positions of the heptagons as well as small positive NICS regions outside the (12,0) fragment. The NICS field inside the (11,0)–(12,0) hybrid is still very homogeneous, but its somewhat distorted structure leads to a smaller NICS inside the tube, which is lowered to about -33 to -39 ppm.

Although the difference in the NICS between a (12,0) and a (11,0) CNT cannot be determined quantitatively at this stage from the calculations so far, the method is in principle capable of delivering such data. This could be used for a variety of purposes, for example, to discriminate different CNT flavors by filling them with test spins such as H_2 and measuring its 1H NMR, or to determine which kind of nanotube is preferably filled by H_2 when a mixture of CNTs is present.

4. Conclusions

I have presented the theoretical and computational details of the implementation of nucleus independent chemical shift (NICS) maps under periodic boundary conditions in the pseudopotential plane-wave code CPMD,^[53] based on its magnetic linear response module.^[41,42,59] The NICS maps are directly obtained at all points of the periodic unit cell by means of Fourier transformations from reciprocal space.

This implementation has the capability of computing NICS maps not only for isolated molecules, but also for extended solids. I have therefore demonstrated this tool by applying it to a series of extended systems. Unless specially extended to periodic boundary conditions, standard quantum chemistry codes with localized basis sets are not suitable for such systems. NICS maps were computed for calixhydroquinone, for the nanotubes it forms by means of a hydrogen-bond network, for graphite, and for two types of carbon nanotubes. The results can provide valuable insight into the electronic properties of extended systems, especially concerning aromaticity issues.

Acknowledgments

I thank H. W. Spiess and B. Kirchner for stimulating discussions. This work has been supported by the Deutsche Forschungsgesellschaft (DFG) under research grant SE 1008/2.

Keywords: carbon • density functional calculations • nanotubes • nucleus-independent chemical shifts • NMR spectroscopy

- [1] S. Brown, H. W. Spiess, *Chem. Rev.* **2001**, *101*, 4125.
- [2] C. J. Jameson, A. C. de Dios, *Nucl. Magn. Reson.* **2004**, *33*, 47–75.
- [3] C. E. Johnson, F. A. Bovey, *J. Chem. Phys.* **1958**, *29*, 1012–1014.
- [4] P. v. R. Schleyer, C. Maerker, A. Dransfeld, H. Jiao, N. J. R. v. E. Hommes, *J. Am. Chem. Soc.* **1996**, *118*, 6317–6318.
- [5] "Aromaticity": P. v. R. Schleyer (Ed.), *Chem. Rev.* **2001**, *101*.
- [6] J. I. Aihara, *Chem. Phys. Lett.* **2002**, *365*, 34–39.
- [7] C. Corminboeuf, T. Heine, J. Weber, *Phys. Chem. Chem. Phys.* **2003**, *5*, 246–251.
- [8] G. V. Lier, P. W. Fowler, F. D. Proft, P. Geerlings, *J. Phys. Chem. A* **2002**, *106*, 5128–5135.

- [9] B. Kovacevic, D. Baric, Z. B. Maksic, T. Muller, *ChemPhysChem* **2004**, *5*, 1352–1364.
- [10] P. Lazzeretti, *Phys. Chem. Chem. Phys.* **2004**, *6*, 217–223.
- [11] Y. Ruiz-Morales, *J. Phys. Chem. A* **2004**, *108*, 10873–10896.
- [12] J. Poater, X. Fradera, M. Duran, M. Sola, *Chem. Eur. J.* **2003**, *9*, 400–406.
- [13] J. Poater, X. Fradera, M. Duran, M. Sola, *Chem. Eur. J.* **2003**, *9*, 1113–1122.
- [14] A. Rapp, I. Schnell, D. Sebastiani, S. P. Brown, V. Percec, H. W. Spiess, *J. Am. Chem. Soc.* **2003**, *125*, 13284–13297.
- [15] T. Heine, P. v. R. Schleyer, C. Corminboeuf, G. Seifert, R. Reviakine, J. Weber, *J. Phys. Chem. A* **2003**, *107*, 6470–6475.
- [16] E. Steiner, P. W. Fowler, *Phys. Chem. Chem. Phys.* **2004**, *6*, 261–272.
- [17] P. v. R. Schleyer, M. Manoharan, Z.-X. Wang, B. Kiran, H. Jiao, R. Puchta, N. J. R. v. E. Hommes, *Org. Lett.* **2001**, *3*, 2465–2468.
- [18] N. H. Martin, J. D. Brown, H. Kimberly, H. Nance, H. F. Schaefer III, P. v. R. Schleyer, Z. X. Wang, H. L. Woodcock, *Org. Lett.* **2001**, *3*, 3823–3826.
- [19] C. Corminboeuf, T. Heine, G. Seifert, P. v. R. Schleyer, J. Weber, *Phys. Chem. Chem. Phys.* **2004**, *6*, 273–276.
- [20] G. Merino, T. Heine, G. Seifert, *Chem. Eur. J.* **2004**, *10*, 4367–4371.
- [21] D. Moran, F. Stahl, H. F. Bettinger, H. Schaefer, P. v. R. Schleyer, *J. Am. Chem. Soc.* **2003**, *125*, 6746–6752.
- [22] J. Juselius, D. Sundholm, J. Gauss, *J. Chem. Phys.* **2004**, *121*, 3952–3963.
- [23] S. Klod, E. Kleinpeter, *J. Chem. Soc. Perkin Trans.* **2001**, *2*, 1893–1898.
- [24] P. Lazzeretti, *Chem. Phys. Lett.* **2005**, *401*, 164–169.
- [25] E. Steiner, P. Fowler, *Org. Biomol. Chem.* **2004**, *2*, 34–37.
- [26] E. Steiner, P. W. Fowler, L. W. Jenneskens, R. W. A. Havenith, *Eur. J. Org. Chem.* **2002**, *365*, 163–169.
- [27] J. I. Aihara, *Bull. Chem. Soc. Jpn.* **2004**, *77*, 101–102.
- [28] J. Poater, M. Sola, R. G. Viglione, R. Zanasi, *J. Org. Chem.* **2004**, *69*, 7537–7542.
- [29] J. I. Aihara, S. Oe, *Bull. Chem. Soc. Jpn.* **2003**, *76*, 1363–1364.
- [30] J. I. Aihara, *J. Phys. Org. Chem.* **2005**, *18*, 235–239.
- [31] B. Kirchner, D. Sebastiani, *J. Phys. Chem. A* **2004**, *108*, 11728–11732.
- [32] P. W. Fowler, E. Steiner, R. W. A. Havenith, L. W. Jenneskens, *Magn. Reson. Chem.* **2004**, *42*, S68–S78.
- [33] P. W. Fowler, A. Soncini, *Chem. Phys. Lett.* **2004**, *383*, 507–511.
- [34] W. H. Press, S. A. Teukoldky, W. T. Vetterling, B. P. Flannery, *Numerical Recipes*, 2nd ed., Cambridge University Press, **1992**.
- [35] D. Marx, J. Hutter in *Modern Methods and Algorithms in Quantum Chemistry*, Vol. 1, *NIC Series*, Forschungszentrum Juelich, **2000**, pp. 301–449.
- [36] W. Kutzelnigg, *Isr. J. Chem.* **1980**, *20*, 193.
- [37] T. A. Keith, R. F. W. Bader, *Chem. Phys. Lett.* **1993**, *210*, 223.
- [38] R. Ditchfield, *J. Chem. Phys.* **1972**, *56*, 5688.
- [39] F. Mauri, S. Louie, *Phys. Rev. Lett.* **1996**, *76*, 4246–4249.
- [40] F. Mauri, B. Pfrommer, S. Louie, *Phys. Rev. Lett.* **1996**, *77*, 5300–5303.
- [41] D. Sebastiani, M. Parrinello, *J. Phys. Chem. A* **2001**, *105*, 1951.
- [42] D. Sebastiani, G. Goward, I. Schnell, H.-W. Spiess, *J. Mol. Struct.* **2003**, *625*, 283–288.
- [43] F. Mauri, B. Pfrommer, S. Louie, *Phys. Rev. Lett.* **1997**, *79*, 2340.
- [44] Y. Yoon, B. Pfrommer, F. Mauri, S. Louie, *Phys. Rev. Lett.* **1998**, *80*, 3388.
- [45] F. Mauri, N. Vast, C. J. Pickard, *Phys. Rev. Lett.* **2001**, *87*, 085506.
- [46] D. Sebastiani, M. Parrinello, *ChemPhysChem* **2002**, *3*, 675.
- [47] B. Pfrommer, F. Mauri, S. Louie, *J. Am. Chem. Soc.* **2000**, *122*, 123–129.
- [48] G. Goward, M. F. Schuster, D. Sebastiani, I. Schnell, H. W. Spiess, *J. Phys. Chem. B* **2002**, *106*, 9322.
- [49] D. Sebastiani, *Mod. Phys. Lett. B* **2003**, *17*, 1301–1319.
- [50] T. M. Alam, T. Friedmann, P. A. Schultz, D. Sebastiani, *Phys. Rev. B* **2003**, *67*, 245309.
- [51] A. Hoffmann, D. Sebastiani, E. Sugiono, S. Yun, K. S. Kim, H. W. Spiess, I. Schnell, *Chem. Phys. Lett.* **2004**, *388*, 164–169.
- [52] D. Sebastiani, *Int. J. Quantum Chem.* **2005**, *101*, 849–853.
- [53] J. Hutter, et al. Computer code CPMD, version 3.9, 1990–2004. Copyright IBM Corp. and MPI-FKF Stuttgart, <http://www.cpmd.org>.
- [54] P. Hohenberg, W. Kohn, *Phys. Rev.* **1964**, *136*, B864.
- [55] W. Kohn, L. J. Sham, *Phys. Rev.* **1965**, *140*, A1133.
- [56] R. O. Jones, O. Gunnarsson, *Rev. Mod. Phys.* **1989**, *61*, 689–746.
- [57] X. Gonze, J. P. Vigneron, *Phys. Rev. B* **1989**, *39*, 13120.
- [58] X. Gonze, *Phys. Rev. A* **1995**, *52*, 1096.
- [59] A. Putrino, D. Sebastiani, M. Parrinello, *J. Chem. Phys.* **2000**, *113*, 7102–7109.
- [60] R. Resta, *Phys. Rev. Lett.* **1998**, *80*, 1800–1803.

- [61] R. Resta, D. Ceresoli, T. Thonhauser, D. Vanderbilt, *ChemPhysChem* **2005**, *6*, 1815–1819.
- [62] G. Berghold, C. Mundy, A. Romero, J. Hutter, M. Parrinello, *Phys. Rev. B* **2000**, *61*, 10040.
- [63] V. G. Malkin, O. L. Malkina, M. E. Casida, D. R. Salahub, *J. Am. Chem. Soc.* **1984**, *106*, 5898.
- [64] M. Bühl, M. Kaupp, O. L. Malkina, V. Malkin, *J. Comput. Chem.* **1999**, *20*, 91–105.
- [65] K. Kobayashi, M. Tsukada, *Phys. Rev. B* **1988**, *38*, 8566–8578.
- [66] P. Flükiger, H. P. Lüthi, S. Portmann, J. Weber, Molecular visualization program MOLEKEL, version 4.0. Swiss Center for Scientific Computing, Manno (Switzerland), **2000**.
- [67] S. Kimball, P. Mattis, GNU Image Manipulation Program GIMP, version 2.0. released under the GNU public license, <http://www.gimp.org>.
- [68] A. D. Becke, *Phys. Rev. A* **1988**, *38*, 3098.
- [69] C. Lee, W. Yang, R. G. Parr, *Phys. Rev. B* **1988**, *37*, 785–789.
- [70] S. Goedecker, M. Teter, J. Hutter, *Phys. Rev. B* **1996**, *54*, 1703.
- [71] C. Hartwigsen, S. Goedecker, J. Hutter, *Phys. Rev. B*, **1998**, *58*, 3641.
- [72] G. Schreckenbach, S. K. Wolff, T. Ziegler, *J. Phys. Chem. A* **2000**, *104*, 8244–8255.
- [73] M. Straka, M. Kaupp, *Chem. Phys. Lett.* **2005**, *411*, 45–56.
- [74] B. H. Hong, J. Y. Lee, C.-W. Lee, J. C. Kim, S. C. Bae, K. S. Kim, *J. Am. Chem. Soc.* **2001**, *123*, 10748–10749.
- [75] K. S. Kim, S. B. Suh, J. C. Kim, B. H. Hong, E. C. Lee, S. Yun, P. Tarakeswar, J. Y. Lee, Y. Kim, H. Ihm, H. G. Kim, J. W. Lee, J. K. Kim, H. M. Lee, D. Kim, C. Cui, S. J. Youn, H. Y. Chung, H. S. Choi, C.-W. Lee, S. J. Cho, S. Jeong, J.-H. Cho, *J. Am. Chem. Soc.* **2002**, *124*, 14268–14279.
- [76] S. Iijima, *Nature* **1991**, *354*, 56–58.
- [77] J. W. Mintmire, B. I. Dunlap, C. T. White, *Phys. Rev. Lett.* **1992**, *68*, 631.
- [78] A. Thess, R. Lee, P. Nikolaev, H. Dai, P. Petit, J. Robert, C. Xu, Y. H. Lee, S. G. Kim, D. T. Colbert, G. Scuseria, D. Tománek, J. E. Fischer, R. E. Smalley, *Science* **1996**, *273*, 483.
- [79] S. Berber, Y.-K. Kwon, D. Tománek, *Phys. Rev. Lett.* **2000**, *84*, 4613–4616.
- [80] Y. Matsuo, K. Tahara, E. Nakamura, *Org. Lett.* **2003**, *5*, 3181–3184.
- [81] J. L. Ormsby, B. T. King, *J. Org. Chem.* **2004**, *69*, 4387–4391.
- [82] The initial atomic geometries were taken from the website of Ph. Lambin at www.fundp.ac.be/~phlambin/Nanotube/knee.html. Further geometry optimization was done as described in the text.

Received: August 2, 2005

Published online on December 6, 2005

Ab-initio and experimental ^1H NMR signatures of solvated ions: the case of $\text{HCl}(\text{aq})$

Tatiana Murakhtina[†], Jasper Heuft[‡], Evert Jan Meijer[‡] and Daniel Sebastiani^{†*}

[†] Max-Planck-Institute for Polymer Research

Ackermannweg 10, 55128 Mainz, Germany

[‡] Van 't Hoff Institute for Molecular Sciences (HIMS)

Universiteit van Amsterdam

Nieuwe Achtergracht 166

NL-1018 WV Amsterdam

June 13, 2006

*Dr. Daniel Sebastiani, Email: sebastia@mpip-mainz.mpg.de, Fax: +49-6131-379-100.

Abstract

We present a combined experimental and ab-initio study of the ^1H NMR chemical shift resonance of aqueous hydrochloride solution as a function of acid concentration, based on Car-Parrinello molecular dynamics simulations and fully periodic NMR chemical shift calculations. The agreement of computed and experimental spectra is very good. From the first-principles calculations, we can show that the individual contributions of Eigen and Zundel ions, regular water molecules and the chlorine solvation shell to the NMR resonance line are very distinct, and almost independent on the acid concentration. From the computed instantaneous NMR distributions, it is further possible to characterize the average variation in hydrogen bond strength of the different complexes.

1 Introduction

The determination of the detailed microscopic structure and dynamics of complex aqueous solutions is still a challenge for modern physics and chemistry. The nature of water interaction with dissolved ions, dissolved molecules and at interfaces is crucial for a broad range of chemical, biological, and physical processes that occur in solution. Biomacromolecular folding and self-assembly, for example, which take place in aqueous solutions are strongly affected by the microscopic surrounding [1]. In order to investigate the solvation of ions and molecules, a variety of experimental methods are successfully applied, such as Raman and IR spectroscopy [2], ultrafast spectroscopy [3, 4, 5, 6, 7] and neutron and x-ray diffraction techniques [8]. However, precise quantitative results are still rare due to severe difficulties in extracting accurate and unambiguous information from experimental data.

In crystalline systems, scattering experiments can provide very accurate atomic coordinates. Aqueous systems, however, lack the required long-range order, which limits the applicability of these scattering techniques. Complementary to this, NMR experiments are able to probe local structure without the need of long-range order. Their sensitivity to the local chemical environment of an atom is one of the key advantages of this method. The dependence of NMR chemical shifts of a given stable molecule on its chemical surrounding is well-established for solutions, where the change in the NMR resonance is called solvent shift. Its nature and a magnitude are due to the interaction of the solvent molecules with the solute, which can be hydrogen bond networks, van-der-Waals forces, or other non-bonded interactions. While the NMR signal is very sensitive to change in the average structural configuration, fast fluctuations of the molecular arrangement in aqueous solutions do not allow to get individual lines of protons involved in exchange processes. A particular case in point are acidic molecules, which dissociate in aqueous solution and give a free proton to the solvent. Such an excess proton will

migrate and exchange with regular water protons via Grotthus-style hopping process. This process happens on a sub-picosecond timescale and is therefore averaged in the ^1H NMR spectrum.

It has become increasingly common to supplement the experimental data with adequate numerical simulations. Classical molecular dynamics (MD) techniques are performed for structures obtained via X-rays in order to test their conformational stability; quantum chemical calculations of vibrational frequencies can often help interpreting Raman and IR spectra [9, 10, 11, 12, 13]. In NMR, dihedral angles are probed by spin-spin coupling constants and cross-relaxation rates due to dipole-dipole interactions provide distance constraints for MD simulations. For magnetic resonance experiments, accompanying ab-initio calculations have become standard for isolated molecules [14, 15, 16], and are becoming increasingly popular also for the solid state [17, 18, 19, 20, 21], as well as for liquids and solutions [1, 22, 23, 24, 25].

In case of pure water, important progress has been achieved in the direct simulation of the molecular structure in the liquid phase [26, 27], the understanding of its IR spectrum [11, 25], the Raman spectrum of ice [9], the NMR parameters in the liquid and supercritical phases [24, 22], and last not least the hydrogen bond network of water on surfaces [28, 29, 30]. In recent years, much attention has been dedicated also to the solvation shell structures and dynamics of ions in aqueous solutions and a variety of ab initio molecular dynamics simulations of aqueous acids were performed [11, 27, 12, 31, 32, 33, 34, 35, 36, 37, 38]. While the full microscopic structure of solutions are easily accessible from ab initio simulations [26, 27, 39], there is often no immediate comparison with experiment possible except the assignment of radial distribution functions to X-ray experimental data [40, 41]. However, the ab-initio simulation of structure and magnetic resonance properties of liquid water and aqueous solutions is not yet routinely done. This is partly due to the dynamically fluctuating hydrogen bond network as the central structural driving force, which requires an extensive phase-space

sampling of the NMR parameters. The theoretical investigation of nuclear shieldings and chemical shifts can not only improve greatly our knowledge about detailed structure of ionic solvation shells but also bridge the gap between experiment and theory. Proton chemical shifts are very sensitive to the character of hydrogen bond network and accessible via ab initio calculations. Moreover, they provide us with possibility to compute individual NMR signatures of a variety of species and sub-structures that cannot be resolved in experiment.

In this work, we present the first-principles calculation of the ^1H NMR chemical shift distribution of HCl aqueous solution as a function of concentration. We validate our ab initio results by comparing our computed averaged chemical shifts with experimental spectra obtained by liquid-state ^1H NMR experiments for the same concentration values. To clarify the origin of the obtained chemical shift distributions, we decompose the set of ab initio proton shifts into contributions from different types of geometrical configurations: Eigen-/Zundel-complexes, the first solvation shells of the Cl^- ions, and the regular water molecules. Finally, we analyze and discuss the computed histograms of instantaneous ^1H NMR chemical shifts in term of calculated individual NMR chemical shift signatures of solvated species.

2 Methods and computational details

Ab-initio molecular dynamics simulations

We studied a pure water system consisting of 64 H_2O molecules, a singly protonated water (64 H_2O molecules and one H^+), as well as HCl solutions at two concentrations ($c=2.6\text{M}$ and $c=4.9\text{M}$). These acids contained three and six (dissociated) H^+Cl^- molecules, with 61 and 58 water molecules, respectively. A periodic supercell of $a=15.6\text{\AA}$ box length was used, such that the known experimental densities at the two different acid concentrations are reproduced.

The MD simulations were done at an average temperature of $T=330\text{K}$. This value is somewhat higher than the corresponding experimental T° , in agreement with recent findings about the role of temperature in Car-Parrinello MD simulations [42, 43]. The calculations were performed in the framework of density functional theory using the gradient corrected exchange- correlation functionals proposed by Becke [44] and Lee, Yang, and Parr (BLYP) [45], and a plane wave basis set at a cutoff of 70 Ry. All MD simulations and NMR chemical shift calculations were performed within the CPMD program suite [46, 47].

NMR chemical shift calculations

As the basis for our spectroscopic calculations, we use trajectories obtained previously via canonical Car-Parrinello molecular dynamics simulations [36]. The calculations of the NMR chemical shifts were always done at the same computational setup for all

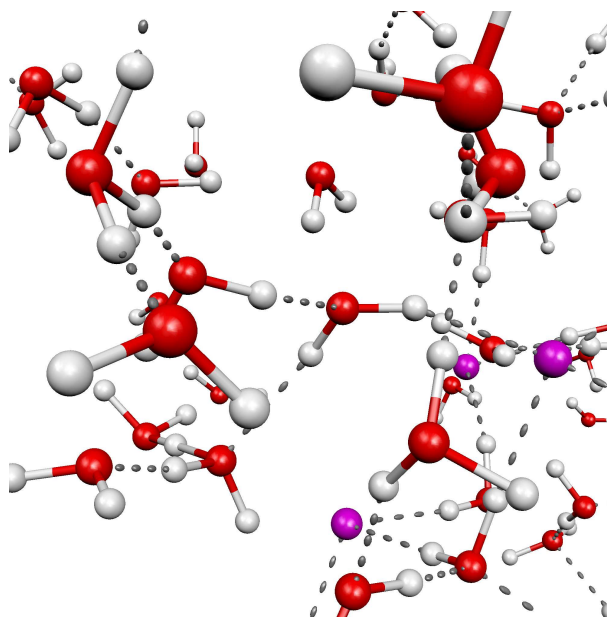


Figure 1: (Color online) Geometry of a snapshot taken from the MD-simulations at 4.9M HCl concentration. Apart of the normal hydrogen bonding network of water, the solvation of some of the chlorine ions (right) as well as a Zundel ion (bottom left) and two hydronium ions (top left and bottom right) are visible.

systems, in order to provide a consistent description for the comparison. Twenty snapshots for acids and sixteen for water were extracted from the MD simulations, and their proton nuclear shieldings were computed under full consideration of the periodic boundary conditions, following the method described in refs. [48, 49, 50]. For illustration, a snapshot taken from one of the simulations at high concentration is shown in figure 1. This scheme provided about 2000 individual shielding values for water and 2500 for each of the considered acid concentrations. These values would correspond to a sample where the atoms were frozen at their instantaneous positions. The computed nuclear shieldings were referenced to the time- and atom-averaged shielding (indicated by $\langle \rangle$ brackets) of the pure liquid water system, $\sigma^{\text{ref}} = \langle \sigma(\text{pure H}_2\text{O}) \rangle$, according to the usual experimental convention:

$$\delta(X) = 1/3\text{Tr}[\sigma^{\text{ref}}] - 1/3\text{Tr}[\sigma(X)] \quad (1)$$

so that $\langle \delta(\text{pure H}_2\text{O}) \rangle = 0\text{ppm}$. With respect to TMS (i.e. using $\sigma^{\text{ref}} = \sigma(\text{TMS})$ instead of eq. (1)), our liquid water would have its NMR chemical shift resonance at $\delta^{\text{TMS}}(\text{H}_2\text{O}) = 5.9\text{ppm}$. While this value is somewhat above the experimental one (4.8ppm), it is in agreement with previous ab-initio NMR calculations for several liquid water systems [22, 24], which also overestimated the proton shifts. The observed deviations illustrate the difficulties of the BLYP xc-functional to describe the hydrogen bond network of water, which turns out to be somewhat over-structured [51, 42, 43]. Nevertheless, the computational methods used here have already been successfully used to predict and interpret experimental solid-state NMR data [52].

Experiments measure the average of the ^1H NMR chemical shift over all hydrogen nuclei and over a measuring time in the range of microseconds or more. Thus, it is important to verify that within the comparatively short simulations time of 12 ps, all relevant relaxation processes have taken place, and that our statistical averages are accurate. In order to verify this point, we have compared the results for different simulation

windows out of the trajectories. Ten momentaneous configurations were extracted from each of the trajectories pieces between 10-12ps and 19-21ps for diluted acid as well as between 6-8ps and 11-13ps for concentrated ones, and eight snapshots for each of intervals between 10-15ps and 26-31ps for water trajectories. The results show that our statistical averages are sufficiently converged in this respect.

Experimental NMR chemical shifts

We have prepared diluted and concentrated HCl(aq) solutions with $c \approx 2.6\text{M}$ and $c \approx 4.9\text{M}$. The solutions were titrated against a high-precision 0.1M NaOH solution in order to determine the exact experimental concentrations, which deviated only insignificantly ($\pm 0.07\text{M}$) from the desired values, as used in the simulations. Liquid-state NMR spectra were recorded on a Bruker DPX spectrometer operating at 250 MHz ^1H Larmor frequency, and referenced to the NMR resonance line of pure water.

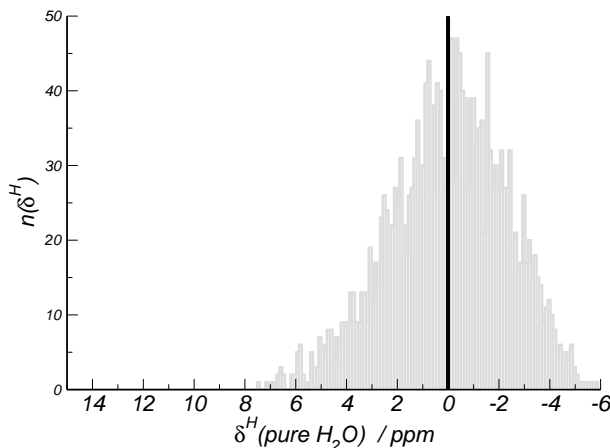


Figure 2: Histogram of the computed instantaneous NMR chemical shift values for pure water. The nuclear shieldings are referenced such that the averaged NMR shift, which is shown as a solid line, appears at $\delta(\text{pure H}_2\text{O})=0\text{ppm}$.

3 Results and discussion

We have computed the histograms of instantaneous ^1H NMR chemical shift values for the four liquids systems. For the pure water sample, the resulting distribution is shown in figure 2. As mentioned above, the calculated nuclear shieldings are referenced such that the average value of the chemical shifts (marked by a solid line in the distribution) is $\delta(\text{H}_2\text{O})=0\text{ppm}$. The distribution has a similar shape to the one obtained previously for a different liquid water sample [24]. It resembles a slightly non-symmetric Gaussian with a half-width of about 6ppm. This large spread is due to the variety of hydrogen bonding situations in liquid water, ranging from very weak (towards negative δ -values) to very strong (towards positive δ -values). The observed asymmetry in $n(\delta)$ is due to the fact that the H-bonding strength cannot be significantly weaker than that of an isolated molecule (which corresponds to about $\delta^{\text{H}_2\text{O}} \approx -6\text{ppm}$ when using our referencing to the shielding of pure liquid water), while there is in principle no limit in the direction of increasing H-bonding strength.

The NMR chemical shift histograms of the acidic samples with $c(\text{HCl})=2.6\text{M}$ and

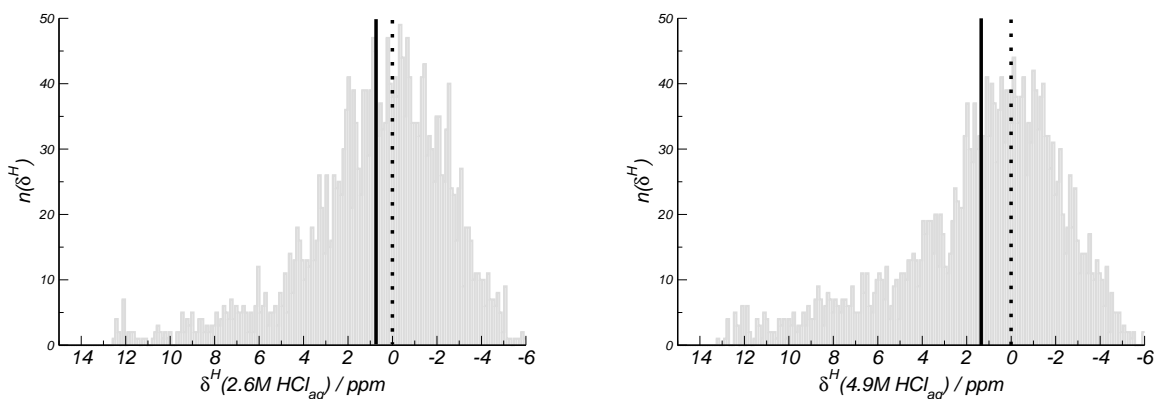


Figure 3: Histogram of the computed instantaneous NMR chemical shift values for $c=2.6\text{M}$ (left) and $c=4.9\text{M}$ (right), referenced to pure water. The averaged NMR resonances and the water lines are shown as solid and dotted lines, respectively.

$c(\text{HCl})=4.9\text{M}$ are shown in figure 3. While the shape of the distributions around their central peaks is still of Gaussian type, they exhibit a significantly more pronounced tail towards positive δ -values. Their intensity is almost twice as strong for the higher acid concentration.

Here, these tails move the *average* chemical shifts away from the *maximum* of the central peak, which in both acids is still located at the value found for pure water ($\delta=0\text{ppm}$, dotted lines). The shift difference between the high concentrated acid and pure water turns out to be about twice as large as for the more diluted solution.

In a neutral water system, our observed high-frequency shift values would correspond to very strong hydrogen bonding of the concerned protons. Hence, the question arises which structural features are responsible for these signals. While it could simply be a consequence of stronger distortions of the H-bonding network due to the solvated ions, it could also be a characteristic NMR resonance from both the protons in the H_3O^+ complexes and those in the direct neighborhood of the Cl^- ions. The fact that the deviation of the average shift appears to have a roughly linear dependency on the HCl concentration is already an indication for the latter assumption.

To clarify the origine of the observed chemical shifts distribution, a decomposition of the set of obtained proton shifts into contributions from different geometrical classes of configurations has been done, using simple geometric criteria derived from the radial distribution functions given in ref. [36]. We distinguish between $\text{H}_3\text{O}^+/\text{H}_5\text{O}_2^+$ complexes, protons in the first solvation shell of Cl^- ions, and the remaining protons in regular water molecules. The Eigen/Zundel cations were defined via the protonation number of the central oxygen atoms. An Eigen cation was assumed when an oxygen was bonded to three protons with $d_{\text{O-H}} \leq 1.3\text{\AA}$, while a Zundel complex corresponds to the case where two (previously detected) Eigen cations share one proton. In contrast to the common definition of Eigen complexes (H_9O_4^+), the three waters surrounding the central hydronium (H_3O^+) were not included in the averaging of our NMR data, since their

hydrogen bonding situation is closer to that of regular water. A proton was considered part of the first solvation shell of a chlorine anion if $d_{\text{Cl-H}} \leq 2.85\text{\AA}$. Finally, all protons which were neither part of an Eigen/Zundel complexes nor sufficiently close to any Cl^- ion were defined as regular water hydrogens.

The NMR chemical shift contributions corresponding to these different types of geometrical configurations is shown in table 1. The correlation between the structural arrangement in which a proton is found and the resulting chemical shifts is striking. While the regular water molecules are almost completely unaffected by the presence of the chlorine and hydronium ions, the protons which are part of an Eigen or Zundel cations are high-frequency shifted by about 7.4ppm (H_3O^+) and 5.8ppm (H_5O_2^+). The opposite is found for hydrogens in water molecules which solvate the chlorine anions: their NMR signal is located at low-frequency values, -0.3/-0.8ppm with respect to regular water.

Qualitatively, this trend can be explained via electron density considerations. In a hydronium ion, the water electrons are shared by three protons, so that with respect to neutral water, there is less electronic density available per hydrogen. The same – to a lesser extent – is the case for a Zundel complex. In contrast to this, the hydrogens in a chlorine solvation shell point into a large electron cloud. In addition, this cloud is

system	regular water	Eigen cations	Zundel complexes	1 st Cl^- solv. shell	all protons (comp.)	all protons (exp.)
pure H_2O	0.0	-	-	-	0.0	0.0
single H_{aq}^+	0.0	7.4	-	-	0.2	-
2.7M HCl_{aq}	0.1	7.5	5.9	-0.8	0.7	0.7
4.9M HCl_{aq}	0.2	7.3	5.6	-0.3	1.3	1.4

Table 1: Individual ^1H NMR chemical shift signatures of the protons in Eigen-/Zundel-complexes, in the first solvation shells of the Cl^- ions, and in the regular water molecules. The total average and the corresponding experimental values are also shown.

somewhat more delocalized than the lone pairs of a water oxygen, due to the negative charge of the chlorine. This results in a stronger shielding of the proton spin, and hence a more negative shift than for a normal proton that is H-bonded to a water oxygen.

Interestingly, the chemical shifts of these complexes depend only little on the total concentration of ions; the protons in Eigen cations have almost the same shift for a single solvated H^+ as for the strongly concentrated acid. For the Zundel complexes, the situation is similar; the small change of 0.3ppm between the 2.6M and 4.9M acids can be explained by the decreased amount of water molecules which are available for building the solvation shells. The same tendency towards smaller absolute shifts is seen for protons in the chlorine solvation shells; they also approach the shift of regular water (0.0ppm).

This data explains the histograms shown in figure 3: the maximum of the distribution, which corresponds to protons from regular water molecules, is essentially unmodified by the addition of the acid; the high-frequency tails in the region around 5-8ppm are exclusively due to the solvated H^+ cations. Since the protons which solvate the Cl^- yield an NMR signal very close to that of regular water, their contributions are not clearly visible in the histograms. If our statistics were sufficiently improved, the NMR signatures of those protons would possibly appear as a low-frequency-shoulder in the shift distributions. However, with the data available from our calculations, this effect can only be seen in the decomposition of the shifts.

Finally, the comparison of the averaged NMR shifts from the ab-initio calculations with our measured liquid-state ^1H NMR spectra of the HCl acids at the two concentrations is presented in figure 4. As for the calculated shifts, the experimental values were referenced to pure liquid water. The agreement is essentially perfect for the low concentration and still very good for the sample at 4.9M. While the agreement at $c_{\text{HCl}}=2.6\text{M}$ is probably fortuitous, the accuracy at the higher concentrated acid is in line with previous ab-initio calculations in similar systems [24, 22, 18, 53, 54]. We believe that our

numerical overall accuracy allows for an estimated error bar of $\sim 0.3\text{ppm}$, due to the deficiencies of density functional theory in describing hydrogen bonds, the use of the pseudopotential approximation, the incomplete basis set, the finite size of our computational water box, the thermodynamical equilibration of the Car-Parrinello simulations and similar numerical approximations. The very good agreement also provides support that, despite these computational issues, the description of disordered and highly fluctuating liquids and solutions by means of Car-Parrinello molecular dynamics simulations as well as the ensemble averages of spectroscopic parameters based on them do give a realistic picture of microscopic structure of complex solutions.

4 Conclusions

We have presented a first principles analysis of the ^1H NMR chemical shift distributions and spectra of aqueous HCl at two concentrations, accompanied by the corresponding experimental NMR resonance lines. The agreement between experiment and the calculations is very good, giving us confidence that the underlying Car-Parrinello molecular

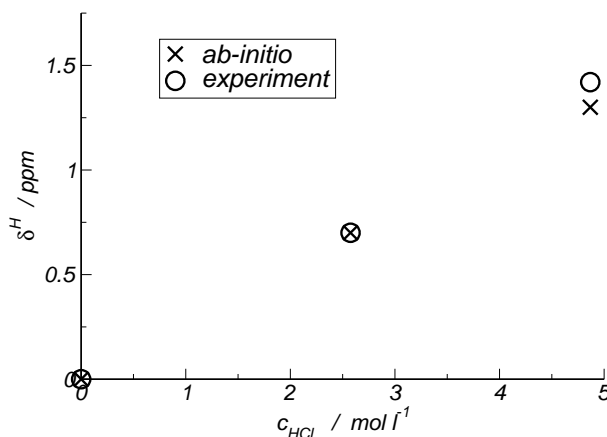


Figure 4: Dependence of the experimental and calculated NMR chemical shifts on the HCl concentration. In all cases, the actual concentrations (as obtained from titration, and computed in the simulation parameters, respectively) are used.

dynamics simulations are well equilibrated and give a representative description of the acidic solutions. Both the trajectory generation and the determination of the NMR parameters was done under periodic boundary conditions, at consistent consideration of the spatial and temporal fluctuations in the atomic structure and hydrogen bonding network of the liquids.

We have investigated the structural origins of the observed chemical shift trends in terms of Eigen and Zundel cations, the first chlorine solvation shell, and the remaining regular water molecules. This data shows in unprecedented details the correlation between microscopic configurations and NMR parameters in this class of systems, giving access to structure-property relationships which are difficult to obtain from experiment alone.

Finally, our study elucidates the potential of the powerful combination of first principles computer simulations and spectroscopy calculations based on them with the corresponding experiments. The typical NMR signatures of packing effects in supramolecular systems (in particular hydrogen bonding) could be clearly assigned to geometric features.

5 Acknowledgements

We would like to thank Dr. A. Koch for supporting us in the accurate determination of the different acid concentrations, as well as Dr. C. Deller and P. Kindervater for assistance in the liquid NMR measurements. Prof. H.W. Spiess is gratefully acknowledged for critically reading the manuscript. This work was supported by the German Science Foundation (DFG) through its program "SFB 625".

References

- [1] A. Soper and P. Rossky, *Chem. Phys.* **258**, 107 (2000).
- [2] N. B. Colthup, L. H. Daly and S. E. Wiberley, *Introduction to infrared and Raman spectroscopy*, Academic Press, New York, 1975.
- [3] P. Wernet et al., *Science* **304**, 995 (2004).
- [4] J. D. Smith et al., *Science* **306**, 851 (2004).
- [5] A. Nilsson et al., *Science* **308**, 793a (2005).
- [6] J. D. Smith et al., *Science* **308**, 793b (2005).
- [7] E. Pines, D. Pines, Y. Z. Ma and G. R. Fleming, *ChemPhysChem* **5**, 1315 (2004).
- [8] B. E. Warren, *X-Ray Diffraction*, Dover, Mineola, 1990.
- [9] A. Putrino and M. Parrinello, *Phys. Rev. Lett.* **88**, 176401 (2002).
- [10] P. Umari and A. Pasquarello, *Diam. rel. mat.* **14**, 1255 (2005).
- [11] P. L. Silvestrelli, M. Bernasconi and M. Parrinello, *Chem. Phys. Lett.* **277**, 478 (1997).
- [12] M. Gaigeot and M. Sprik, *J. Chem. Phys.* **107**, 10344 (2003).
- [13] T. Murakhtina, L. Delle Site and D. Sebastiani, *ChemPhysChem* **7**, 1215 (2006).
- [14] M. Bühl, M. Kaupp, O. L. Malkina and V. Malkin, *J. Comput. Chem.* **20**, 91 (1999).
- [15] C. J. Jameson and A. C. de Dios, *Nuc. Mag. Res.* **33**, 47 (2004).
- [16] M. Kaupp, M. Bühl, M. Malkin and G. Vladimir, editors, *Calculations of NMR and EPR parameters*, Wiley-VCH, Weinheim, 2004.

- [17] G. Goward, D. Sebastiani, I. Schnell and H. W. Spiess, *J. Am. Chem. Soc.* **125**, 5792 (2003).
- [18] J. R. Yates et al., *J. Am. Chem. Soc.* **127**, 10216 (2005).
- [19] C. Gervais et al., *J. Phys. Chem. A* **109**, 6960 (2005).
- [20] J. Schmidt and D. Sebastiani, *J. Chem. Phys.* **123**, 074501 (2005).
- [21] M. Schulz-Dobrick, T. Metzroth, H. W. Spiess, J. Gauss and I. Schnell, *ChemPhysChem* **6**, 315 (2005).
- [22] B. Pfrommer, F. Mauri and S. Louie, *J. Am. Chem. Soc.* **122**, 123 (2000).
- [23] R. A. Klein, B. Mennuci and J. Tomasi, *J. Phys. Chem. A* **108**, 5851 (2004).
- [24] D. Sebastiani and M. Parrinello, *ChemPhysChem* **3**, 675 (2002).
- [25] M. Sharma, R. Resta and R. Car, *Phys. Rev. Lett.* **95**, 187401 (2005).
- [26] K. Laasonen, M. Sprik, M. Parrinello and R. Car, *J. Chem. Phys.* **99**, 9080 (1993).
- [27] P. Silvestrelli and M. Parrinello, *J. Chem. Phys.* **111**, 3572 (1999).
- [28] D. Sebastiani and L. Delle Site, *J. Chem. Theory Comp.* **1**, 78 (2005).
- [29] M. A. Henderson, *Surf. Sc. Rep.* **46**, 1 (2002).
- [30] R. Ludwig, *Angew. Chem. Int. Ed. Engl.* **42**, 3458 (2003).
- [31] S. Raugei and M. Klein, *J. Chem. Phys.* **116**, 196 (2002).
- [32] T. von Rosenvinge, M. E. Tuckerman and M. L. Klein, *Farad. Disc.* **106**, 273 (1997).
- [33] A. J. Sillanpaa, C. S. C, M. L. Klein and K. Laasonen, *J. Phys. Chem. B* **106**, 11315 (2002).

- [34] S. L. Raugai and M. L. Klein, *ChemPhysChem* **5**, 1569 (2004).
- [35] C. Simon and M. L. Klein, *ChemPhysChem* **6**, 148 (2005).
- [36] J. M. Heuft and E. J. Meijer, *Phys. Chem. Chem. Phys.*, in press (2006).
- [37] M. Boero, T. Ikeshoji and K. Terakura, *chemphyschem* **6**, 1775 (2005).
- [38] F. C. Lightstone, E. Schwegler, M. Allesch, F. Gygi and G. Galli, *chemphyschem* **6**, 1745 (2005).
- [39] M. Sprik, J. Hutter and M. Parrinello, *J. Chem. Phys.* **105**, 1142 (1996).
- [40] B. Hetényi, F. D. Angelis, P. Giannozzi and R. Car, *J. Chem. Phys.* **120**, 8632 (2004).
- [41] B. Hetenyi, F. D. Angelis, P. Giannozzi and R. Car, *J. Chem. Phys.* **124**, 099901 (2006).
- [42] I.-F. W. Kuo et al., *J. Phys. Chem. B* **108**, 12990 (2004).
- [43] J. VandeVondele et al., *J. Chem. Phys.* **122**, 014515 (2005).
- [44] A. D. Becke, *Phys. Rev. A* **38**, 3098 (1988).
- [45] C. Lee, W. Yang and R. G. Parr, *Phys. Rev. B* **37**, 785 (1988).
- [46] J. Hutter et al., Computer code CPMD, version 3.10, 1990-2005, Copyright IBM Corp. and MPI-FKF Stuttgart, <http://www.cpmd.org>.
- [47] J. Hutter and A. Curioni, *ChemPhysChem* **6**, 1788 (2005).
- [48] D. Sebastiani and M. Parrinello, *J. Phys. Chem. A* **105**, 1951 (2001).
- [49] D. Sebastiani, G. Goward, I. Schnell and H. W. Spiess, *J. Mol. Struct. (THEOCHEM)* **625**, 283 (2003).

- [50] D. Sebastiani, *ChemPhysChem* **7**, 164 (2006).
- [51] J. C. Grossman, E. Schwegler, E. W. Draeger, F. Gygi and G. Galli, *J. Chem. Phys.* **120**, 300 (2003).
- [52] D. Sebastiani, *Mod. Phys. Lett. B* **17**, 1301 (2003).
- [53] J. R. Yates et al., *Phys. Chem. Chem. Phys.* **7**, 1402 (2005).
- [54] T. Gregor, F. Mauri and R. Car, *J. Chem. Phys.* **111**, 1815 (1999).